Modelling the Breakup of Droplets in a Turbulent Jet



Rachel Philip

St Anne's College

University of Oxford

A thesis submitted for the degree of

Doctor of Philosophy

Trinity 2018

Acknowledgements

I would like to thank my supervisors, Ian Hewitt and Peter Howell, for all of their guidance and patience. Their ideas, advice and feedback throughout these last three years have been invaluable. I would also like to thank Rob Style for his help and direction as one of my supervisors during my first year of research.

I would like to express my appreciation to those at BP who supported this project for their input and insight. In particular, I'd like to thank my current and former industrial supervisors, Dan Touzel and Peter Evans, for many interesting and helpful discussions.

I am grateful to the EPSRC CDT in Industrially Focused Mathematical Modelling and its co-directors Chris Breward and Colin Please for supporting and setting up this DPhil project.

Thanks to my friends for the many enjoyable times throughout the past few years.

Finally, I'd like to thank my parents and sister for their support, encouragement and prayers.

Abstract

In this thesis, we model the breakup of oil droplets in a turbulent jet and the effect of surfactants in enhancing this process. The problem is motivated by deep-sea oil spills where, hundreds of metres below the sea surface, a pipe transporting oil ruptures and a turbulent oil jet is released into the sea. The jet's turbulent mixing breaks up the oil into smaller droplets. These droplets are then eaten by microbes in the sea. To encourage this natural clean-up process, surfactants are added to the oil jet to reduce the oil-water surface tension and encourage droplet breakup. Our aim is to understand how to best apply the surfactant to maximise droplet breakup. To do so, we first examine and unify the large scale jet and small scale droplets without the presence of surfactants. We then incorporate the effect of surfactant addition to these models.

We begin by modelling an axisymmetric turbulent oil jet. Our key approach is to take advantage of the self-similarity of a jet to find similarity solutions for its velocity field and energy. Scaling laws are then used to understand the breakup of droplets due to turbulent mixing. We combine these large-scale jet models and small-scale drop models, using droplet population models to predict the droplet size distributions at different locations in the jet. We first do so numerically. We then find similarity solutions for the drop size distribution, by taking advantage of the self-similarity of the jet.

Finally we include the effect of surfactants. We use numerical and asymptotic methods to model their effect on the drop size distribution. This allows us to address two important questions: how much surfactant should be used and where should it be injected.

Contents

1 Introduction **1**

1.1 Background 1

1.2 Existing approaches to the problem 3

1.2.1 Small-scale oil spill experiments by SINTEF 3

1.2.2 Other approaches 4

1.3 Parameters and scales 5

1.4 Our approach and plan of thesis 6

2 Mathematical modelling of turbulent jets **9**

2.1 Modelling assumptions 10

2.2 Modelling turbulent flows 11

2.2.1 Background 11

2.2.2 Reynolds averaged Navier-Stokes equations 11

2.2.3 Energy equation 12

2.2.4 Closure 13

2.3 Numerics - CFD 14

2.3.1 Numerics for $k - \epsilon$ model 14

2.3.2 Other turbulence models 17

2.3.3 Discussion 20

2.4 Similarity solution 21

2.4.1 Dimensionless model 21

2.4.2 Velocity 22

2.4.3 Energy 25

2.4.4 Comparisons to numerics for $k - \epsilon$ model 28

2.4.5 Full similarity solution for $k - \epsilon$ model 33

2.4.6 Discussion 33

2.5 Width-averaged models 35

2.6 Conclusions 39

3 Droplet breakup **40**
3.1 Master equation . . . 40
3.1.1 Discrete-volume model . . . 41
3.1.2 Continuous-volume model . . . 43
3.1.3 Non-dimensionalisation . . . 43
3.1.4 Coalescence . . . 44
3.1.5 Comparison to literature . . . 44
3.2 Scaling laws . . . 44
3.2.1 Maximum stable drop size . . . 44
3.2.2 Breakup rate . . . 47
3.2.3 Daughter drop distribution . . . 51
3.3 Evolution of drop size distribution with time . . . 54
3.3.1 Numerical method . . . 54
3.3.2 Results . . . 55
3.3.3 Testing convergence . . . 56
3.3.4 Different χ . . . 58
3.4 Conclusions . . . 60

4 Combining large-scale jet and small-scale droplets **61**
4.1 Modelling assumptions . . . 62
4.2 Modelling distribution of droplet sizes . . . 63
4.2.1 A note on the turbulent transport of scalars . . . 63
4.2.2 Master equation . . . 64
4.3 Total oil fraction Φ . . . 65
4.3.1 Discussion . . . 67
4.4 Two-dimensional models . . . 67
4.4.1 Full numerical approach . . . 67
4.4.2 Efficiency of droplet breakup . . . 71
4.4.3 Sensitivity to initial conditions . . . 73
4.4.4 Variation of fully-developed distribution with dimensionless parameters . . . 75
4.4.5 Using similarity solution for velocity and dissipation . . . 75
4.4.6 Discussion . . . 77
4.5 One-dimensional width-averaged models . . . 77
4.5.1 Assumptions and governing equations . . . 77
4.5.2 Total Oil Fraction . . . 79

4.5.3 Two bin volume fraction model . . . 80
4.5.4 Full distribution model . . . 81
4.5.5 Compare one and two dimensional models . . . 83
4.5.6 Fitting to experimental results . . . 85
4.5.7 Discussion . . . 88
4.6 Conclusions . . . 89

5 Droplet size distribution - similarity solution 92
5.1 Model setup and outlook . . . 93
5.1.1 Converting to similarity coordinates . . . 93
5.1.2 Assumptions about breakup rate . . . 94
5.1.3 Simplifications and outlook . . . 95
5.1.3.1 Approximate similarity solution for ϵ . . . 96
5.1.3.2 Volume discretised model . . . 96
5.1.3.3 Monotonic breakup rate . . . 97
5.1.3.4 Outlook . . . 98
5.2 Eigenvalues and eigenfunctions of the linear operator . . . 98
5.2.1 Eigenvalue equation . . . 99
5.2.2 Leading eigenvalues and eigenfunctions . . . 100
5.2.2.1 Small K . . . 100
5.2.2.2 Large K . . . 102
5.2.3 Higher eigenvalues and eigenfunctions . . . 103
5.2.4 Using true similarity solution for ϵ . . . 104
5.2.4.1 Small K . . . 105
5.2.4.2 Large K . . . 107
5.3 Approximate similarity solutions . . . 109
5.3.1 Two bins . . . 111
5.3.2 Three bins . . . 116
5.3.3 N bins . . . 118
5.3.4 Continuous distribution . . . 120
5.3.4.1 An analytical solution . . . 122
5.3.4.2 Similarity solution compared to numerics . . . 124
5.3.5 Discussion . . . 125
5.3.5.1 Using true similarity solution for ϵ . . . 126
5.3.5.2 Comparing to full CFD numerics . . . 127
5.3.5.3 Limitations . . . 128

5.4 Full solutions . . . 128
5.4.1 Drawback of the assumptions made in Section 5.3 . . . 128
5.4.2 General approach . . . 131
5.4.3 Total oil fraction Φ - 'zero bins' . . . 134
5.4.4 Three bins . . . 135
5.4.5 Comparison with approximate similarity solution . . . 137
5.4.6 N bin and continuous volume model . . . 140
5.4.7 Discussion . . . 141
5.5 Non-monotonic breakup rates . . . 142
5.5.1 What goes wrong? . . . 142
5.5.2 Approximate similarity solution . . . 142
5.5.3 Full similarity solution . . . 146
5.5.4 Discussion . . . 149
5.6 Conclusions . . . 151

6 Surfactants **154**
6.1 Assumptions . . . 155
6.2 Surfactant models . . . 155
6.2.1 Introduction to surfactants . . . 155
6.2.2 Relating surface tension to surfactant concentration . . . 156
6.2.3 Surfactant interactions . . . 157
6.2.3.1 Formation of micelles . . . 157
6.2.3.2 Adsorption of surface monomers onto droplets . . . 158
6.2.3.3 Production of free monomers . . . 159
6.2.4 Non-dimensionalisation . . . 159
6.2.5 Equilibrium . . . 161
6.2.6 Parameter values from literature . . . 161
6.3 Zero-dimensional model . . . 163
6.3.1 Model . . . 164
6.3.2 Moments . . . 164
6.3.3 $\mathcal{R}_0$, $1/\mathcal{K}_0$, $1/\mathcal{K}_a$, $1/N_m$ small . . . 167
6.3.4 Small η . . . 171
6.3.5 Full distribution model . . . 173
6.4 Combining jet, droplet and surfactant models . . . 175
6.5 One-dimensional jet models . . . 177
6.5.1 Boundary conditions . . . 178

6.5.2 Moments . . . 179
6.5.3 $\mathcal{R}_0$, $1/\mathcal{K}_0$, $1/\mathcal{K}_a$, $1/N_m$ small . . . 180
6.5.4 η small . . . 184
6.5.5 Full distribution models . . . 188
6.5.6 Evaluating the efficiency of dispersants . . . 191
6.6 Comparison to experiments . . . 193
6.7 Adding different surfactant concentration . . . 197
6.8 Addition of surfactant at different heights . . . 199
6.9 Conclusions . . . 203

7 Conclusions **207**
7.1 Summary of Results . . . 207
7.2 Future Work . . . 210

A Boundary conditions for $k-\epsilon$ numerical implementation **213**
A.1 Wall functions . . . 213

B Extra surfactant asymptotics **216**
B.1 Box - η, $\mathcal{R}_0$, $1/\mathcal{K}_0$, $1/\mathcal{K}_a$, $1/N_m$ small . . . 216

Bibliography **221**

List of Figures

1.1 Oil jet produced in a deep-sea oil spill. 2
1.2 Experimental drop size distribution from Brandvik et al. (2014), showing effect of increasing surfactant concentration. 3
1.3 Model overview - macroscale and microscale. 6

2.1 Numerical simulations of an axisymmetric turbulent jet: (a) velocity, (b) turbulent kinetic energy and (c) energy dissipation using $k-\epsilon$ turbulence model. 16
2.2 Comparison of $k-\epsilon$ model with realisable $k-\epsilon$ model and $k-\omega$ model. 19
2.3 Similarity solution for (a) vertical velocity and (b) transverse velocity. 25
2.4 Similarity solution for turbulent kinetic energy and energy dissipation, and asymptotic approximations for small $\hat{\nu}$. 27
2.5 Unscaled and scaled numerics ($k-\epsilon$ model) for jet velocity components with their similarity solutions. 30
2.6 Unscaled and scaled numerics ($k-\epsilon$ model) for jet energy with their similarity solutions. 31
2.7 Scaled numerics for eddy viscosity with its similarity solution. 32
2.8 Scaled numerics ($k-\epsilon$ model) for jet velocity components with full similarity solution as calculated in Ghazzawi and Rabadi (1994). . . . 34
2.9 Jet Schematic. 35
2.10 (a) Vertical velocity and (b) energy dissipation from similarity solution in Subsections 2.4.2–2.4.3 compared to width-averaged models at $z=5$. 38

3.1 Different choices for the breakup rate γ. 50
3.2 Daughter drop distributions. 52
3.3 Drop size distribution without spatial dependence and with fixed energy dissipation 56
3.4 Drop size distribution ϕ for different bin sizes N 57

3.5 Drop size distribution without spatial dependence and with fixed energy dissipation: effect of different forms of χ 59

4.1 Drop size distributions in two spatial dimensions calculated fully numerically, with a reminder of the variation in total oil fraction and energy dissipation with space. 69
4.2 Full developed state at fixed height $z = 115$ obtained from numerical drop size distributions in two spatial dimensions. 71
4.3 Cumulative distribution from two-dimensional models. 72
4.4 Comparison of drop size distributions with different initial size distributions. 74
4.5 Variation of fully developed drop size distribution with non-dimensional parameters K_0 and C_1. (a) We set $C_1 = 3.51 \times 10^{-7}$ and vary K_0. (b) We take $K_0 = 0.290$ and vary C_1. 76
4.6 Comparison between using full numerics for velocity and dissipation and their similarity solutions in determining droplet size distribution, for parameter $\hat{z} = 5, 10$. 78
4.7 width-averaged, two bin model of drop size distribution. 81
4.8 Comparison between $\overline{\gamma}(\epsilon)$ and our approximation $\gamma(\overline{\epsilon})$ for parameter values $K_{00} = 0.25$, $C = 0.725$ and $d_\infty = 500\mu$m for fixed $z = 10$. . . . 82
4.9 Drop size distributions from width-averaged model, taking $\hat{z} = 2, 5, 10$. 84
4.10 Comparisons between drop size distributions for two-dimensional models and one-dimensional width-averaged models. We take (a) $\hat{z} = 2$; (b) $\hat{z} = 5$. 86
4.11 Comparison between model and small-scale experiments (Brandvik et al., 2014, 2013; Johansen et al., 2013). 88

5.1 Eigensolution and eigenvalues of the main similarity equation. Eigenvalues when breakup parameter K is small and large are also shown. 101
5.2 Comparison of asymptotics for eigensolution when K is small. 102
5.3 Comparison of asymptotics for eigensolution when K is large. 103
5.4 Higher eigenvalues and eigenfunctions of linear operator. 104
5.5 Eigenfunctions and eigenvalues of the similarity equation using the true similarity solution for ϵ. 106
5.6 Eigenfunctions and eigenvalues of the similarity equation using the true similarity solution for ϵ, for small K. 107

5.7 Eigenfunctions and eigenvalues of the similarity equation using the true similarity solution for ϵ, for small K. 110
5.8 Similarity solution for ϕ_2 in two bin model, compared to numerical solution. 115
5.9 Similarity solution for drop size distribution with two bins. 115
5.10 Comparing similarity solution for drop size distribution with three bins to numerics. 119
5.11 Schematic showing the order in which we solve the C_{ij} using recurrence relations (5.3.33)–(5.3.34). 121
5.12 Analytic continuous volume similarity solution for breakup rate $K(v) = v^{-1/2}$ and $\chi(v, \tilde{v}) = 1/\tilde{v}$. 124
5.13 Comparison of discrete volume similarity solution for ϕ with full numerical results. 125
5.14 Comparison of discrete volume similarity solution for ϕ with full numerical results using true similarity solution for ϵ. 126
5.15 Comparison of similarity solution for ϕ with full numerical results using CFD numerics for velocity fields and ϵ. 129
5.16 Comparison of numerics, approximate similarity solution and full similarity solution for ϕ_1 in three bin case, for the same problem as in Figure 5.10. 139
5.17 Comparison of numerics, approximate similarity solution and full similarity solution for ϕ_1 in three bin case, for a similar problem to that in Figure 5.10 but with $\hat{z}_n = 5$ and $\hat{z} = 5.1$. 140
5.18 Comparison of discrete volume similarity solution for ϕ with full numerical results when breakup rate is non-monotonic. 146
5.19 Comparing different approaches for solution to ϕ_2 in three bin case for non-monotonic K. 150
5.20 Schematic of $m(v)$ for an example when the breakup rate is non-monotonic. 151

6.1 Schematic of interactions between surfactant micelles and monomers, and oil drops. 157
6.2 Variation of drop and surfactant behaviour with time, when $\mathcal{R}_0$, $1/\mathcal{K}_0$, $1/\mathcal{K}_a$ and $1/N_m$ are small. 166
6.3 Variation of droplet and surfactant behaviour with time, when $\eta, \mathcal{R}_0$, $1/\mathcal{K}_0$, $1/\mathcal{K}_a$ and $1/N_m$ are small. 172

6.4 Full numerical solution for droplet and surfactant behaviour with time, using more realistic breakup rate (6.3.43) and full-volume range. . . . 174
6.5 Variation of droplet and surfactant behaviour with height in jet using moments to average over volume. We consider the case where $\mathcal{R}_0$, $1/\mathcal{K}_0$, $1/\mathcal{K}_a$ and $1/N_m$ are small. 181
6.6 Variation of droplet and surfactant behaviour with height in jet using moments to average volume. We consider the case where $\eta, \mathcal{R}_0$, $1/\mathcal{K}_0$, $1/\mathcal{K}_a$ and $1/N_m$ are small. 186
6.7 Variation of drop and surfactant behaviour with height, using width-averaged, full-volume models. 189
6.8 Effectiveness of droplet breakup in the presence of surfactant using width-averaged, full-volume models. 192
6.9 Comparison between model and small-scale experiments for different surfactant concentrations. 194
6.10 Variation of drop size distribution with varying k_0^- 196
6.11 Changing c_0, the starting free monomer concentration at $z = \hat{z}$. . . . 197
6.12 The effect of the addition of different concentrations of surfactant on the surfactant and droplet properties. 198
6.13 Evolution of droplet and surfactant properties with height, for different values of z_a. 200
6.14 Drop size distribution when injecting surfactant in the jet at different heights $z = z_a$. 201
6.15 Comparison between model and small-scale experiments for different heights of surfactant injection. 204

B.1 Variation of droplet and surfactant behaviour with time, when η, $\mathcal{R}_0$, $1/\mathcal{K}_0$, $1/\mathcal{K}_a$ and $1/N_m$ are small. 217

Chapter 1

Introduction

1.1 Background

An increasing demand for energy has led oil producers to turn to less readily accessible sources of oil and gas. In particular, offshore deep-sea extraction has become more common. However, as with all oil production, this comes with a risk of an accidental blow-out, that is, an uncontrollable release of oil and gas into the sea. The most famous recent example of a deep-sea blow-out is BP's Gulf of Mexico oil spill: oil flowed upwards from a broken pipe at the bottom of the sea for 87 days, releasing 800 million litres of oil and forming an oil slick which covered an area of up to 175,000 km^2 (Michel et al., 2013; Norse and Amos, 2010). Oil spills like the Gulf of Mexico, pose significant risks to marine wildlife and plant life: in the water column, at the ocean surface and (once surface oil has washed ashore) in shoreline habitats (Clark et al., 2014). Whilst spill prevention is the first priority, in the event a blow-out occurs, oil production companies such as BP aim to minimise the impact of these environmental hazards. BP have put forward and supported this project to better understand what happens in a deep-sea oil spill and the effectiveness of certain response options.

To minimise environmental damage in oil spills, there are a number of common response options (Clark et al., 2014). Floating barriers called booms are used to contain the oil and prevent it from polluting environmentally sensitive areas. Skimmers and in situ burning of oil can then be applied to remove it from the water. Labour intensive shoreline cleaning is often necessary. Additionally, dispersant is sprayed, traditionally at the sea surface. Dispersants consist of surfactants dissolved in solvents; the surfactants lower the oil-water surface tension and thus facilitate the break up of oil. These response options predominantly aim to break down and remove oil at the surface of the sea and on the shore.



Figure 1.1: Oil jet produced in a deep-sea oil spill.

In a deep-sea oil spill, a natural clean-up process occurs. When a pipe bursts hundreds of metres below the sea surface, a highly turbulent oil jet is released into the sea, as seen in Figure 1.1. The jet's vigorous turbulent mixing breaks up oil drops into smaller droplets. These droplets are mixed with the seawater and consumed by naturally occurring microbes in the sea. It is beneficial to take advantage of this natural clean-up process since, when oil is broken down and dispersed in the water column, less reaches the sea surface and washes ashore.

This process works best when small oil droplets are produced since these rise less rapidly (in a matter of days or weeks rather than a few hours as large drops would) and are more likely to be transported away from the spill location by undersea ocean currents (Brandvik et al., 2016). Moreover, they provide a greater surface area for microbial degradation to occur. Thus, smaller droplets will lead to a thinner oil slick forming. Drops preferably need to have diameters less than 50-70 microns for droplet rise and microbial degradation to be maximally effective (Clark et al., 2014; Lehr, 2001).

To facilitate the breakup of oil drops into these 50 micron droplets, dispersants can be injected into the oil jet near the sea-bed, rather than at the sea surface. Whilst spraying dispersants at the sea surface relies on waves to provide a mixing action, injecting them into the rising oil jet means its highly turbulent motion induces more effective breakup of the oil into droplets. This technique was implemented, with some success, in the Gulf of Mexico oil spill. Therefore, it would be useful to further explore its effectiveness. Currently, vast quantities of dispersant are used: the dispersant to oil ratio can be as high as 1:7. However, there are practical and logistical constraints to their use. Injecting dispersant at an optimum jet location should reduce the amount required.

Our aim is to better understand the oil droplet breakup process and the effect of adding dispersant to a deep-sea oil jet. Ultimately, we want to address the questions

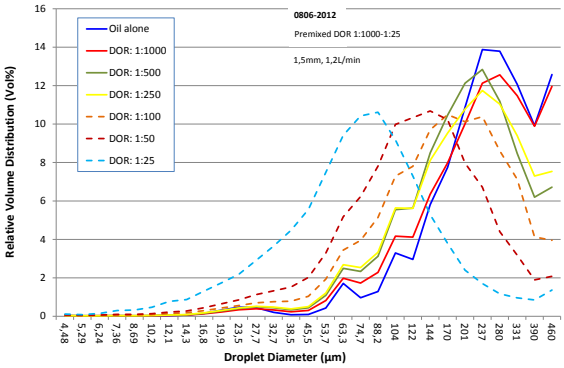


Figure 1.2: Experimental drop distribution with varying surface tension (controlled by changing dispersant to oil ratio DOR) reproduced from Brandvik et al. (2014).

of how much dispersant should be added and where, and provide some 'best practice principles' for the use of dispersants in oil spills.

1.2 Existing approaches to the problem

1.2.1 Small-scale oil spill experiments by SINTEF

There are many complexities in modelling a deep-sea oil spill and these are compounded by the lack of data on these real world scenarios available for comparison. Therefore, experiments by Brandvik et al. (2014), Brandvik et al. (2013) and Johansen et al. (2013) have considered a smaller scale oil spill scenario, investigating the distribution of drops emanating from a jet in a tower tank facility. This tower tank is intended to mimic the aspect ratio of a real life oil jet and, while it obviously cannot capture the full behaviour of the system, it provides interesting insights into droplet breakup in a turbulent jet. Plots like Figure 1.2 are made which show the fully developed drop size distribution at a large height in the tank. Here they take several logarithmically spaced drop size ranges and illustrate the volume fraction of the oil drops whose diameter is in each size range. The different curves correspond to experiments with different amounts of dispersant, with dispersant to oil ratios (DORs) of up to 1:25.

These experiments provide insights into the effects, on drop size distribution, of varying:

- **Nozzle diameter**: smaller nozzle diameter corresponds to smaller drop sizes.
- **Flow rate**: faster flow rates produce smaller drops (due to increased shear).

- **Dispersant to oil ratio**: increasing the amount of dispersant reduces the surface tension and thus enables the formation of smaller droplets.

- **Dispersant application**: adding dispersants to the oil before it is released produces smaller droplets than injecting the dispersant into the jet. Injecting dispersant closer to the nozzle produces smaller droplets.

These experiments will be further discussed in Chapter 4 and compared with our models in Chapters 4 and 6.

1.2.2 Other approaches

Other previous examinations of droplet breakup in turbulent flow have also been largely experimental. These experimental results are compared to scaling laws for maximum stable drop sizes. These laws are derived by Hinze (1955) and Calabrese et al. (1986) and used throughout the literature (Brandvik et al., 2013; Vankova et al., 2007). See Chapter 3 for more details. Several authors take this further, considering semi-empirical relations for droplet collision frequency, breakage efficiency and breakup probability density functions, to better understand the breakup of a drop in turbulence (Bandara and Yapa, 2011; Coulaloglou and Tavlarides, 1977; Martínez-Bazán et al., 1999a,b; Tsouris and Tavlarides, 1994; Zhao et al., 2014b,a). These are outlined in Chapter 3.

There have been some attempts in the literature to unify droplet breakup models with jet models to determine how breakup varies at various heights of the jet (Bandara and Yapa, 2011; Zhao et al., 2014a; Nissanka and Yapa, 2016). However, these use complex breakup rates and do not include the effects of varying surface tension, which is important to understand the application of dispersants. We use a similar approach to these authors but use simpler and perhaps more reasonable breakup rates to be able to make more progress, particularly in including the effects of surfactant.

The approach BP currently use could be considered the opposite of this, focussing on tracking the fate of the oil as it rises to the sea surface rather than the droplet breakup. They use the SINTEF Oil Spill Contingency and Response (OSCAR) model which consists of three main aspects (Johansen, 2000; Socolofsky et al., 2015; Yapa and Li, 1997; Zheng et al., 2003):

- At the nozzle exit the model uses scaling laws for maximum stable droplet size (similar to those in Chapter 3) to obtain an initial distribution of drop and bubble sizes.

- A Lagrangian plume model represents the plume as a collection of non-interacting spherical particles. Each particle is characterised by parameters such as mass, velocity, temperature, gas to oil ratio etc, which change as a particle moves up the plume.

- Lagrangian particle tracking is used to model the transport of oil and gas in the far field region where the plume dynamics is no longer important.

1.3 Parameters and scales

Parameter	Typical Values	
	Real	Experimental
Radius of Hole b_0 (m)	0.25	7.5×10^{-4}
Diameter of Hole D (m)	0.5	1.5×10^{-3}
Jet Height Below Sea Surface (m)	200	6
Velocity of Jet at Exit W_0 ($\mathrm{m\,s^{-1}}$)	10	11.3
Untreated oil-seawater surface tension σ_0 ($\mathrm{kg\,s^{-2}}$)	0.03	0.0155
Density of oil ρ_o ($\mathrm{kg\,m^{-3}}$)	837	846.54
Density of water ρ_w ($\mathrm{kg\,m^{-3}}$)	1000	1000
Dynamic viscosity of oil μ_o ($\mathrm{kg\,m^{-1}\,s^{-1}}$)	4×10^{-3}	5×10^{-3}
Dynamic viscosity of water μ_w ($\mathrm{kg\,m^{-1}\,s^{-1}}$)	8.94×10^{-4}	8.94×10^{-4}
Kinematic viscosity of oil ν_o($\mathrm{m^2\,s^{-1}}$)	4.78×10^{-6}	5.91×10^{-6}
Kinematic viscosity of water ν_w ($\mathrm{m^2\,s^{-1}}$)	8.94×10^{-7}	8.94×10^{-7}
Velocity of drops with respect to mean flow u_d ($\mathrm{m\,s^{-1}}$)	0.1 - 1	0.1 - 1
Typical drop diameter d (m)	100×10^{-6}	100×10^{-6}
Momentum flux at jet exit $M_0 = \pi b_0^2 W_0^2$ ($\mathrm{m^4\,s^{-2}}$)	19.63	9.03×10^{-4}
Buoyancy flux at jet exit $F_0 = g(\rho_w - \rho_o)\pi b_0^2 W_0/\rho_o$ ($\mathrm{m^4\,s^{-2}}$)	3.14	1.42×10^{-4}
Shear timescale $\tau = D/W_0$ (s)	0.05	1.33×10^{-4}
Reynolds number $Re = b_0 W_0/\nu_o$	5×10^5	2868
Droplet Reynolds number $Re_d = du_d/\nu_o$	1 - 10	1 - 10
Weber number $We = \rho_o u_d^2 d/\sigma$	0.03 - 3	0.05 - 5

Table 1.1: Typical material parameters and scales for the real and the experimental scale and the values of dimensionless numbers determined from these.

In real-life oil spills, the parameters vary widely. The pipe nozzle size, the velocity at which oil jets out of this hole, the seawater conditions and the type of oil being released will all vary depending on location. We will use some indicative values in our models, which are based on common situations but do not represent any one specific real scenario. It is reasonable to take the released oil to be a Brent crude: a standard blend of oils commonly sold by oil producers, whose properties are detailed in (B. P., 2014). The literature (Bandara and Yapa, 2011) and conversations with BP (personal communication, BP) suggest the typical parameter values shown in Table 1.1, which we shall use henceforth. For comparison we also present the corresponding values in small-scale experiments from (Brandvik et al., 2013, 2014) which will be discussed in Chapters 4 and 6.

1.4 Our approach and plan of thesis

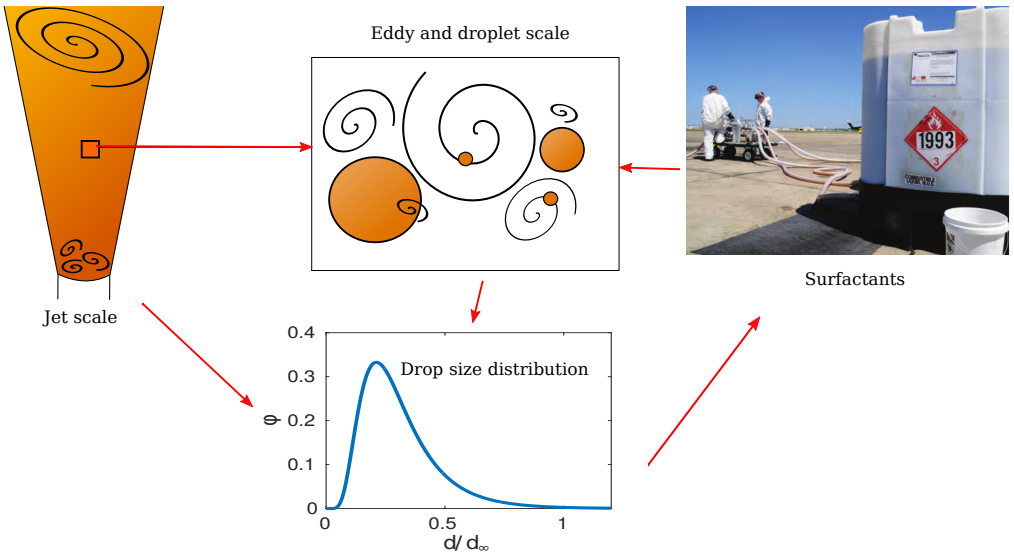


Figure 1.3: Model overview - macroscale and microscale.

Our aim is to model the distribution of oil droplet sizes. To do so, we examine and unify macroscopic scales (the large scale turbulent jet) and microscopic scales (the different sized oil drops and turbulent eddies), as illustrated in the schematic in Figure 1.3.

We first address the macroscopic turbulent jet scale in Chapter 2. Turbulent jets are characterised by their velocity, turbulent kinetic energy and energy dissipation. It is important to understand the energy dissipation as it is used as a measure of the energy available for droplet breakup. We solve turbulence models to model the

axisymmetric jet. We then simplify our approach by finding similarity solutions, and then average these over width to reduce the problem to only one spatial dimension.

Next we turn to the microscopic droplet scale in Chapter 3. This is predominantly a literature review. We discuss how interactions between droplets and the eddies in the surrounding turbulent flow lead to droplet deformations and breakup. We consider different scaling relations for the rate at which droplets break up. This depends on the droplet size, the energy dissipation in the flow surrounding the drop, and the surface tension. Macroscopic and microscopic scales come together in this breakup rate since it depends on the macroscopic energy dissipation in the jet. We use these breakup rates and combine them with droplet population models to predict the droplet size distributions in a homogeneous environment, with constant energy dissipation and surface tension. This enables us to understand how the distributions evolve before introducing the complications of jet flow.

In Chapter 4 we relax the assumption of homogeneous turbulence and predict droplet size distributions along a turbulent jet, combining the large-scale jet models and the small-scale droplet models. We make the simplifying assumption that the coupling of macroscopic and microscopic scales is one way so that, whilst the behaviour of the jet affects droplet breakup, the motion and breakup of droplets has a negligible influence on the macroscopic flow. This is true provided the water and oil have similar densities and viscosities, buoyancy is not significant, and surface tension effects are not too large. We use models in both two spatial dimensions and simplified width-averaged models to predict the droplet size distribution. The width-averaged models are then compared with small-scale experiments to validate them and to fix an unknown parameter in our models.

Determining the drop size distribution in two spatial dimensions in Chapter 4 is computationally expensive. Therefore, in Chapter 5, we use the self-similar jet model obtained in Chapter 2 to find similarity solutions for the droplet size distribution. Assuming the jet's velocity and energy dissipation are given by their similarity solutions, we can find an analytical formula for the droplet size distribution.

Finally, we consider the effect of injecting surfactants into the system, in Chapter 6. The addition of surfactants reduces the surface tension and this increases the droplet breakup rate. This leads to a shift in the droplet size distribution towards smaller drop sizes. However, by changing the droplet size distribution and producing more small drops, the addition of surfactants increases the surface area of drops. Thus, there is a greater area across which the surfactant must spread and this, combined with the effects of dilution, means the efficacy of the surfactants eventually diminishes.

To better understand the interactions between the surfactant and oil droplets, we first neglect the complications of the jet; we model the evolution of droplet and surfactant behaviour in a region of homogeneous turbulence, with constant energy dissipation. We then incorporate the effects of the jet. We predominantly use one-dimensional jet models here since they are simpler to understand and, in Chapter 4, we find that they replicate the two-dimensional behaviour well. Our models are compared with a range of small-scale experiments for validation. Once we are confident of their predictions, we use these models to assess the use of dispersants in various possible scenarios. We investigate the concentration of surfactant needed and the best place to inject it.

Chapter 2

Mathematical modelling of turbulent jets

In this chapter we investigate the turbulent jet, with the aim of determining the macroscopic quantities in the jet which control droplet breakup, namely its velocity, turbulent kinetic energy and energy dissipation. The turbulent energy dissipation rate provides a measure of the intensity of the turbulent flow and thus, is used prevalently in the literature to characterise the energy that goes into deforming and breaking up the droplets in the jet. It is, therefore, an important ingredient in determining the rate at which droplets break up and hence in determining the droplet size distribution (Martínez-Bazán et al., 1999b; Zhao et al., 2014b).

Our initial approach is to apply various well-known turbulence models to numerically compute the flow in the jet. This computational approach produces very detailed and complex simulations. However, we are most interested in the gross features of the flow which ultimately determine the behaviour of droplets in the jet. We, therefore, exploit the approximate scale invariance of the fully developed jet to find universal similarity solutions for the flow. It is well known that, provided the eddy viscosity does not vary with jet width, there are analytical similarity solutions for the jet velocity, which agree well with experimental results (Davidson, 2015; Pope, 2000). We extend this idea to produce similarity solutions for the turbulent kinetic energy and energy dissipation in the jet. Our approach can be compared with that of Paullay et al. (1985) and Ghazzawi and Rabadi (1994), who find similarity solutions for the fully coupled $k-\epsilon$ model system of equations describing the jet's velocity and energy.

The simplest models which capture the basic physics of the problem are width-averaged models, following the classical approach of Morton et al. (1956). These are obtained by averaging our similarity solutions across the jet width, thereby reducing the problem to one spatial dimension, namely height.

2.1 Modelling assumptions

We model a steady jet; this is reasonable for most of the lifetime of the blowout. We also take it to be axisymmetric. Exterior to the jet, the seawater is assumed to have no additional source of disturbance other than the jet. Thus, the seawater will have negligible vertical velocity but a small horizontal velocity due to the entrainment of seawater into the jet, causing it to grow in width. It is observed in experiments and numerical simulations that turbulent jets tend to be long and thin, and this allows for simplification of the relevant mathematical models.

This thesis is ultimately interested in the effects of spraying surfactants in the region where its turbulent mixing energy coupled with the decrease in surface tension due to the addition of surfactants will be able to contribute significantly to the droplet breakup process. Therefore, we focus on the region where the flow is driven mainly by momentum rather than by buoyancy. (Note that when we refer to the 'jet', this usually means the momentum-driven region whilst 'plume' refers to the buoyancy-driven region.)

Scalings can be used to approximate the length up the plume where it is momentum driven and where buoyancy becomes significant. Using dimensional analysis, as in Papanicolaou and List (1988), we construct a length-scale L_b in terms of the momentum flux $M_0 = \pi b_0^2 W_0^2$ and the buoyancy flux $F_0 = g(\rho_w - \rho_0)\pi b_0^2 W_0/\rho_0$. We find $L_b = M_0^{3/4} F_0^{-1/2}$ and so

$$\frac{L_b}{2b_0} = \frac{\pi^{1/4}}{2}\sqrt{\frac{\rho_o}{\rho_w - \rho_o}}\frac{W_0}{\sqrt{gb_0}}. \tag{2.1.1}$$

(Recall that b_0 is the inlet nozzle radius, W_0 is the inlet velocity, ρ_o is the oil density, ρ_w is the water density and g is the gravitational constant.) Experiments by Papanicolaou and List (1988) suggest that above the height $5L_b$, the flow is a buoyancy driven plume. For a typical real life situation (with $b_0 = 0.25\,\mathrm{m}$ and $W_0 = 10\,\mathrm{m/s}$) $5L_b$ corresponds to around 26 m or 52 nozzle diameters and for the experimental scenario (with $b_0 = 7.5 \times 10^{-4}\,\mathrm{m}$ and $W_0 = 11.3\,\mathrm{m/s}$), $5L_b$ is around 1.54 m or 1030 nozzle diameters. Thus, our assumption that buoyancy can be neglected is reasonable below these heights. Having neglected buoyancy, we treat density as constant since buoyancy is the only place where the density variations would be important.

We are modelling a momentum dominated turbulent jet, in which relatively small variations in density and viscosity are not expected to be very important. Hence, we treat the spill as a turbulent water flow with a low oil fraction to avoid the complexities

of multiphase fluids. In a deep-sea oil spill, sand and dissolved gases may be released as well as oil and saline water.

2.2 Modelling turbulent flows

2.2.1 Background

Throughout this chapter we model the flow of a turbulent jet. Before we begin, however, let us first briefly outline some principles and motivation behind the modelling of turbulent flows (Hinze, 1975; Pope, 2000; Kuzmin et al., 2007; Davidson, 2015; Tennekes and Lumley, 1972; Schlichting and Gersten, 2003).

Turbulent flows are characterised by complex, irregular and chaotic motions, where the velocity field fluctuates over time and space. The generally accepted picture is that a turbulent flow consists of a range of eddies of different sizes. These eddies can be thought of as parcels of energy and vorticity, which are "stretched and twisted" by their velocity field (Davidson, 2015). The larger eddies (called energy-carrying eddies) carry large amounts of energy, which goes into creating and supplying smaller eddies. This process can be thought of as a cascade where larger eddies use their energy to create smaller eddies and give their energy to these smaller eddies, which in turn create even smaller eddies. Finally, at the scale of the smallest eddies, the local Reynolds number is no longer large, viscous effects become important and the energy of these smallest eddies is dissipated.

The multi-scale nature of turbulence presents significant difficulties in modelling turbulent flows. There is a compromise to be met in producing manageable models whilst also resolving the important properties of the flow. We focus on Reynolds Averaged Navier-Stokes (RANS) models, which decompose the flow into the mean flow and the turbulent fluctuations, which scale with the amplitude of the larger eddies. Such models rely on closure equations, which approximate the fluctuations due to the eddies and thereby enable us to resolve the mean flow.

2.2.2 Reynolds averaged Navier-Stokes equations

Let us consider the Navier-Stokes equations for an incompressible fluid given by

$$\frac{\partial u_i}{\partial x_i} = 0, \tag{2.2.1}$$

$$\rho \frac{Du_i}{Dt} = -\frac{\partial p}{\partial x_i} + \mu \frac{\partial^2 u_i}{\partial x_j \partial x_j}, \tag{2.2.2}$$

where u_i are the velocity components, p is the pressure, x_i are the spatial coordinates, t is time, and ρ and μ are the constant density and viscosity. In RANS models, the velocity is decomposed as

$$u_i = U_i + \tilde{u}_i, \tag{2.2.3}$$

so it comprises U_i, the mean velocity (averaged over some time T which is large compared to the time-scale of the fluctuations), and $\tilde{u}_i$, the velocity fluctuations in time. Note here the mean velocity U_i is independent of t. As with velocity, pressure is similarly decomposed into $p = P + \tilde{p}$. In this section, we denote standard properties of the flow with lower case letters, fluctuations with tildes and time-averages by a bar or with capital letters (so $\overline{u_i} = U_i$). We substitute these Reynolds decompositions into the Navier-Stokes equations (2.2.1)-(2.2.2) and time-average, yielding

$$\frac{\partial U_i}{\partial x_i} = 0 \tag{2.2.4}$$

and

$$U_j \frac{\partial U_i}{\partial x_j} = -\frac{1}{\rho}\frac{\partial P}{\partial x_i} + \nu \frac{\partial^2 U_i}{\partial x_j \partial x_j} - \frac{1}{\rho}\frac{\partial \tau_{ij}}{\partial x_j}, \tag{2.2.5}$$

where $\nu = \mu/\rho$ is the kinematic viscosity. Here $\tau_{ij} = -\rho\overline{\tilde{u}_i \tilde{u}_j}$ is known as the Reynolds stress tensor. Its important components are the off diagonal terms, which correspond to apparent shear stresses. They control the transfer of momentum by the turbulent motion (Tennekes and Lumley, 1972).

2.2.3 Energy equation

To understand the effect of turbulent fluctuations on the flow, we consider the equation governing $k = \frac{1}{2}\overline{\tilde{u}_i \tilde{u}_i}$, the mean kinetic energy of turbulence. Note that k has dimensions of $\mathrm{J\,kg^{-1}}$, which are not those of energy; the quantity $\rho k = \rho\overline{\tilde{u}_i \tilde{u}_i}/2$ actually has dimensions of energy density but it is conventional to refer to k as the kinetic energy. Subtracting the Reynolds momentum equation (2.2.5) from the Navier-Stokes momentum equation (2.2.2), multiplying by $\tilde{u}_i$ and averaging yields

$$U_i \frac{\partial k}{\partial x_i} = -\frac{\partial}{\partial x_i}\left(\frac{1}{2}\,\overline{\tilde{u}_i \tilde{u}_j \tilde{u}_j} + \frac{1}{\rho}\overline{\tilde{u}_i \tilde{p}}\right) + \nu \frac{\partial^2 k}{\partial x_i \partial x_i} + \left(-\overline{\tilde{u}_i \tilde{u}_j}\frac{\partial U_j}{\partial x_i}\right) - \nu\,\overline{\frac{\partial \tilde{u}_j}{\partial x_i}\frac{\partial \tilde{u}_j}{\partial x_i}}. \tag{2.2.6}$$

The rate of energy dissipation rate, ϵ, is defined such that

$$\epsilon = \nu\,\overline{\frac{\partial \tilde{u}_j}{\partial x_i}\frac{\partial \tilde{u}_j}{\partial x_i}}, \tag{2.2.7}$$

namely ϵ corresponds to the final term in (2.2.6). Note that, as with k, the dimensions of ϵ, namely $\mathrm{J\,kg^{-1}\,s^{-1}}$, are not consistent with its standard name: the rate of energy dissipation.

The first and second groups of terms on the right-hand side of (2.2.6) refer, respectively, to turbulent and viscous diffusion (since they are divergences of energy flux). The third term is production and signifies the extraction of energy from the mean flow into the kinetic energy of turbulence. The final term is the energy dissipation term; turbulent kinetic energy is dissipated by the deformation work of viscous stresses.

The turbulent kinetic energy equation (2.2.6) can be related to the accepted picture of turbulence outlined in Section 2.2.1. The turbulent fluctuations are of the scale of the larger eddies. Energy is extracted from the mean flow and goes into the turbulent kinetic energy of these large-eddy fluctuations (turbulent production). This energy is transferred into smaller eddies and the gain in energy of the large eddies (turbulent production) is balanced by viscous dissipation which occurs at the smaller scale (dissipation).

The energy dissipation, ϵ, is an important element in our models. As the energy cascades, passing from the larger eddies to the smaller eddies, the majority is transferred between the different scales; very little energy is lost in this process. It is at the small scale where most of the dissipation occurs in the form of viscous deformation, at a rate ϵ. Therefore a good measure of the rate at which kinetic energy is supplied into and through the eddy scales, from the large to the small eddies, is given by the dissipation ϵ. Hence it dictates the energy supplied by the larger eddies and so the energy of the turbulent fluctuations which drive droplet deformation. The dissipation is the main macroscopic quantity of the jet which is assumed to influence the microscopic droplet breakup.

2.2.4 Closure

We face the classic closure problem that the momentum equation (2.2.5) involves the Reynolds stresses τ_{ij}, which must be additionally determined. The governing equation for the Reynolds stress involves yet higher moments of the velocity and so forth. To proceed we must introduce closure assumptions, i.e. constitutive relations that close the model.

The turbulent viscosity hypothesis assumes that the Reynolds stress tensor can be written in a similar form to the Newtonian constitutive law for the viscous stress

tensor, namely

$$\tau_{ij} = -\rho\widetilde{u_i}\widetilde{u_j} = -\frac{2}{3}\rho k\delta_{ij} + \rho\nu_T\left(\frac{\partial U_i}{\partial x_j} + \frac{\partial U_j}{\partial x_i}\right), \tag{2.2.8}$$

where ν_T is called the kinematic eddy viscosity or the eddy viscosity. For future reference, $\mu_T = \rho\nu_T$ is known as the dynamic eddy viscosity. Closure relations involve choosing an appropriate form for ν_T.

Using (2.2.8), the RANS equations (2.2.4) and (2.2.5) then have the same form as the Navier-Stokes equations, with (2.2.5) reducing to

$$U_j\frac{\partial U_i}{\partial x_j} = -\frac{1}{\rho}\frac{\partial \hat{P}}{\partial x_i} + \frac{\partial}{\partial x_j}\left[(\nu + \nu_T)\frac{\partial U_i}{\partial x_j}\right], \tag{2.2.9}$$

where $\hat{P} = P + 2k/3$ is the effective pressure. The hypothesis (2.2.8) is very commonly used, and although it has significant weaknesses in many types of flow, for instance wall bounded flows, it is known to be a reasonable assumption in free shear flows, such as jets and mixing layers (see Pope (2000) chapter 10).

To close the turbulent energy equation (2.2.6), the turbulent diffusion term (the first term on the right hand side of (2.2.6)) is typically written as a diffusion term with diffusion coefficient ν_T,

$$-\frac{\partial}{\partial x_i}\left(\frac{1}{2}\,\overline{\widetilde{u_i}\widetilde{u_j}\widetilde{u_j}} + \frac{1}{\rho}\overline{\widetilde{u_i}\widetilde{p}}\right) = \frac{\partial}{\partial x_i}\left(\nu_T\frac{\partial k}{\partial x_i}\right). \tag{2.2.10}$$

Using (2.2.7), (2.2.8) and (2.2.10), the turbulent energy equation (2.2.6) is then simplified to

$$U_i\frac{\partial k}{\partial x_i} = \frac{\partial}{\partial x_i}\left[(\nu + \nu_T)\frac{\partial k}{\partial x_i}\right] + \nu_T\frac{\partial U_j}{\partial x_i}\left(\frac{\partial U_j}{\partial x_i} + \frac{\partial U_i}{\partial x_j}\right) - \epsilon, \tag{2.2.11}$$

where recall the terms on the right-hand side refer to turbulent diffusion, production and dissipation, respectively. A further equation for ϵ is needed to close the model, and we will discuss some popular choices below.

2.3 Numerics - CFD

2.3.1 Numerics for $k - \epsilon$ model

The $k - \epsilon$ model is one of the most commonly used RANS turbulence models and is known to have fairly good accuracy for a variety of applications. It consists of

the mass, momentum and energy conservation equations (2.2.4), (2.2.9) and (2.2.11), along with a closure equation for the energy dissipation ϵ, namely

$$U_i \frac{\partial \epsilon}{\partial x_i} = \frac{\partial}{\partial x_i}\left[\left(\nu + \frac{\nu_T}{\sigma_\epsilon}\right)\frac{\partial \epsilon}{\partial x_i}\right] + C_{1\epsilon}\frac{\epsilon}{k}\nu_T \frac{\partial U_j}{\partial x_i}\left(\frac{\partial U_j}{\partial x_i} + \frac{\partial U_i}{\partial x_j}\right) - C_{2\epsilon}\frac{\epsilon^2}{k}. \tag{2.3.1}$$

This is chosen to have the same form as the equation (2.2.11) for k, except that the diffusion, production and dissipation terms are multiplied by experimentally fitted constants given, respectively, by $\sigma_\epsilon = 1.30$, $C_{1\epsilon} = 1.44$ and $C_{2\epsilon} = 1.92$. From dimensional analysis, the closure relation for the turbulent viscosity takes the form

$$\nu_T = C_\mu \frac{k^2}{\epsilon}, \tag{2.3.2}$$

where C_μ is a dimensionless parameter, found by fitting to different flows to be given by $C_\mu = 0.09$.

We use $k - \epsilon$ turbulence models to investigate the problem of an axisymmetric momentum-driven jet. We use a finite element method in OpenFOAM (Weller et al., 1998) to solve the full $k - \epsilon$ equations. Note that, we take the flow to be in the z direction and the jet width to correspond to the r direction.

We assume fluid is ejected at velocity $W_0 = 10\,\mathrm{m\,s^{-1}}$ from a hole of diameter $D = 0.5\,\mathrm{m}$. These are representative values corresponding to a real oil spill. At the nozzle exit we impose

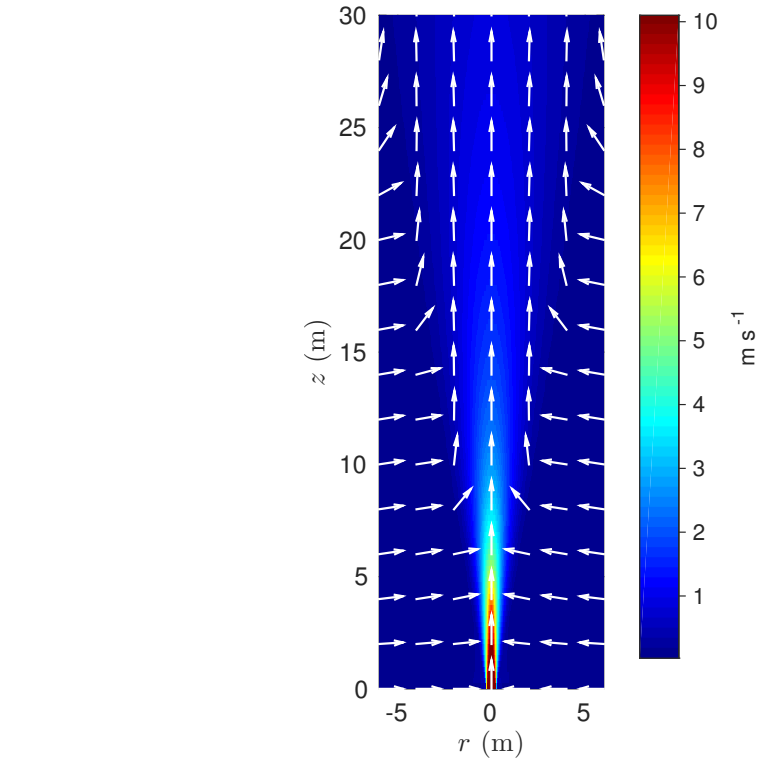
$$W = W_0, \quad U = 0, \quad k = \frac{3}{2}W_0^2 I_T^2, \quad \epsilon = C_\mu^{3/4}\frac{k^{3/2}}{L_T}, \quad \text{at} \;\; z = 0, \;\; 0 \le r \le D/2. \tag{2.3.3}$$

These inlet values of k and ϵ are experimentally based approximations; I_T is a constant corresponding to the turbulent intensity, which is set as $I_T = 0.05$, and the mixing length L_T is given by $L_T = 0.0375\,D$ (Versteeg and Malalasekera, 2007) page 66.

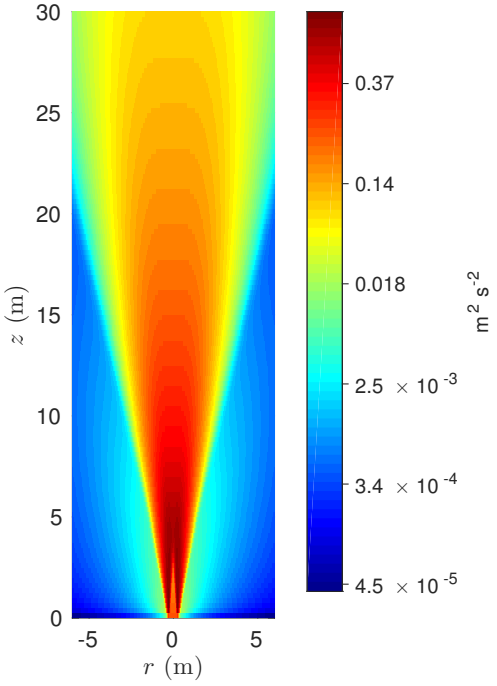
The problem is solved in a finite box with height $H_0 = 140\,D$ (so $0 \le z \le H_0$) and half-width $B_0 = 160\,D$ (so $r < B_0$). This width is taken to be large enough so that the sides of the box do not have a significant effect on the evolution of the jet. We take the side and top of this box to be open boundaries, satisfying

$$\nabla W \cdot \mathbf{n} = \nabla U \cdot \mathbf{n} = \nabla k \cdot \mathbf{n} = \nabla \epsilon \cdot \mathbf{n} = 0, \quad \text{at} \;\; r = B_0 \;\; \text{and at} \;\; z = H_0. \tag{2.3.4}$$

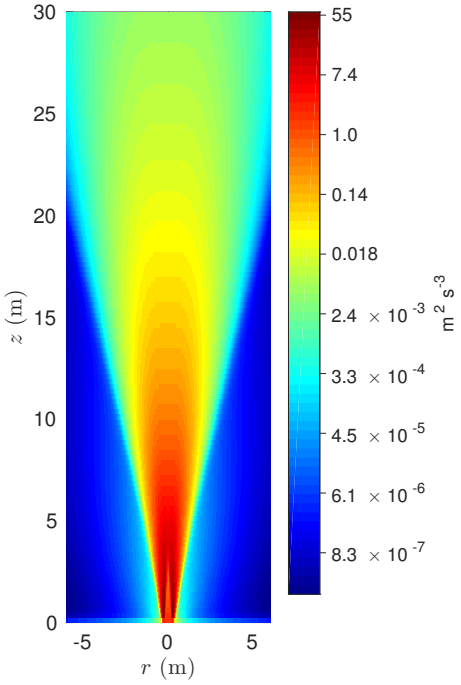
Akin to the sea floor, the base of the box is taken to be a solid wall by using wall functions. Near a wall, there is a thin boundary layer where viscous effects become important. Instead of resolving the flow here, which is computationally difficult,



(a) Velocity magnitude



(b) Turbulent kinetic energy, k



(c) Energy dissipation, ϵ

Figure 2.1: Numerical simulations of an axisymmetric turbulent jet with nozzle diameter 0.5 m and inlet velocity $10\,\mathrm{ms}^{-1}$ using the $k-\epsilon$ model. (a) Velocity magnitude with direction shown by the arrows; (b) turbulent kinetic energy; (c) energy dissipation. Note a log colour scale is used in (b) and (c).

wall functions impose the behaviour at a small distance from the wall. For further clarification about the precise nature of the boundary conditions used see Appendix A.

Typical results are shown in Figure 2.1. We see that the velocity near the nozzle is large and decreases with height. At the base of the jet, mixing layers form between the quiescent seawater and the high-velocity rising jet. These eventually merge to form the fully developed jet. Further up the jet, in the fully developed flow, the velocity is greatest at the centre of the jet and decreases with width. As the jet travels, it is entraining the surrounding seawater, causing it to grow in width. Nonetheless, we observe that the jet is long and thin.

We gain some initial insights into the turbulent kinetic energy and energy dissipation. The value of k in Figure 2.1(b) increases with height in the mixing layer region and reaches its maximum when the mixing layers combine, decreasing thenceforth. The energy dissipation behaves similarly. It is most significant in the mixing layers; in fact we see in Figure 2.1(c) that, except in the mixing layers, ϵ is generally less than $1\,\mathrm{m}^2\,\mathrm{s}^{-3}$. The energy dissipation is defined in (2.2.7) in terms of derivatives of velocity fluctuations (2.2.7). Thus, the regions with the greatest energy dissipation are not necessarily those with greatest velocity, such as the centre of the jet, but correspond more closely to those with the greatest shear.

2.3.2 Other turbulence models

$k-\epsilon$ models are known to be surprisingly accurate given the approximate nature of the ϵ equation, (2.3.1) (Pope, 2000). However, a well-known limitation is that they often do not accurately predict the spreading of both planar and axisymmetric jets. Different experimental constants $C_{1\epsilon} = 1.6$ and $C_{2\epsilon} = 1.92$ have been suggested to improve the accuracy of their predictions, but in spite of this there is still some disparity with experimental observations (Ganesan, 2005).

There are various extensions and improvements to the $k-\epsilon$ model. The $k-\omega$ model of Wilcox (1993) considers $\omega = \epsilon/(C_\mu k)$ instead of ϵ. Numerical experiments by Wilcox (1993) suggest this model demonstrates closer agreement with physical measurements in a number of situations; in particular, it can be seen to better predict the spreading rate and velocity profile of an axisymmetric jet than the $k-\epsilon$ model. As with the $k-\epsilon$ model, it solves (2.2.4) and (2.2.9). However, the turbulent kinetic energy, k, now satisfies

$$U_i \frac{\partial k}{\partial x_i} = \frac{\partial}{\partial x_i}\left[\left(\nu + \frac{\nu_T}{2}\right)\frac{\partial k}{\partial x_i}\right] + \nu_T \frac{\partial U_j}{\partial x_i}\left(\frac{\partial U_j}{\partial x_i} + \frac{\partial U_i}{\partial x_j}\right) - C_\mu k\omega, \tag{2.3.5}$$

where $C_\mu = 0.09$ as before and, instead of an equation for the energy dissipation, we set ω as

$$U_i \frac{\partial \omega}{\partial x_i} = \frac{\partial}{\partial x_i}\left[\left(\nu + \frac{\nu_T}{2}\right)\frac{\partial \omega}{\partial x_i}\right] + \alpha \frac{\omega}{k}\nu_T \frac{\partial U_j}{\partial x_i}\left(\frac{\partial U_j}{\partial x_i} + \frac{\partial U_i}{\partial x_j}\right) - \beta\omega^2, \tag{2.3.6}$$

where $\alpha = 0.52$ and $\beta = 0.072$. The closure assumption for ν_T is equivalent to (2.3.2) and so

$$\nu_T = \frac{k}{\omega}. \tag{2.3.7}$$

Note that apart from a change of variable from ϵ to ω and the constant coefficients multiplied by each term, this model is very similar to the $k-\epsilon$ model.

The "realizable $k-\epsilon$ model" is also known to resolve the difficulties the $k-\epsilon$ model encounters with jets and provide better agreement with experimental results (Shih et al., 1995). As with the $k-\epsilon$ model, it solves (2.2.4), (2.2.9) and (2.2.11) but (unlike both the $k-\epsilon$ and $k-\omega$ models) uses different and more mathematically justified closure assumptions for ϵ and ν_T (Shih et al., 1995). The energy dissipation is governed by

$$U_i \frac{\partial \epsilon}{\partial x_i} = \frac{\partial}{\partial x_i}\left[\left(\nu + \frac{\nu_T}{\sigma_\epsilon}\right)\frac{\partial \epsilon}{\partial x_i}\right] + C_1\sqrt{2S_{ij}S_{ij}}\epsilon - C_2\frac{\epsilon^2}{k+\sqrt{\nu\epsilon}}, \tag{2.3.8}$$

where $\sigma_\epsilon = 1.2$,

$$C_1 = \max\left\{0.43, \frac{\sqrt{2S_{ij}S_{ij}}k/\epsilon}{5+\sqrt{2S_{ij}S_{ij}}k/\epsilon}\right\}, \tag{2.3.9}$$

$$S_{ij} = \frac{1}{2}\left(\frac{\partial U_i}{\partial x_j} + \frac{\partial U_j}{\partial x_j}\right), \tag{2.3.10}$$

and $C_2 = 1.9$. The eddy viscosity is again given by (2.3.2), i.e.

$$\nu_T = C_\mu \frac{k^2}{\epsilon}, \tag{2.3.11}$$

where C_μ is no longer a constant but given by

$$C_\mu = \frac{1}{A_0 + A_s U^* k/\epsilon}, \tag{2.3.12}$$

where $A_0 = 6.5$, $A_s = \sqrt{6}\cos\phi$, and $\phi = \cos^{-1}\left(\sqrt{6}W^*\right)/3$, with

$$W^* = \frac{S_{ij}S_{jk}S_{ki}}{\left(2S_{ij}S_{ij}\right)^{3/2}} \tag{2.3.13}$$

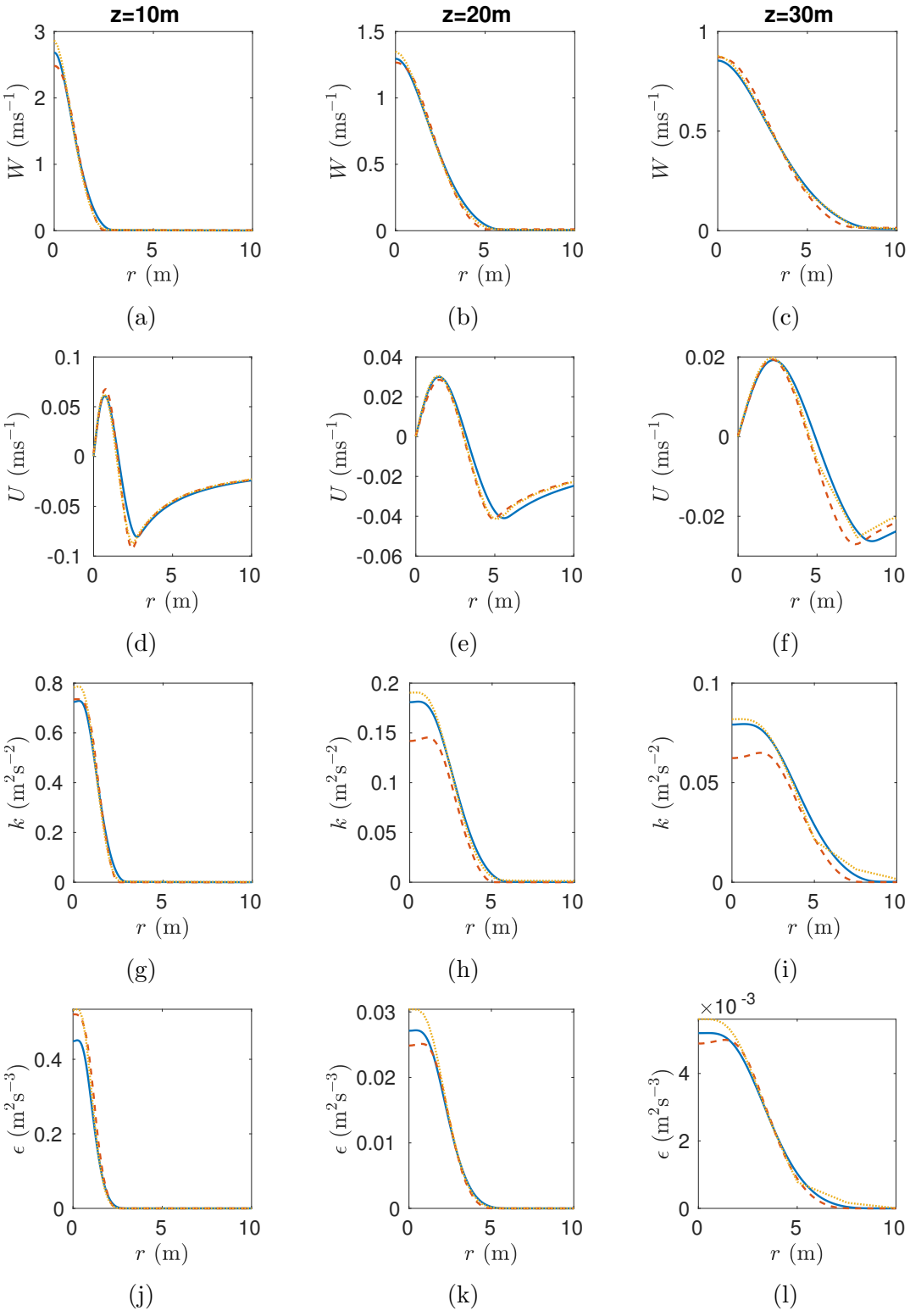


Figure 2.2: Comparison of $k-\epsilon$ model (blue) with realisable $k-\epsilon$ model (red dashed) and $k-\omega$ model (yellow dotted) at heights (from left to right) $z = 10\,\mathrm{m}, z = 20\,\mathrm{m}$ and $z = 30\,\mathrm{m}$. We plot the vertical velocity component W in (a)–(c), the horizontal velocity U in (d)–(f), the turbulent kinetic energy k in (g)–(i), and the energy dissipation ϵ in (j)–(l). The nozzle diameter is 0.5 m and the inlet velocity is $10\,\mathrm{ms}^{-1}$.

and

$$U^* = \sqrt{\frac{\partial U_i}{\partial x_j}\frac{\partial U_i}{\partial x_j}} \tag{2.3.14}$$

We solve the $k-\omega$ and realizable $k-\epsilon$ models in the same domain and with the same boundary conditions as the $k-\epsilon$ model in Subsection 2.3.1. Our results, compared to the $k-\epsilon$ model, are shown in Figure 2.2. Here we consider the axial and radial velocity components, turbulent kinetic energy and energy dissipation at various fixed heights z in the jet. Reassuringly, the models both predict quantitatively very similar results. One main difference is that the realizable $k-\epsilon$ model predicts a local maximum in the energy dissipation a little away from the jet centre whilst it seems that this maximum disappears more quickly with z in the $k-\epsilon$ and $k-\omega$ models (see Figure 2.2(l)).

2.3.3 Discussion

Numerical simulations like those shown in Figures (2.1)–(2.2) enable us to capture the detail of the jet's motion for a given set of parameter values. We observe that the velocities and energy decrease significantly with height. Interestingly, there is some evidence that the regions with the greatest energy dissipation correspond to those with the greatest shear rather than those with the greatest velocity. Thus, such regions are where the most rapid droplet breakup is expected to occur.

Whilst we gain interesting insights from these full numerical simulations, they can be a little computationally expensive, with a run time on the order of a few minutes, and would need to be recomputed for different oil spill scenarios, with different oil properties, flow rates and nozzle diameters. However, the fully developed flow of an axisymmetric turbulent jet exhibits self similar behaviour, sufficiently far from the jet nozzle (Davidson, 2015; Pope, 2000). This can be exploited to create simpler universal models for the velocity, turbulent kinetic energy and energy dissipation in a turbulent jet.

2.4 Similarity solution

2.4.1 Dimensionless model

Consider an axisymmetric, long and thin turbulent jet. The $k-\epsilon$ model for a long and thin flow is given by

$$\frac{1}{r}\frac{\partial(rU)}{\partial r}+\frac{\partial W}{\partial z}=0, \tag{2.4.1}$$

$$U\frac{\partial W}{\partial r}+W\frac{\partial W}{\partial z}=\frac{1}{r}\frac{\partial}{\partial r}\left(r\nu_T\frac{\partial W}{\partial r}\right), \tag{2.4.2}$$

$$U\frac{\partial k}{\partial r}+W\frac{\partial k}{\partial z}=\frac{1}{r}\frac{\partial}{\partial r}\left(\nu_T\frac{\partial k}{\partial r}\right)+\nu_T\left(\frac{\partial W}{\partial r}\right)^2-\epsilon, \tag{2.4.3}$$

$$U\frac{\partial \epsilon}{\partial r}+W\frac{\partial \epsilon}{\partial z}=\frac{1}{r}\frac{\partial}{\partial r}\left(\frac{r\nu_T}{\sigma_\epsilon}\frac{\partial \epsilon}{\partial r}\right)+C_{1\epsilon}\nu_T\frac{\epsilon}{k}\left(\frac{\partial W}{\partial r}\right)^2-C_{2\epsilon}\frac{\epsilon^2}{k}, \tag{2.4.4}$$

$$\nu_T=\frac{C_\mu k^2}{\epsilon}, \tag{2.4.5}$$

where, recall, the parameter $C_\mu = 0.09$. These are just equations (2.2.4), (2.2.9), (2.2.11), (2.3.1) and (2.3.2) expressed in axisymmetric coordinates, where the axial diffusion terms, involving $\partial/\partial z$, are neglected compared to those involving $\partial/\partial r$, due to the assumed small aspect ratio of the jet. For the same reason, in the production terms of the energy equations (2.2.11)–(2.3.1), only the terms involving $\partial W/\partial r$ are included. In addition, the molecular viscosity ν is neglected compared to the eddy viscosity ν_T.

At this point we should verify the assumption made here, that a turbulent jet is long and thin. The parameter, C_μ, is small and thus, to achieve a balance between all the terms in (2.4.1)–(2.4.4), we must rescale $r = C_\mu^{1/2}\hat{r}$ and $U = C_\mu^{1/2}\hat{U}$, where $\hat{r}, \hat{U} \sim \mathcal{O}(1)$, and all other variables are order one. This implies that $r \ll z$ and $U \ll W$; the jet is long and thin.

Symmetry of the jet about the z-axis suggests that

$$\frac{\partial W}{\partial r}(0,z)=0, \quad U(0,z)=0, \quad \frac{\partial k}{\partial r}(0,z)=0, \quad \frac{\partial \epsilon}{\partial r}(0,z)=0. \tag{2.4.6}$$

Far from the source of the jet, the flow will be quiescent and thus

$$W(r,z),\ \nu_T,\ k,\ \epsilon \to 0, \text{ as } r\to\infty. \tag{2.4.7}$$

We also impose the values of U, W, k and ϵ at $z = 0$, for example

$$W=\begin{cases} W_0, & r \le D/2, \\ 0, & r > D/2. \end{cases} \tag{2.4.8}$$

Note that integrating the momentum equation (2.4.2) from $r = 0$ to $r = \infty$ and using the far-field boundary conditions (2.4.7) produces an equation for the conservation of momentum flux

$$\frac{d}{dz}\left(\int_0^\infty rW^2\,\mathrm{d}r\right) = 0. \tag{2.4.9}$$

The mass flux, however, is not conserved since water is entrained into the jet.

We non-dimensionalise

$$z = Dz^*,\ r = Dr^*,\ W = W_0W^*,\ U = W_0U^*,\ \nu_T = DW_0\nu_T^*,\ k = W_0^2k^*,\ \epsilon = \frac{W_0^3}{D}\epsilon^*, \tag{2.4.10}$$

where D and W_0 are the nozzle diameter and initial jet velocity. Dropping asterisks, we again obtain equations (2.4.1)–(2.4.5) and (2.4.9). This scale invariance of the model equations suggests the existence of self-similar solutions, as shown below.

2.4.2 Velocity

Let us first examine the velocity components in the jet, which satisfy (2.4.1)–(2.4.2) subject to (2.4.6) and (2.4.7). We can construct similarity solutions for the velocities since, away from the jet nozzle, the jet sees only one natural velocity scale, which we take to be the velocity at the centreline of the jet,

$$W(0, z) = W_c(z), \tag{2.4.11}$$

and one natural length-scale, which we take to be the width or diameter of the jet, $\delta(z)$. Note that close to the source, this is not the case; the nozzle diameter is another imposed length scale. The models in this section are, therefore, of the fully developed jet flow which occurs at a large enough distance away from the source that the nozzle width is effectively zero. This means that we cannot use boundary conditions at $z = 0$ like (2.4.8); instead we must match to the non self-similar flow at lower z.

The jet width $\delta(z)$ is defined such that, at $r = \delta/2$, the vertical velocity is one tenth of its value at the centreline, that is

$$W\left(\frac{\delta(z)}{2}, z\right) = 0.1W_c(z). \tag{2.4.12}$$

This specific value of 0.1 is somewhat arbitrary and chosen to be small enough so that $r = \delta/2$ corresponds roughly to the 'edge of the jet'; this is also the same value chosen by Davidson (2015).

We make the key assumption that the turbulent viscosity ν_T is constant across the jet width, so that

$$\nu_T = \nu_T(z). \tag{2.4.13}$$

Note this is not consistent with the far field boundary condition for ν_T in (2.4.7), which shall be neglected here, but is a very common assumption used in the literature (Davidson, 2015; Pope, 2000). As we shall see, it enables us to obtain analytical similarity solutions. According to experiments cited by Pope (2000), (2.4.13) is a reasonable approximation, except in the outer region of the jet, where the entrainment of seawater causes extra complications. The assumption (2.4.13) has not previously been used in determining similarity solutions for the turbulent energy in the jet (Paullay et al., 1985), but we will investigate how to do so in Section 2.4.3 .

We look for similarity solutions of the form

$$W = W_c(z)f(\xi), \qquad U = W_c(z)j(\xi), \qquad \nu_T = \delta(z)W_c(z)\tilde{\nu}_T \tag{2.4.14}$$

where we have introduced the similarity variable

$$\xi = \frac{\sqrt{\beta}r}{\delta(z)}. \tag{2.4.15}$$

Here β is a constant, which will later be chosen for convenience.

We substitute the self-similar forms (2.4.14) into the conservation of mass, momentum and momentum flux equations, namely (2.4.1), (2.4.2) and (2.4.9). For self similarity to hold, $d\delta/dz$ and $W_c^2\delta^2$ must be constant. We thus set

$$\delta(z) = \delta_0 + \alpha z, \tag{2.4.16}$$

for constants δ_0 and α. By doing so, we have taken the dimensionless jet radius at $z = 0$ to equal δ_0. However, the similarity solution is not valid for small z. Therefore, we cannot necessarily set $\delta_0 = 1$ (which would correspond to the jet width being equal to the nozzle diameter at $z = 0$). Instead we treat δ_0 and α as fitting constants so we can fit to the flow at small z, where the jet is not self-similar. We also obtain

$$W_c(z) = \frac{\omega_0\delta_0}{\delta} = \frac{\omega_0\delta_0}{\delta_0 + \alpha z}. \tag{2.4.17}$$

The parameter ω_0 is set by conservation of momentum flux, (2.4.9), which is given by

$$\int_0^\infty rW^2 \,\mathrm{d}r = M, \tag{2.4.18}$$

where M is a constant. By calculating the momentum flux at $z = 0$, using the non-dimensional equivalent of (2.4.8), we obtain $M = 1/8$. Hence, using (2.4.14) and (2.4.17), ω_0 satisfies

$$\frac{8\omega_0^2\delta_0^2}{\beta}\int_0^\infty \xi f(\xi)^2 d\xi = 1. \tag{2.4.19}$$

We set the constant

$$\beta = \frac{\alpha}{8\tilde{\nu}_T} \tag{2.4.20}$$

and conservation of mass and momentum (2.4.1)–(2.4.2) then yield, respectively,

$$\frac{\sqrt{\beta}}{\alpha}\frac{d\,(\xi j)}{d\xi} - \xi^2\frac{df}{d\xi} - \xi f = 0, \tag{2.4.21}$$

$$\frac{8\sqrt{\beta}}{\alpha}\xi j\frac{df}{d\xi} - 8\xi f^2 - 8\xi^2 f\frac{df}{d\xi} - \frac{d}{d\xi}\left(\xi\frac{df}{d\xi}\right) = 0. \tag{2.4.22}$$

The symmetry boundary conditions (2.4.6) and the definition of the centreline velocity (2.4.11) are written in similarity variables as

$$f(0) = 1, \quad f'(0) = 0, \quad j(0) = 0. \tag{2.4.23}$$

Equations (2.4.21)–(2.4.23) can be solved to obtain

$$f(\xi) = \frac{1}{(1+\xi^2)^2}, \tag{2.4.24}$$

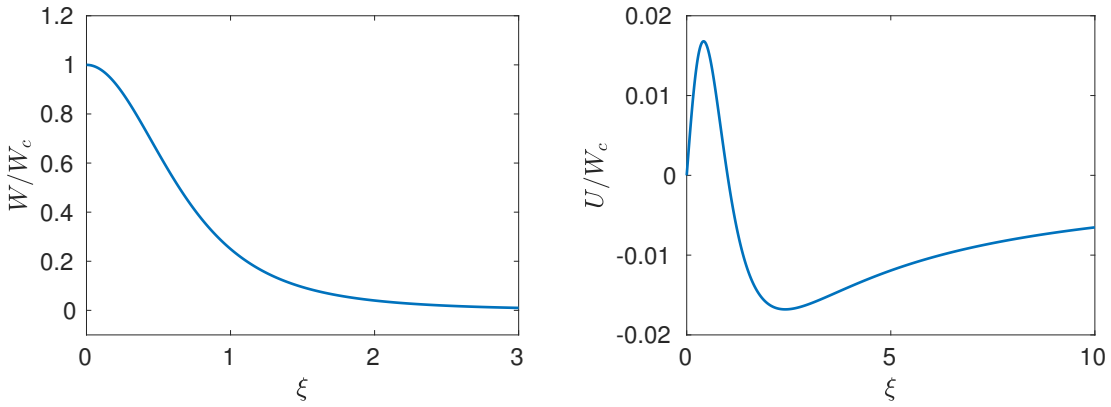
$$j(\xi) = \frac{\alpha}{2\sqrt{\beta}}\frac{\xi\,(1-\xi^2)}{(1+\xi^2)^2}. \tag{2.4.25}$$

By the definition of $\delta(z)$ in (2.4.12), $f(1/2) = 0.1$ and thus $\beta = 4(\sqrt{10}-1) = 8.65$. (Hence $\tilde{\nu}_T = 0.0145\alpha$.) In addition, from (2.4.19), ω_0 is given by

$$\omega_0 = \frac{\sqrt{6\beta M}}{\delta_0}, \tag{2.4.26}$$

where here $M = 1/8$.

The solutions for the rescaled velocities given by (2.4.24)–(2.4.25) are plotted in Figure 2.3. These give an indication of the velocities W and U, respectively, at some fixed height. The vertical velocity is at its maximum at the jet's centre, and decreases to zero across the width of the jet. The radial velocity increases from zero and then decreases, becoming negative. Positive j corresponds to the fluid in the jet moving outwards towards the exterior seawater whilst negative j corresponds to the entrainment of seawater into the jet from the exterior.



(a) (b)

Figure 2.3: Similarity solutions for the velocity components in a turbulent axisymmetric jet. We plot the rescaled vertical velocity $f = W/W_c$ as a function of the similarity variable $\xi = \sqrt{\beta}r/\delta$, given by (2.4.24), in (a). The corresponding rescaled transverse velocity $j = U/W_c$, given by (2.4.25), is plotted in (b). Note the ξ-axes in (a) and (b) are not the same.

2.4.3 Energy

In modelling the breakup of droplets in this turbulent jet, we are not only interested in its velocity but also in the energy dissipation, which corresponds to the energy available for droplet breakup. To obtain the turbulent kinetic energy and energy dissipation, we do not use the exact $k-\epsilon$ model (in Equations (2.4.3)–(2.4.4)) but instead use an approach similar to the $k-\epsilon$ model. The equation for turbulent kinetic energy k in a free shear flow is given by (2.4.3). We combine this with the closure relation for the turbulent kinematic viscosity, (2.4.5), and the assumption (used above) that ν_T is constant across the jet's width. This enables us to first find U, W and ν_T as in Section 2.4.2, then find k using

$$U\frac{\partial k}{\partial r} + W\frac{\partial k}{\partial z} = \frac{1}{r}\frac{\partial}{\partial r}\left(\nu_T \frac{\partial k}{\partial r}\right) + \nu_T\left(\frac{\partial W}{\partial r}\right)^2 - \frac{C_\mu k^2}{\nu_T}. \tag{2.4.27}$$

and finally determine the decoupled ϵ using the algebraic equation

$$\epsilon = \frac{C_\mu k^2}{\nu_T}. \tag{2.4.28}$$

Unlike the traditional $k-\epsilon$ model, we do not use the experimental PDE, (2.4.4), for ϵ but have obtained closure by specifying the turbulent viscosity in (2.4.14).

Note that our approach and the full $k-\epsilon$ model, whilst similar, do not reduce to each other. Our model is simpler to solve, since there is no longer an additional

PDE for ϵ but might be a less accurate representation of reality than the $k-\epsilon$ model. We can perhaps feel justified in neglecting the ϵ equation, (2.4.4) in the $k-\epsilon$ model since it is not derived from the same physical equations as the equations for the velocities and turbulent kinetic energy but rather is chosen to have the same form as the equation for k (Pope, 2000). In any case, (as will be discussed in Section 2.4.4) the similarity solution for ϵ, using our approximation, agrees well with the numerical solution of the $k-\epsilon$ equation, giving strong justification for it.

The form of (2.4.27)–(2.4.28) suggests we look for similarity solutions for k and ϵ given by

$$k = \frac{\alpha}{8\sqrt{\beta C_\mu}} W_c(z)^2 H(\xi), \tag{2.4.29}$$

$$\epsilon = \frac{\alpha}{8} \frac{W_c(z)^3}{\delta(z)} H(\xi)^2, \tag{2.4.30}$$

which reduces the problem to solving

$$\hat{\nu}\xi \frac{d^2H}{d\xi^2} + \hat{\nu}\left[1 + \frac{4\xi^2}{1+\xi^2}\right]\frac{dH}{d\xi} + \frac{16\hat{\nu}\xi}{(1+\xi^2)^2}H - \xi H^2 + \frac{16\xi^3}{(1+\xi^2)^6} = 0, \tag{2.4.31}$$

subject to

$$\frac{dH}{d\xi}(0) = 0, \qquad H(\xi) \to 0 \ \text{ as } \ \xi \to \infty, \tag{2.4.32}$$

where

$$\hat{\nu} = \tilde{\nu}_T \sqrt{\beta/C_\mu} = \alpha/(8\sqrt{\beta C_\mu}). \tag{2.4.33}$$

Equation (2.4.31) subject to (2.4.32) can be numerically solved using the boundary value solver in Chebfun (Driscoll et al., 2014). However, to do so, we first need to determine the value of the parameter $\hat{\nu} = \alpha/(8\sqrt{\beta C_\mu})$, which contains the as yet undetermined constant α. More generally, to obtain W, U, k and ϵ, we must choose values for the fitting parameters δ_0 and α.

We determine α and δ_0 by fitting our final expressions for W and ϵ to the numerical results for the $k-\epsilon$ model from Section 2.3.1. We fit these parameters so that the scaled numerical results collapse and also to obtain the best agreement with the numerics for fixed $z = 120$ (or dimensional $z = 60\,\text{m}$) since we expect the similarity solution to be most accurate for large z. We find $\alpha = 0.483$ and $\delta_0 = -0.4$. This then yields $\omega_0 = -6.37$, $\tilde{\nu}_T = 0.0070$ and $\hat{\nu} = 0.0684$. Recall also that we also have $C_\mu = 0.09$.

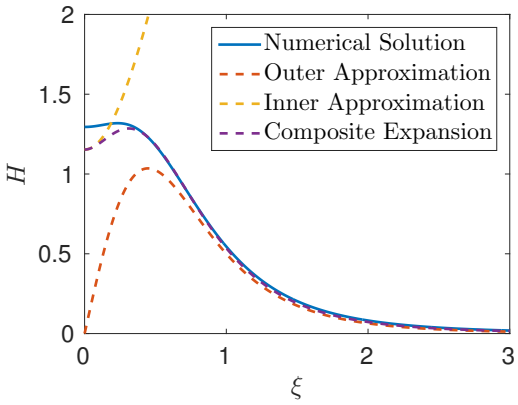


Figure 2.4: Similarity solutions for turbulent kinetic energy and energy dissipation. We plot $H(\xi)$, to which the scaled turbulent kinetic energy, k/W_c^2 is proportional. The scaled energy dissipation, $\delta\epsilon/W_c^2$, is proportional to the square of H. We illustrate the numerical solution to (2.4.31)–(2.4.32), the outer approximation given by (2.4.35), the inner expansion given by (2.4.37)–(2.4.39), and the composite solution given by (2.4.40).

Using this value of $\hat{\nu}$, we numerically solve (2.4.31) subject to (2.4.32) and the solution for $H(\xi)$ is shown in Figure 2.4. However, further simplifications can also be made, which enable us to find an approximate expression for H.

Equation (2.4.31) depends solely on the small parameter $\hat{\nu} = 0.0684 \ll 1$. The presence of this small parameter in front of the highest derivative in (2.4.31) suggests this can be treated as a singular perturbation problem. Thus, we first seek an outer solution of the form

$$H(\xi) \sim H_0 + \hat{\nu} H_1 + \cdots \tag{2.4.34}$$

as $\hat{\nu} \to 0$, and the leading order outer solution to this problem is then

$$H_0(\xi) = \frac{4\xi}{(1+\xi^2)^3}. \tag{2.4.35}$$

This corresponds to the dissipation terms equalling the production of turbulence due to shear. The outer solution is illustrated in Figure 2.4. There is excellent agreement with the numerical solution to (2.4.31)–(2.4.32) except for smaller values of ξ.

When ξ is small, we rescale $\xi = \hat{\nu}^{1/3} X$ and $H = \hat{\nu}^{1/3} G$ and set

$$G \sim G_0 + \hat{\nu}^{2/3} G_1 + \cdots \tag{2.4.36}$$

to obtain the leading order inner equation

$$X \frac{d^2 G_0}{dX^2} + \frac{dG_0}{dX} - X G_0^2 + 16 X^3 = 0 \tag{2.4.37}$$

with

$$G_0'(0) = 0 \tag{2.4.38}$$

from (2.4.32). Matching with (2.4.35), yields

$$G_0(X) \to 4X, \text{ as } X \to \infty. \tag{2.4.39}$$

Equations (2.4.37)–(2.4.39) must then be solved numerically and the resulting canonical solution for G_0 is shown in Figure 2.4. We see that G_0 does not very closely agree with the numerics for small ξ, probably because $\hat{\nu} = 0.0684$ so $\hat{\nu}^{1/3} = 0.4090$, which is not significantly smaller than 1. Nonetheless, the composite solution, given by

$$H_c(\xi) = H_0(\xi) + \hat{\nu}^{1/3} G_0 - 4\xi \tag{2.4.40}$$

in Figure 2.4, shows fairly good agreement with the full numerical solution to (2.4.31)–(2.4.32). Note that using artificially small values of $\hat{\nu}$, say $\hat{\nu} \sim \mathcal{O}(10^{-3})$, we do find very good agreement between G_0 and the numerics.

We obtain $G_0(0) \approx 2.8190$, and so, for different possible parameters, can determine the value of $H(0) \approx \hat{\nu}^{1/3} G_0(0)$.

Recall, from (2.4.29)–(2.4.30) that $H(\xi)$ is a measure of the turbulent energy in the jet. If we look at $H(\xi)$ in Figure 2.4, we see that the shape is very similar to that of f in Figure 2.3(a). Nonetheless, the maximum of $H(\xi)$ (which corresponds to the region with the greatest turbulent energy dissipation and thus the greatest opportunity for droplet breakup) is not at the centre of the jet but lies in the region between the edge of the jet and the centre. Recall the presence of this maximum was observed in our numerical results, particularly for the realisable $k-\epsilon$ model as seen in Figure 2.2. In contrast, the outer solution (2.4.35) assumes that the only contribution to the turbulent energy is from turbulent production due to shear, and so predicts that H is maximal where the shear is maximal.

2.4.4 Comparisons to numerics for $k - \epsilon$ model

We have numerically modelled a turbulent jet using the $k - \epsilon$ model, as shown in Section 2.3. We now scale these CFD results to determine how effective the similarity scaling is. The rescaled numerical results are then compared to our similarity solution, whose free parameters, α and δ_0, have previously been fitted to these numerical results at one particular value of z. Note that in Sections 2.4.2–2.4.3 we obtain similarity solutions to a set of equations which are similar to the $k - \epsilon$ model but not identical

to it, particularly the equation for ϵ. Therefore, even for very large z when the approximation of self-similarity is believed to be very good, we cannot expect the rescaled $k-\epsilon$ numerics to agree perfectly with this similarity solution.

In Figures 2.5–2.6, we compare the unscaled and scaled numerical results in blue. These are shown for the fully developed jet region (which we take to be $z > 7.5$m or 15 nozzle diameters away from the inlet). Using the numerical results, in Figures 2.5(a), 2.5(c), 2.6(a) and 2.6(c), we plot the unscaled velocities and energies as functions of r for several fixed values of z, that is for slices through the width of the jet. We compare the unscaled numerics to the rescaled versions plotting, in Figures 2.5(b), 2.5(d), 2.6(b) and 2.6(d), W/W_c, U/W_c, k/W_c^2 and $\epsilon\delta/W_c^3$, respectively, as functions of the similarity variable ξ for fixed values of z. Following this similarity rescaling, the numerical results collapse very well, affirming the appropriateness of the similarity scaling. The vertical velocity component, W, collapses well after only a couple of nozzle diameters. The energy dissipation takes a little longer, around 7.5 m or 15 nozzle diameters, to be self-similar.

Note that in Figure 2.5(d), for the scaled transverse velocity U, the collapse is not as good. Numerical experiments show that increasing the width of the box improves the collapse. This suggests that these discrepancies are perhaps an artefact of the finite box in which the equations are numerically solved. The similarity solution is solved on an infinite domain, so the fluid is drawn from the sides at infinity. However, in the numerics, fluid is pulled from the top of the box downwards and into the sides of the jet.

A comparison of the similarity solutions (given by (2.4.24), (2.4.25), and the solution to (2.4.29)–(2.4.32)) and the numerical results in the fully developed jet region is also shown in Figures 2.5(b), 2.5(d), 2.6(b) and 2.6(d), in red. These rescaled numerical results and the similarity solutions compare well. In our similarity solutions for the turbulent kinetic energy and dissipation, we have used much simpler closure assumptions than the full $k-\epsilon$ equations. It is thus additionally encouraging that the results from this similarity solution are not very far off the full results from the more complicated models.

Our similarity solution has shown good agreement with the numerics for the full $k-\epsilon$ model. We can also fit it to the numerical results of the realisable $k-\epsilon$ model from Section 2.3.2, which is considered a better model of reality. Using different fitting parameters, $\delta_0 = -0.38$ and $\alpha = 0.46$, we find that the similarity solution agrees well with the rescaled numerics and we obtain similar results to those in Figures 2.5–2.6.

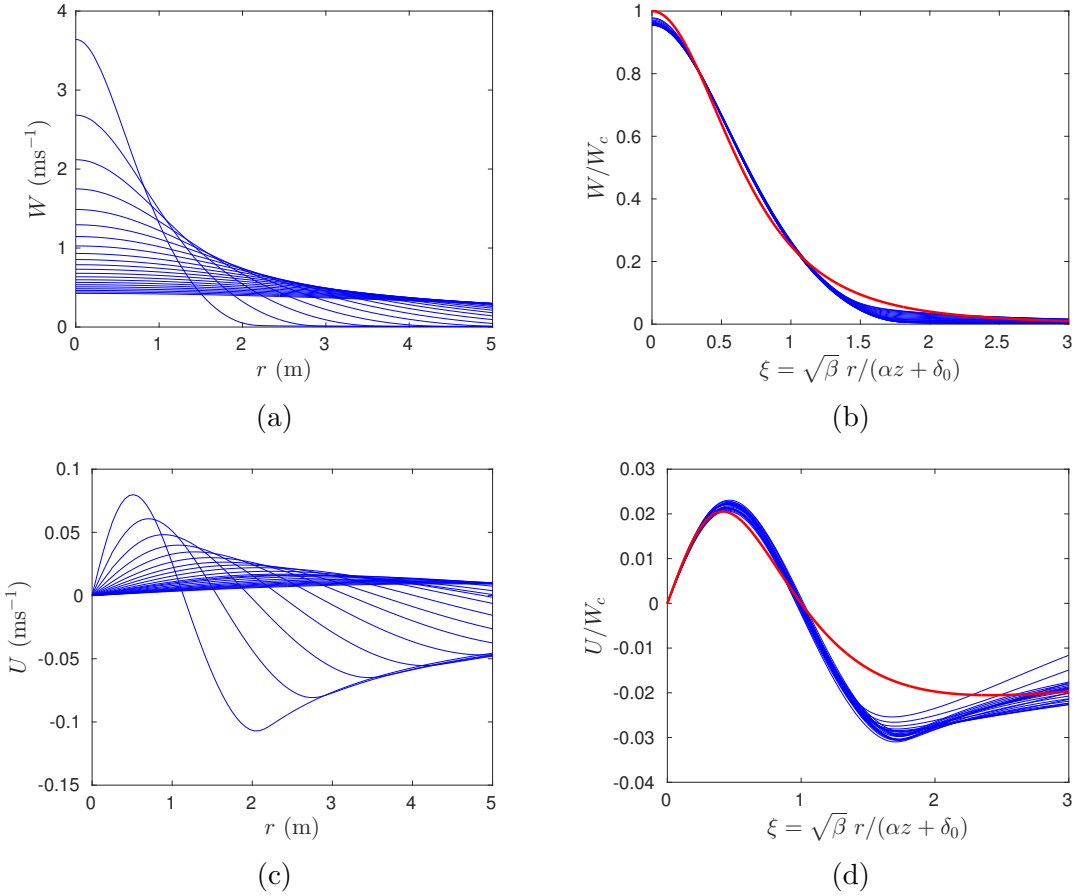


Figure 2.5: The velocity components W (in the z-direction) and U (in the r-direction). Results from the numerical simulations obtained by solving (2.2.4), (2.2.9), (2.2.11), (2.3.1) and (2.3.2) subject to (2.3.3), (2.3.4) and wall function boundary conditions as discussed in Subsection 2.3.1, for different fixed values of z, for $z = 7.5 : 2.5 : 60\,\mathrm{m}$ shown in blue. (a) W as a function of r; (b) the scaled velocity W/W_c as a function of ξ, where W_c is given by (2.4.17); (c) U as a function of r; (d) the scaled velocity U/W_c as a function of ξ. The scaled numerical results are compared to the similarity solutions given by (2.4.24) and (2.4.25) (for parameter values $\alpha = 0.483$ and $\delta_0 = -0.4$) in (b) and (d), respectively. The similarity solutions are shown in red.

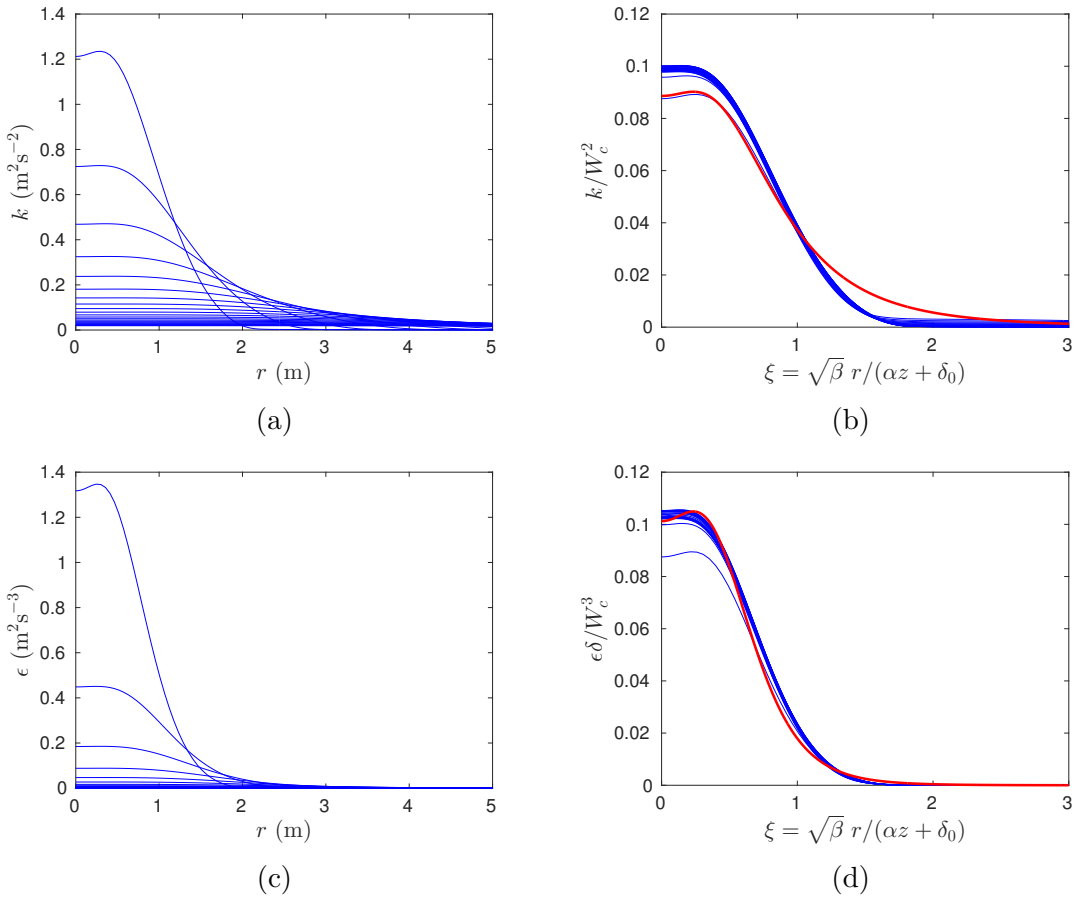


Figure 2.6: The turbulent kinetic energy k and turbulent energy dissipation rate ϵ. Results from the numerical simulations obtained by solving (2.2.4), (2.2.9), (2.2.11), (2.3.1) and (2.3.2) subject to (2.3.3), (2.3.4) and wall function boundary conditions as discussed in Section 2.3.1, for different fixed values of z, for $z = 7.5 : 2.5 : 60\,\mathrm{m}$ shown in blue. (a) k as a function of r; (b) the scaled turbulent kinetic energy k/W_c^2 as a function of ξ, where W_c is given by (2.4.17); (c) ϵ as a function of r; (d) the scaled dissipation $\epsilon\delta/W_c^3$ as a function of ξ. The scaled numerical results are compared to the similarity solutions given by solving (2.4.29)–(2.4.32) (for parameter values $\alpha = 0.483$ and $\delta_0 = -0.4$) in (b) and (d). The similarity solutions are shown in red.

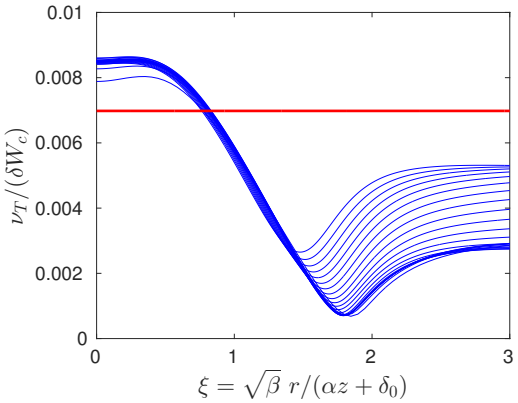


Figure 2.7: The rescaled eddy viscosity $\nu_T \delta W_c$. Results from the numerical simulations obtained by solving (2.2.4), (2.2.9), (2.2.11), (2.3.1) and (2.3.2) subject to (2.3.3), (2.3.4) and wall function boundary conditions as discussed in Section 2.3.1, for different fixed values of z, for $z = 7.5 : 2.5 : 60\,\mathrm{m}$ shown in blue. The scaled numerical results are compared to the similarity solution given by (2.4.14) and (2.4.20) (for parameter values $\alpha = 0.483$ and $\delta_0 = -0.4$). It is shown in red.

At this point, it is useful to go back to the simple closure assumptions that were made, in particular our assumption that ν_T is constant along the width of the jet. In Figure 2.7, we compare the numerical results for the rescaled eddy viscosity $\nu_T/(\delta W_c)$ with its assumed constant value, $\tilde{\nu}_T$, used in our similarity solution. Note that the numerics for ν_T does not tend to zero in the limit $\xi \to \infty$ as we would have expected. This, as well as poor collapse in the rescaled eddy viscosity for larger ξ, is probably an artefact of the finite box in which the equations are numerically solved. (This is similar to the lack of collapse in the horizontal velocity component in Figure 2.5(d).) Nonetheless, even if we take this into account, there is generally poor agreement between the similarity solution and the full numerics for the eddy viscosity. Thus, the otherwise good agreement between the similarity solution and the numerics seems highly surprising.

However, the important thing to note here is that the agreement between the numerics and similarity solution for ν_T is fairly good for $\xi < 1.5$. For larger ξ, the effects of turbulence are almost negligible, as can be seen in Figures 2.6(b) and (d). This suggests that for larger ξ the precise value of ν_T is unimportant and, as long as ν_T is small, which it is in the similarity solution, the assumption of constant eddy viscosity is acceptable.

2.4.5 Full similarity solution for $k-\epsilon$ model

We have calculated a similarity solution which describes the flow in an axisymmetric turbulent jet, using a model which is similar to but not exactly the same as the $k-\epsilon$ model. The obvious next question to ask is whether we can find a similarity solution to the full $k-\epsilon$ model, given by (2.4.1)–(2.4.5). This has been found by Paullay et al. (1985) and Ghazzawi and Rabadi (1994). We can, thus, compare our approach to the full similarity solution for an axisymmetric turbulent jet, computed by Ghazzawi and Rabadi (1994).

Their approach is very similar to that taken in Sections 2.4.2–2.4.3 except they insert the self similar ansatzes into (2.4.1)–(2.4.5) instead of using the approximate equations (2.4.27)–(2.4.28).

The results of the similarity solution of Ghazzawi and Rabadi (1994) are compared with the full $k-\epsilon$ model in Figure 2.8. We fit the parameters $\alpha = 0.50$ and $\delta_0 = -0.24$ so this full similarity solution collapses and agrees with the numerics. Note that these parameter values are different from the ones chosen for our reduced similarity solution. We see there is excellent agreement here. Let us now compare with the results for the similarity solution in Subsections 2.4.2–2.4.3, which can be seen in Figures 2.5(b), 2.5(d),2.6(b) and 2.6(d). As we would have expected, the numerical solution to the full $k-\epsilon$ model shows better agreement with the similarity solution to the full $k-\epsilon$ model as computed by Ghazzawi and Rabadi (1994) than with the similarity solution we present in Subsections 2.4.2–2.4.3. Nevertheless, except for perhaps the transverse velocity U, the reduced similarity solution from Sections 2.4.2–2.4.3 captures all the significant features of the turbulent flow while being far easier to compute, and therefore we will use it in subsequent chapters.

2.4.6 Discussion

We have found similarity solutions describing the motion and turbulent energy in a turbulent jet. These have come from using a simplified version of the $k-\epsilon$ model, with the assumption of constant eddy viscosity. Our similarity solution compares well with numerical results for $k-\epsilon$ and realisable $k-\epsilon$ models, and with the full similarity solution for the $k-\epsilon$ model.

Attempting to couple turbulent flow with droplet dynamics and surfactant transport is a difficult task, and thus using this reduced similarity solution, which is as simple as possible whilst retaining much of the basic physics of the problem, is advantageous. The limitation to relying on the self-similarity of the jet is that our models

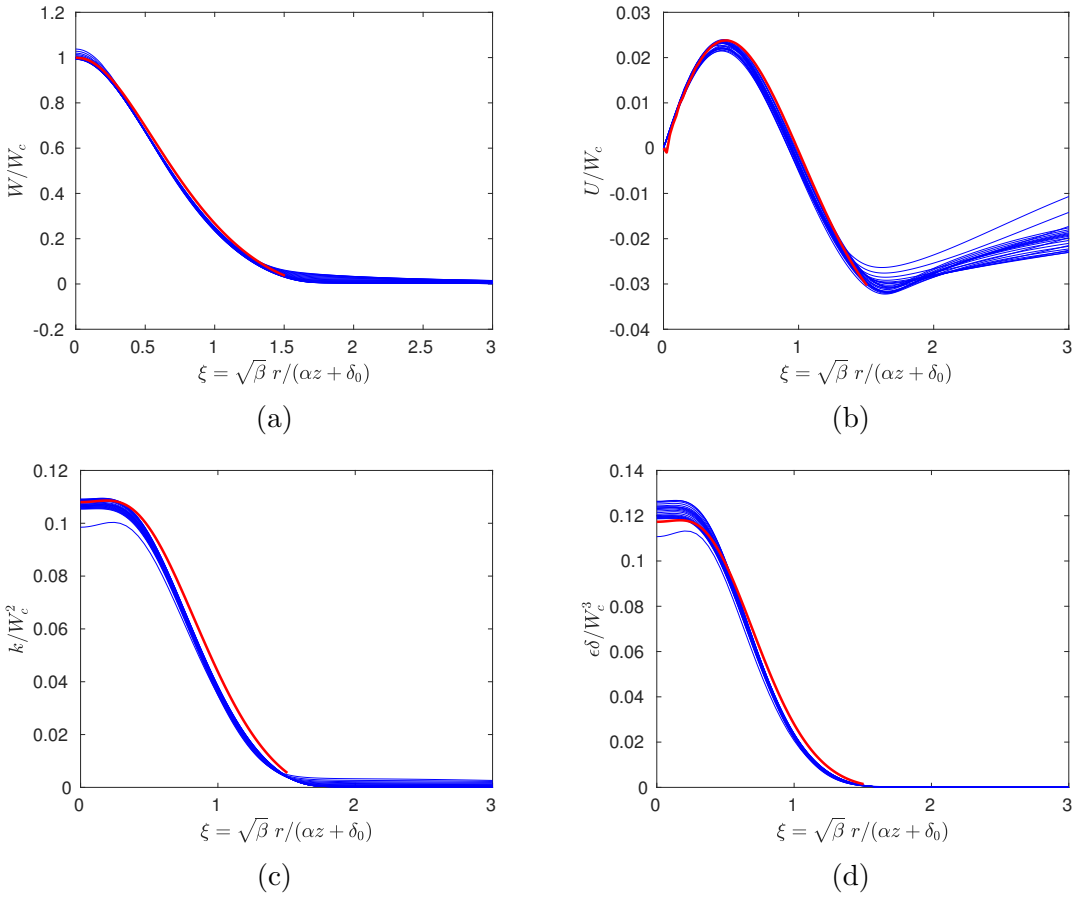


Figure 2.8: The velocity components, W and U, turbulent kinetic energy, k, and energy dissipation, ϵ. Results from the numerical simulations obtained by solving (2.2.4), (2.2.9), (2.2.11). (2.3.1) and (2.3.2) subject to (2.3.3), (2.3.4) and wall function boundary conditions as discussed in Subsection 2.3.1, for different fixed values of z, for $z = 7.5 : 2.5 : 60\,\mathrm{m}$ shown in blue. These are scaled so we show (a) W/W_c, (b) U/W_c, (c) k/W_c^2, and (d) $\delta\epsilon/W_c^3$ as functions of the similarity variable ξ. They are compared to the full similarity solutions as calculated in Ghazzawi and Rabadi (1994) for parameter values $\alpha = 0.50$ and $\delta_0 = -0.24$, which are shown in red.

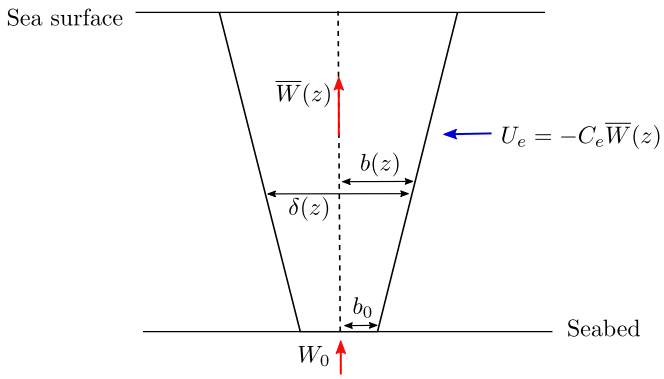


Figure 2.9: Jet Schematic.

are not very representative at the base of the jet, particularly for the first, say, 5 to 10 nozzle diameters. This is a region with high energy dissipation and thus with the potential for a great deal of droplet breakup. Our approaches to this problem are shown in Chapter 4.

2.5 Width-averaged models

We have developed and discussed models for axisymmetric turbulent jets, and produced simplified, analytical similarity solutions to describe the flow. Nevertheless, in order to more easily understand the complex interactions between the jet, droplets and surfactants in future chapters, it is often helpful to use the simplest jet models possible. Thus, we now employ the classic approach of Morton et al. (1956) to model the mechanics of a jet by averaging over its width so the problem involves only one spatial dimension. This, we later find, is equivalent to width averaging the results of the similarity solutions from Subsections 2.4.2–2.4.3.

A schematic of the system we are considering is shown in Figure 2.9. We suppose the jet has a well defined width given by $\delta(z)$ (and corresponding half width $b(z) = \delta(z)/2$). Beyond this is only seawater, which we assume has negligible vertical velocity. This sharp delineation of the jet's width is clearly not evident in a real jet but is a useful modelling assumption. Note that the jet width in this section is not necessarily the same as that used in Subsection 2.4.2 (there, recall, the jet width δ is defined as the width at which the flow is 10 percent of its magnitude at the jet's centre). We assume the vertical velocity has a top-hat profile, so it is uniform across the jet's width and zero in the exterior, i.e.

$$W = \begin{cases} \overline{W}(z), & r \leq \delta(z)/2, \\ 0, & r > \delta(z)/2, \end{cases} \tag{2.5.1}$$

where $\overline{W}(z)$ is the width-averaged vertical velocity inside the jet region, at height z.

We multiply the conservation of mass and momentum equations, (2.4.1) and (2.4.2), by r, and integrate across both the r and θ directions, from $r = 0$ to $r = \delta(z)/2$ and from $\theta = 0$ to $\theta = 2\pi$. Using (2.5.1), we obtain

$$\pi\delta U_e + \frac{d}{dz}\left(\frac{\pi}{4}\delta^2\overline{W}\right) = 0, \tag{2.5.2}$$

where

$$U_e = U(\delta(z)/2, z) \tag{2.5.3}$$

is the velocity at which fluid is entrained into the jet, and

$$\frac{d}{dz}\left(\rho\frac{\pi}{4}\delta^2\overline{W}^2\right) = 0. \tag{2.5.4}$$

Here (2.5.4) represents conservation of momentum flux.

We follow the approach of Morton et al. (1956), who make the assumption that the entrainment velocity is proportional to the vertical velocity with the constant of proportionality, C_e, known as the entrainment coefficient; that is,

$$U_e = -C_e\overline{W}. \tag{2.5.5}$$

Thus, the conservation of mass equation (2.5.2) becomes

$$\frac{d}{dz}\left(\frac{\pi}{4}\delta^2\overline{W}\right) = \pi C_e\delta\overline{W}. \tag{2.5.6}$$

We solve (2.5.6) and (2.5.4) to obtain

$$\delta(z) = C_b + 4C_e z, \tag{2.5.7}$$

and

$$\overline{W}(z) = \frac{C_b C_W}{C_b + 4C_e z}, \tag{2.5.8}$$

where C_b and C_W are constants to be determined. This very simple model appears to capture the main physics of the problem. It exhibits the classical cone shape of a turbulent jet, as can be seen from (2.5.7). Equation (2.5.8) implies the region near the base of the jet has the greatest vertical velocity and it decreases with increasing height in the jet. These observations are consistent with our results in Sections 2.3–2.4.

Note that, here, we have started with the equations for conservation of mass and momentum of a turbulent jet, assumed the velocity follows a width-averaged

profile and then solved to find this profile. An alternative approach might be to start with the similarity solution to the conservation of mass and momentum equations in Subsection 2.4.2, and then width-average so that $\int_0^\infty rW\,\mathrm{d}r$ is conserved. We thus again assume that the vertical velocity has the top-hat profile, (2.5.1), but now

$$\overline{W}(z) = \frac{\int_0^\infty rW(r,z)\,\mathrm{d}r}{\delta^2/8}, \tag{2.5.9}$$

where here $\delta = \delta_0 + \alpha z$ as in (2.4.16) and $W(r,z)$ is given by (2.4.14), (2.4.17) and (2.4.24). This yields

$$\overline{W}(z) = \frac{4\delta_0\omega_0}{\beta}\frac{1}{\delta(z)}. \tag{2.5.10}$$

This has the same form as (2.5.8) obtained using the approach of Morton et al. (1956) above (up to the evaluation of the parameters C_e, C_b and C_W). Therefore, we choose the values of C_e, C_b and C_W so the two approaches give the same results, setting $C_e = \alpha/4$, $C_b = \delta_0$ and $C_W = 4\omega_0/\beta$.

To calculate a width-averaged value of ϵ we, likewise, average the results of our similarity solutions obtaining

$$\overline{\epsilon}(z) = \frac{\alpha\omega_0^3\delta_0^3}{\beta}\int_0^\infty \xi H(\xi)^2\,\mathrm{d}\xi\frac{1}{\delta(z)^4}, \tag{2.5.11}$$

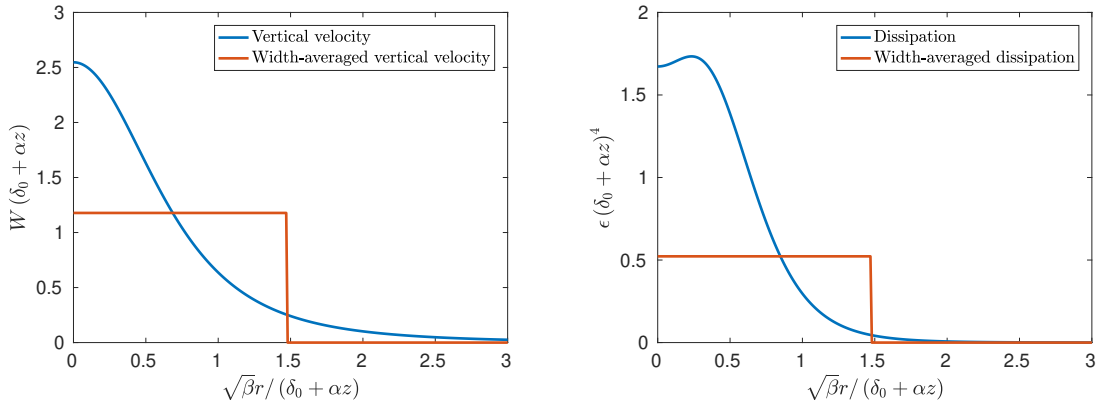
where $H(\xi)$ is given by the numerical solution to (2.4.31)–(2.4.32) and the value of the integral is given by $\int_0^\infty \xi H(\xi)^2\,\mathrm{d}\xi = 0.5662$.

Therefore, in summary, we have

$$\delta = \delta_0 + \alpha z, \quad \overline{W}(z) = 0.46\frac{\delta_0\omega_0}{\delta(z)}, \quad \overline{\epsilon}(z) = \frac{\epsilon_0}{\delta(z)^4}, \tag{2.5.12}$$

where $\epsilon_0 = 0.0316\ \omega_0^3\delta_0^3$.

The width-averaged W and ϵ, compared to the similarity solution from Sections 2.4.2–2.4.3 are shown in Figure 2.10. In using these width-averaged results, we must be slightly wary of the fact that they are averaged and therefore do not capture the significant variation of W and ϵ across the jet's width. Our main concern would involve the energy dissipation. Droplets can only break up when there is enough turbulent energy to do so; this means that, in some cases, only in the regions with very high ϵ would droplets break up. However, using this averaged approach, the model may predict the energy dissipation is lower in certain regions which actually have high ϵ. Thus, the model may predict that there is no droplet breakup in regions where this is not actually the case. In summary, this approach correctly predicts the



(a) (b)

Figure 2.10: (a) Vertical velocity and (b) energy dissipation from similarity solution in Subsections 2.4.2–2.4.3 compared to width-averaged models at $z = 5$.

gross features of the jet, but not the detailed behaviour — and the detailed behaviour may be important when it comes to droplet breakup.

In this section, by assuming that the variables have a top-hat profile, we reduce the problem to one dimension i.e. height. There are other alternative ways to do so. For instance, Morton et al. (1956) assume that the profile of the vertical velocity component can be approximated by a Gaussian, namely

$$W(r,z) = W_G(z)\exp(-r^2/b(z)^2). \tag{2.5.13}$$

Using this assumption, the problem now becomes solving for $b(z)$, the half-width of the jet, and $W_G(z)$, the variation of the vertical velocity with height, similarly to (2.5.2)–(2.5.8). From the results of our similarity solution, (2.4.24), we know that using a Gaussian profile is not strictly correct. Nonetheless, it is a fairly good approximation and, in any case, is a better approximation of the variation of velocity with width than assuming top-hat profiles. Using a Gaussian profile evidently gives a far better approximation of the variation of velocity with width. However, in this framework, it is not obvious how to approximate the equivalent form of the energy dissipation and taking simple choices such as a Gaussian profile do not yield physically realistic results. Therefore, we not pursue this approach further and, in this thesis, all of our one-dimensional models assume top-hat profiles.

2.6 Conclusions

We have explored the macroscopic flow in a turbulent jet. Full numerical simulations provide a detailed picture of the jet's behaviour. They are, however, computationally expensive and need to be recomputed for different physical situations. A turbulent jet is approximately self similar and so similarity solutions can be constructed for the flow which are scale invariant and can be easily applied to different situations. In the numerics, we use the $k - \epsilon$ model, which has a known similarity solution (Ghazzawi and Rabadi, 1994). Its resulting similarity ODEs must still be fully solved numerically as it is highly coupled and non-linear. We have constructed an alternative similarity solution assuming the eddy viscosity is constant; solutions to this problem are much easier to compute as they can either be expressed analytically or involve solving a single boundary value problem. They also show good agreement with the full numerics for the $k - \epsilon$ model. Our similarity solution can also be averaged over the width of the jet; we find that simple width-averaged models, in fact, produce reasonable models of the decay of velocity and energy as the jet evolves.

The jet's velocity and turbulent energy decrease with height, the energy dissipation rapidly so. We find that the regions of greatest energy dissipation are in the mixing layers near the base of the jet. Across the width of the jet, there appears to be a local maximum in the energy dissipation slightly away from the centre of the jet. Therefore, the region with the greatest energy dissipation, and thus with the greatest opportunity for droplet breakup, does not exactly correspond to that with the maximum velocity.

We use the jet models in this chapter throughout the rest of this thesis, combining them with drop models to produce droplet size distributions in Chapters 4–6. To obtain drop size distributions in two-spatial dimension we first use the full numerical results for the $k - \epsilon$ model from Subsection 2.3.1. This can be simplified by instead using the similarity solution calculated in Sections 2.4.2–2.4.3 to model the jet. For simplicity, models for the droplet size distribution in only one spatial dimension are also examined and, for these, the width-averaged models from Section 2.5 are used.

Chapter 3

Droplet breakup

In Chapter 2, we model the macroscopic behaviour of a turbulent jet. Now we turn our attention to the microscopic droplet scale. We explore the mechanisms behind droplet breakup in a turbulent flow and how this breakup affects the distribution of droplet sizes.

To determine the drop size distribution, we introduce droplet size population models. A vital ingredient of these is the rate at which droplets break up. To understand this, we review the relevant literature to examine scaling laws and explore how the turbulent effects, local to a droplet, cause it to deform and break up. We finally solve the droplet population models in the simplest setting, in a homogeneous environment without any of the complications of the jet flow. This gives us an understanding of the effect of the droplet breakup rate, and paves the way to solving the droplet population models in a turbulent jet flow in Chapter 4.

3.1 Master equation

Let $n(v, t, \mathbf{x})$ be the number density of drops of volume v at location $\mathbf{x}$ and time t. Since n is a number density, the total number of drops with volume between v_a and v_b per unit volume is given by

$$\int_{v_a}^{v_b} n(v, t, \mathbf{x}) \, \mathrm{d}v. \tag{3.1.1}$$

Hence, the volume fraction of drops with volume between v_a and v_b is

$$\int_{v_a}^{v_b} n(v, t, \mathbf{x}) v \, \mathrm{d}v. \tag{3.1.2}$$

We denote $\phi(v,t,\mathbf{x}) = n(v,t,\mathbf{x})v$, namely ϕ is the distribution of volume fraction. The total volume fraction of oil droplets is defined as

$$\Phi = \int_0^\infty n(v,t,\mathbf{x})v \,\mathrm{d}v = \int_0^\infty \phi(v,t,\mathbf{x}) \,\mathrm{d}v. \tag{3.1.3}$$

Note that, throughout this thesis, we assume that all drops are smaller than some volume, v_∞, and so the upper limit in the integral in (3.1.3) is generally taken to be v_∞.

For the remainder of this chapter, we consider a spatially homogeneous environment and therefore neglect the dependence on position $\mathbf{x}$. The model is extended to include spatial effects in Chapter 4.

3.1.1 Discrete-volume model

We are interested in modelling the evolution of the drop size distribution, $\phi(v,t)$, due to the break up of droplets under the action of a turbulent flow. For simplicity we first consider a volume discretised model, where drops are categorised into N distinct sizes or bins. We suppose that bin i contains all the droplets of volume $v_i = iv_\infty \triangle v$, where $i \in \{1, \cdots, N\}$, with $\triangle v = 1/N$. Hence drops range in size from $v_1 = v_\infty/N$ to $v_N = v_\infty$. We let $n_i(t)$ and $\phi_i(t)$ be the discrete analogues of n and ϕ, namely the number density and the volume fraction distribution of drops with volume v_i.

Let $\gamma_i(\epsilon,\sigma)$ be the rate at which drops of volume v_i break up. Note that this is assumed to be dependent on only droplet volume, turbulent energy dissipation and surface tension. We let $N_{ij}\triangle v$ be the expected number of drops of volume v_i produced when a drop with volume v_j breaks up. We assume that N_{ij} only depends on droplet volume (i.e. the values of i and j).

We model the rate of change of $n_i \triangle v$, the number of drops of volume v_i, using

$$\frac{dn_i \triangle v}{dt} = -\gamma_i(n_i \triangle v) + \sum_{j=i+1}^{N} \gamma_j (n_j \triangle v)(N_{ij} \triangle v). \tag{3.1.4}$$

The first term on the right hand side of (3.1.4) describes the decrease in the number of drops of volume v_i due to droplets of this size breaking up at a rate γ_i. The second term represents the process by which the number of drops with volume v_i increases because drops larger than v_i break up and produce those of volume v_i. When a drop of volume v_j breaks up (with rate γ_j) it could break into any number of drops of different sizes; to consider only the number of drops of size v_i produced due to breakup, the second term on the right hand side of (3.1.4) is multiplied by $N_{ij}\triangle v$.

Whilst it is perhaps more intuitive to consider the number of drops, we are most interested in determining the drop size distribution, ϕ_i. Multiplying (3.1.4) by v_i, ϕ_i is governed by the master equation

$$\frac{d\phi_i}{dt} = -\gamma_i \phi_i + \sum_{j=i+1}^{N} \gamma_j \chi_{ij} \phi_j \triangle v, \tag{3.1.5}$$

where

$$\chi_{ij} \triangle v = \frac{v_i}{v_j} N_{ij} \triangle v. \tag{3.1.6}$$

Recall since N_{ij} is assumed to only be a function of droplet size, so is χ_{ij}.

What is the physical significance of χ_{ij}? The quantity $N_{ij}\triangle v$ corresponds to the expected number of drops of volume v_i produced when a drop of volume v_j breaks up (with $j > i$). This means that $v_i N_{ij} \triangle v$ is the expected volume of v_i sized droplets produced when a drop of volume v_j breaks. Thus, $\chi_{ij}\triangle v = (v_i/v_j)N_{ij}\triangle v$ is the expected proportion of the volume of v_j which becomes v_i sized drops. In the literature, it is often referred to as the 'daughter size distribution' and we shall do so throughout this thesis.

In this chapter, we consider a spatially independent 'box' in which the total volume fraction of oil must be conserved. Therefore

$$\frac{d\Phi}{dt} = 0, \tag{3.1.7}$$

where, in this discrete-volume setting, the total oil fraction is given by

$$\Phi = \sum_{i=1}^{N} \phi_i \triangle v. \tag{3.1.8}$$

Taking the sum of (3.1.5) between $i = 1$ to $i = N$ and swapping the order of summation in the double sum yields

$$0 = \frac{d\Phi}{dt} = -\sum_{i=1}^{N} \gamma_i \phi_i \triangle v + \sum_{j=1}^{N} \left(\sum_{i=1}^{j-1} \chi_{ij} \triangle v \right) \gamma_j \phi_j \triangle v. \tag{3.1.9}$$

Therefore, for mass to be conserved, χ_{ij} must satisfy

$$\sum_{i=1}^{j-1} \chi_{ij} \triangle v = 1. \tag{3.1.10}$$

Physically, this corresponds to the notion that, if a drop of volume v_j breaks up, the sum of the volume fractions of each of drop sizes produced is equal to one; namely the volume of a drop is equal to the sum of the volumes of all of the droplets produced from it when it breaks up.

3.1.2 Continuous-volume model

The true problem is continuous in volume. The discrete volume model can be extended to the continuous version by taking the limit as the number of bins N is large. Then, from (3.1.5), the volume fraction distribution, $\phi(v,t)$, of drops of volume v is governed by the master equation

$$\frac{\partial \phi(v,t)}{\partial t} = -\gamma(v,\epsilon,\sigma)\phi(v,t) + \int_v^{v_\infty} \gamma(\tilde{v},\epsilon,\sigma)\chi(v,\tilde{v})\phi(\tilde{v},t)\,\mathrm{d}\tilde{v}, \tag{3.1.11}$$

where $\gamma(v,\epsilon,\sigma)$ is the rate at which droplets of volume v break up and $\chi(v,\tilde{v})$ is the daughter size distribution. Analogous to χ_{ij}, $\chi(v,\tilde{v})$ is the distribution of the expected volume fraction of a drop of volume $\tilde{v}$ which becomes v sized drops when it breaks up. Thus, if a drop of volume $\tilde{v}$ breaks up, the expected fraction of the volume of the produced drops which have size between v_a and v_b is

$$\int_{v_a}^{v_b} \chi(v,\tilde{v})\,\mathrm{d}v. \tag{3.1.12}$$

As in the discrete model, the total volume fraction of oil, $\Phi = \int_0^{v_\infty} \phi\,\mathrm{d}v$, must be conserved i.e.

$$\frac{d\Phi}{dt} = 0. \tag{3.1.13}$$

Taking the integral of (3.1.11) from $v = 0$ to $v = 1$, and swapping the order of integration in the resulting double integral yields (3.1.13), provided that

$$\int_0^{\tilde{v}} \chi(v,\tilde{v})\,\mathrm{d}v = 1, \tag{3.1.14}$$

analogous to (3.1.10). The condition (3.1.14) naturally arises from the definition of $\chi(v,\tilde{v})$ in (3.1.12). It states that when a drop breaks up, the expected volume fraction of all the produced drops is one i.e. the volume of the drop which breaks up is equal to the volume of all the droplets that it produces during breakup.

3.1.3 Non-dimensionalisation

We non-dimensionalise using (2.4.10),

$$t = \tau t^*, \quad \sigma = \sigma_0 \sigma^*, \tag{3.1.15}$$

and

$$v = v_\infty v^*, \quad \phi = \frac{\psi}{v_\infty}\phi^*, \quad \gamma = \frac{1}{\tau}\gamma^*, \quad \chi = \frac{1}{v_\infty}\chi^*, \tag{3.1.16}$$

where ψ is the total oil fraction injected into the jet.

We consider here spatial independent 'box' models where the energy dissipation is constant and we track the change in droplet size with time. In the following chapter, we examine a steady turbulent jet, where the behaviour changes with (r, z). For consistency, in both cases, the time-scale is taken to be $\tau = D/W_0$ with typical values for the nozzle diameter, D, and outlet velocity, W_0, taken from the real parameters in Table 1.1.

With asterisks dropped, the non-dimensional evolution equation for the distribution of droplets of volume v is given by

$$\frac{\partial \phi}{\partial t} = -\gamma(v, \epsilon, \sigma)\phi(v) + \int_v^1 \gamma(\tilde{v}, \epsilon, \sigma)\chi(v, \tilde{v})\phi(\tilde{v})\,\mathrm{d}\tilde{v}. \tag{3.1.17}$$

And the total oil fraction is given by

$$\Phi(t) = \int_0^1 \phi\,\mathrm{d}v. \tag{3.1.18}$$

3.1.4 Coalescence

Note that we neglect coalescence throughout this thesis to model droplet breakup in a turbulent jet where we believe the effects of coalescence are weak. See Section 4.1 for justification and further details.

3.1.5 Comparison to literature

The model, (3.1.17), is used widely in the literature in a similar form (Bandara and Yapa, 2011; Coulaloglou and Tavlarides, 1977; Liao and Lucas, 2009; Martínez-Bazán et al., 1999a,b; Tsouris and Tavlarides, 1994; Zhao et al., 2014a). Authors such as Bandara and Yapa (2011) effectively use the same equation, (3.1.17). However, they misinterpret the daughter size distribution, $\chi(v, \tilde{v})$, as the probability a drop of volume $\tilde{v}$ produces a drop of volume v upon breakup. In other papers, such as Coulaloglou and Tavlarides (1977); Martínez-Bazán et al. (1999a,b); Tsouris and Tavlarides (1994); Zhao et al. (2014a), care is not taken to conserve mass. Thus, their results may need to be taken with some skepticism.

3.2 Scaling laws

3.2.1 Maximum stable drop size

Before we consider scaling laws for the breakup rates, we first investigate the range of drop sizes which can be broken up by examining the maximum stable drop size.

This discussion will inform our choice of breakup rate in Section 3.2.2.

We consider the forces exerted on a drop of diameter d by turbulent eddies of diameter l. Pressure fluctuations due to the turbulent eddies act on the droplet and deform it. The magnitude of these fluctuations are given by $\rho\overline{\tilde{u}^2}$, where ρ is the density of water and $\overline{\tilde{u}^2}$ is the mean squared turbulent velocity fluctuation as in (2.2.3). (Note that as in Section 2.2, we denote turbulent fluctuations by a tilde and time-averages by a bar.) The mean squared velocity fluctuations scale like

$$\overline{\tilde{u}^2} \propto l^{2/3}\epsilon^{2/3}, \tag{3.2.1}$$

using Kolmogorov's well known two-thirds law (Pope, 2000).[1] This gives the pressure fluctuations $\rho\overline{\tilde{u}^2}$ as $\rho l^{2/3}\epsilon^{2/3}$. The restoring force is the surface tension of the droplet, given by the Laplace-Young equation as $4\sigma/d$.

It seems reasonable to assume that the main breakup-inducing deformations acting on a droplet would be predominantly caused by an eddy of the same size. Eddies much larger than a drop would simply advect it. Those much smaller than the drop would cause deformations in small regions of the drop, which would not lead to significant breakup. Thus, for our scaling argument, we set $l = d$.

The ratio of the pressure fluctuations to the restoring force of surface tension yields a Weber number

$$We = \frac{\rho\overline{\tilde{u}^2}d}{\sigma} \propto \frac{\rho\epsilon^{2/3}d^{5/3}}{\sigma}. \tag{3.2.2}$$

Drops are unstable and break up if the deformation forces exerted on them are greater than the restoring forces. Hence, breakup will occur if the Weber number is greater than some critical value, namely $We > We_{\text{crit}}$. Equivalently, for fixed ϵ, droplets break up if their diameter is greater than the maximum stable drop diameter $d_{\max}$, given by

$$d_{\max} = C\left(\frac{\sigma}{\rho}\right)^{3/5}\epsilon^{-2/5}. \tag{3.2.3}$$

Here C is an order one constant of proportionality, which is related to the critical Weber number through $C = We_{\text{crit}}^{3/5}$. According to experiments by Clay (1940), (cited

[1] Kolmogorov's two-thirds law holds for eddies in the so-called inertial scale. There are three main ranges of turbulence which exist at scales smaller than the mean flow: large energy-carrying eddies, small eddies which dissipate energy and the intermediate sized inertial scale eddies, where inertial effects drive the energy from larger to smaller eddies. The behaviour on this scale is independent of viscosity and the eddies are solely controlled by the energy dissipation, ϵ, and the eddy size, l.

by Hinze (1955)), its value is approximately given by $C = 0.725 \pm 0.3$. In Martínez-Bazán et al. (1999b), the equivalent parameter is set as $C = 1.26$. In Chapter 4, where we determine the drop size distribution without surfactant addition, we take $C = 0.725$. In Chapter 6, which includes the effects of varying surface tension, a larger value of C is needed to replicate the behaviour of the small-scale experiments with the addition of surfactant (see Section 6.6).

In certain parameter regimes, viscosity, rather than surface tension, is the main force opposing droplet deformation. The viscous stress of the fluid inside the droplet acting against the velocity fluctuations outside it, is of order $\mu\sqrt{\overline{\tilde{u}^2}}/d$, where μ is the viscosity of the oil, assumed to be greater than that of water. Similarly to the argument in (3.2.2)–(3.2.3), the ratio of pressure forces to viscous stresses gives rise to a droplet Reynolds number

$$Re_d = \frac{\rho\sqrt{\overline{\tilde{u}^2}}d}{\mu} \propto \frac{\rho\epsilon^{1/3}d^{4/3}}{\mu}. \tag{3.2.4}$$

Drops break up if $Re_d > Re_{d,crit}$ or equivalently, for fixed ϵ, if $d > d_{\max}$ where

$$d_{\max} = \hat{C}\left(\frac{\mu}{\rho}\right)^{3/4}\epsilon^{-1/4}. \tag{3.2.5}$$

Here $\hat{C}$ is related to the critical Reynolds number through $\hat{C} = Re_{d,crit}^{3/4}$.

The scalings (3.2.3) and (3.2.5) are commonly used in the literature and seem to compare well with experimental results (Johansen et al., 2013; Calabrese et al., 1986; Hinze, 1955; Lyklema, 2005; Vankova et al., 2007). According to (3.2.3) and (3.2.5), with increasing height in the jet, as the energy dissipation decreases, the maximum stable drop size will increase; it is more difficult for droplets to break up and only the very largest will do so. In addition, as dispersants are injected, the surface tension decreases and, by (3.2.3), this reduces the maximum stable droplet size, allowing smaller drops to break up. We thus see the importance of controlling surface tension in facilitating effective droplet breakup.

In the literature, droplets whose main restoring force is surface tension are commonly called inertial drops and those affected by viscosity are called viscous drops (Vankova et al., 2007). To determine which regime is most important in our problem, we consider the capillary number, which is the ratio of the viscous stresses to the surface tension forces i.e.

$$Ca = \frac{\mu\sqrt{\overline{\tilde{u}^2}}}{\sigma} \propto \frac{\mu\epsilon^{1/3}d^{1/3}}{\sigma}. \tag{3.2.6}$$

If $Ca \ll 1$, the drops are inertial, if $Ca \gg 1$, they are viscous, and if $Ca = \mathcal{O}(1)$, then they are in an intermediate regime. In the case without dispersants, using the parameters in Table 1.1, we find that the maximum possible capillary number is around $\mathcal{O}(10^{-3})$–$\mathcal{O}(10^{-2})$ so the drops here are inertial. Therefore, (3.2.3) is a more appropriate law for the maximum stable droplet size in this situation. However, the addition of surfactant will decrease the surface tension, increasing the capillary number. If enough dispersant is added, the magnitude of the capillary number may start to approach order one and then viscosity starts to become important. This is the case if the surface tension decreases to around $\sigma = 10^{-4}\,\mathrm{kg\,s^{-2}}$. In the small-scale experiments this occurs at the largest measured dispersant to oil ratio of 1:25 (Brandvik et al., 2014). Nevertheless, for simplicity, in the remainder of this thesis, we will assume the drops are purely inertial.

3.2.2 Breakup rate

To determine a form for the breakup rate, $\gamma\,(\mathrm{s^{-1}})$, we first use dimensional analysis. The discussion above suggests that, in the regime we are interested in, γ is a function of energy dissipation, $\epsilon\,(\mathrm{m^2\,s^{-3}})$, drop size, $v\,(\mathrm{m^3})$, surface tension, $\sigma\,(\mathrm{kg\,s^{-2}})$, and density, $\rho\,(\mathrm{kg\,m^{-3}})$. There is also a dimensionless number in the problem, namely the Weber number, which, as in (3.2.2), is set as $We = \rho\epsilon^{2/3}d^{5/3}\sigma^{-1} = (6/\pi)^{5/9}\rho\epsilon^{2/3}v^{5/9}\sigma^{-1}$. Hence

$$\gamma \propto F(We)\epsilon^{(2a+1)/3}v^{(5a-2)/9}\left(\frac{\rho}{\sigma}\right)^a, \tag{3.2.7}$$

for some constant a, and function F, which are free to choose. For the behaviour of the breakup rate to be physically reasonable, γ must increase with increasing energy dissipation and with decreasing surface tension. Hence, a must be non-negative.

One straightforward choice might be to assume that the breakup rate is independent of drop size so $a = 2/5$ and $F = 1$. Thus

$$\gamma = K_{00}\frac{\epsilon^{3/5}\rho^{2/5}}{\sigma^{2/5}}, \tag{3.2.8}$$

where K_{00} is a constant of proportionality. Non-dimensionalising ϵ using (2.4.10) and σ as in (3.1.15), i.e. using

$$\epsilon = \frac{W_0^3}{D}\epsilon^*, \quad \sigma = \sigma_0\sigma^*, \tag{3.2.9}$$

and dropping asterisks yields

$$\gamma = K_0\frac{\epsilon^{3/5}}{\sigma^{2/5}}, \tag{3.2.10}$$

where

$$K_0 = \frac{K_{00}\rho^{2/5}W_0^{14/5}}{D^{8/5}\sigma_0^{2/5}}. \tag{3.2.11}$$

We illustrate the variation of (3.2.10) with surface tension in Figure 3.1(a). The simplicity of this breakup rate and its strong dependence on surface tension is useful when considering the effect of surfactant addition on droplet breakup. However, it is unlikely that the breakup rate is independent of drop size.

Another simple choice would be to take $a = 0$ and $F = 1$ so the breakup is independent of surface tension i.e.

$$\gamma = K_{00}\epsilon^{1/3}v^{-2/9} \tag{3.2.12}$$

where K_{00} is a constant of proportionality. Non-dimensionalising ϵ using (2.4.10) and v using (3.1.16) i.e. with

$$\epsilon = \frac{W_0^3}{D}\epsilon^*, \quad v = v_\infty v^*, \tag{3.2.13}$$

yields

$$\gamma = K_0\epsilon^{1/3}v^{-2/9}, \tag{3.2.14}$$

with

$$K_0 = \frac{W_0^2}{D^{4/3}v_\infty^{2/9}}. \tag{3.2.15}$$

The variation of the breakup rate (3.2.14) with volume is illustrated in Figure 3.1(b). The breakup rate (3.2.14) stipulates that larger droplets require larger eddies, with greater kinetic energy, to break up and thus break up less frequently than smaller ones. Note that this is physically unrealistic for smaller drops since surface tension is neglected. The breakup rate (3.2.14) is used in Lee et al. (1987) and its prediction of bubble size distribution in a turbulent flow agrees well with experiments.

Throughout this thesis, we often use a generalisation of (3.2.14) and (3.2.3), given by

$$\gamma = K_{00}\epsilon^{1/3}v^{-2/9}\left(1 - \frac{C^{5/3}(\pi/6)^{5/9}\sigma}{\rho\epsilon^{2/3}v^{5/9}}\right)^{1/2}\mathcal{H}\left(1 - \frac{C^{5/3}(\pi/6)^{5/9}\sigma}{\rho\epsilon^{2/3}v^{5/9}}\right). \tag{3.2.16}$$

Here C is the same order one constant as in (3.2.3) and so $C^{5/3}$ corresponds to a critical Weber number below which breakup cannot occur. Note that the breakup rate

(3.2.16) corresponds to (3.2.7) with $a = 0$ and $F(x) = (1 - C^{5/3}/x)^{1/2}\mathcal{H}(1 - C^{5/3}/x)$. Martínez-Bazán et al. (1999a) obtain (3.2.16) by considering the energy density E, which consists of velocity fluctuations balanced by the surface energy of the drop, namely

$$E = \tilde{C}\rho\epsilon^{2/3}d^{2/3} - 6\sigma d^{-1}. \tag{3.2.17}$$

Here $\tilde{C}$ is some constant, and the equality comes from (3.2.1) and assuming the drop is broken by fluctuations with length-scale d. They model the breakup rate as

$$\gamma \propto \frac{E^{1/2}}{d} \propto \frac{\left(\tilde{C}\epsilon^{2/3}d^{2/3} - 6\sigma/(\rho d)\right)^{1/2}}{d}, \tag{3.2.18}$$

where the first equality comes from dimensional analysis and the second from (3.2.17). Once rearranged and with the implicit Heaviside function accounted for, this yields (3.2.16). Here the breakup rate is zero at the maximum stable drop size (3.2.3), and droplets smaller than this size do not break up. Non-dimensionalising using

$$\epsilon = \frac{W_0^3}{D}\epsilon^*, \quad v = v_\infty v^*, \quad \sigma = \sigma_0\sigma^* \tag{3.2.19}$$

yields

$$\gamma = K_0 v^{-2/9}\epsilon^{1/3}\left(1 - C_1\sigma v^{-5/9}\epsilon^{-2/3}\right)^{1/2}\mathcal{H}\left(1 - C_1\sigma v^{-5/9}\epsilon^{-2/3}\right), \tag{3.2.20}$$

where

$$K_0 = K_{00}D^{2/3}v_\infty^{-2/9} \tag{3.2.21}$$

and

$$C_1 = \frac{C^{5/3}(\pi/6)^{5/9}\sigma_0 D^{2/3}}{\rho W_0^2 v_\infty^{5/9}}. \tag{3.2.22}$$

The breakup rate (3.2.20) encodes the idea, from (3.2.14), that larger drops are harder to break up. It also includes the restoring force of surface tension which makes smaller drops more difficult to break. The Heaviside term imposes the maximum stable drop size from (3.2.3). We illustrate (3.2.20) in Figure 3.1(c). We see that increasing ϵ or decreasing σ increases not only the breakup rate but also the range of droplets which can break up through the Heaviside function. One weakness is that the breakup rate does not become infinite as the surface tension tends to zero, as one might expect.

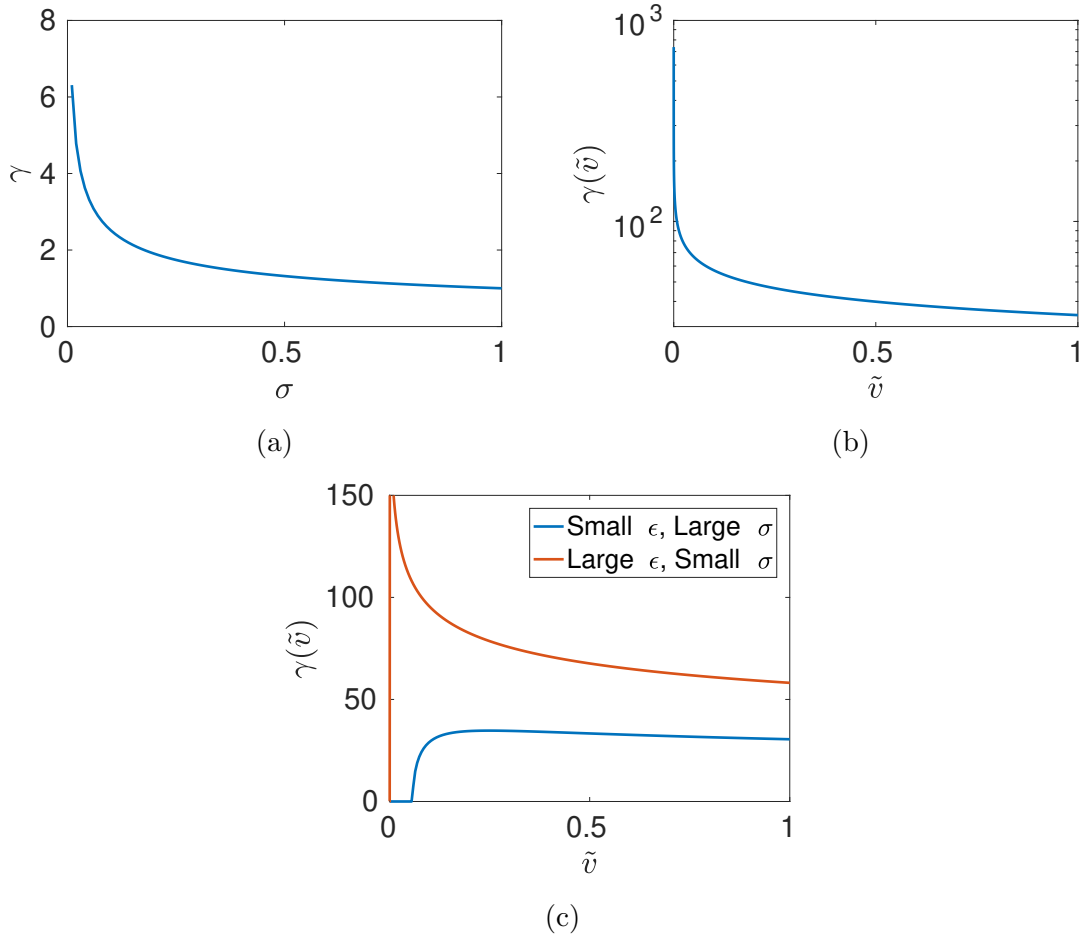


Figure 3.1: Different choices for the breakup rate γ. We take the largest dimensional drop size as $v_\infty = 65\,\mathrm{mm}^3$. (a) (3.2.10) with $\epsilon = 1$ and $K_0 = 1$; (b) (3.2.14) with $\epsilon = 1$ and $K_0 = 1$; (c) (3.2.20) for $C = 1$ and $K_0 = 1$, with $\epsilon = 1$ and $\sigma = 1$ in blue, and $\epsilon = 2$ and $\sigma = 1/6$ in red.

It is possible to empirically evaluate certain elements in models for the breakup rate by noting, from (3.1.17), that the largest drops (with $v = 1$) satisfy

$$\gamma(1, \epsilon, \sigma) = -\frac{1}{\phi(1,t)} \frac{d\phi(1,t)}{dt}. \tag{3.2.23}$$

Martínez-Bazán et al. (1999b) use a similar idea and, from their experimental distribution, they find that $\gamma \propto \epsilon^{0.377} - \epsilon^{0.393}$, which corresponds closely to the notion that $\gamma \propto \epsilon^{1/3}$ in (3.2.20). Martínez-Bazán et al. (1999b) also use their breakup rate to model the size distribution of air bubbles in a turbulent flow and find that their resulting distribution agrees with their empirical distribution.

Much of the literature uses far more complex and involved breakup rates in an attempt to model the droplet eddy interactions (Bandara and Yapa, 2011; Coulaloglou

and Tavlarides, 1977; Liao and Lucas, 2009; Prince and Blanch, 1990; Tsouris and Tavlarides, 1994; Zhao et al., 2014b). The approach used by multiple authors including Tsouris and Tavlarides (1994) and Zhao et al. (2014b) is to suppose the flow is made up of a collection of discrete eddies, which produce droplet deformations by 'colliding' with a drop. However, it is difficult to know which of these many competing theories is correct. Simpler breakup rates can be somewhat checked with the experimental data, as done by Martínez-Bazán et al. (1999b). However, especially when using more complicated forms, the breakup rate can only be validated by using them in droplet population models such as (3.1.17), to predict drop size distributions, and then comparing these resulting distributions to empirical data. Thus, there is little direct experimental justification for these breakup rates. Moreover, many of these breakup rates are validated by experiments involving bubbles rather than droplets, which may break up differently. Therefore, we do not use anything more complicated than (3.2.20), which captures the important features of the droplet-eddy interactions.

Throughout this thesis, we mainly use the breakup rate (3.2.20). In Chapter 5, to make more progress, we use alternative breakup rates which have a somewhat similar form to (3.2.20) but have a simpler separable structure.

3.2.3 Daughter drop distribution

The daughter drop distribution $\chi(v, \tilde{v})$ models the expected fraction of a drop of volume $\tilde{v}$ which becomes volume v drops when it breaks up. Recall that, as previously discussed, to conserve mass, χ must satisfy (3.1.14). Whilst there are some experiments which can be used to somewhat verify the appropriate form of γ, it is not possible to do the same for χ. Therefore, its form is generally even less well understood. We discuss some possibilities and illustrate them in Figure 3.2.

The simplest possible choice would be to take $\chi(v, \tilde{v})$ to be independent of v so $\chi(v, \tilde{v})$, for fixed $\tilde{v}$, is proportional to one. This is often helpful when trying to simplify the model. Taking (3.1.14) into account, this sets

$$\chi(v, \tilde{v}) = \frac{1}{\tilde{v}}. \tag{3.2.24}$$

This means that, when a drop of volume $\tilde{v}$ breaks, it produces the same volume of very small drops as of larger drops. The physical implications of this choice are more apparent from considering the form of $N(v, \tilde{v})$, the continuous equivalent of N_{ij}. It describes the expected number density of drops of volume v produced when a drop

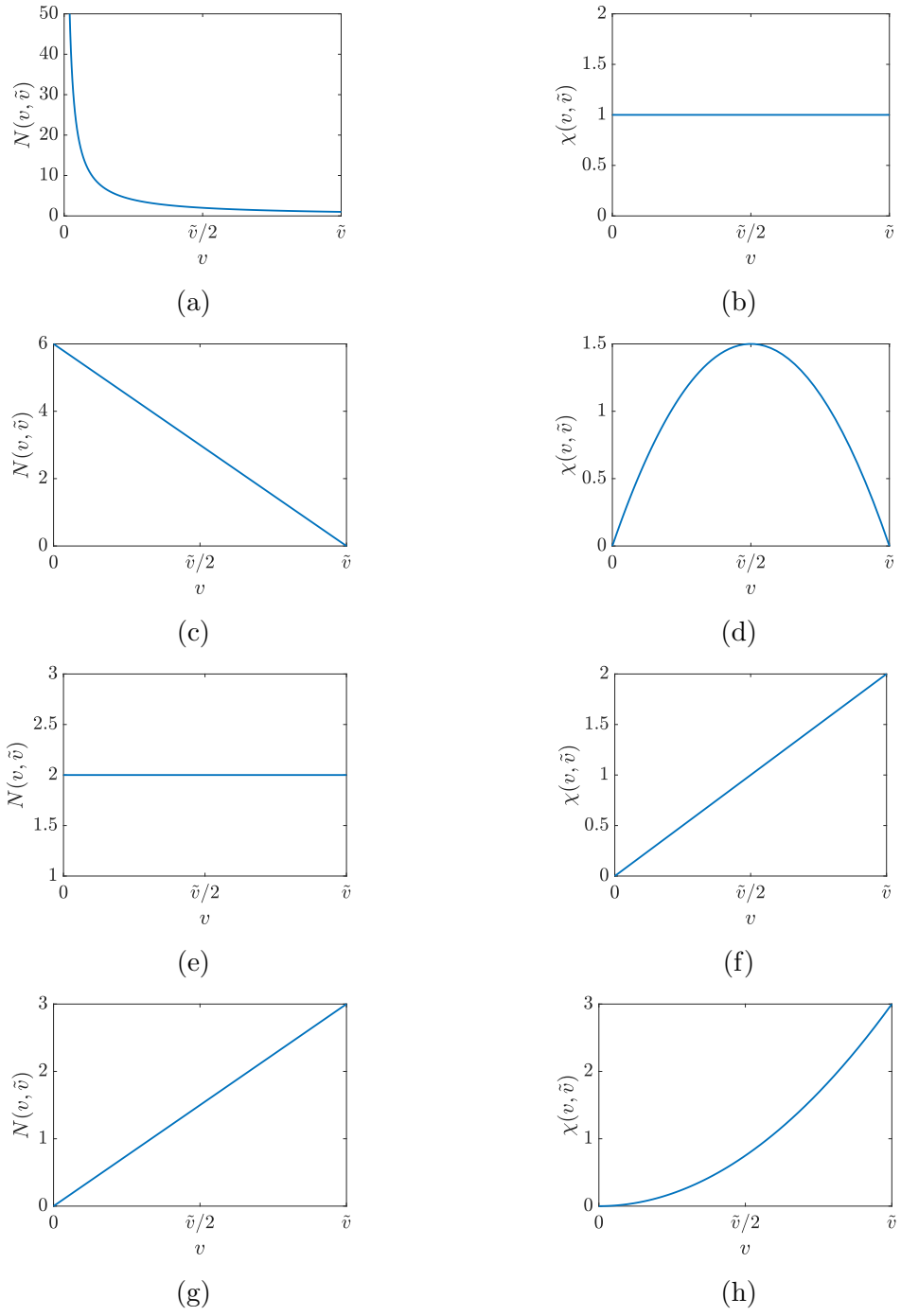


Figure 3.2: In (a), (c), (e) and (g), we plot expected number density, $N(v,\tilde{v})$, of drops of volume v produced when a drop of volume $\tilde{v}$ breaks up. In (b), (d), (f) and (h), we plot expected volume fraction distribution, $\chi(v,\tilde{v})$, of a drop with volume $\tilde{v}$ which becomes volume v drops upon breakup. (a)–(b) $N(v,\tilde{v})$ is given by (3.2.26) and $\chi(v,\tilde{v})$ is uniform, given by (3.2.24); (c)–(d) $N(v,\tilde{v})$ decreases linearly, given by (3.2.31), and $\chi(v,\tilde{v})$ is (3.2.32); (e)–(f) $N(v,\tilde{v})$ is uniform, given by (3.2.27), and $\chi(v,\tilde{v})$ is (3.2.28); (g)–(h) $N(v,\tilde{v})$ increases linearly, given by (3.2.29), and $\chi(v,\tilde{v})$ is (3.2.30).

of volume $\tilde{v}$ breaks up and, analogous to (3.1.6), it is related to $\chi(v, \tilde{v})$ by

$$\chi(v, \tilde{v}) = \frac{v}{\tilde{v}} N(v, \tilde{v}). \tag{3.2.25}$$

In this case

$$N(v, \tilde{v}) = \frac{1}{v} \tag{3.2.26}$$

and so the expected number of drops produced is independent of the size of the drop which breaks up. As seen in Figure 3.2(a), this choice imposes that when any drop breaks up, an infinite number of small drops are produced. For these reasons it is perhaps not the most physically realistic choice.

To investigate more physically realistic forms for $\chi(v, \tilde{v})$, we attempt to determine more plausible choices of $N(v, \tilde{v})$. One option would be to assume uniform droplet breakup, namely that $N(v, \tilde{v})$ is independent of v. Then, for (3.1.14) to hold, we find

$$N(v, \tilde{v}) = \frac{2}{\tilde{v}} \tag{3.2.27}$$

and so

$$\chi(v, \tilde{v}) = \frac{2v}{\tilde{v}^2}. \tag{3.2.28}$$

Here although the number of small drops produced is equal to the number of larger drops produced (see Figure 3.2(e)), because the small drops have such a small volume, their produced volume is small and, for fixed $\tilde{v}$, χ is a monotonically increasing function, as seen in Figure 3.2(f).

Another possible choice would be to take $N(v, \tilde{v})$ for fixed $\tilde{v}$ to be linear. We might suppose

$$N(v, \tilde{v}) = \frac{3v}{\tilde{v}^2} \tag{3.2.29}$$

which sets

$$\chi(v, \tilde{v}) = \frac{3v^2}{\tilde{v}^3}. \tag{3.2.30}$$

This imposes that when a drop breaks up, most of the drops produced are large and very few small drops are produced, as seen in Figures 3.2(g)–(h). This is perhaps unrealistic as we might imagine that small eddies would shear off a collection of very small droplets during breakup. Therefore, an alternative would be to suppose that

$$N(v, \tilde{v}) = \frac{6(\tilde{v} - v)}{\tilde{v}^2} \tag{3.2.31}$$

which proposes that a larger number of small than large drops are produced (see Figure 3.2(c)). This means that

$$\chi(v, \tilde{v}) = \frac{6v(\tilde{v} - v)}{\tilde{v}^3}, \tag{3.2.32}$$

as illustrated in Figure 3.2(d). Hence only a small volume of very small and very large droplets are produced. A significant proportion of the drops which break up goes into producing droplets of around half the volume of the original drop.

In much of this thesis, we set χ as (3.2.32). In reality a much more complex form of χ might be more appropriate. In experiments of droplet breakup in a turbulent flow, drops are commonly observed to deform into a dumbbell shape and subsequently split in two with a very small satellite drop between them (Collins and Knudsen, 1970). Realistically, the two larger drops are likely to have unequal sizes (Hesketh et al., 1991). Therefore, a more realistic form of $N(v, \tilde{v})$ might have a narrow peak at very small drop sizes and another local maximum near $\tilde{v}/2$.

We will investigate the effect of different forms of χ on the droplet size distribution in Section 3.3.

3.3 Evolution of drop size distribution with time

To understand and explore the droplet size distribution model and the effect of the different breakup rate functions presented in Section 3.2, we solve (3.1.17) for $\phi(v, t)$.

3.3.1 Numerical method

Numerically solving integro-differential equations of this nature can be computationally expensive and thus we now outline an effective numerical method for solving (3.1.17). We use the method of lines.

We first discretise drop size in the integral term. Wo do so by categorising each drop into one of N bins, with bin i, say, containing all droplets of volume v_i. The most obvious approach would be to discretise uniformly in volume, as described in Section 3.1.1. However, in this thesis, we will mainly use other discretisations, such as linear spacing in diameter d, linear spacing in $d^{1/2}$ or linear spacing in $\log d$. The different drop size discretisations allow us to consider a greater range of drop sizes (in particular smaller drop sizes) without needing to increase the number of bins. Suppose there are 100 bins and the largest drop has diameter $d = 1$. With uniform spacing in d, the smallest drop has diameter $d = 10^{-2}$ whilst using $d^{1/2}$ the smallest

is $d = 10^{-4}$. Discretising using $\log d$, the smallest drop size can be freely chosen, independent of the number of bins. In droplet breakup, the mode drop diameter can decrease by as much as three orders of magnitude; therefore choosing a discretisation which focuses on the smaller drop sizes is required for accurate solutions. In Chapter 4, it is generally sufficient to discretise using $d^{1/2}$. In Chapter 6, which includes the effect of surfactant addition, we mainly discretise using $\log d$. This is because the addition of surfactants promotes further and more rapid droplet breakup, and smaller droplets are produced here. When discretising using $\log d$, we choose the smallest drop size for a set of simulations by numerically solving for a wider range of drop sizes and then choosing the largest drop size where $\phi \sim 0$.

Once we have discretised drop size, we use either the rectangle rule or the trapezoidal rule to numerically approximate the integral term in (3.1.17). As one might expect, using the trapezoidal rule yields greater convergence in a smaller number of drop size bins.

The master equation, (3.1.17), then becomes a series of N coupled first order ODEs in time. These are solved using the stiff ODE solver, ODE15s, in MATLAB.

3.3.2 Results

We can now solve (3.1.17). We do so for the breakup rate (3.2.20), with dimensionless parameters $K_0 = 0.2$ and $C_1 = 1.5 \times 10^{-4}$. We take χ to be (3.2.32), which is the most common choice in this thesis. The energy dissipation ϵ is taken to be constant with $\epsilon = 1$. We take the largest drop size to have dimensional volume $v_\infty = \pi D^3/6$; this corresponds to assuming the dimensional diameter, d_∞, of the largest drop is $d_\infty = D$. Initially, at $t = 0$, we assume that ϕ is lognormally distributed so

$$\phi(v, 0) \propto \text{lognormal}(\mu_v, \sigma_v), \tag{3.3.1}$$

where μ_v and σ_v are set such that the mode diameter of the distribution is $4/5\,(6/\pi)^{1/3}$ and variance is $1/300\,(6/\pi)^{1/3}$. (The factor of $(6/\pi)^{1/3}$ here arises from the fact that the largest drops have dimensionless volume $v = 1$ and so their diameter is $d = (6/\pi)^{1/3}$.) We normalise so that, at $t = 0$, $\int_0^1 \phi(v, 0)\,\mathrm{d}v = 1$.

We use the numerical method outlined in Section 3.3.1. We discretise drop size uniformly in $\log d$, setting the smallest drop size to correspond to $d = 2 \times 10^{-6}$, and discretise the integral term using the trapezoidal rule. We take the number of drop size bins, N, to be 300.

Figure 3.3 illustrates the variation of $d^2\phi$ with drop diameter $d = (6v/\pi)^{1/3}$. Plotting $d^2\phi$, as opposed to ϕ, provides a better visualisation of the volume fraction

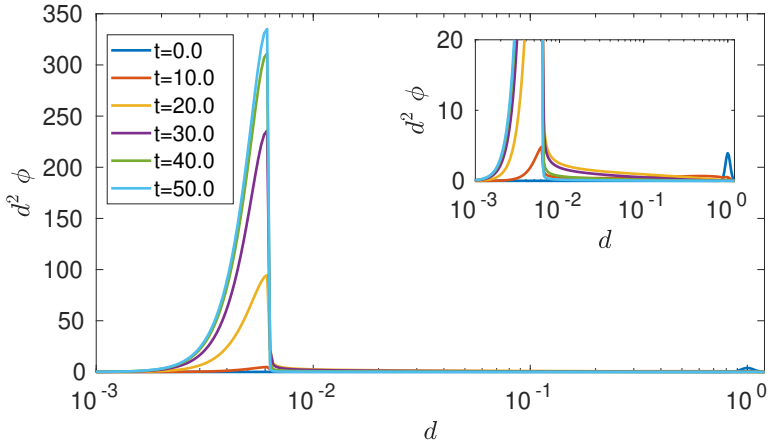


Figure 3.3: Drop size distribution without spatial dependence and with fixed energy dissipation obtained by solving (3.1.17). We set the breakup rate as (3.2.20) with $C_1 = 1.5 \times 10^{-4}$ and $K_0 = 0.2$, and the daughter size distribution (3.2.32). We take $\epsilon = 1$ and $v_\infty = \pi D^3/6$, with $D = 0.5\,\mathrm{m}$. Initially, ϕ is given by (3.3.1). The insert shows the same results but on a zoomed-in y-axis to better illustrate the behaviour at smaller times.

of droplets of different diameters. This is because volume fraction is given by $\phi\,\mathrm{d}v$ and, since $v = \pi d^3/6$, $\phi\,\mathrm{d}v = (\pi/2)d^2\phi\,\mathrm{d}d$. Note that the dimensionless largest drop, with volume $v = 1$, corresponds to the dimensionless drop diameter $d = (6/\pi)^{1/3}$ so d ranges up to $d \approx 1.24$.

We see that the droplets break up with time producing smaller drops. At early times, there is a bimodal distribution as some large drops remain unbroken. There is a spike in the distribution at around $d \approx 6 \times 10^{-3}$ because of the Heaviside function in the breakup rate, (3.2.20), which imposes that droplets below $d \approx 6 \times 10^{-3}$ cannot break up. This ends up being the mode drop size as all larger drops break into this and smaller drop sizes. At large times, because of the Heaviside function, once all the larger drops have broken up, no further breakup can occur and a steady state is reached.

3.3.3 Testing convergence

In order to have confidence in the results of Section 3.3.2, we must verify that the numerical scheme converges to the true solution. To do so we first calculate ϕ for $N = 800$; here N is large enough that it should provide a very good approximation to the solution. We then investigate the convergence, with increasing N, of the steady state solution for ϕ to this solution. Evidently increasing N increases the accuracy of

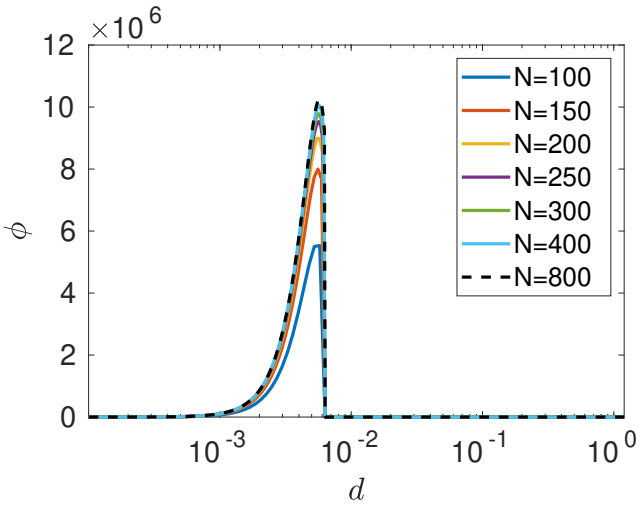


Figure 3.4: Drop size distribution ϕ for different bin sizes N

the solution but, correspondingly, the run-time increases. Therefore, a balance must be achieved between a sufficiently large N for appropriate convergence but a small enough N that the computational cost is not so great.

As an example, we consider the same problem as in Section 3.3.2. The computed steady state drop size distribution, ϕ, for different values of N is shown in Figure 3.4. We observe that increasing N causes ϕ to approach the solution for $N = 800$. By around $N = 250$ bins, increasing the bin size does not significantly improve the results. In Table 3.1 we more quantitatively investigate this convergence. We compute the relative error for different bin sizes N, defined as $||\phi^{\text{true}} - \phi^N||/||\phi^{\text{true}}||$. Here $||\cdot||$ refers to the L_2 norm, ϕ^{true} is the 'true solution' i.e. the steady state solution when $N = 800$, and ϕ^N is the distribution for N bins. If we impose that a suitable value of N is one where the relative error is around 0.1, in further computations we should take $N = 300$.

In general, we find that setting $N = 300$ is usually sufficient to achieve good accuracy. The corresponding run-time ranges between 5 seconds to 30 seconds on a standard desktop computer. In Chapter 4, when combining drop size distributions with one-dimensional jet models, the equation for the drop size distribution essentially reduces to (3.1.17) and so can be solved identically in a similar run-time. In Chapter 6, when we compute the drop size distribution, with additional equations for the surfactant behaviour, the run-time is slightly longer, up to 1–2 minutes on a standard desktop computer.

N	100	150	200	250	300	400
Relative Error	0.491	0.278	0.188	0.143	0.116	0.0817

Table 3.1: Relative error between 'true solution' (computed with $N = 800$ and smaller values of N)

3.3.4 Different χ

The main uncertainty in our models is the form of χ. Therefore, we now explore the effect of the different choices of χ presented in Section 3.2.3 on the drop size distribution. We solve for ϕ as in Section 3.3.2 and compare the resulting distributions in Figures 3.5(a)–(c) and 3.3.

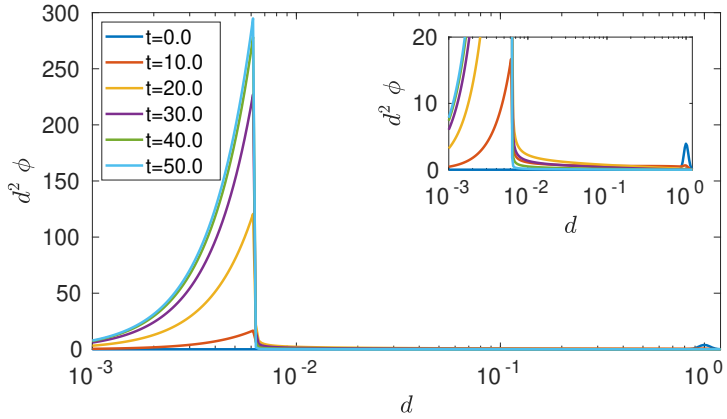
Interestingly, the qualitative behaviour in all cases is very similar and, as observed in Figure 3.3 (where χ is given by (3.2.32)), in steady state the mode of the distributions occurs at the critical drop size (the drop size below which no droplets can break up).

The distributions in Figures 3.5(a), 3.3, 3.5(b) and 3.5(c) correspond to the choices of $N(v, \tilde{v})$ in Figures 3.2(a), 3.2(c), 3.2(e) and 3.2(g) respectively. Notice that, as we go along this list, the number of small drops being produced decreases and that of larger drops increases.

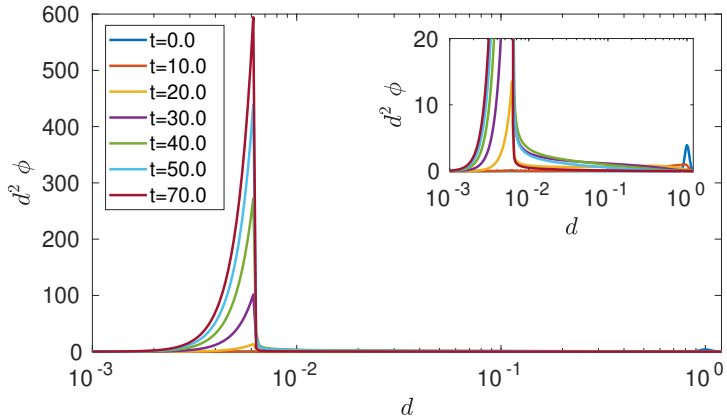
In Figure 3.5(a), we take $N(v, \tilde{v})$ as (3.2.26) and $\chi(v, \tilde{v})$ as (3.2.24). Here χ is uniform so, when a drop breaks up, the fraction of small and large drops produced are equal; this means that, due to their small volume, there are many small drops being produced and fewer larger drops. In Figure 3.5(a) we see that this causes a wide range of droplet sizes to be produced. This choice, as discussed in Section 3.2.3, is not very physically realistic as it assumes that an infinite number of very small drops are produced.

In Figure 3.3, we take $N(v, \tilde{v})$ as (3.2.32) and $\chi(v, \tilde{v})$ as (3.2.32). This also imposes that a large number of small drops are produced but is more physically realistic in that $N(v, \tilde{v})$ is always finite. Fewer very small droplets are produced and so, in Figure 3.3, we see that the steady-state distribution the range of drop sizes is more narrow than in Figure 3.5(a).

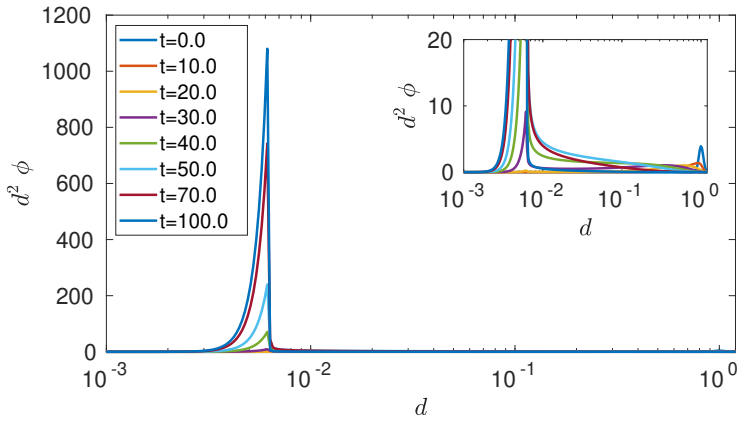
Figure 3.5(b) illustrates the distribution for uniform $N(v, \tilde{v})$ given by (3.2.27). The corresponding $\chi(v, \tilde{v})$ is given by (3.2.28) and so the expected fraction of small droplets produced is small. Thus a narrower range of drop sizes are produced in any breakup event. All drops break into droplets smaller than the critical drop size and when they do so they cannot break any further; thus the distribution is more targeted near the mode of the distribution compared to those in Figures 3.3 and



(a) $\chi(v,\tilde{v}) = \frac{1}{\tilde{v}}, N(v,\tilde{v}) = \frac{1}{v}$



(b) $\chi(v,\tilde{v}) = \frac{2v}{\tilde{v}^2}, N(v,\tilde{v}) = \frac{2}{\tilde{v}}$



(c) $\chi(v,\tilde{v}) = \frac{3v^2}{\tilde{v}^3}, N(v,\tilde{v}) = \frac{3v}{\tilde{v}^2}$

Figure 3.5: Drop size distribution without spatial dependence and with fixed energy dissipation obtained by solving (3.1.17). We set the breakup rate as (3.2.20) with $C_1 = 1.5 \times 10^{-4}$, $K_0 = 0.2$, $\epsilon = 1$ and $v_\infty = \pi D^3/6$, with $D = 0.5\,\mathrm{m}$. Initially, ϕ is given by (3.3.1). We use the daughter size distributions (a) (3.2.24); (b) (3.2.28); (c) (3.2.29). In each graph, the insert shows the same results but on a zoomed-in y-axis to better illustrate the small-time behaviour.

3.5(a). Additionally, when a drop breaks up the droplets produced will be larger than in the cases corresponding to Figures 3.3 and 3.5(a) so multiple breakup events are required for the droplets to be below the critical drop size. Therefore, more breakup is required for a steady state to be achieved. It takes around $t = 70$ for the distribution to reach its steady state whilst in Figures 3.3 and 3.5(a) the steady state was reached by $t = 50$.

In Figure 3.5(c), $N(v, \tilde{v})$ given by (3.2.29) and $\chi(v, \tilde{v})$ by (3.2.30); when a drop breaks up, it will produce a large number and a large volume of bigger drops. Thus, the two phenomenon observed in Figure 3.5(b) are enhanced; the distribution is even more narrowly centered around the critical drop size and the steady state takes even longer, around $t = 100$, to be reached.

Note that, throughout this section, the surface tension is assumed constant. The evolution of these 'box' models with varying surface tension is explored extensively in Chapter 6.

3.4 Conclusions

In this chapter we examine the microscopic scale to understand how droplets in a turbulent flow break up. Droplet break up is precipitated by interactions between eddies and droplets, and we have examined the different types of droplet breakup which might be encountered. We have found that inertial drops, whose breakup is governed by surface tension and energy dissipation, are the most physically relevant and thus have focused on these.

We have presented models which enable us to obtain drop size distributions for the simplified case of a fixed region with fixed turbulence. We have seen that the breakup rates and daughter size distributions are key ingredients of the drop population models. Different choices of these have a significant effect on the ensuing drop size distribution.

The droplet population model and breakup rates introduced in this chapter will form the basis of the discussion in the successive chapters. In Chapter 4, we model the evolution of ϕ in the jet and thus extend (3.1.17) to include spatial effects. In Chapters 4 and 6, we mainly use the breakup rate (3.2.20) with daughter size distribution (3.2.32) to numerically solve the droplet population model. In Chapter 5, we attempt to find similarity solutions for ϕ in a turbulent jet.

Chapter 4

Combining large-scale jet and small-scale droplets

In Chapter 2 we investigate the motion and energy of a turbulent jet. In Chapter 3 we use population models to examine the effect of droplet breakup on the drop size distribution in homogeneous turbulence. Now we combine these macroscopic jet and microscopic droplet models to predict the evolution of drop size distribution through a turbulent jet.

Our approach is to assume that the coupling of macroscopic and microscopic scales is one way so that the behaviour of the oil jet affects droplet breakup but the motion and breakup of droplets has a negligible influence on the macroscopic flow. Therefore, the motion of the jet is assumed to be that of a pure water jet (without the presence of droplets), as modelled in Chapter 2. However, the droplet scale depends on the jet behaviour: droplets are advected and diffused by the large-scale flow, and the rate at which they break up depends on the energy in the jet, quantified by the energy dissipation in Chapter 2.

Note that, at this point, it is sensible to understand and model the oil jet and breakup of oil droplets before adding the effects of varying dispersant concentration. Therefore, in this chapter, we will take surface tension to be constant.

In much of the existing literature, drop size distributions are determined by combining one-dimensional jet models with highly complex breakup rate models (Bandara and Yapa, 2011; Zhao et al., 2014a). We extend this by considering models in both one and two spatial dimensions. We first consider two-dimensional models, using our two-dimensional jet models from Chapter 2. There is a significant variation in the velocity and energy dissipation across the width of the jet and so these models enable us to consider the ensuing effect on droplet breakup. These two-dimensional models are accurate but can be computationally involved. Therefore, for simplicity, we also

consider width-averaged droplet population models, which vary with only one spatial dimension: height. These are validated and their accuracy is assessed by comparison to our more complex two-dimensional models. Finally, we compare the simpler width-averaged models with small-scale experiments in (Brandvik et al., 2014, 2013; Johansen et al., 2013), to fit the unknown parameters in our models.

4.1 Modelling assumptions

Our main assumption (which has been briefly touched on) is that, whilst the jet flow affects droplet dynamics, the breakup of the droplets has a negligible influence on the jet's behaviour. This is a reasonable assumption since we are focusing on the momentum driven region in the jet, where buoyancy effects are negligible. The density and viscosity of the oil is similar to that of water (see Table 1.1). If we imagine a two-phase flow, where the fluids have very similar viscosities and densities, then the system is akin to a single phase flow. The only way the jet would be affected by the droplets would be if surface tension effects are large. We assume this is not the case. To provide some justification of this assumption, we can calculate that the surface energy which goes into the drop breakup is small compared to the energy flux into the jet. The energy flux into the jet is given by

$$\frac{1}{2}\rho\pi b_0^2 W_0^3$$

which is 82,172 $\mathrm{kg\,J\,s^{-1}}$ using the parameters in Table 1.1. Let us consider the surface energy flux required to break up all of the oil droplets, which we assume have diameter $d = 50$ microns. (Most droplets will be larger than this and so require less surface energy to break.) The number of drops with diameter d per unit height is $\pi b_0^2/(\pi d^3/6)$. The surface energy required to break one of these drops is $\pi d^2\sigma$. Therefore, the surface energy flux to break all of these droplets is

$$\frac{\pi b_0^2}{\pi d^3/6}\Phi W_0 \pi d^2\sigma.$$

Note the presence of Φ here, the volume fraction of oil, arises from the fact that the jet is a mixture of oil and water. The droplets require greatest surface energy to break up if all of the ejected fluid is oil ($\Phi = 1$) and the spill is untreated by dispersants ($\sigma = 0.03\,\mathrm{kg\,s^{-2}}$); in this case the required surface energy dissipation is 7,069 $\mathrm{kg\,J\,s^{-1}}$. This means that, in the worst case, the surface energy which goes into breaking up the droplets is much smaller than the energy flux into the jet.

Throughout this chapter, as briefly mentioned in Chapter 3, we neglect the coalescence of droplets. With greater height, the spread of the jet will be wider and thus, away from the jet base, the droplets are likely to drift apart from each other, reducing the likelihood of coalescence. Therefore, especially when surfactant its present, its effect is not thought to be highly significant (Brandvik et al., 2013; Johansen et al., 2013; Paul et al., 2004). We instead focus on droplet breakup.

In terms of the macroscopic flow, we assume throughout this chapter that the jet is axisymmetric and long and thin.

4.2 Modelling distribution of droplet sizes

4.2.1 A note on the turbulent transport of scalars

We want to model the transport and breakup of droplets, which we assume move with the turbulent flow. To motivate the spatial dependence in our model, we first briefly outline how the transport of a species in a turbulent flow is generally modelled. Let us suppose the species has concentration c and satisfies the advection diffusion equation,

$$\frac{\partial}{\partial x_i}\left(u_i c\right) = \frac{\partial}{\partial x_i}\left(D_m \frac{\partial c}{\partial x_i}\right), \tag{4.2.1}$$

with molecular diffusivity D_m. We decompose the mean flow from turbulent fluctuations, writing the velocity as $u = U + \tilde{u}$ and concentration as $c = C + \tilde{c}$. Inserting these into (4.2.1) and averaging yields

$$U_i \frac{\partial C}{\partial x_i} = \frac{\partial}{\partial x_i}\left(D_m \frac{\partial C}{\partial x_i} - \overline{\tilde{u}_i \tilde{c}}\right). \tag{4.2.2}$$

The Péclet number is given by $Pe = l_c u_0 / D_m$, where l_c is the length scale of mean concentration gradients and u_0 is the velocity scale associated with the large turbulent eddies. Turbulence rapidly increases l_c (Tennekes and Lumley, 1972, p. 241) and so Pe is generally large, making molecular diffusion negligible.

Equation (4.2.2) has a similar form to the transport of momentum in (2.2.5). To close the momentum equation, in (2.2.8) we assume the Reynolds shear stresses are generated by the gradient of the mean velocity. In a similar way, here, we assume that the eddy flux $\overline{\tilde{u}_i \tilde{c}}$ is generated by the gradients of mean concentration so

$$-\overline{\tilde{u}_i \tilde{c}} = \mathrm{Sc}\ \nu_T \frac{\partial C}{\partial x_i}, \tag{4.2.3}$$

where recall ν_T is the turbulent kinematic eddy viscosity. Here the turbulent Schmidt number, Sc, is an order one constant of proportionality representing the ratio of turbulent diffusivity to turbulent viscosity (Tominaga and Stathopoulos, 2007). For simplicity we shall take it to be one. Thus, on neglecting molecular diffusion, the mean concentration is determined by

$$U_i \frac{\partial C}{\partial x_i} = \frac{\partial}{\partial x_i}\left(\nu_T \frac{\partial C}{\partial x_i}\right). \tag{4.2.4}$$

4.2.2 Master equation

We examine the distribution, $\phi(v, r, z)$, of droplet volume fraction, which, recall, is defined such that the volume fraction of drops of volume between v_a and v_b is given by

$$\int_{v_a}^{v_b} \phi(v, r, z)\, \mathrm{d}v. \tag{4.2.5}$$

To model ϕ we use the droplet model, (3.1.17), from Chapter 3 to describe the droplet breakup due to the turbulent flow. We extend this model to also include the process by which droplets are advected and diffused through a steady jet by the large-scale fluid motion, as described in Section 4.2.1. Hence, the dimensionless equation for the drop size distribution, (3.1.17), applied to a steady turbulent jet yields

$$\begin{aligned} U\frac{\partial \phi}{\partial r} + W\frac{\partial \phi}{\partial z} = \frac{1}{r}\frac{\partial}{\partial r}\left(r\nu_T \frac{\partial \phi}{\partial r}\right) - \gamma(v, \epsilon(r,z))\phi(v,r,z) \\ + \int_v^1 \gamma(\tilde{v}, \epsilon(r,z))\chi(v,\tilde{v})\phi(\tilde{v},r,z)\, \mathrm{d}\tilde{v}. \end{aligned} \tag{4.2.6}$$

Here $\gamma(v, \epsilon)$ is the rate at which droplets of volume v break up. It now varies spatially, according to the variation of ϵ in the jet. The daughter size distribution $\chi(v, \tilde{v})$ is a distribution corresponding to the expected proportion of the volume of a drop with volume $\tilde{v}$ which becomes v sized droplets upon breakup. When drops of volume $\tilde{v}$ break up, the expected fraction of the volume of the produced droplets which have size between v_a and v_b is

$$\int_{v_a}^{v_b} \chi(v, \tilde{v})\, \mathrm{d}v. \tag{4.2.7}$$

The volume produced when a drop breaks up is equal to the volume of the original drop and so $\chi(v, \tilde{v})$ must satisfy

$$\int_0^{\tilde{v}} \chi(v, \tilde{v})\, \mathrm{d}v = 1, \tag{4.2.8}$$

as in (3.1.14). The terms on the left of (4.2.6) represent the advection of the drops by the flow and the first term on the right corresponds to turbulent diffusion. These terms are (4.2.4), expressed in axisymmetric coordinates with axial diffusion neglected due to the assumed small aspect ratio of the jet (analogous to (2.4.2)). The terms corresponding to droplet breakup are the same as those in (3.1.17) in Chapter 3. The second term on the right hand side of (4.2.6) corresponds to drops of volume v breaking up (they can break into drops of any volume less than v). The integral term represents the process by which larger drops break into those of volume v and thereby increase the volume fraction of droplets of volume v.

Initially, at $z = 0$, the volume fraction distribution is given by some $F(v, r)$, the flow is radially symmetric, and there are no oil drops far from the jet, which yields boundary conditions

$$\phi(v, r, 0) = F(v, r), \qquad \frac{\partial \phi}{\partial r}(v, 0, z) = 0, \qquad \phi(v, r, z) \to 0, \text{ as } r \to \infty. \tag{4.2.9}$$

The total volume fraction of oil is defined as

$$\Phi(r, z) = \int_0^1 \phi \, \mathrm{d}v. \tag{4.2.10}$$

Taking the integral of (4.2.6) from $v = 0$ to $v = 1$, swapping the order of integration in the resulting double integral and using (4.2.8) yields

$$U \frac{\partial \Phi}{\partial r} + W \frac{\partial \Phi}{\partial z} = \frac{1}{r} \frac{\partial}{\partial r} \left(r \nu_T \frac{\partial \Phi}{\partial r} \right). \tag{4.2.11}$$

Taking the integral of the boundary conditions, (4.2.9), for ϕ, from $v = 0$ to $v = 1$ sets

$$\Phi(r, 0) = \int_0^1 F(v, r) \, \mathrm{d}v, \qquad \frac{\partial \Phi}{\partial r}(0, z) = 0, \qquad \Phi(r, z) \to 0, \text{ as } r \to \infty. \tag{4.2.12}$$

4.3 Total oil fraction Φ

Before examining the drop size distributions, let us first consider the total volume fraction of oil Φ at different locations in the jet, satisfying (4.2.10)–(4.2.12). Let us assume, henceforth, that the oil released by the nozzle is much the same across the nozzle width so $\Phi(r, 0)$ follows a top hat distribution, namely

$$\Phi(r, 0) = \begin{cases} 1, & r \leq 1/2, \\ 0, & r > 1/2. \end{cases} \tag{4.3.1}$$

Note this also means $\phi(v, r, 0)$ follows a top hat distribution, so

$$\phi(v, r, 0) = \begin{cases} F(v), & r \leq 1/2, \\ 0, & r > 1/2, \end{cases} \tag{4.3.2}$$

where $\int_0^1 F(v)\,\mathrm{d}v = 1$.

If we substitute W into the equation (4.2.11) and boundary conditions, (4.2.12) and (4.3.1), for the total oil fraction Φ, we obtain the same equation (2.4.2) and boundary conditions, (2.4.6)–(2.4.8), for the jet's vertical velocity, W. This is a fortunate consequence of our assumption that the Schmidt number Sc= 1 in Section 4.2.1. Thus, noting that if Φ is a solution to (4.2.11) any scalar multiple of Φ is also a solution, we find that the total oil fraction is proportional to the vertical velocity W.

This means that, recalling that the similarity solution for W is given by (2.4.14), (2.4.17) and (2.4.24), the similarity solution for the total oil fraction, is

$$\Phi = \frac{\Phi_0 \delta_0}{(1+\xi^2)^2} \frac{1}{\delta_0 + \alpha z}, \tag{4.3.3}$$

where Φ_0 is a constant of proportionality to be determined and, recall,

$$\xi = \frac{\sqrt{\beta} r}{\delta_0 + \alpha z}. \tag{4.3.4}$$

It only remains to fix Φ_0. We do so by imposing conservation of oil flux. Integrating the full equation for the total oil fraction (4.2.11) across radial width, yields

$$\frac{d}{dz}\left(\int_0^\infty rW\Phi dr\right) = 0 \tag{4.3.5}$$

and thus

$$\int_0^\infty rW\Phi\,\mathrm{d}r = M_\Phi, \tag{4.3.6}$$

where the constant $M_\Phi = 1/8$ from the inlet conditions. Using the similarity solutions for W and Φ in (4.3.6), yields

$$\Phi_0 = \frac{6\beta M_\Phi}{\omega_0 \delta_0^2}. \tag{4.3.7}$$

The total oil fraction, Φ, can be illustrated by the full numerical results for W seen in Figure 2.1(a) and Figure 2.2 and the similarity solution for W in Figure 2.3(a). (The total oil fraction Φ will actually be plotted later, in Figure 4.1(c).) We see that, with increasing height and width, the total volume fraction of oil decreases. This is due to the entrainment of water into the oil jet, diluting the oil. Higher up the jet, the oil will be highly diluted.

4.3.1 Discussion

We have considered the variation in total oil fraction with position in the jet. This gives an indication of the regions with the greatest oil. We find that, perhaps unsurprisingly, the oil is advected and diffused in the same way as the mean flow in the z-direction. This means that, using the results from Chapter 2, there is a disparity between the regions where the dissipation is the greatest and where the oil concentration Φ, is maximum.

Examining the total oil fraction, Φ, demonstrates the significant effect of dilution. We see that as we move away from the source, the oil dilutes and its volume fraction decreases significantly. We will later see that, along with droplet breakup, dilution is the other main effect controlling ϕ.

4.4 Two-dimensional models

4.4.1 Full numerical approach

The most straightforward approach to finding the droplet size distribution is to solve (4.2.6)–(4.2.9) numerically, using the full numerical results for U, W and ϵ from Section 2.3.1. Note that the full numerics in Section 2.3.1 uses the full axisymmetric $k-\epsilon$ model, but here, in determining ϕ, we make the assumption that the jet is long and thin.

One difficulty is that, with increasing z, the jet expands considerably in width. At small z, all of the action takes place within a narrow region. However, for larger heights, the width over which the jet's motion affects droplet dynamics is much larger. To address this, we use rescaled variables so that the computational effort is focused on the regions of the jet where breakup occurs. We change variables from r to

$$R = \frac{r}{1+\alpha z}. \tag{4.4.1}$$

Note that this is almost proportional to the jet similarity variable (2.4.15), introduced in Section 2.4.2, but instead of the fitted parameter $\delta_0 < 0$ in the denominator we set this to be 1 so that R is non-negative for small z.

A finite difference scheme is employed. We treat z as a timelike variable, marching forward in z. We discretise implicitly in z and use central differences for the width coordinate R. Drop size is discretised uniformly in $d^{1/2}$, using 200 volume bins. Numerical experiments demonstrate that, with this choice, we can generally capture the

range of droplet sizes which are important in the evolution of the drop size distribution, in particular the smallest droplets which appear in the solution. (See Section 3.3.1 for further justification of this discretisation.)

Throughout this chapter, we use the breakup rate (3.2.20)–(3.2.22), given by

$$\gamma = K_0 v^{-2/9} \epsilon^{1/3} \left(1 - C_1 \sigma v^{-5/9} \epsilon^{-2/3}\right)^{1/2} \mathcal{H}\left(1 - C_1 \sigma v^{-5/9} \epsilon^{-2/3}\right), \tag{4.4.2}$$

with non-dimensional parameters

$$K_0 = K_{00} D^{2/3} v_\infty^{-2/9} \tag{4.4.3}$$

and

$$C_1 = \frac{C^{5/3} (\pi/6)^{5/9} \sigma_0 D^{2/3}}{\rho W_0^2 v_\infty^{5/9}}. \tag{4.4.4}$$

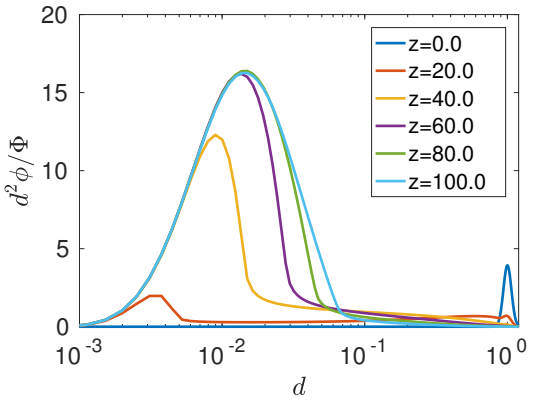
Recall it includes a Heaviside term which imposes that small droplets, subject to high surface stresses, cannot break up. Here we set the parameters in (4.4.2)–(4.4.4) as $K_{00} = 0.25$ and $C = 0.725$. Recall, from Chapter 3, that $C^{5/3}$ is a Weber number. We assume the daughter size distribution is specified by (3.2.32), so a greater number of small rather than large drops are produced upon breakup. In terms of volume, (3.2.32) imposes that a significant fraction of the volume of the drops which break up goes into producing droplets of around half the volume of the parent drop.

The other important input in this model is the initial behaviour, at $z = 0$. We take the initial largest dimensional droplet diameter as $d_\infty = D$ and so the largest dimensional droplet volume as $v_\infty = \pi D^3/6$. Recall that we assume the initial drop size distribution, at $z = 0$, follows a top hat profile in space, as given by (4.3.2). The function $F(v)$ in (4.3.2) is set so that

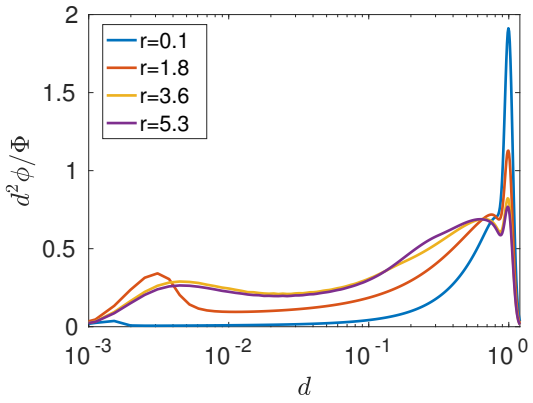
$$F(v) \propto \text{lognormal}(\mu_v, \sigma_v), \tag{4.4.5}$$

where μ_v and σ_v are set such that the mode diameter of the distribution is $4/5\,(6/\pi)^{1/3}$ and variance is $1/300\,(6/\pi)^{1/3}$. (The factor of $(6/\pi)^{1/3}$ here arises from the fact that the largest drops have dimensionless volume $v = 1$ and so their diameter is $d = (6/\pi)^{1/3}$.) We normalise $F(v)$ so that $\int_0^1 F(v)\,\mathrm{d}v = 1$ as in (4.3.1)–(4.3.2).

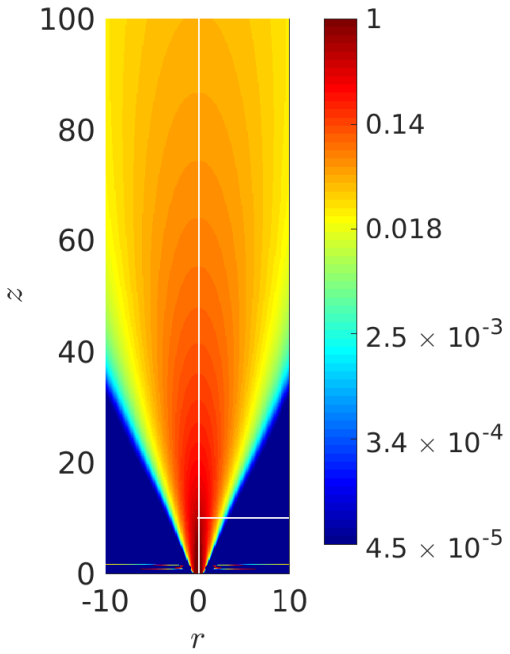
We show the droplet size distribution for fixed $r = 0.1$ and different heights along the jet, and fixed $z = 10$ and different widths across the jet in Figures 4.1(a)–(b). Here we plot $d^2\phi/\Phi$ versus the dimensionless drop diameter. We normalise using the total oil fraction Φ to eliminate the effect of the dilution of oil. In addition, as in



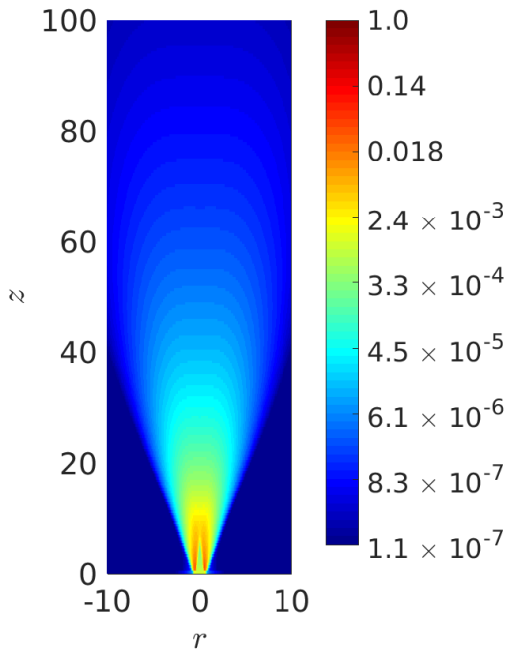
(a) Fixed $r = 0.1$



(b) Fixed $z = 10$



(c) Total volume fraction, Φ



(d) Energy dissipation, ϵ

Figure 4.1: Drop size distribution from two-dimensional models, calculated fully numerically. (a) The drop size distribution with varying heights at fixed $r = 0.1$; (b) the drop size distribution with varying widths at fixed $z = 10$; (c) total oil fraction Φ with $r = 0.1$ and $z = 10$ indicated in white; (d) a reminder of the spatial variation of the energy dissipation.

Section 3.3, to better illustrate the volume occupied by small and large droplets, we plot $d^2\phi$; this is because the volume fraction is given by $\phi \, \mathrm{d}v = \pi/2 d^2 \phi \, \mathrm{d}d$.

We see from Figure 4.1(a) that, with increasing height, the drops break up and smaller droplets are produced. Near the nozzle, the released oil drops are large. At intermediate heights, there is bimodal distribution, with a peak in droplets at the initial larger drop diameter and at a smaller one. As we move higher up the jet, the mode drop size starts to increase. This is perhaps counter intuitive. We can explain this by noting that (due to the Heaviside function in the breakup rate (4.4.2)) higher up the jet, there is only enough energy dissipation for the larger drops (which have lower surface stresses) to break up. The daughter drop distribution (3.2.32) imposes that when drops of volume $\tilde{v}$ break, a significant proportion of the volume of the droplets produced is made up of drops of size $\tilde{v}/2$. Hence the break up of only the larger droplets produces more 'medium' sized drops and so the mode drop size increases. With increasing height, there is a larger range of small droplets (with size less than some critical drop diameter) whose drop size distribution does not change compared to the previous height. This is because there is no longer enough energy dissipation for these smaller droplets to break up, again due to the Heaviside function in (4.4.2). By around 100 nozzle diameters up the jet, the energy dissipation is small enough that droplet breakup slows and starts to end. The drop size distribution stops evolving and so the normalised drop size distribution reaches a fully developed state in height. Note that, above this height, the oil will still be diluted as in Section 4.3; we can see this effect in the spatial variation of the total oil fraction, Φ, in Figure 4.1(c).

We also examine the variation in droplet breakup with increasing width at fixed $z = 10$ in Figure 4.1(b). With increasing width, as the drops are advected outward from the jet, we see much the same qualitative behaviour as with increasing height; the large drops break up and the volume of small droplets increases. Further away from the nozzle, for $r \geq 3$, the energy dissipation, as seen in Figure 4.1(d) is small. There is a small amount of breakup of the very largest drops here which produces some large drops, with $d \approx 3 \times 10^{-1}$. Nonetheless, since both the dissipation, as well as the volume of oil, is small here, as seen in Figures 4.1(c)–(d), there is little variation in the drop size distribution.

We have noted, from Figure 4.1(a), that the drop size distribution, at a fixed width in the jet, reaches a fully developed state in height. At lower heights, as seen in Figure 4.1(b), the drop size distribution varies significantly with width. So an important question to ask is whether this fully developed state is the same across

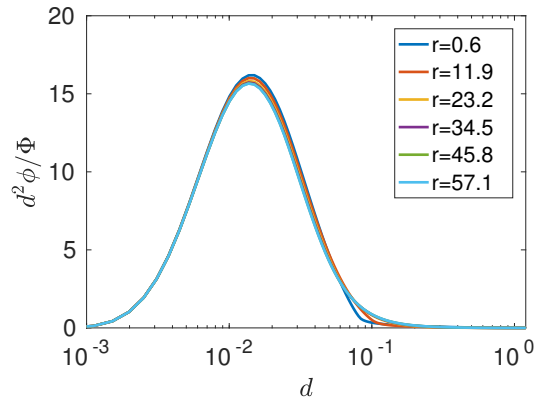


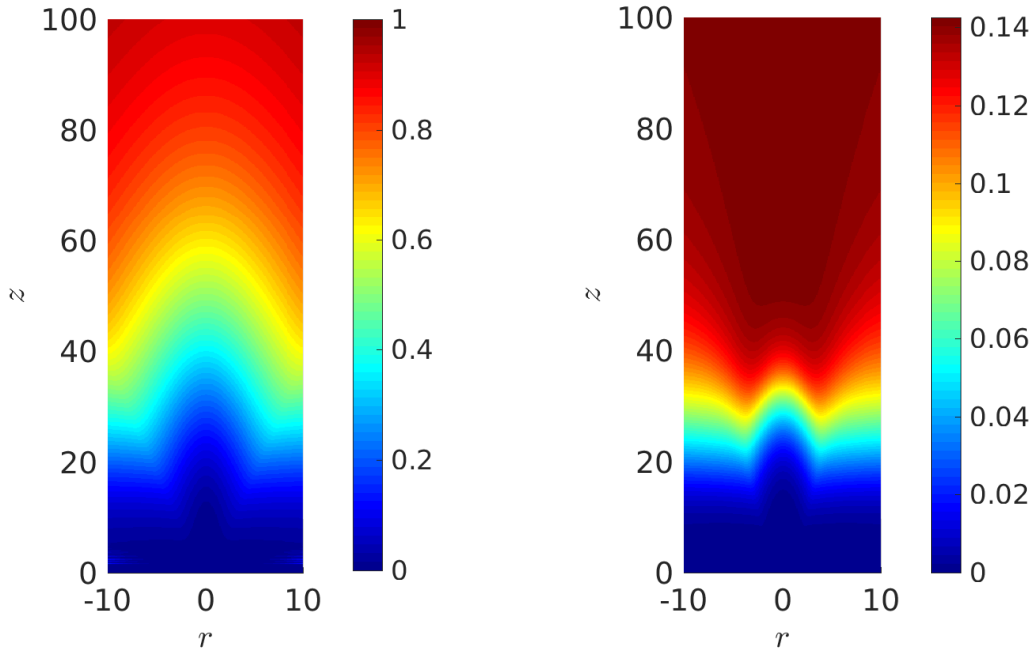
Figure 4.2: Full developed droplet size distributions from two-dimensional fully numerical model. The distribution is plotted at fixed height $z = 115$ for different widths across the jet.

the jet. From Figure 4.2 we see that for sufficiently large heights, the drop size distribution is not only independent of height but also uniform across the jet. This is a key result since, ultimately, the fully developed distribution will determine the fate of the oil as it is eaten by microbes and rises to the sea surface. Thus fully developed distributions like that illustrated in Figure 4.2 are of great interest to oil companies. We will explore the variation of the fully developed distribution with different non-dimensional parameters in Section 4.4.4.

At this point, it is useful to note that, in different regions, different terms in (4.2.6) are larger and dominate the behaviour of the drop size distribution. At smaller r, nearer the centre of the jet, radial advection and diffusion are smaller and the dominant terms are advection in the z direction and droplet breakup. This means that, in Section 4.5, we can width-average and neglect the radial terms without losing a great deal of accuracy. At large heights, droplet breakup ends so (at smaller r) all the terms, except advection in the vertical direction, can be neglected; (4.2.6) reduces to $\partial\phi/\partial z \sim 0$ so the distribution becomes independent of height. At large r, the vertical velocity is negligible and the energy dissipation driving droplet breakup is small, so the dominant terms in (4.2.6) are radial advection and turbulent diffusion. Hence the distribution gets diffused out and, at large heights, the fully developed distribution is both independent of z and r.

4.4.2 Efficiency of droplet breakup

We are interested in producing the greatest possible volume of small drops (as discussed in Section 1.1). It is, thus, useful to consider the total volume fraction of oil



(a) (b)

Figure 4.3: The total volume fraction of drops with diameter less than (a) 0.1; (b) 0.01 of the initial drop size.

which consists of drops smaller than some critical diameter. In Figures 4.3(a)–(b) we consider the volume fraction of drops with diameter less than $d = 0.1$ and $d = 0.01$, respectively. At small heights there are no small droplets. Higher up the jet, more and more small drops are produced. Note that at intermediate heights (see Figure 4.3(a)) the volume of small drops increases with width. This is due to the fact that the droplets further out in the jet have travelled further and thus have been breaking up for longer than those at comparable height in the centre. In Figure 4.3(b) we also observe this behaviour. In addition, in Figure 4.3(b) we see that, at a fixed height, at larger widths, the volume fraction of very small drops reaches a maximum and then decreases. This is consistent with the behaviour in Figure 4.1(b). As we have previously discussed, only the very largest drops break up at large widths. This produces drops which are still fairly large because the daughter drop distribution, χ, imposes that droplet breakup produces a significant volume of droplets around half the size of their original drop size. This means that the volume fraction of the very small drops decreases. Nonetheless, we must note that there is, in fact, a practically negligible volume fraction of oil at these larger widths; thus this effect is not as significant as it may appear in Figure 4.3(b). At large heights, droplet breakup ends and the volume

fraction of the small droplets remains the same.

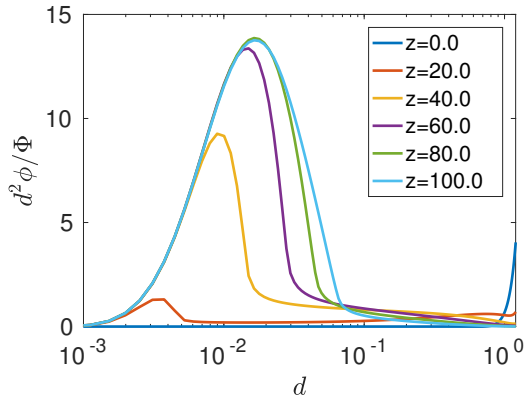
4.4.3 Sensitivity to initial conditions

These models have yielded interesting insights into the interplay between the macroscopic and microscopic scales. At this point it is useful to examine the sensitivity of these droplet size distributions to the initial distribution at $z = 0$, which is controlled by the function $F(v)$ in (4.3.2). We examine and compare results for the drop size distribution given various different choices of $F(v)$. We compare using the initial drop size distribution given by (4.3.2) and (4.4.5), with $d_\infty = D/2$ as opposed to $d_\infty = D$. (Recall d_∞ is the dimensional diameter of the largest drop.) In addition, we choose $F(v)$ in (4.3.2) so that, initially, most of the drops are of the largest size (with volume $v = 1$) and there are very few droplets smaller than this. We set

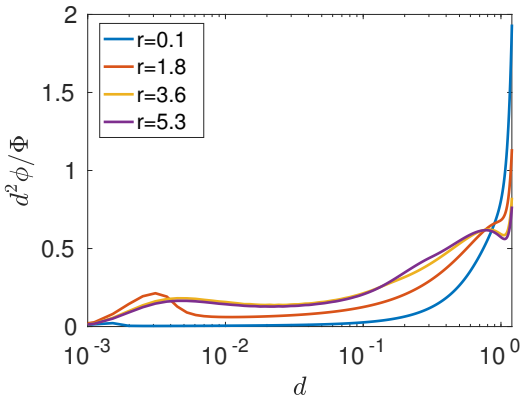
$$F(v) \propto \begin{cases} (v - v_m)^2, & v_m < v < 1, \\ 0, & 0 < v < v_m, \end{cases} \tag{4.4.6}$$

where $v_m = (8/15)^3$. And we use this initial distribution with $d_\infty = \{D/2, D\}$. For both choices of $F(v)$, we again normalise $F(v)$ so that $\int_0^1 F(v)\,\mathrm{d}v = 1$.

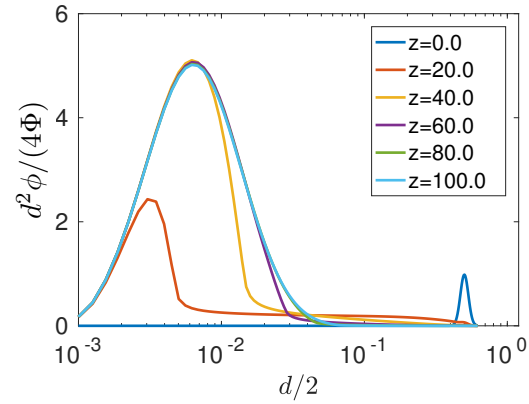
The resulting droplet size distribution using each of these initial conditions is plotted in Figure 4.4. We consider the distribution with varying height at $r = 0.1$ in Figures 4.4(a),(c),(e), and with varying width at $z = 10$ in Figures 4.4(b),(d),(f). We compare Figures 4.4(a)–(b) (which use the initial distribution (4.4.6) whose maximum is at the largest drop size) to Figures 4.1(a)–(b) (which use a lognormal initial distribution (4.4.5)). It seems that the differently shaped initial distributions does not make a great deal of difference in the final droplet size distribution. However, from Figures 4.4(c)–(e) (where $d_\infty = D/2$) having an initial distribution consisting of smaller drops does somewhat affect the droplet dynamics. Comparing for example Figures 4.4(a)–(b) (where $d_\infty = D$) with Figures 4.4(e)–(f) (where $d_\infty = D/2$), we see that up until around $z = 40$ the distribution of all but the very largest drops is fairly similar; the drop size distribution is determined more by the breakup rate and how it depends on droplet size, than the largest drop size. However, beyond this height, the two distributions begin to differ, with the fully developed state in Figure 4.4(e) (where $d_\infty = D/2$) reached at a much lower height than that in Figure 4.4(a) (where $d_\infty = D$). This can be explained by the Heaviside term in our breakup rate (4.4.2), which stops the breakup of all but the largest drops when the energy dissipation is low, namely at large heights. This means that in the case when these largest drops



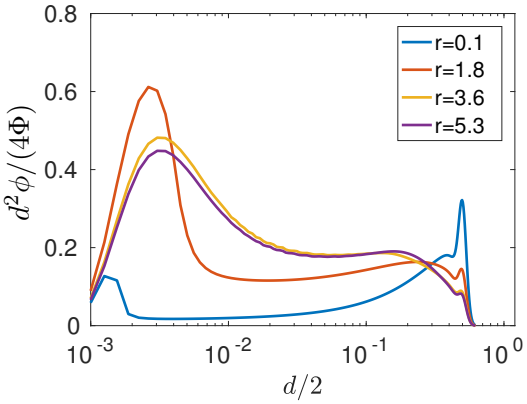
(a) $F(v)$ given by (4.4.6), with $d_\infty = D$



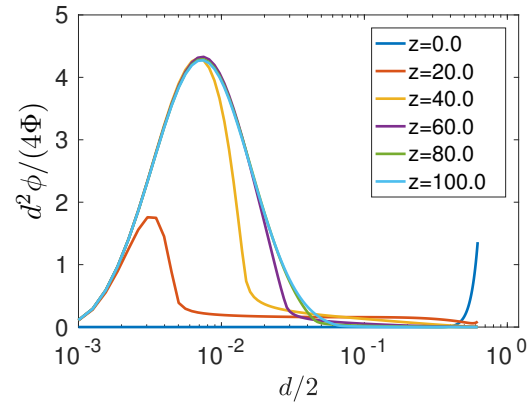
(b) $F(v)$ given by (4.4.6), with $d_\infty = D$



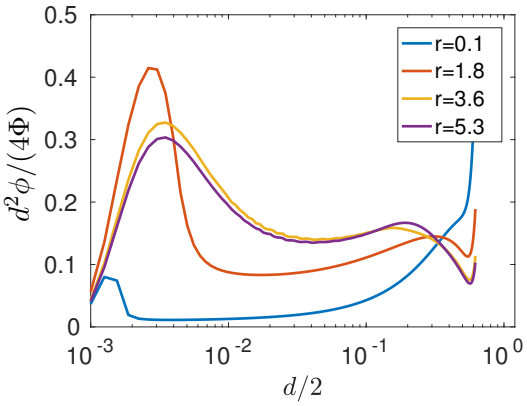
(c) $F(v)$ given by (4.4.5), with $d_\infty = D/2$



(d) $F(v)$ given by (4.4.5), with $d_\infty = D/2$



(e) $F(v)$ given by (4.4.6), with $d_\infty = D/2$



(f) $F(v)$ given by (4.4.6), with $d_\infty = D/2$

Figure 4.4: Comparison of drop size distributions with different initial drop size distributions, computed using full numerical method. We consider different heights at fixed $r = 0.1$ in (a),(c) and (e), analogous to Figure (4.1)(a), and different widths at fixed $z = 10$ in (b), (d) and (f), analogous to (4.1)(b). (a)–(b) Initial distribution (4.4.6) with $d_\infty = D$; (c)–(d) Initial distribution (4.4.5) with $d_\infty = D/2$; (e)–(f) Initial distribution (4.4.6) with $d_\infty = D/2$. Note we non-dimensionalise diameter according to d_∞ (see (3.1.16)) so in order to compare the same physical diameter ranges when $d_\infty = D$ and $d_\infty = D/2$, in (c)–(f) the x axis is $d/2$.

are absent from the system (when $d_\infty = D/2$), all droplet breakup ends at lower heights than when $d_\infty = D$.

4.4.4 Variation of fully-developed distribution with dimensionless parameters

It is useful to not only investigate the sensitivity of the distribution to initial conditions but also to the dimensionless parameters in the model. There are two non-dimensional parameters, K_0 and C_1, both of which occur in the breakup rate (4.4.2). We investigate the dependence of the fully developed drop size distribution on their values.

In Figure 4.5(a) we set $C_1 = 3.51 \times 10^{-7}$ and vary K_0. The parameter K_0, defined by (4.4.3), is a constant of proportionality in the breakup rate. Thus increasing K_0 increases the breakup rate, and this results in more smaller droplets and fewer larger drops.

The parameter C_1, defined in (4.4.4), determines the importance of surface tension effects in preventing droplet breakup. In Figure 4.5(b) we set $K_0 = 0.289$ and vary C_1. Note that, whilst C_1 is small, it is multiplied in (4.4.2) by the dimensionless inverse of $\epsilon^{2/3}$, which is also small, so the term in which it appears is not negligible in size. Decreasing C_1 yields more small drops and fewer larger drops. This is because, for smaller values of C_1, the resistive forces due to surface tension are weaker. Thus, higher up in the jet, the energy dissipation is still sufficient to overcome the surface stresses and further droplet breakup can occur. Physically, from (4.4.4), decreasing C_1 corresponds to decreasing the undisturbed oil-water surface tension or increasing the initial flow velocity, which we would expect to result in greater droplet breakup.

4.4.5 Using similarity solution for velocity and dissipation

Calculating both the velocity and energy dissipation, as well as the droplet size distribution numerically can be computationally expensive. Therefore, in this subsection, we instead use the similarity solutions found in Section 2.4 to determine the velocity and dissipation and then solve for the drop size distribution using the numerical method in Section 4.4.1.

We recall that the similarity solutions do not hold for very small z. Let us say that the similarity solutions are valid for $z > \hat{z}$. Then, we must use the full numerics to solve for ϕ when z is small and can use the resulting solution $\phi(v, r, \hat{z})$ as the starting point when using the similarity solutions.

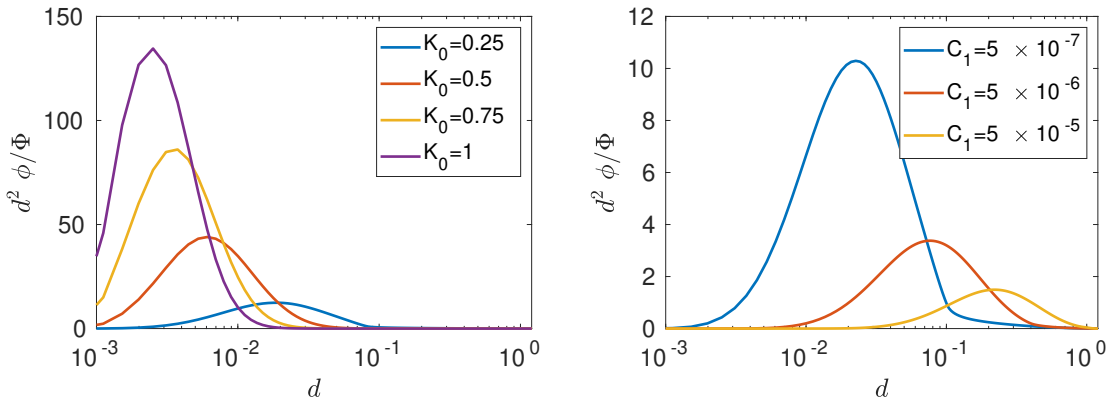


Figure 4.5: Variation of fully developed drop size distribution with non-dimensional parameters K_0 and C_1. (a) We set $C_1 = 3.51 \times 10^{-7}$ and vary K_0. (b) We take $K_0 = 0.290$ and vary C_1.

In Figure 4.6, our results at fixed $r = 0.1$ for different heights, and at fixed $z = 40$ for different widths are compared to the full numerical solution, which was illustrated in Figure 4.1 in Section 4.4.1. We take $\hat{z} = 5$ and $\hat{z} = 10$. We see that our results agree fairly well with the full numerical solution. However, especially when $\hat{z}$ is smaller, namely when $\hat{z} = 5$, there is some discrepancy between the results from this method and the full numerics. We can explain this by noting that, although the similarity solution for the vertical component of velocity agrees very well with the numerical results even when z is fairly small, the dissipation takes around $z = 15$ to match the full numerics. (This can be seen in Figure 2.6.) In fact, the similarity solution overestimates the dissipation for $z < 15$, which is why in Figure 4.6(a)–(b), using the similarity solution yields more smaller droplets and a greater amplitude distribution.

When we take $\hat{z} = 10$, as can be seen in Figures 4.6(c)–(d), the agreement is much better. However, for fixed $z = 40$ there is some disagreement with the amplitude of the distribution at larger r (see Figure 4.6(d)). The main reason for this is likely the fact that the similarity solution solves for velocity and dissipation on an infinite width (see Section 2.4), whilst the full numerics uses a finite box to determine these (see Section 2.3.1). In the far field, since the similarity solution is solved on an infinite domain, fluid is entrained from infinity. However, in the numerics for the velocity field, fluid is pulled downwards and towards the jet. Recall the effect of this was previously illustrated in the discrepancy in U with our similarity solution at larger ξ (see Figure 2.5(d)). In any case, this is probably not a region of great importance since, as illustrated in Figure 4.1, the total volume of oil drops Φ is very small here. In

fact, some of the disparity with the full numerics may be attributed to small absolute errors in the total oil fraction, which then become large relative errors.

4.4.6 Discussion

We use two-dimensional models to obtain detailed insights into the droplet size distribution throughout the jet. They provide accurate and detailed solutions to the droplet size distribution. However, since we have a three-dimensional problem (two spatial dimensions and the volume/diameter dimension), the model is computationally expensive.

We simplify this approach by using the full numerical solution for the velocity and dissipation at small heights and then, after a few jet diameters, use the similarity solutions for these. This approach agrees fairly well with the full numerical solution. However, it does not really make the computation of ϕ any easier.

To simplify even further, we can reduce the problem to one spatial dimension. This is the simplest possible approach, which still maintains the gross features of the jet behaviour and droplet dynamics.

4.5 One-dimensional width-averaged models

4.5.1 Assumptions and governing equations

We now consider the variation of drop size distribution with only one spatial dimension, height. We do so by averaging across the width of the jet, using a similar approach to that used in Section 2.5 to produce width-averaged jet models. Recall in Section 2.5 we averaged the results of our similarity solution from Section 2.4 over width to find the width-averaged vertical velocity and dissipation (2.5.12).

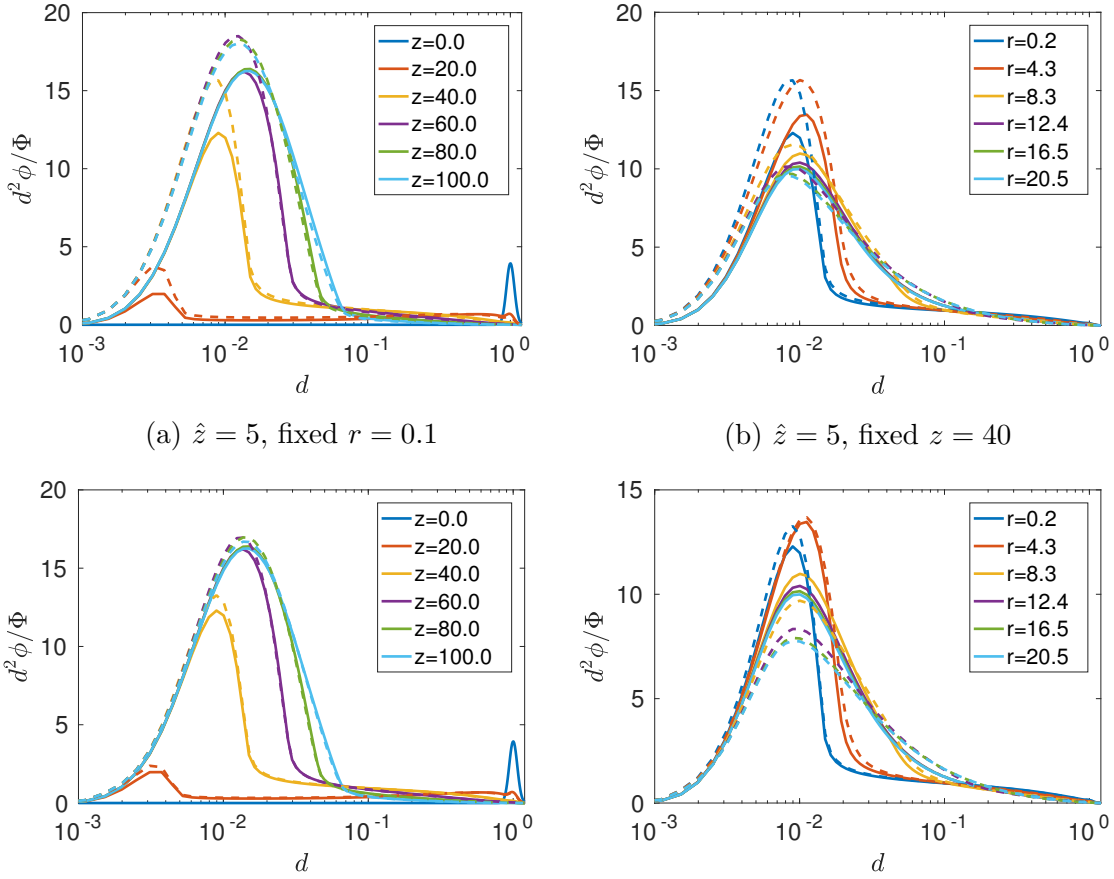
We model the drop size distribution ϕ, the breakup rate γ and the daughter droplet distribution χ with top hat profiles of the form

$$\phi = \begin{cases} \overline{\phi}(v,z), & r \leq \delta(z)/2, \\ 0, & r > \delta(z)/2, \end{cases} \tag{4.5.1}$$

$$\gamma = \begin{cases} \overline{\gamma}(v,z), & r \leq \delta(z)/2, \\ 0, & r > \delta(z)/2, \end{cases} \tag{4.5.2}$$

and

$$\chi = \begin{cases} \overline{\chi}(v,\tilde{v}), & r \leq \delta(z)/2, \\ 0, & r > \delta(z)/2, \end{cases} \tag{4.5.3}$$



(a) $\hat{z} = 5$, fixed $r = 0.1$

(b) $\hat{z} = 5$, fixed $z = 40$

(c) $\hat{z} = 10$, fixed $r = 0.1$

(d) $\hat{z} = 10$, fixed $z = 40$

Figure 4.6: Comparison between using full numerics for velocity and dissipation (solid) and their similarity solutions (dashed) in numerically determining droplet size distribution. We plot drop size distributions (a) for different heights at fixed $r = 0.1$, with $\hat{z} = 5$; (b) for different widths at fixed $z = 40$, with $\hat{z} = 5$; (c) for different heights at fixed $r = 0.1$, with $\hat{z} = 10$; (d) for different widths at fixed $z = 40$, with $\hat{z} = 10$.

where, for example, $\overline{\phi}$ is defined as the width-averaged drop size distribution in the jet region. Integrating (4.2.6) across the width of the jet, from $r = 0$ to $r = \delta(z)/2$, and assuming the above forms for ϕ, γ and χ yields

$$\frac{Q_0}{\delta^2}\frac{\partial}{\partial z}\left(\delta\overline{\phi}(v,z)\right) = -\overline{\gamma}(v,\epsilon)\overline{\phi}(v,z) + \int_v^1 \overline{\gamma}(\tilde{v},\epsilon)\overline{\chi}(v,\tilde{v})\overline{\phi}(\tilde{v},z)\,\mathrm{d}\tilde{v}, \tag{4.5.4}$$

where

$$Q_0^2 = \delta^2\overline{W}^2 = \frac{16\delta_0^2\omega_0^2}{\beta^2} \tag{4.5.5}$$

is proportional to the momentum flux into the jet and recall δ and $\overline{W}$ are given by (2.5.12). Here by width-averaging, we have neglected the advection and diffusion terms in the radial direction. Thus, the only spatial component in the equation is advection in the z direction, which corresponds to the left hand term in (4.5.4). The two terms on the right hand side of (4.5.4) are the width-averaged versions of the two final terms on the right hand side of (4.2.6); they correspond, respectively, to drops of volume v breaking up, and drops larger than v breaking up and producing those with volume v.

Note that the similarity solutions, on which these width-averaged models are based, are not valid at small z. Therefore, we cannot set a boundary condition at $z = 0$, analogous to (4.3.2). Instead we set ϕ at $z = \hat{z}$ and solve in the region $z > \hat{z}$. We can think of this as a matching condition to the region with small z.

If we discretise drop size linearly in volume, into N bins of equal size $\triangle v$, the equivalent of (4.5.4) is

$$Q_0\frac{d}{dz}\left(\delta\overline{\phi_i}\right) = -\overline{\gamma_i}\overline{\phi_i}\delta^2, \quad i = N, \tag{4.5.6}$$

$$Q_0\frac{d}{dz}\left(\delta\overline{\phi_i}\right) = -\overline{\gamma}_i\overline{\phi}_i\delta^2 + \sum_{j=i+1}^{N}\overline{\gamma}_j\overline{\chi}_{ij}\overline{\phi}_j\triangle v, \quad i \in [2, N-1], \tag{4.5.7}$$

$$Q_0\frac{d}{dz}\left(\delta\overline{\phi}_i\right) = \sum_{j=i+1}^{N}\overline{\gamma}_j\overline{\chi}_{ij}\overline{\phi}_j\triangle v, \quad i = 1. \tag{4.5.8}$$

4.5.2 Total Oil Fraction

Integrating (4.5.4) across v, we find that the total oil fraction, given by $\overline{\Phi} = \int_0^1 \overline{\phi}\,\mathrm{d}v$ satisfies

$$\frac{d}{dz}\left(\delta\overline{\Phi}\right) = 0 \tag{4.5.9}$$

and so

$$\overline{\Phi} \propto \frac{1}{\delta_0 + \alpha z}. \tag{4.5.10}$$

We fix the constant of proportionality in (4.5.10) in the same way as in Section 2.5, by width averaging the similarity solution for Φ, given by (4.3.3). Hence

$$\overline{\Phi} = T_\Phi \frac{1}{\delta}, \tag{4.5.11}$$

where $T_\Phi = 4\Phi_0\delta_0/\beta$. As in Section 4.3, we see that the total oil droplet volume fraction decreases with height due to dilution.

4.5.3 Two bin volume fraction model

Let us first consider the simplest non-trivial case, where there are only two sizes of drops: 'large' drops, whose volume fraction has distribution $\overline{\phi}_l(z)$ and 'small' drops, with distribution $\overline{\phi}_s(z)$. This corresponds to the discrete volume model (4.5.6)–(4.5.8), with the number of bins $N = 2$. Thus, conservation of 'large' and 'small' droplets gives, respectively,

$$\frac{d}{dz}\left(\delta\overline{\phi}_l\right) = -K\overline{\phi}_l\delta^2 \tag{4.5.12}$$

and

$$\frac{d}{dz}\left(\delta\overline{\phi}_s\right) = K\overline{\phi}_l\delta^2, \tag{4.5.13}$$

where $K = \gamma_l/Q_0$. Near the base of the nozzle (at a large enough height that the similarity solution from Section 2.4 is valid) we impose our boundary conditions. We assume that water with a low oil volume fraction is being ejected, with $\overline{\phi}_s + \overline{\phi}_l = A$ at $z = \hat{z}$ or $\delta = \hat{\delta}$, where A is a constant. We suppose that there are only large droplets being released into the jet, namely $\overline{\phi}_s(\hat{z}) = 0$ and $\overline{\phi}_l(\hat{z}) = A$.

For simplicity, we initially assume the breakup rate γ_l does not depend on the energy dissipation ϵ and thus is constant. The solution is then

$$\overline{\phi}_l = \frac{A\hat{\delta}}{\delta_0 + \alpha z} \exp\left(-\frac{K}{2}\left(2\delta_0(z - \hat{z}) + \alpha(z^2 - \hat{z}^2)\right)\right), \tag{4.5.14}$$

$$\overline{\phi}_s = \frac{A\hat{\delta}}{\delta_0 + \alpha z}\left[1 - \exp\left(-\frac{K}{2}\left(2\delta_0(z - \hat{z}) + \alpha(z^2 - \hat{z}^2)\right)\right)\right], \tag{4.5.15}$$

The variation of $\overline{\phi}_s$ and $\overline{\phi}_l$ along the height of the plume (assuming $K = 2$, $A = 0.5$ and $\hat{z} = 1$) is plotted in Figure 4.7. We see that this very simple model

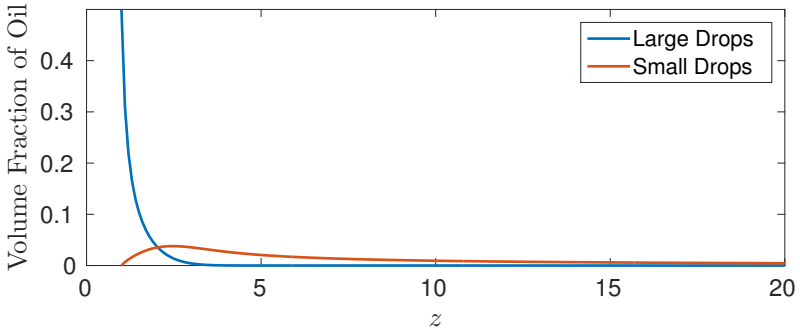


Figure 4.7: Volume fraction of 'small' droplets $\overline{\phi}_s$ (red) and 'large' droplets $\overline{\phi}_l$ (blue) along the height of the jet with $K = 2$, $A = 0.5$ and $\hat{z} = 1$.

captures some of the key features we observed from the two-dimensional models in Section 4.4.1. The volume fraction of large droplets rapidly decreases whilst that of small droplets increases due to droplet breakup. As we more further up the jet, the volume fraction of small drops reaches a maximum and then decreases, due to increased dilution by entrained water.

Looking at models where droplets are categorised into two size classes captures much of the problem's important physics. However, splitting droplets into those which break up and those which do not is perhaps not wholly physically sensible. In reality, the range of droplet sizes which can break varies with jet location, for instance higher up the jet, there is not enough energy for the smaller drops (which have greater resistive surface stresses) to break up. Therefore, the range of drops covered by each of the two bins would, in fact, depend on the position in the jet.

4.5.4 Full distribution model

To obtain drop size distributions along the jet's height, we now consider multiple droplet sizes. Moreover, to obtain more representative models, unlike the simple two bin model in Subsection 4.5.3, the breakup rate will now vary with drop size and dissipation.

We consider the width-averaged droplet size distribution, given by (4.5.4). We use the breakup rates $\gamma(v, \epsilon)$ and $\chi(v, \tilde{v})$ given by (4.4.2)–(4.4.4) and (3.2.32), respectively. We set the parameters $K_{00} = 0.25$ and $C = 0.725$ in (4.4.2)–(4.4.4).

Note the model (4.5.4) depends on the width-averaged breakup rate $\overline{\gamma}$. By definition, in order that $\int_0^\infty r\gamma \, \mathrm{d}r$ is conserved,

$$\overline{\gamma} = \frac{1}{\delta^2/8} \int_0^\infty r\gamma(v, \epsilon(r, z)) \, \mathrm{d}r. \tag{4.5.16}$$

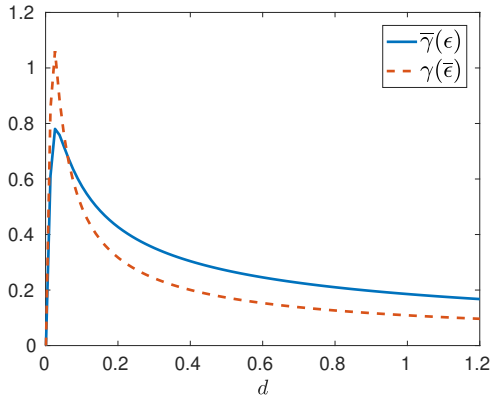


Figure 4.8: Comparison between $\overline{\gamma}(\epsilon)$ and our approximation $\gamma(\overline{\epsilon})$ for parameter values $K_{00} = 0.25$, $C = 0.725$ and $d_\infty = 500\mu$m for fixed $z = 10$.

However, for simplicity, we assume the closure relation

$$\overline{\gamma}(v, \epsilon) \approx \gamma(v, \overline{\epsilon}), \tag{4.5.17}$$

where recall $\overline{\epsilon}$ is given by (2.5.12). Thus we take

$$\overline{\gamma} = K_0 v^{-2/9} \overline{\epsilon}^{1/3} \left(1 - C_1 \sigma v^{-5/9} \overline{\epsilon}^{-2/3}\right)^{1/2} \mathcal{H}\left(1 - C_1 \sigma v^{-5/9} \overline{\epsilon}^{-2/3}\right). \tag{4.5.18}$$

The closure assumption (4.5.17) is evaluated in Figure 4.8. We use the value of ϵ from our similarity solutions in Chapter 2 to determine $\overline{\gamma}(v, \epsilon)$ and compare this to the approximation (4.5.18). We see that $\gamma(\overline{\epsilon})$ is a reasonable approximation of $\overline{\gamma}(\epsilon)$. However, it underestimates the breakup rate of larger drops, and overestimates that of smaller drops. In particular, it overestimates the breakup rate at the local maxima. The disparity at the local maximum occurs in the region of greatest droplet breakup and thus appears to be a significant limitation. Furthermore, we have found that this error increases with height. Nonetheless, this does not actually have such a great effect on the resulting drop size distribution. Because of the Heaviside term, after a certain height, only the larger drops can break up and thus it is the breakup rate of the larger drops which has the greatest effect on the drop size distribution. Since the breakup rate of the larger drops is underestimated by (4.5.17), we might expect that the width-averaged model will underestimate droplet breakup.

We solve the width-averaged problem, (4.5.4), numerically. Note that if we take $\hat{\phi} = \delta\overline{\phi}$ and $\hat{\gamma} = \delta\gamma$, (4.5.4) is of the same form as (3.1.17), with z as the time-like variable. This means that (4.5.4) can be numerically solved as in Section 3.3.1. The only added complication here is that the energy dissipation, and so the breakup rate, varies with height, z. As in Section 3.3.1, we use the method of lines to solve for ϕ; we

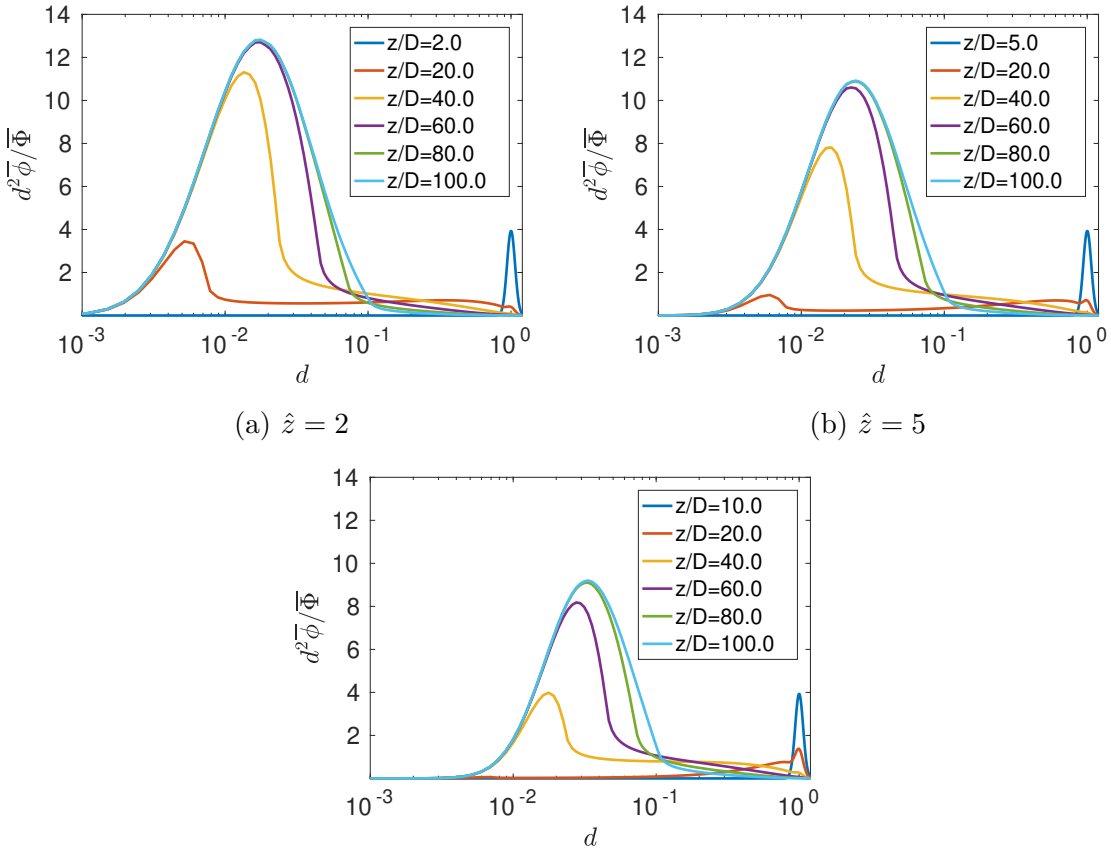
discretise drop size using the square root of the diameter, $d^{1/2}$, (which enables us to capture the behaviour of the smallest drops) and then solve the resulting ODEs using ODE15s in MATLAB. As in Section 3.3.3, we find that, generally, the numerical scheme converges for $N = 200 - 300$ drop size bins. The corresponding run-time ranges between 5 seconds and 30 seconds on a standard desktop computer. Note that, in Chapter 6, where we compute the drop size distribution with additional equations for the surfactant behaviour, the run-time can be slightly longer, up to 1-2 minutes on a standard desktop computer.

Since our similarity solution is not valid for small z, we use (4.4.5) as an initial condition at $z = \hat{z}$ and we take $d_\infty = D$. Our results are shown in Figure 4.9 for different values of $\hat{z}$. As before, we normalise to remove the effects of dilution and to obtain a better illustration of the volume occupied by the different sized drops, plotting $d^2\overline{\phi}/\overline{\Phi}$. This model captures much of the same behaviour as the variation of the two-dimensional models with height in Figure 4.1(a). This is not unexpected since, as discussed at the end of Section 4.4.1, by looking at the size of the terms in the two-dimensional equation for ϕ, in the jet region, where breakup is significant, advection and diffusion in the radial direction are of lower order and can be neglected. We again see that the drops break up and many small droplets are produced. With increasing height, the mode drop size increases, as noted in Section 4.4.1. At larger heights, the distribution reaches a steady state in height as the droplets no longer have enough energy to break up.

For comparison, in Figure 4.9 we have plotted the drop size distributions when choosing $\hat{z} = \{2, 5, 10\}$. For different values of $\hat{z}$, the droplet behaviour agrees fairly well and the mode droplet sizes are very similar in each of these cases. The main difference is that, since for $\hat{z} = 2$ the drops have experienced greater dissipation, the amplitude of the distribution is greater here; there are more small droplets. Nonetheless, the similarity between the three cases is reassuring. It suggests that, whilst the behaviour at small z is important, we need not be overly concerned that the width-averaged similarity solutions cannot capture the behaviour at small z.

4.5.5 Compare one and two dimensional models

Our one-dimensional models encouragingly demonstrate much the same behaviour as the two-dimensional models at fixed widths. In this section, we compare these models to evaluate the accuracy of the more approximate width-averaged models.



(a) $\hat{z} = 2$

(b) $\hat{z} = 5$

(c) $\hat{z} = 10$

Figure 4.9: Drop size distribution at different heights using one-dimensional models, with $K_{00} = 0.25, C = 0.725, d_\infty = D$ and (a) $\hat{z} = 2$; (b) $\hat{z} = 5$; (c) $\hat{z} = 10$.

We use the results from the full two-dimensional numerical models (using CFD numerics for the velocity fields and energy) as seen in Figure 4.1. These are width-averaged by taking

$$\overline{\phi}(v,z) = \frac{\int_0^\infty r\phi(v,r,z)\,\mathrm{d}r}{\delta^2/8}. \tag{4.5.19}$$

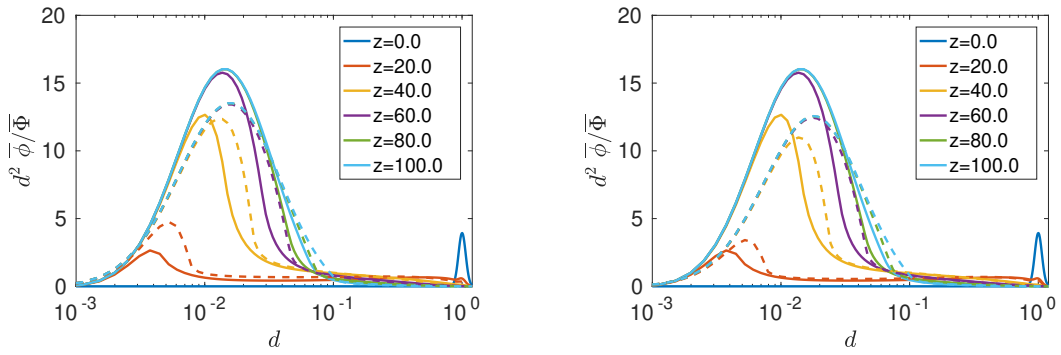
In evaluating the one-dimensional models, we determine the starting drop size distribution, at $z = \hat{z}$, from the results of the two-dimensional model. As in Section 4.4.5, we use the full two-dimensional numerical models to determine the drop size distribution up until some $z = \hat{z}$, average this over width, as in (4.5.19), and then use our one-dimensional models for $z > \hat{z}$.

We use the breakup rates $\gamma(v,\epsilon)$ and $\chi(v,\tilde{v})$ given by (4.4.2)–(4.4.4) and (3.2.32) respectively, setting the parameters $K_{00} = 0.25$ and $C = 0.725$ in (4.4.2)–(4.4.4). For the width-averaged model, as in Section 4.5.4, we use the approximate breakup rate (4.5.18). We consider the cases where both $\hat{z} = 2$ and $\hat{z} = 5$ since these values are commonly used in the remainder of this thesis. Our results are shown in Figure 4.10.

We see that there is generally reasonable agreement between the one-dimensional and two-dimensional models. In particular, the fully developed distribution at $z = 100$ (which as discussed with Figure 4.2, is the desired output for an oil company) is similar when using the one-dimensional model. The one-dimensional models use the similarity solutions and then width-average them so there are two sources of error here. We might expect that taking $\hat{z}$ to be larger, e.g. $\hat{z} = 5$ would provide better results than when taking $\hat{z} = 2$ (as in Section 4.4.5) because this will mean the similarity solution has had more time to develop and agrees very well with the full numerical results. However, this is not the case because the errors due to width averaging are greater and propagate with height. The width-averaged breakup rate (4.5.17) slightly underestimates the breakup of the larger drops, as seen in Figure 4.8. Therefore, the one-dimensional model predicts larger drop sizes.

4.5.6 Fitting to experimental results

There are a number of unknown parameters in our models. The main one is the breakup rate strength, K_{00}, which appears in the parameter K_0 (see (4.4.3)) in the breakup rate. To determine it, we now seek to fit the simple one-dimensional models to small-scale experiments by SINTEF (Brandvik et al., 2014, 2013; Johansen et al., 2013).



(a) $\hat{z} = 2$ (b) $\hat{z} = 5$

Figure 4.10: Comparisons between drop size distributions for two-dimensional models and one-dimensional width-averaged models. We take (a) $\hat{z} = 2$; (b) $\hat{z} = 5$.

The experimentalists release a pure oil jet at high velocity from a nozzle of the order of 1 mm in diameter into a cylindrical tank of water with a depth of 6 m and width of 3 m. Approximately 3 m from the base of the jet, at a location where it is assumed the drop size distribution has reached a full developed state in height, oil droplet measurements are made, approximately directly above the nozzle. They do not take measurements at different widths across the jet as they have found, anecdotally, that the fully developed distributions are fairly uniform with width. Note that we have also made this observation from our numerical two-dimensional models in Section 4.4.1. Measurements are made of the volume fraction of the observed drops which lie in each of 29 logarithmically spaced diameter ranges between 4 and 500 microns. Droplets outside this range cannot be measured.

We compare the experimental results to the fully developed state found by our width-averaged model in Section 4.5.4. We take the breakup rate to be (4.5.18), with $C = 0.725$ in the parameter C_1, given by (4.4.4). The initial distribution at $\hat{z} = 5$, is set by (4.4.6) with $d_\infty = D$.

We solve the model as before, discretising linearly in diameter, d, with 300 drop size bins. The main issue in replicating the experiments is that the experimentalists are not able to measure the very largest drop sizes. Therefore, we take the computed ϕ from our model and truncate it so it only varies over the experimental drop sizes. For each bin i, we then calculate $\int_{v_i}^{v_{i+1}} \phi \, \mathrm{d}v$, namely the volume fraction of oil between v_i and v_{i+1}, from the model. We normalise the resulting distribution by its sum, as in Brandvik et al. (2013).

To avoid any problems which may arise due to the experiments not including drop sizes greater than 500 microns, we choose to fit with an experiment where the

	D (m)	W_0 (m/s)	σ_0 (kg s^{-1})
Exp 1 (fitted)	1.5×10^{-3}	14.1	0.0132
Exp 2	1.5×10^{-3}	26.4	0.015
Exp 3	3×10^{-3}	18.86	0.015
Exp 4	1.5×10^{-3}	11.3	0.0151

Table 4.1: Table of parameters for different experiments compared to model.

majority of droplets are smaller than this. The inlet diameter, velocity and the surface tension for this experiment (denoted experiment 1) are given in Table 4.1. We fit the dimensionless parameter K_{00} to minimise the L2 norm between the experimental distribution and that from the model.

From fitting with Experiment 1 in Table 4.1, we set the parameter $K_{00} = 0.17$. Our results are shown in Figure 4.11(a). We see that there is an encouragingly good fit between the model and experimental results, given the fact that we use only one fitting parameter and an approximate width-averaged model.

We can now compare our model to various other experiments, with different initial jet widths and velocities, which are given in Table 4.1. These comparisons are illustrated in Figure 4.11(b)–(d). In Figure 4.11(b) we see that, whilst the agreement is not as good as in the fitted case, it still matches the data reasonably well. The experiments in Figures 4.11(c)–(d) do not show as good agreement. However, it must be noted that part of the distribution in Figures 4.11(c)–(d) is outside the range of experimentally measurable drop sizes and this may account for some of the disparity between the model and experiments. In particular, there is a second peak at the largest drop size in the experimental distribution in Figure 4.11(d). This occurs because the experimentalists can only measure drops with diameter less than 500 microns and so the 500 micron bin erroneously measures some of the larger drops. Note that the error bars in all the experiments are quite large as these experiments are difficult to replicate precisely, and wiggles in the experimental distributions, especially in Figure 4.11(d) for smaller drop sizes, can be attributed to measurement error.

The amplitude of the distribution predicted by the model is consistently lower than that in the experimental results. This is true even in experiments 1 and 2, where the majority of drop sizes are within the measurable range. This suggests that there may be an aspect of our model which is not allowing sufficient breakup of larger drops and production of medium-sized drops. This issue is briefly considered in Section 4.5.7 and further discussed and addressed in Section 6.6.

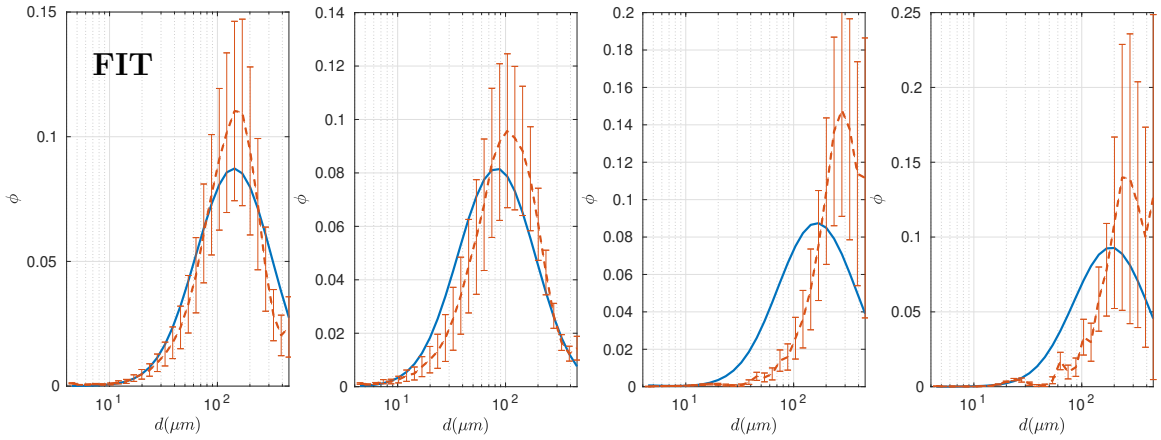


Figure 4.11: Comparison between one-dimensional model (blue) and experimental results (red) for (a) experiment 1 (the distribution we use to fit the parameter K_0); (b) experiment 2; (c) experiment 3; (d) experiment 4. Experimental error bars are shown in red.

4.5.7 Discussion

To simplify our problem, we have used width-averaged models, which vary in only one spatial dimension. Compared to the two-dimensional methods, these models are simpler to understand and have significantly lower computational time. In addition, we see that these simplified width-averaged models capture much of the essential dynamics and exhibit much of the same behaviour as the more complicated two-dimensional models.

We choose to fit this simpler model with the results of small-scale experiments. The measured data does not contain information about variation across the width of the jet. Thus, one could argue that it does not make sense to use the spatially two-dimensional models, which are much more detailed than the data that is available to calibrate and validate it.

We have found good agreement between our model and the experimental results using only one fitting parameter. However, whilst the chosen value of K_{00} seems appropriate to match with this specific set of experiments, we can question whether it is appropriate for more realistic oil spill scenarios. The experiments are relatively small-scale with Reynolds number of the order of $10^3 - 10^4$. This is large enough to be in the turbulent regime but in a real oil spill the Reynolds number would be more like $10^5 - 10^6$. We would like to verify whether this fitted parameter scales up well. There is a data set from a much larger scale experiment, in which oil was released off

the coast of Norway in a much more realistic set-up (Johansen et al., 2001). However, the data from this, the authors warn, is inaccurate.

Note that we have chosen to only fit the parameter K_{00} in the breakup rate given by (4.5.18) and (4.4.3)–(4.4.4). However, there is another parameter here, C, which appears in the dimensionless parameter C_1 (see (4.4.4)). Dimensionally, $C^{5/3}$ corresponds to a Weber number. It controls the drop size below which no droplets break up when surface stresses are too large to be overcome by the deforming turbulent flow. In Chapter 6 we find that the value of C is, in fact, important in obtaining the correct dependence on surface tension and we fit it there, setting $C = 11$. We will find that this also solves the problem we observed where the model under-predicts the amplitude of the distribution. This is because increasing C reduces the rate at which droplets break up and increases the drop size below which no breakup occurs. Therefore it makes it harder for the medium size drops to break up, more of these remain, and hence fewer of the very small drops are produced. This means that the distribution is narrower and has a greater amplitude near the mode drop size.

A significant physical unknown in our model is the initial drop size distribution. This is too difficult to measure experimentally. We generally assume that the initial largest drop size, d_∞ is equal to the nozzle diameter D. This would be a pseudo-natural choice for a pure oil jet. However, it is somewhat inconsistent with our assumption of a water jet with a low oil fraction. Its value does not significantly impact the behaviour of the dimensionless model. However, as we will see in Chapter 6, taking $d_\infty = D$, leads to some possibly questionable dimensional values, such as the fraction of droplets with diameter less than 50 microns. It would be advantageous to fit this to experiments. However, there is not a great deal of empirical data available and it predominantly only measures the fully developed drop size distribution. Therefore, wary of over-fitting, we set $d_\infty = D$ throughout this thesis. In future work, if we had access to reliable experimental data on the evolution of the drop size distribution with height, we could fit d_∞. Alternatively, a multiphase approach, where we no longer make the assumption of a water jet with a low oil fraction, would eliminate this issue.

4.6 Conclusions

Using population models, we explore the evolution of the droplet size distribution in a turbulent jet. We first consider the full problem, using models involving two spatial dimensions and then simplify this approach, using width-averaged models.

We begin by modelling the total volume fraction of oil in the jet, Φ. We find that it is proportional to the jet's vertical velocity so the oil is advected, diffused and diluted in the same way as the jet flow. The dilution of oil droplets is an important effect and its spatial variation is described by Φ.

Full numerical simulations for the droplet size distribution are useful in capturing the detail of the droplet dynamics. We see that the droplets break up and so decrease in size with increasing height. At lower heights, the distribution is bimodal, with one peak corresponding to the smaller droplets produced by breakup and the other peak corresponding to the largest drops which still remain. With increasing height, we observe that the mode drop size increases. The main reason for this lies in the Heaviside term in the droplet breakup rate; with increasing height, the size of the drops which can break up increases and so the size of the produced drops increases. Similar behaviour is seen in the evolution of the drop size distribution with increasing width.

At large heights, the energy dissipation is too low for droplet breakup to occur and the drop size distribution reaches a fully developed state. Here, the drop size distribution is not only uniform with height but also with width. This fully-developed distribution is very important for oil production companies, comparing it for different parameters and (as we will do in Chapter 6) for different surfactant applications can be insightful. The final distribution could also be used as the initial condition for the oil fate models, such as the OSCAR model discussed in Section 1.2.2, to give a better prediction of the volume of oil which rises to the sea surface.

We investigate the effect of the initial distribution on the final drop size distribution and find that, whilst its shape does not greatly affect the fully developed distribution, changing the size of the largest drop is important. In particular, since our breakup rate includes a Heaviside term which prevents smaller droplets from breaking up, decreasing the size of the initial largest drop means that the breakup ends at much smaller heights in the jet.

Full numerical simulations offer a great deal of insight into the features of the drop size distribution. However, due to their computational time, they are not so useful at exploring the effect of different parameter values and the variation of surface tension on the drop size distribution. Therefore, to simplify the problem, we use the similarity solutions for the velocity components and energy dissipation from Section 2.4 and then solve the numerical problem for the droplet size distribution. This agrees fairly well with the full numerical approach but it is still fairly computationally expensive to determine ϕ.

We thus average over the width of the jet to produce simpler models for the droplet size distribution. These have the benefit of being computationally cheap but also are simpler to understand than the two-dimensional models; therefore, they will be helpful when incorporating the extra complications of surfactant addition into the model in Chapter 6. An important consideration in the width-averaged models is how to choose a closure relation for the breakup rate, γ, which is a function of spatially varying energy dissipation, ϵ. We find that inaccuracies in our chosen breakup rate at the smallest drop sizes are allowable because the smallest drops only break up at lower heights (when the energy dissipation is large) and, when they do break up, they do not produce a large volume of droplets. Our width-averaged models agree fairly well with and exhibit much of the same behaviour as the two-dimensional models. In particular, the fully developed distribution agrees relatively well with results from the full two-dimensional models. However, we cannot, of course, capture the variation of droplet size distribution with jet width.

We fit the simple width-averaged models to experimental results and find that, with only one fitting parameter, the agreement is fairly good. However, the model consistently underestimates the amplitude of the distribution. In Chapter 6, we will find that this is because our choice of the parameter C is too small and must also be fitted with the experiments.

In the rest of this thesis, we use the models we have constructed in this chapter to predict the droplet size distribution in a turbulent jet. In Chapter 5, we extend the approach of Section 4.4.5, using the jet similarity variable ξ to find similarity solutions for ϕ in two spatial dimensions. We compare with the results in Sections 4.4.1–4.4.5. In Chapter 6 we mainly use the width-averaged models, extending these to incorporate the effects of varying surfactant tension on the drop size distribution.

Chapter 5

Droplet size distribution - similarity solution

In the previous chapter, we solved droplet population models to determine the drop size distribution at different locations in a turbulent jet. The simplest approach was to use width averaged models to find the variation of droplet size distribution with jet height. However, the behaviour of the jet varies significantly across its width, and this has a corresponding effect on the droplet size distributions, so there is much to be learnt from considering models in two spatial dimensions. In the previous chapter we determined the drop size distribution in two spatial dimensions using the full numerical velocity and turbulent energy in the jet (calculated using CFD) and subsequently using the self-similar velocity and energy. In the second case, since the velocity and energy are scale invariant, it is only ϕ which requires any considerable numerical computation.

We now look to simplify this process further. We assume, throughout this chapter, that the velocity and energy are given by the self-similar solutions in Chapter 2. Using these, we look for a self-similar droplet size distribution ϕ which satisfies the droplet population model (4.2.6)–(4.2.9). Second kind self-similar solutions emerge here, in which the exponent is also an unknown and must be determined as part of the solution (Barenblatt, 1996). It transpires that the exponents are eigenvalues of a Sturm-Liouville eigenproblem.

In this chapter we split our discussion into two cases: the case when the breakup rate is a monotonic function of droplet size and the case when it is not.

We are able to find formulae for the similarity solution under the restriction that the breakup rate is monotonic in drop size. We first find approximate similarity solutions for ϕ. The full solution is made up of a superposition of eigenfunctions; the eigenproblem corresponding to each of these has an infinite number of eigenvalues

and corresponding eigensolutions. In these approximate solutions, we assume that only the smallest eigenvalue in each eigenproblem has any relevance as it contributes the largest term for large z. We assume all other terms are negligible everywhere in the jet. This is not necessarily the case and can lead to some inconsistencies and inaccuracies in our solutions. We evaluate the validity of these solutions by comparing to numerical results.

For completeness, to understand the errors incurred by the similarity solutions, and to gain greater insights, we then fully solve the equation for ϕ, motivated by insights from the approximate similarity solution. This yields exact analytical solutions for the drop size distribution when the breakup rate is a monotonic function of drop size. We can then compare these to the approximate similarity solutions to determine their applicability.

If the breakup rate is a non-monotonic function of drop size, the form of the solution becomes more complicated. We discuss why the formulae we find for ϕ when the breakup rate is monotonic cannot be applied and then attempt to modify them accordingly.

5.1 Model setup and outlook

The drop size distribution ϕ satisfies the problem (4.2.6)–(4.2.9) in (v, r, z) coordinates. To find a similarity solution for ϕ we convert to the jet similarity variables and then determine the conditions which must be met so that the equation for ϕ is in self-similar form. We make additional simplifications to enable us to understand how to determine the similarity solution; we provide some explanation of how these simplifications will be relaxed.

5.1.1 Converting to similarity coordinates

To investigate whether ϕ has a scale-invariant form, we change variables to the self-similar coordinates (v, ξ, z), where $\xi = \sqrt{\beta} r/\delta$ is the similarity variable introduced in Section 2.4. In terms of (v, ξ, z), the problem (4.2.6)–(4.2.9) for the droplet size distribution becomes

$$\begin{aligned} L[0]\phi + \frac{\xi\delta}{\alpha}\frac{\partial\phi}{\partial z} = &- \frac{1}{\alpha\delta_0\omega_0}\xi(1+\xi^2)^2\delta^2\gamma(v,\epsilon)\phi(v,\xi,z) \\ &+ \frac{1}{\alpha\delta_0\omega_0}\xi(1+\xi^2)^2\delta^2\int_v^1 \gamma(\tilde{v},\epsilon)\chi(v,\tilde{v})\phi(\tilde{v},\xi,z)\,\mathrm{d}\tilde{v}, \end{aligned} \tag{5.1.1}$$

where the linear operator $L[0]$ is defined such that

$$L[0]\phi = -\frac{1}{8}\frac{\partial}{\partial\xi}\left[\xi\left(1+\xi^2\right)^2\frac{\partial\phi}{\partial\xi}\right], \qquad \frac{\partial\phi}{\partial\xi} = 0 \text{ at } \xi = 0, \quad \phi \to 0 \text{ as } \xi \to \infty. \quad (5.1.2)$$

As will be later discussed, the linear operator will be more fully written as $L[K]$, a function of a variable K; the zero in $L[0]$ here denotes that this is a particular case where the argument K is zero. The terms on the left hand side of (5.1.1) represent advection and diffusion, whilst those on the right-hand side correspond to droplet breakup. Note that, unlike in the previous chapter, we do not impose the boundary condition for ϕ at $z = 0$, as in (4.2.9). Instead, we must impose a matching condition on the droplet size distribution, which serves to fit to the behaviour in the non-self similar inlet region of the jet.

If there were no droplet breakup, the equation, (5.1.1), for ϕ would reduce to

$$L[0]\phi + \frac{\xi\delta(z)}{\alpha}\frac{\partial\phi}{\partial z} = 0. \quad (5.1.3)$$

(This is why we denote the linear operator (5.1.2) as $L[0]$; the zero here represents no droplet breakup.) Equation (5.1.3) is also satisfied by the total oil fraction, given by $\Phi = \int_0^1 \phi \, \mathrm{d}v$. Recall from Section 4.3, that Φ has the similarity solution

$$\Phi = \frac{\Phi_0\delta_0}{\delta(z)}\frac{1}{\left(1+\xi^2\right)^2}, \quad (5.1.4)$$

where, from conservation of oil flux, $\Phi_0 = 6\beta M_\Phi/(\omega_0\delta_0^2)$ and M_Φ is the constant momentum flux given by $M_\Phi = \int_0^\infty rW\Phi \, \mathrm{d}\xi$.

5.1.2 Assumptions about breakup rate

The form of (5.1.1) suggests that, to have any chance of finding a self-similar solution, we must scale γ with δ^{-2}. (Note that χ is assumed to be spatially independent and so only depends on droplet volume.) From (2.4.30), the similarity solution for the energy dissipation ϵ scales with δ^{-4} so a natural choice is to scale the breakup rate γ with $\epsilon^{1/2}$. We are thus led to consider a dimensionless breakup rate of the form

$$\gamma = \sqrt{\frac{\alpha}{2\omega_0\delta_0}}K(v)\epsilon^{1/2}, \quad (5.1.5)$$

where the decoupled dependence of the breakup rate on volume is encoded in the function $K(v)$. Recall, the similarity solution for energy dissipation is given by

$$\epsilon = \frac{\alpha\omega_0^3\delta_0^3}{8\delta^4}H(\xi)^2, \quad (5.1.6)$$

where $H(\xi)$ is the solution to (2.4.31) subject to (2.4.32). Hence

$$\frac{\delta^2\gamma}{\alpha\delta_0\omega_0} = \frac{K(v)H(\xi)}{4} \tag{5.1.7}$$

and so (5.1.1) can be written as

$$L[K(v)]\phi + \frac{\xi\delta}{\alpha}\frac{\partial\phi}{\partial z} = \xi(1+\xi^2)^2 H(\xi)\int_v^1 \frac{K(\tilde{v})}{4}\chi(v,\tilde{v})\phi(\tilde{v},\xi,z)\,\mathrm{d}\tilde{v}, \tag{5.1.8}$$

where $L[K]$ is the linear operator defined as

$$L[K]\phi = -\frac{1}{8}\frac{\partial}{\partial\xi}\left[\xi\left(1+\xi^2\right)^2\frac{\partial\phi}{\partial\xi}\right] + \frac{K}{4}\xi(1+\xi^2)^2 H(\xi)\phi, \tag{5.1.9}$$

with boundary conditions

$$\frac{\partial\phi}{\partial\xi} = 0 \text{ at } \xi = 0, \qquad \phi \to 0 \text{ as } \xi \to \infty. \tag{5.1.10}$$

When $K = 0$, (5.1.9)–(5.1.10) yields $L[0]$ as defined in (5.1.2).

The breakup rate (5.1.5) is not the most general that might be used. In some ways this may not be so much of an issue since, as discussed in Chapter 3, it is difficult to determine the precise form of the breakup rate. Therefore, choosing a simple separable formula for this is not necessarily a bad idea. Indeed, scaling the breakup rate with $\epsilon^{1/2}$ is a physically reasonable assumption and satisfies the requirement, outlined in Chapter 3, that a higher energy dissipation rate leads to faster droplet breakup. However, we cannot include some of the effects that were present in the breakup rate (3.2.20), which was predominantly used in Chapter 4. This breakup rate includes a Heaviside term which imposes that, high up in the jet, only the larger drops can break up. This is a physical effect which affects the evolution of the droplet size distribution, but cannot be captured by the similarity solutions.

Nonetheless, in this chapter we will take (5.1.8)–(5.1.10) as the full problem, for which we find similarity solutions.

5.1.3 Simplifications and outlook

The process of finding similarity solutions to (5.1.8)–(5.1.10) can be simplified by making a number of assumptions. These simplifications either make the form of the problem a little more amenable to making analytical progress, make the problem easier to understand, or remove some inherent difficulties which would occur in the solution.

5.1.3.1 Approximate similarity solution for ϵ

In the breakup rate (5.1.5), we can approximate the similarity solution for the energy dissipation, (5.1.6), by using the outer solution, (2.4.35), for $H(\xi)$, namely by setting $H(\xi) = 4\xi/(1+\xi^2)^3$. Hence (5.1.8) reduces to

$$L[K(v)]\phi + \frac{\xi\delta}{\alpha}\frac{\partial\phi}{\partial z} = \frac{\xi^2}{1+\xi^2}\int_v^1 K(\tilde{v})\chi(v,\tilde{v})\phi(\tilde{v},\xi,z)\,\mathrm{d}\tilde{v}, \tag{5.1.11}$$

where now, instead of (5.1.9)–(5.1.10), we define $L[K]$ such that

$$L[K]\phi = -\frac{1}{8}\frac{\partial}{\partial\xi}\left[\xi\left(1+\xi^2\right)^2\frac{\partial\phi}{\partial\xi}\right] + K\frac{\xi^2}{1+\xi^2}\phi, \quad \frac{\partial\phi}{\partial\xi} = 0 \text{ at } \xi = 0, \quad \phi \to 0 \text{ as } \xi \to \infty. \tag{5.1.12}$$

The form of (5.1.11) is slightly easier to deal with than (5.1.8) as the function $H(\xi)$ in (5.1.8) must be calculated by numerically solving the ODE (2.4.31) subject to (2.4.32).

In this chapter, for simplicity, unless otherwise stated, we use the approximate form of the problem, (5.1.11)–(5.1.12). We explore the difference in the operator $L[K]$ when using the real energy dissipation in Section 5.2.4. In Section 5.3.5.1, we show that it is straightforward to extend our approach to use the true similarity solution to the energy dissipation. In addition, the results using both approaches are fairly similar.

5.1.3.2 Volume discretised model

One of the main difficulties in arriving at a self-similar form for ϕ is understanding how to deal with the integral term in (5.1.8) or (5.1.11). To simplify this we first discretise volume into N possible droplet volumes. We discretise uniformly in volume, by setting $v_i = i\triangle v$ for $i \in [1, N]$, where $\triangle v = 1/N$. Note, in this chapter, whenever we use the simplified volume discretised model, we will also make the simplification of approximate energy dissipation as in Section 5.1.3.1. Hence, the discrete version of (5.1.11) is

$$L[K_i]\phi_i + \frac{\xi\delta}{\alpha}\frac{\partial\phi_i}{\partial z} = \frac{\xi^2}{1+\xi^2}\sum_{j=i+1}^{N} K_j\chi_{ij}\phi_j(\triangle v), \ i > 1, \tag{5.1.13}$$

where ϕ_i is the volume fraction distribution of drops with volume v_i. Here K_i and χ_{ij} are the discrete analogues of $K(v)$ and $\chi(v,\tilde{v})$, respectively, and $L[K_i]$ is defined by (5.1.12).

In the discrete case, the smallest drops do not break up so ϕ_1 satisfies (5.1.13) with $L[K_1] := L[0]$. However, it is sometimes simpler, in practice, to use conservation of mass to determine ϕ_1. By definition, the discretised total oil fraction is given by $\Phi = \sum_{i=1}^{N} \phi_i \triangle v$ so,

$$\phi_1 = \frac{\Phi}{\triangle v} - \sum_{i=2}^{N} \phi_i, \tag{5.1.14}$$

where Φ is the similarity solution for the total volume fraction of oil, given by (5.1.4).

As can be seen in (5.1.13), the variation of ϕ_i is driven by drops of size v_i breaking up and larger drops (with drop size distribution ϕ_j where $j > i$) breaking into drops of size v_i. There is a cascade here whereby oil droplets in large bins break up and increase the volume of drops in smaller bins; in turn these drops break up and so on. By using this discretised approach, we can take advantage of this cascade; the natural way to solve for the drop size distribution is to first find ϕ_N, then ϕ_{N-1} etc. In this chapter, a lot of insight is gained by discretising volume and considering cases when N is small, such as $N = 2$ or $N = 3$.

5.1.3.3 Monotonic breakup rate

If the breakup rate $K(v)$ is monotonic, we will be able to make considerable progress and find full similarity solutions. However, when $K(v)$ is non-monotonic, repeated values of K at different v bring forth additional terms which significantly complicate the form of the solution.

Therefore, for the first half of this chapter, in Sections 5.3–5.4, we assume that $K(v)$ is a monotonic function of v. We either take it to reflect the smaller droplet behaviour of the breakup rate (3.2.20), choosing

$$K(v) = v \tag{5.1.15}$$

or the large drop behaviour of (3.2.20), with

$$K(v) = \frac{1}{v^{1/2}}. \tag{5.1.16}$$

Here (5.1.15) incorporates the notion that, due to surface stresses, very small droplets are harder to break up whilst (5.1.16) says that, for larger droplets, as they increase in size, they become harder to break. However, (5.1.16) is unphysical for small v; as the droplet volume v tends to zero, the breakup rate becomes infinite.

We later, in Section 5.5, consider more complex and realistic choices for the variation of the breakup rate with drop size. In the literature, the breakup rate is often

assumed to increase with volume, reach some local maximum and then decrease, as with (3.2.20). This means that $K(v)$ is most likely non-monotonic. We attempt to replicate this non-monotonic behaviour in a simple form by choosing

$$K(v) = v(1 - v). \tag{5.1.17}$$

In Section 5.5, we mainly consider the discrete volume model. Nevertheless, it takes quite a bit of work to find an explicit form for the full similarity solution to ϕ_i; we demonstrate how to do so in the $N = 3$ bin case.

5.1.3.4 Outlook

Our aim, in this chapter, is to find a similarity solution for ϕ. We will find that we can write the solution as a combination of powers of $1/\delta(z)$, with the exponent given by eigenvalues of the linear operator $L[K]$. The eigenfunctions of $L[K]$ will determine the variation of ϕ with the width variable ξ.

An important element in determining a similarity solution for ϕ is finding the eigenvalues and eigenfunctions of the linear operator, $L[K]$. We first use these to find similarity solutions when the breakup rate function, $K(v)$, is monotonic. For simplicity, we initially approximate the leading order similarity solution for large z. We do so by only including the terms corresponding to the smallest eigenvalue of $L[K]$ for each fixed value of K, which decay slowest at large z. We then generalise to find the full similarity solution, including all higher eigenvalue terms.

Once we have understood the case where the breakup rate is monotonic, we apply the same methods to the non-monotonic case. We find we can reduce the problem for ϕ. However, it is more difficult here to find an explicit formula for ϕ since, rather than merely powers of $1/\delta(z)$, terms proportional to $\log(\delta(z))$ additionally arise. Using the discrete volume framework, we find approximate similarity solutions and discuss how to find the full similarity solution.

5.2 Eigenvalues and eigenfunctions of the linear operator

We begin by investigating the eigenvalues and eigenfunctions of the linear operator, $L[K]$, as they will form the basis of our similarity solutions. For some fixed value of K, the eigenvalues m and eigenfunctions g of the operator $L[K]$ satisfy

$$L[K]g = m\xi g. \tag{5.2.1}$$

The linear operator $L[K]$ is given by (5.1.9)–(5.1.10) in the true dissipation case and (5.1.12) in the approximate dissipation case. In both cases, the only volume dependent element in the operator is the function $K(v)$. Therefore, in this section, our approach to this problem is to fix K so (5.2.1) becomes an ODE for the eigenfunction $g(\xi)$ and eigenvalue m. The breakup rate K then acts as a parameter; different values of v correspond to different values of this parameter.

In this section, we mainly use the approximate energy dissipation and, later, consider the differences when using the true dissipation.

5.2.1 Eigenvalue equation

The operator, $L[K]$, is given by (5.1.12) so, for each fixed value of K, (5.2.1) can be written as

$$-\frac{1}{8}\frac{d}{d\xi}\left[\xi\left(1+\xi^2\right)^2\frac{dg(\xi)}{d\xi}\right]+\frac{K\xi^2}{1+\xi^2}g(\xi)=m\xi g(\xi) \tag{5.2.2}$$

with associated boundary conditions

$$\frac{dg}{d\xi}(0)=0, \qquad g(\xi)\to 0, \text{ as } \xi\to\infty. \tag{5.2.3}$$

Note that (5.2.2)–(5.2.3) is a self-adjoint Sturm-Liouville problem. Therefore, for each fixed value of K, it has an infinite number of eigenvalues and corresponding eignfunctions. We denote the nth smallest eigenvalue, m^n, and its corresponding eigenfunction, $g^n(\xi)$. (Note, in this chapter, we will occasionally refer to the smallest eigenvalue and its corresponding eigenfunction without the superscript 1, so $m=m^1$ and $g(\xi)=g^1(\xi)$.) The set of eigenfunctions forms an orthogonal basis in ξ so

$$\left\langle g^n, g^l\right\rangle = 0, \tag{5.2.4}$$

for $n\neq l$, where the functional inner product is defined by

$$\langle a(\xi), b(\xi)\rangle = \int_0^\infty \xi a(\xi)b(\xi)\,\mathrm{d}\xi. \tag{5.2.5}$$

Now, we have the freedom to multiply g, in (5.2.2)–(5.2.3), by any non-zero constant and a natural choice is to normalise so the norm of the eigenfunction is one, that is

$$\langle g^n, g^n\rangle = \int_0^\infty \xi(g^n(\xi))^2\,\mathrm{d}\xi = 1. \tag{5.2.6}$$

5.2.2 Leading eigenvalues and eigenfunctions

Let us first consider only the smallest eigenvalue and its corresponding eigenfunction. If $K = 0$, $m = 1$ and

$$g^1(\xi) = \frac{\sqrt{6}}{(1+\xi^2)^2}. \tag{5.2.7}$$

Recall, from the discussion in (5.1.3) –(5.1.4), that the case when $K = 0$ corresponds to considering the total oil fraction. It is thus not unexpected that (5.2.7) is proportional to the total oil fraction Φ in (5.1.4) and, in fact, captures the entire variation of Φ with width.

For non-zero values of K, g must be found by solving (5.2.2)–(5.2.3) numerically. Since the equation is singular at $\xi = 0$, we use its behaviour as $\xi \to 0$,

$$g^1(\xi) \sim a_0 \left(1 - 2m^1\xi^2 + \frac{8K}{9}\xi^3 \cdots\right) \quad \text{as } \xi \to 0 \tag{5.2.8}$$

as an effective boundary condition and shoot with the parameter m to satisfy the far-field condition in (5.2.3). The smallest suitable non-negative value of m is chosen. Note that the parameter a_0 is fixed by the choice of normalisation of g^1, namely by (5.2.6).

Solutions for $g^1(\xi)$ with $K \in [0, 50]$ are shown in Figure 5.1(a). We also illustrate the variation of the smallest eigenvalue, m^1, with K in Figure 5.1(b). We observe that the eigenvalue m^1 increases monotonically with the breakup rate K; m^1 corresponds to the strength of the droplet breakup.

It is insightful to corroborate our numerical results by exploring the asymptotic behaviour of m^1 and $g^1(\xi)$ in the limits where the breakup rate parameter K is small and large.

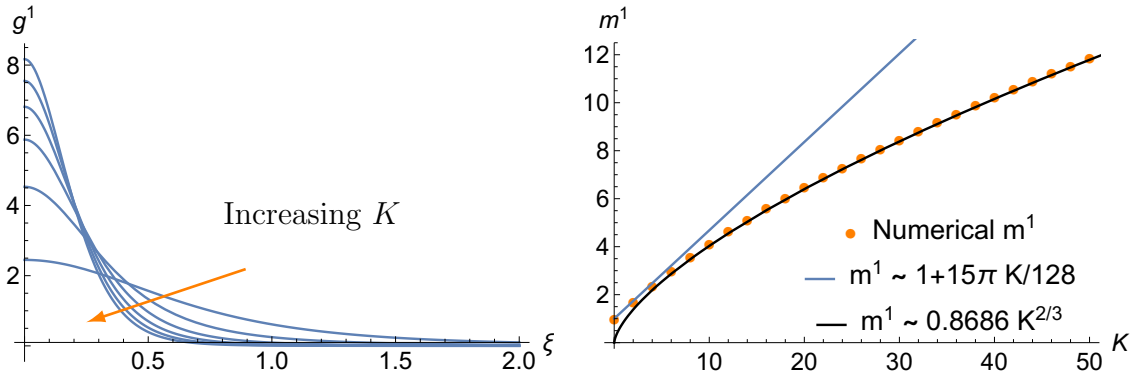
5.2.2.1 Small K

When $K = 0$, we have $m^1 = 1$ and, from (5.2.7), $g^1(\xi) \propto 1/\left(1+\xi^2\right)^2$. Therefore, to examine the behaviour near $K = 0$, we expand

$$m^1 = 1 + \widetilde{m}K + \cdots \tag{5.2.9}$$

$$g^1(\xi) = a_0 \left(\frac{1}{\left(1+\xi^2\right)^2} + K\tilde{g}(\xi) + \cdots\right), \tag{5.2.10}$$

where $\widetilde{m}$ is a constant to be determined and $\tilde{g}(\xi)$ is a function of ξ to be determined. (Here a_0 is a constant of proportionality which, after determining $\tilde{g}(\xi)$, will be set so



(a) (b)

Figure 5.1: The solution to the eigenproblem (5.2.2)–(5.2.3). We illustrate (a) the eigenfunction $g^1(\xi)$ for $K = 0 : 10 : 50$ and (b) the eigenvalue m^1 as it varies with the parameter K. In (b) we also plot the asymptotic approximations, (5.2.14) and (5.2.23), of $m^1(K)$ for small and large K.

that the normalisation (5.2.6) is satisfied.) We put (5.2.9)–(5.2.10) in (5.2.2)–(5.2.3) and find that $\widetilde{m}$ and $\tilde{g}(\xi)$ are determined by

$$L[0]\tilde{g} - \xi\tilde{g} = \frac{\xi}{(1+\xi^2)^2}\left[\widetilde{m} - \frac{\xi}{1+\xi^2}\right], \tag{5.2.11}$$

with boundary conditions

$$\frac{d\tilde{g}}{d\xi}(0) = 0, \qquad \tilde{g}(\xi) \to 0, \text{ as } \xi \to \infty. \tag{5.2.12}$$

We note that the homogeneous version of (5.2.11) is the similarity equation for $K = 0$, which has solution proportional to $1/(1+\xi^2)^2$. Hence, using the Fredholm alternative, we deduce that

$$\widetilde{m} = \frac{\int_0^\infty \xi^2/(1+\xi^2)^5\,\mathrm{d}\xi}{\int_0^\infty \xi/(1+\xi^2)^4\,\mathrm{d}\xi} = \frac{15\pi}{128}. \tag{5.2.13}$$

Therefore, as $K \to 0$

$$m^1 \sim 1 + \frac{15\pi K}{128}, \tag{5.2.14}$$

which is illustrated in Figure 5.1(b). We see this corresponds well with the numerically calculated values of m for small K.

The solution to (5.2.11)–(5.2.12) for $\tilde{g}$ can be found analytically (noting that $\tilde{g}(0) = 0$) and the normalised approximation for $g^1(\xi)$ is illustrated in Figure 5.2. It shows very good agreement with the numerical solution when $K = 0.3$. The asymptotics also demonstrates good agreement with the numerical solution for values of K up to around $K = 4$.

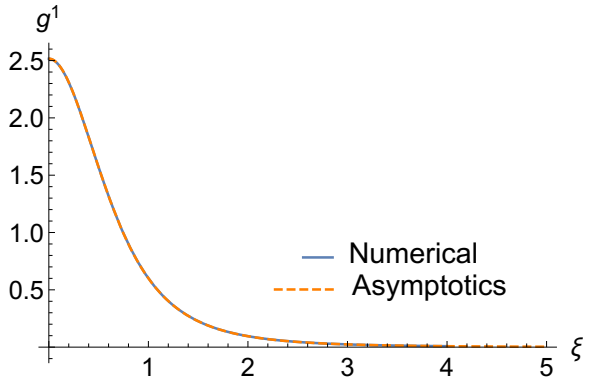


Figure 5.2: Comparison of the numerical solution to (5.2.2)–(5.2.3), for the eigenfunction $g^1(\xi)$, with the asymptotic expression for small K, given by (5.2.10) and the solution to (5.2.11)–(5.2.12). Here we take $K = 0.3$.

5.2.2.2 Large K

We now consider the case when K is large. We expand $m^1 = \hat{m}K^{-b} + \cdots$, where b and $\hat{m}$ are constants to be determined. Then (5.2.2)–(5.2.3) yields

$$\frac{1}{K}\xi\frac{d^2g^1}{d\xi^2} + \frac{1}{K}\left[1 + \frac{4\xi^2}{1+\xi^2}\right]\frac{dg^1}{d\xi} + 8\xi\left[\frac{\hat{m}}{K^{1+b}\left(1+\xi^2\right)^2} - \frac{\xi}{\left(1+\xi^2\right)^3}\right]g^1 = 0, \quad (5.2.15)$$

subject to

$$\frac{dg^1}{d\xi}(0) = 0, \quad g^1(\xi) \to 0 \text{ as } \xi \to \infty. \quad (5.2.16)$$

Irrespective of the value of b, to leading order $g^1 = 0$. This suggests that there is a boundary layer at $\xi = 0$.

We set

$$\xi = K^{-c}X, \quad (5.2.17)$$

for some constant $c > 0$, which yields, to lowest order in K,

$$X\frac{d^2g^1}{dX^2} + \frac{dg^1}{dX} + 8Xg^1\left[\hat{m}K^{-2c-b} - K^{1-3c}X\right] = 0. \quad (5.2.18)$$

For all terms to balance, we must take $1 - 3c = 0$ so $c = 1/3$ and $-2c - b = 0$ so $b = -2/3$. Therefore

$$m^1 \sim \hat{m}K^{2/3}. \quad (5.2.19)$$

The inner solution and $\hat{m}$ are obtained by solving (5.2.18), which reduces to

$$X\frac{d^2g^1}{dX^2} + \frac{dg^1}{dX} + 8Xg^1(\hat{m} - X) = 0 \quad (5.2.20)$$

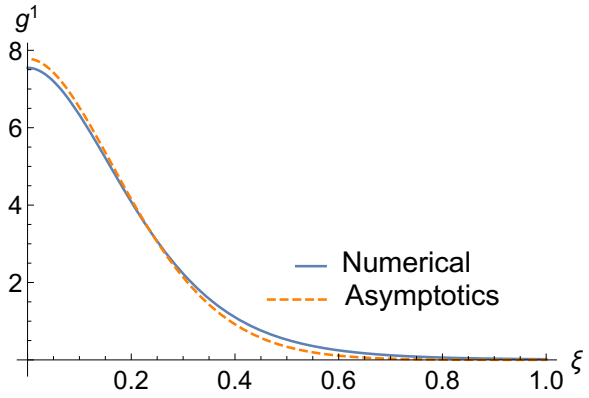


Figure 5.3: Comparison of the numerical solution to (5.2.2)–(5.2.3), for the eigenfunction $g^1(\xi)$, with the asymptotic expression for large K, given by the numerical solution to (5.2.20) subject to (5.2.22). Here we take $K = 40$.

with associated boundary conditions

$$\frac{dg^1}{dX}(0) = 0, \quad g^1(X) \to 0 \text{ as } X \to \infty. \tag{5.2.21}$$

As $X \to 0$, equation (5.2.20) is singular, and we find the local behaviour

$$g^1(\xi) \sim a_0 \left(1 - 2\hat{m}X^2 + \frac{8}{9}X^3 + \cdots\right). \tag{5.2.22}$$

We solve (5.2.20) subject to (5.2.22), shooting with $\hat{m}$ to satisfy the far-field boundary condition in (5.2.21). (Note the parameter a_0 is later fixed by the choice of normalisation of g, namely (5.2.6).) This yields $\hat{m} = 0.8686$ so

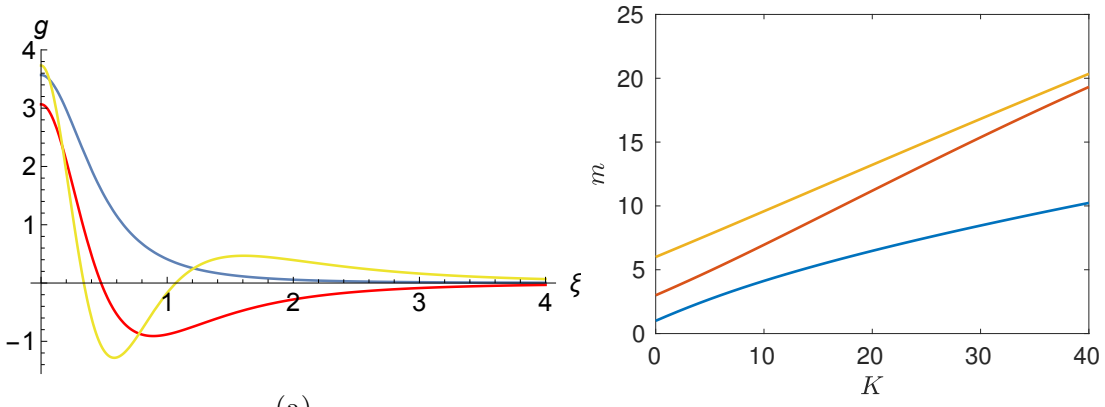
$$m^1 \sim 0.8686K^{2/3}. \tag{5.2.23}$$

This shows very good agreement with the numerically-computed values, as plotted in Figure 5.1(b). We also see, in Figure 5.3, that the numerical solution to the inner problem, (5.2.20) subject to (5.2.21)–(5.2.22), compares well with the full solution, $g^1(\xi)$, for large K (here $K = 40$).

5.2.3 Higher eigenvalues and eigenfunctions

We now consider the higher eigenvalues and corresponding eigenfunctions. Recall, for some fixed K, we denote the nth smallest eigenvalue as m^n and the corresponding eigenfunction as $g^n(\xi)$. In the case when $K = 0$, the nth eigenvalue is given by $m^n = n(n+1)/2$ and the corresponding eigenfunction is given by

$$g^n(\xi) = \sqrt{2(2n+1)}\ {}^2F_1(-(n+1), -(n-1), 1, -\xi^2)\left(1+\xi^2\right)^{-(n+1)}, \tag{5.2.24}$$



(a) (b)

Figure 5.4: Higher eigenvalues and eigenfunctions of the linear operator, $L[K]$. (a) Eigenfunctions g^j when $K = 5$, for $j = 1$ (blue), $j = 2$ (red) and $j = 3$ (yellow) ; (b) variation of the eigenvalues m_j with K for $j = 1$ (blue), $j = 2$ (red) and $j = 3$ (yellow).

where ${}^2F_1$ denotes a hypergeometric function. The form of $g^n(\xi)$ in (5.2.24) represents $(1+\xi^2)^{-(n+1)}$ times a polynomial of degree $2(n-1)$. For $K > 0$ we cannot express the eigenvalues m^n and eigenfunctions g^n in analytical form but their behaviour is similar and is illustrated in Figure 5.4 for $K = 5$.

In Figure 5.4(a), we compare the first three eigenfunctions, at fixed $K = 5$. We see that, while the first eigenfunction g^1 decreases monotonically with ξ, the higher eigenfunctions become increasingly oscillatory and take negative values. Figure 5.4(b) shows the variation of the first three eigenvalues with K. We see that each of the m^n monotonically increases with breakup rate K and so is bounded below by the eigenvalue at $K = 0$, given by $m^1 = 1$, $m^2 = 3$ and $m^3 = 6$ respectively.

5.2.4 Using true similarity solution for ϵ

We have thus far approximated the similarity solution for the energy dissipation by (2.4.35), so $L[K]$ is given by (5.1.12). We now consider the full linear operator, (5.1.9)–(5.1.10), which uses the true similarity solution for ϵ. In this chapter we predominantly use the approximate dissipation, as outlined in Section 5.1.3.1, so it is useful to identify here the differences when using the true dissipation. In this section, we do so by discussing the smallest eigenvalue and its corresponding eigenfunction.

Using the true similarity solution for ϵ, the eigenvalues and eigenfunctions of the

operator $L[K]$, given by (5.1.9)–(5.1.10), satisfy

$$-\frac{1}{8}\frac{d}{d\xi}\left[\xi\left(1+\xi^2\right)^2\frac{dg(\xi)}{d\xi}\right]+\frac{K}{4}\xi(1+\xi^2)^2H(\xi)g(\xi)=m\xi g(\xi) \tag{5.2.25}$$

subject to

$$\frac{dg}{d\xi}(0)=0, \qquad g(\xi)\to 0, \text{ as } \xi\to\infty. \tag{5.2.26}$$

Note that, as in (5.2.6), g is normalised so that $\int_0^\infty \xi g^2\,\mathrm{d}\xi=1$. The difference with the approximate ϵ case is that, here, $H(\xi)$ is given by the solution to (2.4.31)–(2.4.32), whilst in the approximate dissipation case, we took the form of $H(\xi)$ as (2.4.35), which is a good approximation to $H(\xi)$ except at small ξ.

We solve the eigenproblem (corresponding to the smallest eigenvalue m^1) for various values of the parameter K. To do so, we use the behaviour at the singular point $\xi=0$, i.e.,

$$g^1(\xi)\sim a_0\left(1-2\left(m^1-\frac{KH(0)}{4}\right)\xi^2+\cdots\right) \quad \text{as } \xi\to 0, \tag{5.2.27}$$

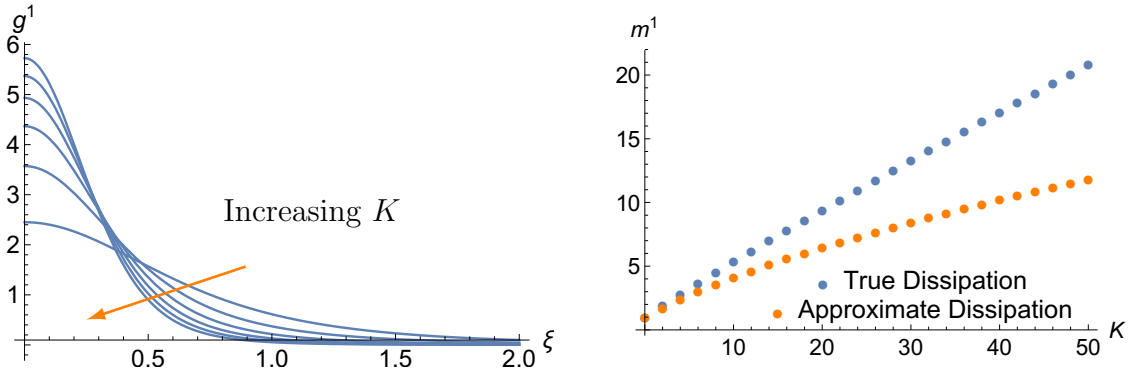
and shoot using the parameter m^1 so the far field condition in (5.2.26) is satisfied.

We plot the eigensolution $g^1(\xi)$ in Figure 5.5(a) and note that the dependence of g^1 on ξ exhibits much the same qualitative behaviour as in the approximate ϵ case, shown in Figure 5.1(a). We also plot the variation of m^1 with the free parameter K in Figure 5.5(b). We see that the behaviour of m^1 when K is relatively small is very similar to that in the approximate energy dissipation case. However, the large K behaviour is quite different. This is to be expected; in (5.1.9), the function $H(\xi)$, which arises from the energy dissipation, only appears multiplied by K. Thus, when K is large, the energy dissipation becomes more significant. Recall, from Figure 2.4, that the approximation underestimates the energy dissipation, and thus underestimates droplet breakup. In the same way, the approximation yields a smaller increase in m^1 with K compared to using the true value of ϵ (see Figure 5.5(b)). Thus, the eigenvalues m^1 appear to reflect the strength of droplet breakup. It is, therefore, interesting to examine the limits where K is small and large in greater detail.

5.2.4.1 Small K

We consider the case when K is small, analogous to Section 5.2.2.1. Again we expand

$$m^1=1+\widetilde{m}K+\cdots, \tag{5.2.28}$$



(a) (b)

Figure 5.5: Eigenfunctions and eigenvalues of the similarity equation using the true similarity solution for ϵ. (a) Eigenfunction $g^1(\xi)$ for $K = 0 : 10 : 50$; (b) variation of eigenvalues m^1 with the parameter K using true and approximate dissipation.

and

$$g^1(\xi) = a_0 \left(\frac{1}{(1+\xi^2)^2} + K\tilde{g}(\xi) + \cdots \right) \tag{5.2.29}$$

and insert into (5.2.25)–(5.2.26). Then $\widetilde{m}$ and $\tilde{g}$ are determined by solving the eigenproblem

$$L[0]\tilde{g} - \xi\tilde{g} = \frac{\widetilde{m}\xi}{(1+\xi^2)^2} - \frac{\xi H(\xi)}{4} \tag{5.2.30}$$

subject to

$$\frac{d\tilde{g}}{d\xi}(0) = 0, \qquad \tilde{g}(\xi) \to 0 \text{ as } \xi \to \infty. \tag{5.2.31}$$

Using the Fredholm alternative, we deduce that

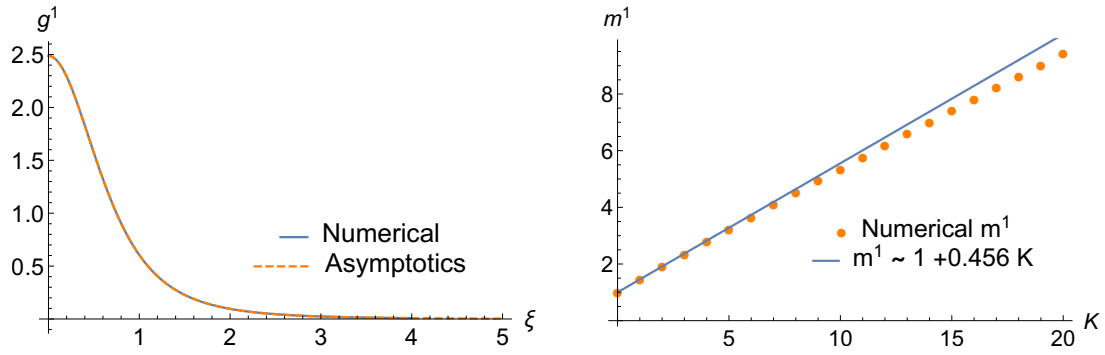
$$\widetilde{m} = \frac{\int_0^\infty \xi H(\xi)/(4(1+\xi^2)^2)\,\mathrm{d}\xi}{\int_0^\infty \xi/(1+\xi^2)^4\,\mathrm{d}\xi} = 0.456. \tag{5.2.32}$$

Note that the value of $\widetilde{m}$ here depends on the value of the parameter $\hat{\nu}$ in the problem (2.4.31)–(2.4.32) for $H(\xi)$. Hence

$$m^1 \sim 1 + 0.456K \tag{5.2.33}$$

as $K \to 0$, which is illustrated in Figure 5.6(b). The inner solution $\tilde{g}$ can be found numerically, noting that $\tilde{g}(0) = 0$. It is shown in Figure 5.6(a). Good agreement between the numerical solution and the asymptotics for both the eigenfunction and the eigenvalue is evident in Figure 5.6.

This discussion confirms our observation, from Figure 5.5(b), that the small K behaviour of m^1 when using the approximate dissipation, (5.2.14), is very similar to that for the true dissipation, (5.2.33).



(a) (b)

Figure 5.6: Small K behaviour of eigenfunction $g^1(\xi)$ and eigenvalue m^1. (a) Comparison of numerical solution for the eigenfunction g^1, given by the solution to (5.2.25)–(5.2.27), and the asymptotics given by solving (5.2.30)–(5.2.31). Here we take $K = 0.3$. (b) Eigenvalue m^1 versus parameter K, comparing the numerical values with asymptotic approximation (5.2.33).

5.2.4.2 Large K

We also examine the case when K is large. When $K \gg 1$, from (5.2.25), we have

$$\frac{1}{K}\xi\frac{d^2g^1}{d\xi^2} + \frac{1}{K}\left[1 + \frac{4\xi^2}{1+\xi^2}\right]\frac{dg^1}{d\xi} + 8\xi g^1\left[\frac{m^1}{K\left(1+\xi^2\right)^2} - \frac{H(\xi)}{4}\right] = 0, \tag{5.2.34}$$

so the leading-order outer solution is $g^1 = 0$ and again there is a boundary layer at $\xi = 0$. The main difference between the true similarity solution for ϵ and its approximation is the behaviour of $H(\xi)$ at small ξ (as was illustrated in Figure 2.4). Therefore, the main difference in the behaviour of g^1, and hence in the drop size distribution, will occur in this region.

Recall from Section 2.4.3 that there is an inner region for H, when ξ is small. To focus on the small ξ region, we scale into this inner region, setting (as in Section 2.4.3) $\xi = \hat{\nu}^{1/3}X$ and $H = \hat{\nu}^{1/3}G$, where $\hat{\nu} = \alpha/(8\sqrt{\beta C_\mu}) = 0.0684$ is treated as a small parameter. Then (5.2.34) becomes

$$X\frac{d^2g^1}{dX^2} + \left(1 + \frac{4\hat{\nu}^{2/3}X^2}{1+\hat{\nu}^{2/3}X^2}\right)\frac{dg^1}{dX} + 8Xg^1\left[\frac{\hat{\nu}^{2/3}m^1}{\left(1+\hat{\nu}^{2/3}X^2\right)^2} - \frac{\hat{\nu}KG(X)}{4}\right] = 0, \tag{5.2.35}$$

with boundary conditions (5.2.26).

We assume $\widetilde{m} = \hat{\nu}^{2/3}m^1 = \mathcal{O}(1)$ and $\widetilde{K} = \hat{\nu}K = \mathcal{O}(1)$, and recall $G(X) \sim G_0(X)$, where $G_0(X)$ satisfies (2.4.37)–(2.4.39). Then, to leading order

$$X\frac{d^2g^1}{dX^2} + \frac{dg^1}{dX} + 8X\left(\widetilde{m} - \frac{\widetilde{K}G_0(X)}{4}\right)g^1 = 0 \tag{5.2.36}$$

with

$$\frac{dg^1}{dX}(v,0)=0, \quad g^1(\xi)\to 0 \text{ as } \xi\to\infty. \tag{5.2.37}$$

To numerically solve (5.2.36)–(5.2.37), we use the behaviour at the singular point $\xi=0$, namely

$$g^1 \sim a_0\left(1-2\left(\widetilde{m}-\frac{\widetilde{K}G_0(0)}{4}\right)+\cdots\right), \tag{5.2.38}$$

and shoot with the parameter $\widetilde{m}$ to satisfy the far-field boundary condition in (5.2.37). The numerically computed solution (for $K=40$ so $K\hat{\nu}=2.7$) is plotted in Figure 5.7(a) and $m^1=\hat{\nu}^{-2/3}\widetilde{m}(\hat{\nu}K)$ is shown in Figure 5.7(b).

However, this approximation only holds when $K\hat{\nu}=\mathcal{O}(1)$. Let us now consider even larger values of K such that $K\hat{\nu}\gg 1$. We let $\varepsilon=(K\hat{\nu})^{-1/2}\ll 1$ and scale $X=\varepsilon^{1/2}y$ so (5.2.35) becomes

$$y\frac{d^2g^1}{dy^2}+\left(1+\frac{4\hat{\nu}^{2/3}\varepsilon y^2}{1+\hat{\nu}^{2/3}\varepsilon y^2}\right)\frac{dg^1}{dy}+8yg^1\left[\frac{\hat{\nu}^{2/3}\varepsilon m^1}{(1+\hat{\nu}^{2/3}\varepsilon y^2)^2}-\frac{\varepsilon^{-1}G\left(\varepsilon^{1/2}y\right)}{4}\right]=0. \tag{5.2.39}$$

The term in square brackets can be written as

$$\left(\hat{\nu}^{2/3}\varepsilon m^1-2\hat{\nu}^{4/3}\varepsilon^2 m^1y^2+\cdots\right)+\left(-\frac{\varepsilon^{-1}G(0)}{4}-\frac{y^2}{8}G''(0)+\cdots\right) \tag{5.2.40}$$

and, to achieve a dominant balance in (5.2.40), we set $m^1\sim m_0\hat{\nu}^{-2/3}\varepsilon^{-2}$. For the terms in square brackets in (5.2.39) to balance with the order one terms, we find

$$m^1\sim\frac{G(0)}{4\hat{\nu}^{2/3}}\varepsilon^{-2}+\frac{m_1}{\hat{\nu}^{2/3}}\varepsilon^{-1}+\cdots, \tag{5.2.41}$$

for some m_1 to be determined and then from (5.2.39)–(5.2.41), to leading order, g is given by

$$y\frac{d^2g^1}{dy^2}+\frac{dg^1}{dy}+8y(m_1-Ay^2)g^1=0, \tag{5.2.42}$$

where $A=G''(0)/8+\hat{\nu}^{2/3}G(0)/2$. Using the behaviour of the equation, (2.4.31), for $H=\hat{\nu}^{1/3}G$ as $\xi\to 0$, we can alternatively write

$$A=G(0)^2/16-\hat{\nu}^{2/3}G(0)/2. \tag{5.2.43}$$

To obtain a bounded, positive solution of (5.2.42) we must set $m_1 = \sqrt{A/2}$ so

$$m^1 \sim \frac{H(0)}{4}K + \frac{H(0)}{4\sqrt{2\hat{\nu}}}\sqrt{1 - \frac{8\hat{\nu}}{H(0)}}\sqrt{K} \tag{5.2.44}$$

and the solution is given by

$$g^1(y) \sim a_0 \exp\left(-\sqrt{2A}y^2\right), \tag{5.2.45}$$

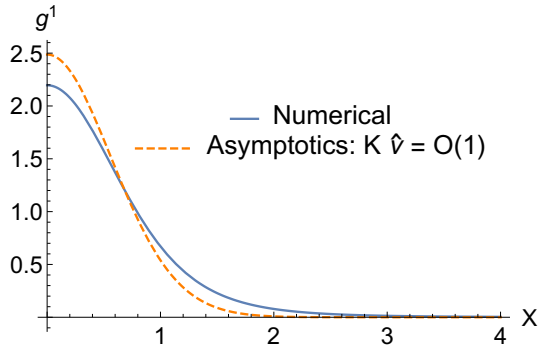
where recall the constant a_0 is fixed to satisfy (5.2.6). The asymptotic expression (5.2.45) for g^1 is shown in Figures 5.7(a)–(b), and (5.2.44) for m^1 is shown in Figure 5.7(c).

There is generally good agreement between the numerics and asymptotics. In Figure 5.7(a), we consider the case where $K = 40$, namely where $\hat{\nu}K = 2.7$. The asymptotics for the case where $K\hat{\nu} = \mathcal{O}(1)$ agree reasonably well with the numerics but there is some disparity here. This can be attributed to the fact that $\hat{\nu} = 0.068$ is not very small and so, as seen in Figure 2.4, the inner solution G_0 is slightly inaccurate. (For smaller values of $\hat{\nu}$, say $\hat{\nu} \sim \mathcal{O}(10^{-3})$, we find that the agreement between the numerics and asymptotics is very good.) For larger values of K, the asymptotics for $K\hat{\nu} = \mathcal{O}(1)$ become less appropriate, as seen in Figure 5.7(c), and those for $K\hat{\nu} \gg 1$ are more valid. There is very good agreement between the $K\hat{\nu} \gg 1$ asymptotics and the numerics as seen in Figures 5.7(b)–(c).

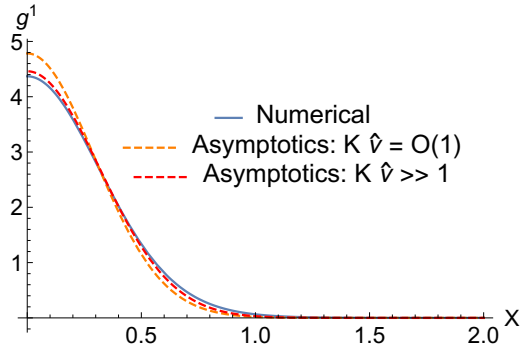
In summary, when K is small, the breakup rate is not so significant and so approximating the energy dissipation leads to few differences in the eigenvalues and eigenfunctions of the operator. If K is larger, the differences from the approximate ϵ assumption become more significant. Using the true dissipation yields larger values of m. The disparity is driven by the behaviour of the eigenproblem (5.2.25) at small ξ (since it is at small ξ where the approximate dissipation and true similarity solution for ϵ differ greatest). For higher eigenvalues and eigenfunctions, similar comparisons between using the approximate and true dissipation can be made.

5.3 Approximate similarity solutions

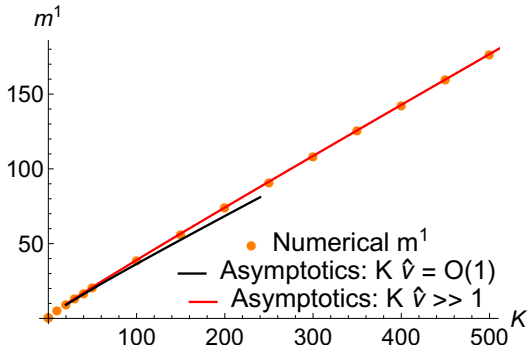
Now that we understand the behaviour of the operator $L[K]$, we look for similarity solutions for ϕ. We restrict our discussion here to monotonic breakup rate $K(v)$ and use the approximation (2.4.35) for ϵ. In addition, for simplicity, the similarity solutions we find for ϕ only take into account the smallest eigenvalue and its corresponding eigenfunction.



(a) $K = 40, \hat{\nu} = -0.0684 \implies K\hat{\nu} = 2.7$



(b) $K = 500, \hat{\nu} = -0.0684 \implies K\hat{\nu} = 34$



(c)

Figure 5.7: Large K behaviour of eigenfunction $g^1(\xi)$ and eigenvalue m^1. (a) Eigenfunction g^1 for $K = 40$ or $K\hat{\nu} = 2.7$. We show the variation with inner variable $X = \hat{\nu}^{-1/3}\xi$. Numerical solution of (5.2.25)–(5.2.27) is compared to asymptotics for $K\hat{\nu} = \mathcal{O}(1)$, given by solution to (5.2.36)–(5.2.38). (b) We show a similar comparison between numerics and the asymptotics for $K\hat{\nu} = \mathcal{O}(1)$, taking $K = 500$ or $K\hat{\nu} = 34$. We also show the asymptotic expression for large $K\hat{\nu}$, given by (5.2.45). (c) Eigenvalue m^1 versus parameter K, comparing the numerical values with asymptotic expressions given by the solution to (5.2.36)–(5.2.38) for $K\hat{\nu} = \mathcal{O}(1)$, and (5.2.44) for $K\hat{\nu} \gg 1$.

5.3.1 Two bins

We begin by considering the simplest possible scenario, where we discretise volume into two bins. Here there are only two sizes of droplets: large droplets of size v_2 break into small droplets of size v_1, thereby increasing the volume fraction of the small droplets. The largest droplets, with volume fraction distribution ϕ_2, are advected, diffused and break up, satisfying (5.1.13) with $N = 2$ and $i = 2$, namely

$$L[K_2]\phi_2 + \frac{\xi\delta}{\alpha}\frac{d\phi_2}{dz} = 0, \tag{5.3.1}$$

where L is defined by (5.1.12). Once ϕ_2 is calculated, the volume fraction distribution ϕ_1 can be determined using mass conservation,

$$\phi_1 = \frac{\Phi}{\triangle v} - \phi_2. \tag{5.3.2}$$

We seek a self-similar solution to (5.3.1). If $K_2 = 0$ the solution is given by the first kind similarity solution

$$\phi_2 = \frac{\widetilde{C}_{22}}{\left(1+\xi^2\right)^2}\frac{1}{\left(\delta(z)/\hat{\delta}\right)}\triangle v, \tag{5.3.3}$$

where $\widetilde{C}_{22}$ is a fitting constant found by matching to the flow in the non-self similar region at small z. Here we introduce the factor $\hat{\delta} = \delta_0 + \alpha\hat{z}$ as we will match the similarity solution to the non-self similar flow at some sufficiently large height $z = \hat{z}$ or $\delta = \hat{\delta}$. Equation (5.3.3) is proportional to (5.1.4) for the total oil fraction Φ, since (5.3.1) reduces to the equation for the total volume fraction of oil Φ if $K_2 = 0$. However, for non-zero K_2, there does not exist a first kind similarity solution which satisfies the far field boundary condition in (5.1.12). We instead look for a second kind similarity solution of the form

$$\phi_2(\xi, z) = \widetilde{C}_{22}\frac{g_2(\xi)}{\left(\delta(z)/\hat{\delta}\right)^{m_2}}\triangle v, \tag{5.3.4}$$

where the constants $\widetilde{C}_{22}$ and m_2 and the function $g_2(\xi)$ are to be determined. Unlike the first kind similarity solution, (5.3.3), here the exponent of $\delta(z)$ is not fixed: m_2 must be determined along with the solution and is set so that the far field boundary condition in (5.1.12) is satisfied.

Using the ansatz (5.3.4), we find that (5.3.1) reduces to the eigen-problem (5.2.2)–(5.2.3), for the linear operator L. Hence the constant m_2 in (5.3.4) is an eigenvalue of

$L[K_2]$ and function $g_2(\xi)$ in (5.3.4) is its corresponding eigenfunction, as calculated in Section 5.2. This means that the eigenfunction, $g^1(\xi)$, captures the variation of ϕ_2 with radius. From Figure 5.1(a), we see that most of the large drops are at the jet centre and, with increasing radius, the volume fraction decreases. The eigenvalue m_2 is the exponent of $1/\delta(z)$ in (5.3.4) and so determines the rate of decay of ϕ_2 with height up the jet. From Figure 5.1(b) we see that, as K increases (which corresponds to a greater breakup rate), the exponent m_2 increases; the fraction of the large drops decreases more rapidly with height.

As discussed in Section 5.2.1, there is a countably infinite set of positive eigenvalues m_2 and eigenfunctions g_2 and so ϕ_2 is actually a linear combination of terms such as (5.3.4), with each term corresponding to one of the eigenvalues. However, throughout this section, we simplify by using only the smallest eigenvalue and its corresponding eigenfunction. We are looking for similarity solutions, which are expected to be valid when z (or δ) is sufficiently large. For δ sufficiently large, we expect the term of the form (5.3.4) which has the smallest value of m_2 to dominate. In Section 5.4, we discuss the implications of such assumptions and the effect of higher eigenvalues.

To determine ϕ_2, it remains to evaluate the constant, $\widetilde{C}_{22}$, in (5.3.4). We do this by imposing the volume flux of droplets of volume v_2 at $z = \hat{z}$ or $\delta = \hat{\delta}$. Evidently, the similarity solution does not hold for small z (since there is more than one important lengthscale here: the nozzle width as well as the jet width). Therefore, this can be treated as a matching condition to the non-self similar flow near the base of the jet. We impose that the flux of ϕ_i (for $i = 1, 2$) at $\delta = \hat{\delta}$ is given by some prescribed constant s_i, namely

$$\int_0^\infty rW\phi_i dr = s_i. \tag{5.3.5}$$

This yields

$$\widetilde{C}_{22} \int_0^\infty \frac{\xi g_2}{(1+\xi^2)^2}\, \mathrm{d}\xi \triangle v = S_2, \tag{5.3.6}$$

with

$$S_2 = \frac{\beta s_2}{\hat{\delta}\omega_0\delta_0}. \tag{5.3.7}$$

Note that the flux of the total volume fraction of oil drops is a constant, given by M_Φ. So for net mass conservation we must have

$$(s_1 + s_2)\triangle v = M_\Phi. \tag{5.3.8}$$

Here, for convenience, we introduce h_2, which is proportional to g_2 but is normalised such that

$$\int_0^\infty \frac{\xi h_2}{\left(1+\xi^2\right)^2}\,\mathrm{d}\xi = 1, \tag{5.3.9}$$

and C_{22}, which is given by

$$C_{22}\triangle v = \widetilde{C}_{22}\int_0^\infty \frac{\xi g_2}{\left(1+\xi^2\right)^2}\,\mathrm{d}\xi\triangle v. \tag{5.3.10}$$

Hence

$$\phi_2 = C_{22}\frac{h_2(\xi)}{(\delta(z)/\hat{\delta})^{m_2}}\triangle v, \tag{5.3.11}$$

where, from (5.3.6) and (5.3.10),

$$C_{22}\triangle v = S_2. \tag{5.3.12}$$

It is important to note here that using only the leading order eigenvalue term may yield some inaccuracies in the value of the constant C_{22}. If we include all higher eigenvalues, ϕ_2 in fact takes the form

$$\phi_2 = \sum_{n=1}^{\infty} C_{22}^n \frac{h_2^n(\xi)}{(\delta(z)/\hat{\delta})^{m_2^n}}\triangle v, \tag{5.3.13}$$

where the superscripts n correspond to the n smallest eigenvalue and its corresponding eigfunction. (Note C_{22} in (5.3.11)–(5.3.12) corresponds to C_{22}^1.) By imposing the flux of ϕ_2 as in (5.3.5)–(5.3.7), we find

$$\sum_{n=1}^{\infty} C_{22}^n\triangle v = S_2. \tag{5.3.14}$$

This means that, in setting C_{22}^1 according to (5.3.12), we have implicitly assumed that the values of C_{22}^n for $n>1$ are approximately zero, i.e. that the terms in (5.3.13) arising from the higher eigenvalues contribute negligible mass at $\delta(z)=\hat{\delta}$. These terms will, of course, be small at very large z because of the more rapid decay of the $\delta(z)^{-m_2^j}$ term. However, this does not necessarily mean that the higher eigenvalue terms are small at our starting height $\delta=\hat{\delta}$ or that the C_{22}^n are also small. This means we may need to take the value of C_{22}^1 with some scepticism.

For verification, let us compare the similarity solution for ϕ_2 to the numerical solution to (5.3.1), with $K_2=1$. We use a finite difference scheme, marching forward implicitly in z and using central differences for r, as described in Section 4.4.1. For

the numerical solution we must solve for $z > \hat{z}_n$ for some $\hat{z}_n > 0$ since our similarity solutions for velocity and energy dissipation are not valid at small z. We set $\hat{z}_n = 2$. At $z = \hat{z}_n$ (or $\delta = \hat{\delta}_n$), we impose the initial conditions $\phi_1 = 0$ and

$$\phi_2 = \begin{cases} \dfrac{4M_\Phi \beta}{\omega_0 \delta_0 \hat{\delta}_n (\triangle v)}, & \xi \leq 1, \\ 0, & \xi > 1. \end{cases} \tag{5.3.15}$$

The scaling here ensures that the momentum flux of total oil fraction, M_Φ, given by (4.3.6), is satisfied. The constants M_Φ, β, ω_0 and δ_0 are set as in Chapters 2 and 4.

At $z = \hat{z}$, with $\hat{z} = 5$, we extract the value of s_2, the momentum flux, from the numerics and then use the formula (5.3.11) for the similarity solution for ϕ_2. The variation of ϕ_2 with ξ, from both the numerics and similarity solution, is plotted in Figure 5.8 for $z = 10$ and $z = 50$. We observe that the similarity solution agrees very well with the numerics, despite the assumption that the coefficients of the higher eigenvalue terms are negligible. This is because, by $z = \hat{z}$, the flow has developed enough that ϕ_2 has become self-similar and qualitatively resembles $h_2^1(\xi)$. The h_2^n for different n are orthogonal and so, if ϕ_2 at $\delta = \hat{\delta}$ is close to $h_2^1(\xi)$, then the other higher eigenvalue terms must make small contributions to ϕ_2 at $\delta = \hat{\delta}$. This observation gives us confidence to proceed with this approach. Nevertheless, we must note that, if we took values of $\hat{z}$ close to $\hat{z}_n$, we would not expect the agreement, especially at small heights, to be as good because ϕ_2 would not yet be self-similar. This is a consequence of the way we construct ϕ_2. We illustrate the issues which arise in this case and how they can be resolved in Section 5.4.

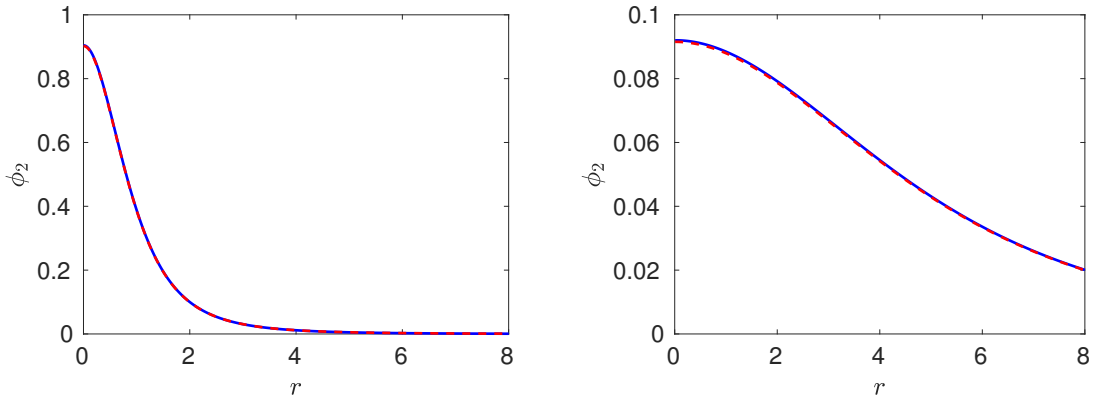
Now that we have determined ϕ_2, using (5.3.2), we find that

$$\phi_1 = \frac{\Phi_0 \delta_0}{(\triangle v)\left(1+\xi^2\right)^2} \frac{1}{\delta} - C_{22} h_2(\xi) \frac{1}{(\delta/\hat{\delta})^{m_2}} \triangle v. \tag{5.3.16}$$

To leading order in z, since $m_2 > 1$, the volume fraction of small drops, $\phi_1 \triangle v$ is equal to the leading order total oil fraction, Φ. This corresponds to the fact that, at large enough heights, all the drops ultimately break into small droplets. The second term in (5.3.16) tells us about the behaviour at intermediate heights, where the volume fraction of small droplets is increasing due to the break up of large drops.

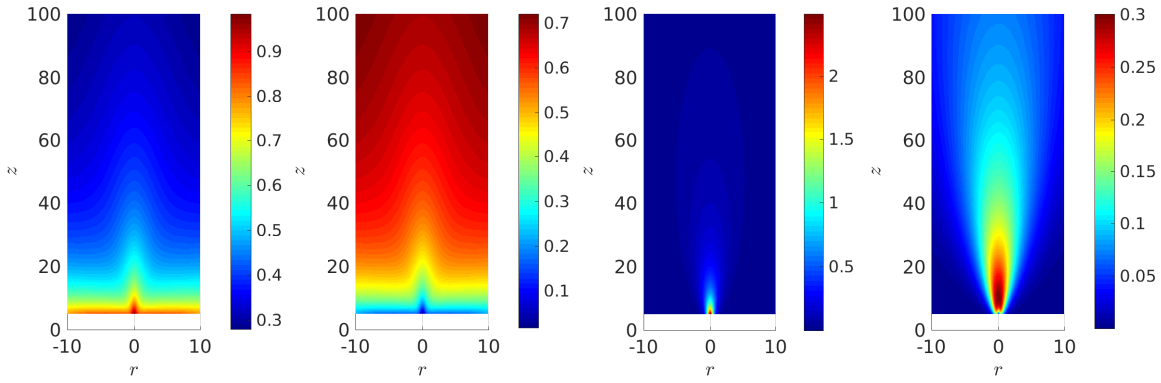
The behaviour of $\phi_2(\xi, z)$ and $\phi_1(\xi, z)$ is plotted in Figure 5.9. We set $\hat{z} = 5$ and assume that most of the oil drops here are large so, from (5.3.8), $s_2 = 0.9 M_\Phi/(\triangle v)$ and $s_1 = 0.1 M_\Phi/(\triangle v)$. We take the breakup rate K_2 as $K_2 = 1$.

Figures 5.9(a)–(b) illustrate the volume fraction of large and small drops respectively, normalised to eliminate the effects of dilution. We see that large drops are



(a) $z = 10$ (b) $z = 50$

Figure 5.8: Similarity solution to (5.3.1) for ϕ_2 compared to numerical solution. At $z = 2$, we set ϕ_2 as in (5.3.15) and solve numerically for $z > 2$ (in blue). This is compared with solving numerically for $z \in [2, 5]$ and then using the similarity solution for $z > 5$ (in red). We set $K_2 = 1$. The variation of drop size distribution with ξ is plotted at fixed values of z, namely (a) $z = 10$ and (b) $z = 50$.



(a) $\phi_2 \triangle v/\Phi$ (b) $\phi_1 \triangle v/\Phi$ (c) ϕ_2 (d) ϕ_1

Figure 5.9: Similarity solution for drop size distribution in the two bin case. The spatial variations of ϕ_2 and ϕ_1 are plotted. We consider the distributions normalised by Φ to eliminate the effect of dilution in (a)–(b) and include the effect of dilution in (c)–(d). (a) Volume fraction of large drops normalised with Φ, given by $\phi_2 \triangle v/\Phi$; (b) volume fraction of small drops normalised with Φ, given by $\phi_1 \triangle v/\Phi$; (c) volume fraction distribution of large drops including dilution effects, given by ϕ_2; (d) volume fraction distribution of small drops including dilution effects, given by ϕ_1. We take the breakup rate parameter $K_2 = 1$, set $\hat{z} = 5$, and $s_1 = 0.1 M_\Phi/\triangle v$ and $s_2 = 0.9 M_\Phi/\triangle v$.

breaking up into small drops; the volume fraction of large drops decreases with increasing height and width, whilst that of the small drops increases. Figures 5.9(c)–(d) show the combined effects of breakup, which is significant at smaller heights, and dilution, which dominates further up the jet. We see in Figure 5.9(d) that, with increasing height, ϕ_1 reaches a maximum and then, for greater heights, decreases as the effect of dilution dominates over the breakup of the large drops. This phenomenon was also seen in the width-averaged two-bin models of Section 4.5.3.

The simple two-bin approach followed in this section yields similarity solutions which provide a great deal of intuition into the physical effects at play and agree well with numerical results. We, therefore, now extend this approach by investigating a three-bin model.

5.3.2 Three bins

We now consider the case where there are three possible droplet volumes. Large drops have volume v_3. Medium drops, with volume v_2, are formed when drops of volume v_3 break up. In turn, the medium drops, as well as the large drops, break into small droplets of volume v_1. These smallest droplets do not break up.

The volume distribution of the largest drops, ϕ_3, satisfies (5.1.13) with $N = 3$ and $i = 3$, which gives the same problem as the largest drops in the two bin case (5.3.1), but with breakup rate K_3 instead of K_2. Thus, by an identical argument to that in Subsection 5.3.1 it has a second kind similarity solution given by

$$\phi_3 = \frac{C_{33} h_3(\xi)}{(\delta/\hat{\delta})^{m_3}} \triangle v, \tag{5.3.17}$$

where m_3 and $h_3(\xi)$ are the smallest eigenvalue and corresponding eigenfunction of the linear operator $L[K_3]$, satisfying (5.2.2)–(5.2.3). Here h_3 is normalised such that,

$$\int_0^\infty \frac{\xi h_3}{(1+\xi^2)^2}\,\mathrm{d}\xi = 1, \tag{5.3.18}$$

as in (5.3.9). We evaluate C_{33} by setting the volume flux of large drops at $\delta = \hat{\delta}$ equivalently to (5.3.12), i.e.

$$C_{33} \triangle v = S_3, \tag{5.3.19}$$

with $S_3 = \beta s_3/(\hat{\delta}\omega_0\delta_0)$, where $s_3 = \int_0^\infty rW\phi_3\,\mathrm{d}r$ at $\delta = \hat{\delta}$. Once we have determined ϕ_2, it is straightforward to use mass conservation to find

$$\phi_1 = \frac{\Phi}{\triangle v} - \phi_2 - \phi_3. \tag{5.3.20}$$

How then do we determine a self-similar solution for ϕ_2? The volume fraction distribution, ϕ_2, satisfies (5.1.13) with $N = 3$ and $i = 2$, which, using (5.3.17), can be written as

$$L[0]\phi_2 + K_2\frac{\xi^2}{1+\xi^2}\phi_2 + \frac{\xi\delta}{\alpha}\frac{d\phi_2}{dz} = K_3\chi_{23}C_{33}\frac{\xi^2 h_3(\xi)}{1+\xi^2}\frac{1}{(\delta/\hat{\delta})^{m_3}}(\triangle v)^2. \tag{5.3.21}$$

The appearance of δ^{-m_3} in the last term of (5.3.21) suggests that we cannot simply take ϕ_2 to have a form proportional to δ^{-m_2}, similar to (5.3.11) and (5.3.17). In fact, motivated by the expression, (5.3.16), for ϕ_1 in the two bin case, we look for solutions of the form

$$\phi_2 = \left[\frac{C_{22}\ h_2(\xi)}{(\delta/\hat{\delta})^{m_2}} + \frac{C_{23}\ h_{23}(\xi)}{(\delta/\hat{\delta})^{m_3}}\right]\triangle v, \tag{5.3.22}$$

where m_3 is the lowest eigenvalue of $L[K_3]$ and the constants m_2, C_{22} and C_{23}, and functions $h_2(\xi)$ and $h_{23}(\xi)$ are to be determined.

Using (5.3.22) in (5.3.21), and separating out the δ^{-m_3} and δ^{-m_2} terms, we obtain

$$L[K_2]h_2 = m_2\xi h_2 \tag{5.3.23}$$

and

$$L[K_2]h_{23} = m_3\xi h_{23} + K_3\chi_{23}\frac{C_{33}}{C_{23}}\frac{\xi^2 h_3(\xi)}{1+\xi^2}\triangle v. \tag{5.3.24}$$

From (5.3.23), we deduce that m_2 and h_2 are the smallest eigenvalue and corresponding eigenfunction of $L[K_2]$. We again normalise so that $\int_0^\infty \xi h_2/(1+\xi^2)^2\,\mathrm{d}\xi = 1$.

We rewrite equation (5.3.24) as

$$L[K_3]h_{23} - m_3\xi h_{23} = \frac{\xi^2}{1+\xi^2}\left[\frac{C_{33}}{C_{23}}K_3\chi_{23}(\triangle v)h_3 - (K_2 - K_3)h_{23}\right] \tag{5.3.25}$$

and compare with the eigenvalue equation, (5.2.1), for $L[K_3]$, namely $L[K_3]h_3 = m_3\xi h_3$. Then it is clear that a particular solution for h_{23} is

$$h_{23} = h_3 \tag{5.3.26}$$

when C_{23} is chosen such that

$$C_{23} = \frac{C_{33}K_3\chi_{23}\triangle v}{K_2 - K_3}. \tag{5.3.27}$$

Therefore,

$$\phi_2 = \left[\frac{C_{22}\ h_2(\xi)}{(\delta/\hat{\delta})^{m_2}} + \frac{C_{23}\ h_3(\xi)}{(\delta/\hat{\delta})^{m_3}}\right]\triangle v \tag{5.3.28}$$

is a self-similar solution to (5.3.21).

We finally fix C_{22} so that at $\delta = \hat{\delta}$, the volume flux of drops of size v_2 is given by $\int_0^\infty rW\phi_2 \,\mathrm{d}r \;=\; s_2$. Hence

$$(C_{22} + C_{23})\triangle v = S_2, \tag{5.3.29}$$

where $S_2 = \beta s_2/(\hat{\delta}\delta_0\omega_0)$ so

$$C_{22}\triangle v = S_2 - \frac{S_3 K_3 \chi_{23}\triangle v}{K_2 - K_3}. \tag{5.3.30}$$

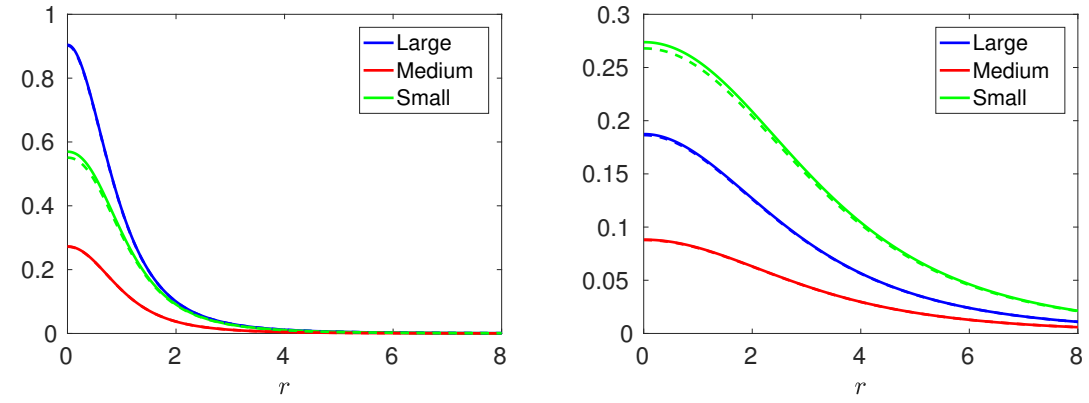
We have found self-similar solutions for $\phi_i(\xi, z)$ in the three bin case and, as in Section 5.3.1, we now verify whether they agree with numerical solutions for sufficiently large z. To do so we numerically solve (5.1.13) for the case $N = 3$, as discussed for the $N = 2$ case in Section 5.3.1. We use the similarity solutions for the velocity components and the approximation to the similarity solution for the energy dissipation rather than their full numerical solutions so that we are not picking up on errors in these quantities and only assessing the suitability of our similarity solutions for ϕ_i. For the numerical solution we solve for $z > \hat{z}_n$ with $\hat{z}_n = 2$, imposing the boundary condition at $z = \hat{z}_n$ that $\phi_1 = \phi_2 = 0$ and ϕ_3 is given by (5.3.15). For the similarity solution, at $z = \hat{z}$, with $\hat{z} = 5$, we extract the values of s_2 and s_3 from the numerics and then use the formulae (5.3.17), (5.3.28) and (5.3.20) for similarity solutions for ϕ_3, ϕ_2 and ϕ_1, respectively.

We assume K is given by (5.1.16) and χ is uniform, as in (3.2.24). This sets $K_i = v_i^{-1/2}$ and $\chi_{ij} = 1/v_{j-1}$. Note the unusual discretisation of χ_{ij} comes from the discretised version of (4.2.8), namly $\sum_{i=1}^{j-1} \chi_{ij}\triangle v = 1$, and ensures the total volume of oil droplets is conserved.

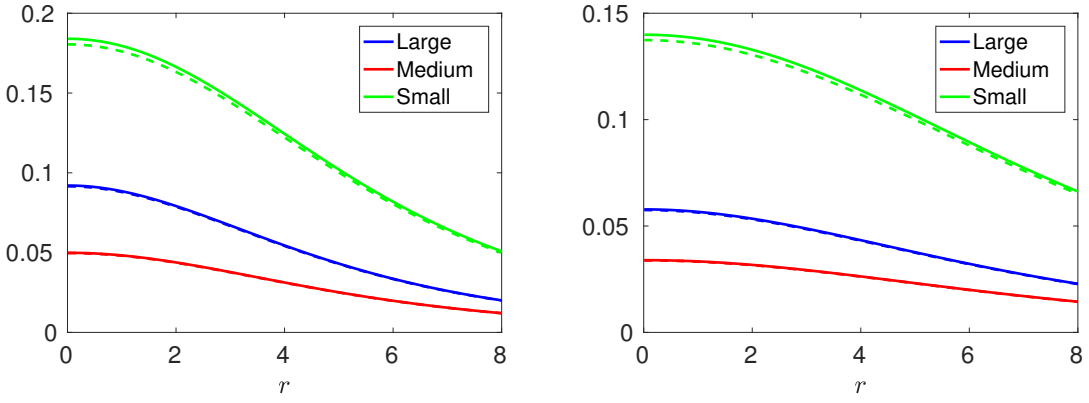
The variations of the drop size distributions, ϕ_i, with radial co-ordinate r, at fixed heights, is shown in Figure 5.10. Note that here we have not normalised to remove dilution effects so the range of the y-axis decreases with increasing z. The drop size distribution for the bins of volume v_1 agree the least well. Nonetheless, there is generally good agreement between the numerics and similarity solution which suggests the form of the similarity solution is appropriate.

5.3.3 N bins

The good agreement between the numerics and the similarity solutions for the two and three bin cases gives us confidence to extend this approach for a general number



(a) $z = 10$ (b) $z = 30$



(c) $z = 50$ (d) $z = 70$

Figure 5.10: Similarity solution for drop size distribution in the three bin case compared with numerical solution to (5.1.13). We take the parameters $\hat{z}_n = 2$, $\hat{z} = 5$, $K_i = v_i^{-1/2}$ and $\chi_{ij} = 1/v_{j-1}$. We assume that the velocity field is as determined by the similarity solutions in Chapter 2 and, in the breakup rate, use the approximate energy dissipation. At $z = \hat{z}_n$ we set $\phi_1 = \phi_2 = 0$ and take ϕ_3 to be (5.3.15). We solve numerically for $z > \hat{z}_n$. This is compared with solving numerically for $z \in [\hat{z}_n, \hat{z}]$ and then, using the similarity solution, for $z > \hat{z}$. The variation of drop size distribution ϕ_i with r is plotted at fixed values of z, namely (a) $z = 10$; (b) $z = 30$; (c) $z = 50$; (d) $z = 70$.

of bins N. In general, as in (5.3.28), we set

$$\phi_i = \sum_{j=i}^{N} \frac{C_{ij}\ h_j(\xi)\triangle v}{\left(\delta(z)/\hat{\delta}\right)^{m_j}}. \tag{5.3.31}$$

The eigenvalue m_i and corresponding eigenfunction $h_i(\xi)$ are found by solving the eigenproblem (5.2.2)–(5.2.3) as in Section 5.2 for different values of the breakup rate parameter K_i. We consider only the smallest eigenvalue and its corresponding eigenfunction for each K_i and normalise $h_i(\xi)$ such that

$$\int_0^\infty \frac{\xi h_i}{(1+\xi^2)^2}\,\mathrm{d}\xi = 1. \tag{5.3.32}$$

Following the procedure demonstrated above with $N = 3$, we find that the constants C_{ij} are determined by the recurrence relations:

$$C_{ij} = \frac{\sum_{k=i+1}^{j} C_{kj}K_k\chi_{ik}\triangle v}{K_i - K_j}, \tag{5.3.33}$$

for $i < j$ and

$$S_i = \sum_{j=i}^{N} C_{ij}\triangle v, \tag{5.3.34}$$

where the total flux of drops of volume v_i at $z = \hat{z}$ is $\int_0^\infty rW\phi_i dr = s_i$, with $S_i = \beta s_i/(\hat{\delta}\omega_0\delta_0)$. For $i > j$, $C_{ij} = 0$. Here (5.3.33) depends on the choice of breakup rate through K and χ, and (5.3.34) is determined by matching to the non-self- similar region near the jet nozzle. Since $C_{ij} = 0$ for $i > j$, the recurrence relations (5.3.33)–(5.3.34) are easily solved by back substitution, as illustrated in Figure 5.11.

5.3.4 Continuous distribution

Discretising volume as in Sections 5.3.1–5.3.3 is insightful. However, the real problem ((5.1.11)–(5.1.12)) is continuous in the volume variable v. This corresponds to taking the limit $N \to \infty$ in the discrete formulation, where N is the number of discrete volumes. The continuous limit of (5.3.31) as $N \to \infty$, is

$$\phi(v,\xi,z) = \int_v^1 \frac{C(v,\tilde{v})\ h(\tilde{v},\xi)}{\left(\delta(z)/\hat{\delta}\right)^{m(\tilde{v})}}\,\mathrm{d}\tilde{v}, \tag{5.3.35}$$

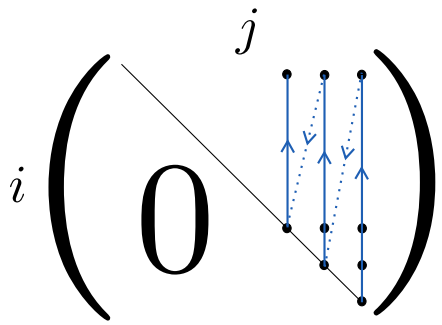


Figure 5.11: Schematic showing the order in which we solve the C_{ij} using recurrence relations (5.3.33)–(5.3.34).

and so we look for solutions of this form. Note that, in writing (5.3.35), we have implicitly assumed that the largest drops, with volume $v = 1$, are big enough that $\phi(v, \xi, z) = 0 \; \forall v \geq 1$.

Substituting the ansatz (5.3.35) into (5.1.11) and rearranging yields

$$\int_v^1 \frac{C(v,\tilde{v})}{\left(\delta(z)/\hat{\delta}\right)^{m(\tilde{v})}} \left[L[K(\tilde{v})]h(\tilde{v}) - m(\tilde{v})\xi h(\tilde{v})\right] - \frac{C(v,\tilde{v})}{\left(\delta(z)/\hat{\delta}\right)^{m(\tilde{v})}} \frac{\xi^2 h(\tilde{v},\xi)}{(1+\xi^2)} \left[\int_v^{\tilde{v}} K(s)\chi(v,s)\frac{C(s,\tilde{v})}{C(v,\tilde{v})}ds - (K(v) - K(\tilde{v}))\right] \mathrm{d}\tilde{v} = 0. \tag{5.3.36}$$

So that (5.3.36) is satisfied identically for all (v, ξ, z), we set the two terms in square brackets to zero. Therefore, $h(\tilde{v}, \xi)$ satisfies

$$L[K(\tilde{v})]h(\tilde{v}) - m(\tilde{v})\xi h(\tilde{v}) = 0. \tag{5.3.37}$$

As in the discrete case, (5.3.37) is just the eigenproblem, (5.2.2)–(5.2.3), for the operator $L[K(\tilde{v})]$. Given $K(\tilde{v})$, it can be solved as in Section 5.2 to find the eigenvalue $m(\tilde{v})$ and eigenfunction $h(\tilde{v}, \xi)$. We have the freedom to normalise h and do so by imposing

$$\int_0^\infty \frac{\xi h(\tilde{v},\xi)}{(1+\xi^2)^2} \mathrm{d}\xi = 1. \tag{5.3.38}$$

Note that we take the smallest eigenvalue of (5.3.37) here as this corresponds to the larger terms at large z.

In addition, setting the second term in square brackets to zero in (5.3.36) yields

$$C(v,\tilde{v}) = \int_v^{\tilde{v}} \frac{K(s)\chi(v,s)C(s,\tilde{v})}{K(v) - K(\tilde{v})} ds, \tag{5.3.39}$$

for $v < \tilde{v}$. Taking the limit $v \to \tilde{v}$ and using l'Hopital's rule, we find that $C(v, v)$ must be zero.

Now the solution to (5.3.39) can be multiplied by any function of $\tilde{v}$ and still satisfy (5.3.39). Therefore, we need another condition. We impose a matching condition with the non-self-similar entry region, as in the discrete case. We set the volume flux, $s(v)$, of drops of volume v at $\delta = \hat{\delta}$ so

$$\int_0^\infty rW(r, \hat{z})\phi(v, r, \hat{z})\,\mathrm{d}r = s(v). \tag{5.3.40}$$

In terms of the similarity variable ξ, this yields

$$\int_0^\infty \frac{\xi\phi(v, \xi, \hat{z})}{(1+\xi^2)^2}\,\mathrm{d}\xi = S(v), \tag{5.3.41}$$

where $S(v) = \beta s(v)/(\hat{\delta}\omega_0\delta_0)$. Here $s(v)$ and $S(v)$ are equivalent to the discrete variables s_i and S_i. Note that for conservation of the flux of oil droplets at $\delta = \hat{\delta}$, from (4.3.6), s must satisfy

$$\int_0^1 s\,\mathrm{d}v = M_\Phi \tag{5.3.42}$$

or

$$\int_0^1 S\,\mathrm{d}v = \frac{M_\Phi\beta}{\hat{\delta}\delta_0\omega_0}, \tag{5.3.43}$$

where M_Φ is the constant total flux of oil, namely $M_\Phi = \int_0^\infty rW\Phi\,\mathrm{d}\xi$. Substituting (5.3.35) into (5.3.41) and using (5.3.38) yields

$$\int_v^1 C(v, \tilde{v})\,\mathrm{d}\tilde{v} = S(v). \tag{5.3.44}$$

5.3.4.1 An analytical solution

We can calculate $C(v, \tilde{v})$ analytically in the case where $K(v) = v^{-1/2}$ and $\chi(v, \tilde{v}) = 1/\tilde{v}$. Using these specific choices, (5.3.39) becomes

$$C(v, \tilde{v}) = \int_v^{\tilde{v}} \frac{s^{-3/2}}{(v^{-1/2} - \tilde{v}^{-1/2})} C(s, \tilde{v})ds \tag{5.3.45}$$

and, differentiating with respect to v, we obtain the solution

$$C(v, \tilde{v}) = A(\tilde{v})B(v, \tilde{v}) = A(\tilde{v})\left[\left(\frac{\tilde{v}}{v}\right)^{1/2} - 1\right], \tag{5.3.46}$$

where $A(\tilde{v})$ is to be determined.

To find $A(\tilde{v})$, we use the matching condition (5.3.41). We find $A(\tilde{v})$ is implicitly given by

$$S(v) = \int_v^1 A(\tilde{v}) \left[\left(\frac{\tilde{v}}{v} \right)^{1/2} - 1 \right] \mathrm{d}\tilde{v}. \tag{5.3.47}$$

For illustrative purposes, at $z = \hat{z}$, we choose, say

$$\phi(v, \xi, \hat{z}) = \begin{cases} \frac{48 M_\Phi \beta}{\hat{\delta}\omega_0 \delta_0} v(1-v)^2, & \xi \leq 1, \\ 0, & \xi > 1, \end{cases} \tag{5.3.48}$$

where the constant of proportionality here has been chosen so that the conserved total flux of oil is M_Φ. This choice sets

$$S(v) = \frac{12 M_\Phi \beta}{\hat{\delta}\omega_0 \delta_0} v(1-v)^2, \tag{5.3.49}$$

which we note satisfies (5.3.43). Then differentiating (5.3.47) twice, it has solution

$$A(\tilde{v}) = \frac{12 M_\Phi \beta}{\hat{\delta}\omega_0 \delta_0} \left(3 - 20\tilde{v} + 21\tilde{v}^2 \right), \tag{5.3.50}$$

giving

$$C(v, \tilde{v}) = \frac{12 M_\Phi \beta}{\hat{\delta}\omega_0 \delta_0} \left(3 - 20\tilde{v} + 21\tilde{v}^2 \right) \left[\left(\frac{\tilde{v}}{v} \right)^{1/2} - 1 \right]. \tag{5.3.51}$$

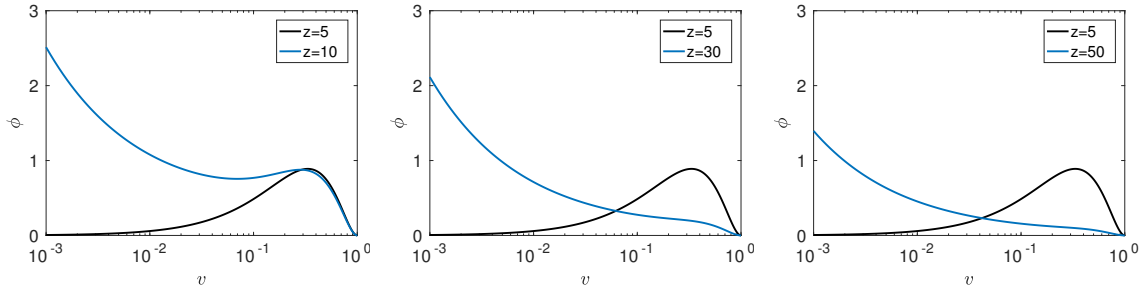
and

$$\phi(z, \xi, v) = \int_v^1 \frac{12 M_\Phi \beta}{\hat{\delta}\omega_0 \delta_0} \left(3 - 20\tilde{v} + 21\tilde{v}^2 \right) \left[\left(\frac{\tilde{v}}{v} \right)^{1/2} - 1 \right] h(\xi, \tilde{v}) \frac{1}{\left(\delta(z)/\hat{\delta} \right)^{m(\tilde{v})}} \mathrm{d}\tilde{v}. \tag{5.3.52}$$

The solution (5.3.52) is illustrated in Figure 5.12. To calculate the integral in (5.3.52), we discretise based on diameter and use the trapeziodal rule. We see that, with increasing height, the drops break up and eventually the mode drop size becomes very small. In fact, at larger heights ϕ seems to reach a maximum at $v = 0$. This is because the breakup rate we use, $K(v) = v^{-1/2}$ is singular as $v \to 0$.

Because of the singularity in the breakup rate at $v = 0$, it is important to check that we conserve mass in (5.3.52). Taking the integral over all volumes v and rearranging, we find that the total oil fraction is given by

$$\int_0^1 \phi \, \mathrm{d}v = \int_0^1 \frac{12 M_\Phi \beta}{\hat{\delta}\omega_0 \delta_0} \left(3 - 20\tilde{v} + 21\tilde{v}^2 \right) \tilde{v} h(\xi, \tilde{v}) \frac{1}{\left(\delta(z)/\hat{\delta} \right)^{m(\tilde{v})}} \mathrm{d}\tilde{v}. \tag{5.3.53}$$



(a) $z = 10$ (b) $z = 30$ (c) $z = 50$

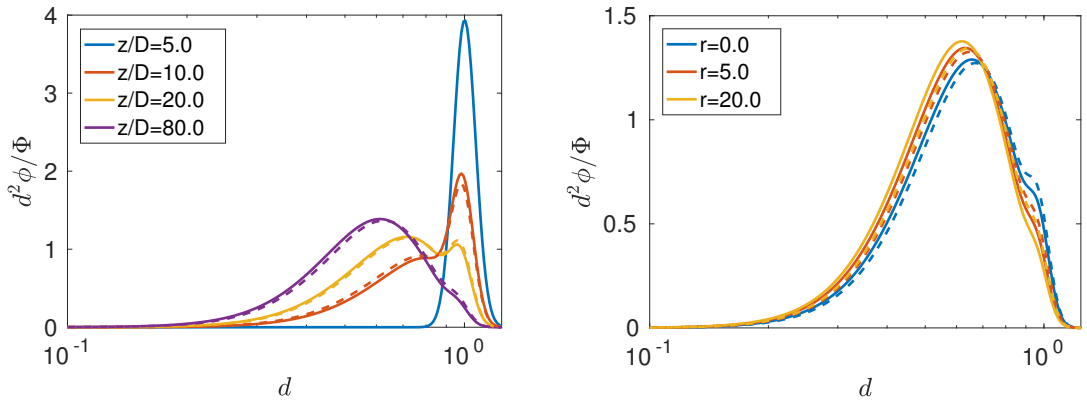
Figure 5.12: Analytic continuous volume similarity solution for breakup rate $K(v) = v^{-1/2}$ and $\chi(v, \tilde{v}) = 1/\tilde{v}$. At $\hat{z} = 5$, we set ϕ according to (5.3.48). The drop size distribution ϕ is plotted in blue for fixed $r = 0.1$ at non-dimensional heights (a) $z = 10$; (b) $z = 30$; (c) $z = 50$. In each plot we also illustrate the initial distribution (5.3.48) in black.

This can be calculated numerically and we find fairly good agreement with Φ given by (5.1.4) for heights up to $z \approx 40$. However, there is some error here. This can be partially attributed to the truncation of eigenvalues. Nevertheless, much of the error probably arises from our numerical discretisation of drop size. With increasing height, as the behaviour of very small drop sizes becomes more important, discretising based on diameter misses more of the important drop sizes. To eliminate this we would have to use a drop size discretisation which takes the behaviour of the singularity in $K(v)$ into account.

5.3.4.2 Similarity solution compared to numerics

In most cases, even when limited to only monotonic breakup rate functions, we will not be able to find analytic solutions like (5.3.52) to the continuous problem. Nonetheless, in general, to calculate ϕ we just need to solve (5.3.39)–(5.3.44) for $C(v, \tilde{v})$ and we can do so numerically. In the integrals, drop size is discretised into N bins (similar to the formulation in Subsection 5.3.3) except, instead of v, we generally discretise with d or $d^{1/2}$ to be able to capture a greater range of droplet sizes without significantly increasing N.

As in Sections 5.3.1 and 5.3.2, we validate the continuous volume approximate similarity solution by comparing with numerical solutions to ϕ. We solve for ϕ numerically using the same approach as in Section 4.4.1. We discretise volume using $d^{1/2}$, as in Section 4.4.1, and take 200 volume bins. In the numerics, we use the similarity solutions for velocity field and the approximate dissipation in the breakup rate (5.1.5). The breakup rate is set so $K = 5v$ and χ is given by (3.2.32). At $z = \hat{z}_n = 5$



(a) Fixed $r = 0.1$ (b) Fixed $z = 40$

Figure 5.13: Comparison of similarity solution for ϕ_i (dotted line) with full numerical results (full line). We consider different heights at fixed $r = 0.1$ in (a) and different widths at fixed $z = 40$ in (b). We set $K = 5v$ and the daughter size distribution as (3.2.32). The initial condition for ϕ at $z = \hat{z}_n = 5$, for the numerics, is given by (4.4.5), and the similarity solution is used from $\hat{z} = 10$.

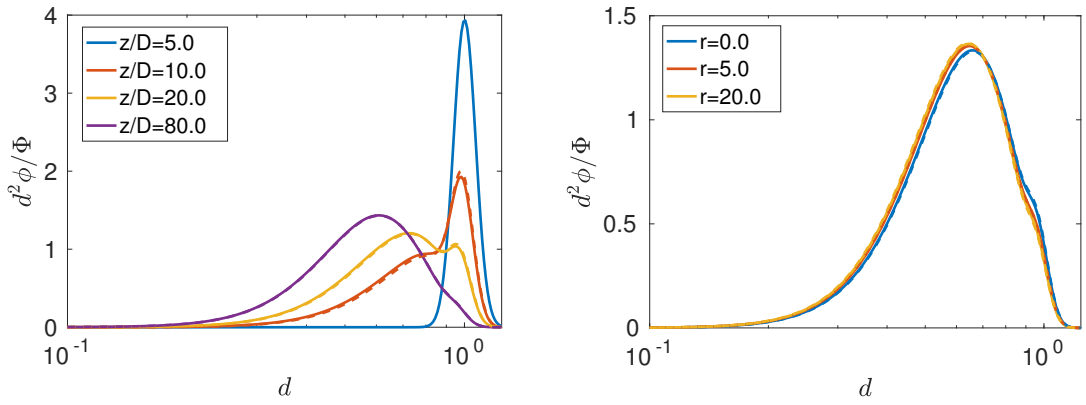
we assume ϕ has a lognormal distribution (4.4.5), where μ_v and σ_v are set such that the mode diameter of the distribution is $4/5\,(6/\pi)^{1/3}$ and variance is $1/300\,(6/\pi)^{1/3}$. The largest dimensional drop diameter is taken to be $d_\infty = D$.

For $z > \hat{z}$, where $\hat{z} = 10$, we take the flux of oil droplets at this height from the numerics, namely $s(v)$, and use it to compute the similarity solution (5.3.35). We calculate the volume integrals in (5.3.35) by discretising drop size using $d^{1/2}$.

The similarity solution for ϕ is compared to the numerics in Figure 5.13. We plot the variation of $d^2\phi/\Phi$ with drop diameter at fixed $r = 0.1$, with increasing height, in Figure 5.13(a), and at fixed $z = 40$, with increasing width, in Figure 5.13(b). (The quantity $d^2\phi/\Phi$ is used since, as mentioned in Sections 3.3 and 4.4.1, we want to eliminate the effects of dilution and also we want to illustrate the volume fraction of drops, given by $\phi\,\mathrm{d}v \propto d^2\phi\,\mathrm{d}d$.) Although this is a more complicated model than the two or three bin ones in Sections 5.3.1–5.3.2, there is similarly good agreement here between the similarity solution and numerics.

5.3.5 Discussion

In this section we have examined the simplest possible problem for ϕ. In the breakup rate, we have approximated the similarity solution for the energy dissipation, as described in Section 5.1.3.1. We have also assumed that $K(v)$, the volume dependent term in the breakup rate, is monotonic as outlined in Section 5.1.3.3. Using these two



(a) Fixed $r = 0.1$ (b) Fixed $z = 40$

Figure 5.14: Comparison of similarity solution for ϕ_i (dotted line) with full numerical results (full line). In both we use the true similarity solution for ϵ. We consider (a) different heights at fixed $r = 0.1$ and (b) different widths at fixed $z = 40$. We set $K = 5v$ and the daughter size distribution as (3.2.32). The initial condition for ϕ at $z = \hat{z}_n = 5$, for the numerics, is given by (4.4.5), and the similarity solution is used from $\hat{z} = 10$.

assumptions we have found the similarity solution for $\phi(v, \xi, z)$, the drop size distribution of drops of volume v. It is given by a linear superposition of eigenfunctions, each of which corresponds to the advection and breakup of the droplets with size equal to or larger than v. These similarity solutions are approximate in the sense that, for each of the drop sizes larger than or equal to v, there are an infinite set of possible eigenfunctions but we have only taken the one corresponding to the smallest eigenvalue. Despite this approximation, our results agree well with numerical solutions for ϕ.

5.3.5.1 Using true similarity solution for ϵ

We now briefly discuss what difference is made to the solution procedure outlined above when using the similarity solution for the dissipation rather than the approximation (2.4.35). In calculating the self-similar form of ϕ using (5.3.35), the energy dissipation only appears in the eigenproblem (5.3.37) for finding the eigenfunction $h(v, \xi)$ and corresponding eigenvalue $m(v)$. Thus the only change when using the real dissipation is in the eigenproblem, which was examined in Section 5.2.4. Recall that, because the approximation underestimates dissipation rate (as seen in Figure 2.4), the eigenvalues $m(v)$ (which correspond to the exponents of $\delta(z)^{-1}$ in (5.3.35)) are slightly underestimated (see Figure 5.5). Thus, we expect the approximation will

underestimate droplet breakup and predict slightly larger drops.

We ask the question of how this difference translates to the similarity solution for ϕ and whether this affects the accuracy of the similarity solution. To do so we compare the similarity solution, using the true energy dissipation, to the numerics. This is identical to the comparison in Section 5.3.4.2 except we use the true similarity solution for ϵ in the breakup rate rather than the approximation. In Figure 5.14, as in Figure 5.13, we plot $d^2\phi/\Phi$ for various heights at fixed $r = 0.1$, and for various widths at fixed $z = 40$.

We see that the similarity solution and numerics agree well. In addition, a comparison of Figure 5.14 with Figure 5.13 indicates that using the approximate dissipation predicts fewer smaller drops and more larger drops. At $z = 80$, using the approximate dissipation, the mode drop size is around $d = 0.6$ whereas, using the true similarity solution for ϵ predicts this as $d = 0.5$.

In fact, using the true similarity solution for ϵ agrees well with the numerics and is not actually significantly more difficult to implement. Nonetheless, we present results when using the approximate ϵ for the rest of this chapter as the resulting problem is more straightforward to understand.

5.3.5.2 Comparing to full CFD numerics

Now that we have examined the full problem, (5.1.8)–(5.1.9), which uses the true similarity solution for the dissipation, we are in a position to compare our similarity solution to the full numerics. Thus far, in comparing to the numerical solution for ϕ, we have only used the similarity solutions for the velocity field and energy dissipation. This ensures we are only evaluating the appropriateness of the similarity solution for ϕ. Before we move on, it is interesting to compare the full numerics, using the CFD numerics for the velocity fields and energy dissipation, to the similarity solution. We do so in Figure 5.15. Here we again use the same breakup rates as in Section 5.3.4.2 and the same initial condition except here we impose it at $z = 0$ rather than $z = \hat{z}_n$. In Figures 5.15(a)–(b), we begin computing the similarity solution at $\hat{z} = 5$. For Figures 5.15(c)–(d) we set $\hat{z} = 8$.

Let us first consider the results in Figures 5.15(a)–(b). As expected, there are some differences between the similarity solution for ϕ and numerics. Here the similarity solution predicts slightly smaller droplets than the numerics. These additional discrepancies come about because, at smaller heights, the similarity solution for the energy dissipation over-predicts the numerics. The discrepancies here are similar to those seen in Section 4.4.5, where the numerical solution for ϕ is compared when

using the numerical CFD for the velocity fields and dissipation, and when using their similarity solutions. Nonetheless, in Figures 5.15(a)–(b), we observe generally good agreement between the similarity solution and the full numerics, which improves with increasing z. In Figures 5.15(c)–(d), where we instead start the similarity solution slightly higher up, at $\hat{z} = 8$, there is very good agreement between the similarity solution and the full numerics. This is not unexpected - the similarity solutions are, by construction, more appropriate for larger heights.

5.3.5.3 Limitations

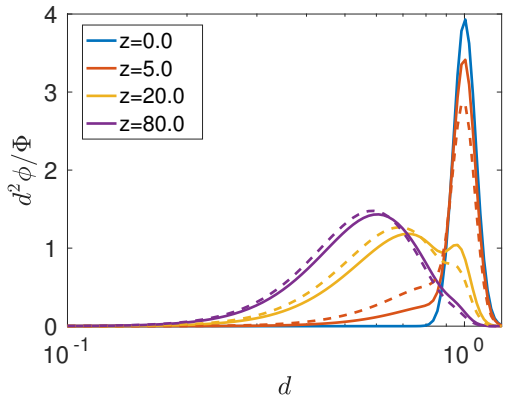
There are two main issues with the approach in this section. The first is that the procedure only works when the breakup rate, $K(v)$, is monotonic since the equation (5.3.39) for the coefficients is singular for repeated values of K. In Section 5.5, this limitation will be further discussed and the solution will be modified for non-monotonic K. The second issue is that, for each value of K, we have neglected all but the smallest eigenvalue and its corresponding eigenfunction. Generally this approach works well and agrees closely with the numerics. However, there are some inaccuracies and inconsistencies here. These inaccuracies have not been so apparent in the numerical comparisons in this section because we consistently match the similarity solution some way downstream of the height, $\hat{z}_n$, at which the numerics begins. This is because, by construction, we do not expect the similarity solutions to accurately replicate the behaviour at smaller heights, where the self-similarity of ϕ has not yet developed. The inaccuracy at smaller heights is discussed in detail in Section 5.4, in particular see Section 5.4.5. In Section 5.4 we address this and other issues with the approximate similarity solution and resolve them by considering the full solution.

5.4 Full solutions

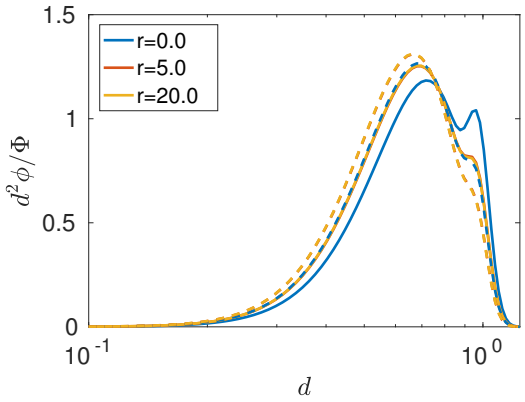
In this section, we seek the full solution for ϕ when K is monotonic. We no longer neglect higher eigenvalue terms and also do not make any assumptions about the self-similar form of ϕ. Before proceeding, let us discuss why the higher eigenvalue terms are necessary and what exactly are the inaccuracies and inconsistencies which come from neglecting the higher eigenvalue terms.

5.4.1 Drawback of the assumptions made in Section 5.3

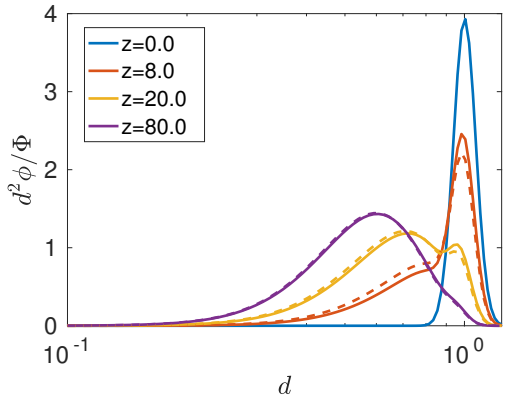
In Section 5.3, we express the drop size distribution, $\phi(v, \xi, z)$, of drops of volume v, with breakup rate $K(v)$, as a function of $h(K(v), \xi)$. For fixed $K(v)$, there are



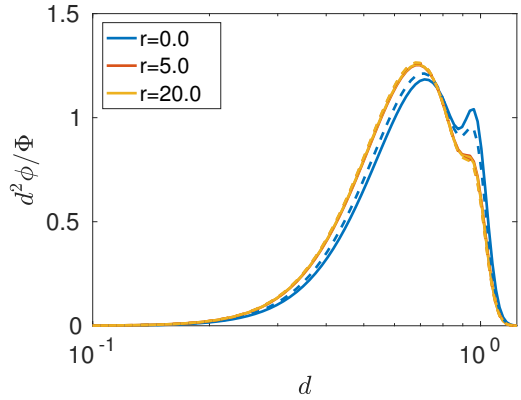
(a) $\hat{z} = 5$, fixed $r = 0.1$



(b) $\hat{z} = 5$, fixed $z = 20$



(c) $\hat{z} = 8$, fixed $r = 0.1$



(d) $\hat{z} = 8$, fixed $z = 20$

Figure 5.15: Comparison of similarity solution for ϕ (dotted line) with full numerical results using CFD numerics for the velocity fields and ϵ (full line). In the similarity solution we use the true similarity solution for ϵ. We set $K = 5v$ and the daughter size distribution as (3.2.32). The initial condition for ϕ at $z = 0$, for the numerics, is given by (4.4.5), and the similarity solution is used from $\hat{z} = 5$ in (a)–(b) and from $\hat{z} = 8$ in (c)–(d). We consider different heights at fixed $r = 0.1$ in (a) and (c) and different widths at fixed $z = 20$ in (b) and (d).

an infinite number of eigenvalues $m^n(K)$ and eigensolutions $h^n(K,\xi)$ for $n = 1, 2, \cdots$. However, in Section 5.3 we have only considered the smallest eigenvalue and its corresponding eigensolution. This is because they produce terms which decay most slowly at large z. There are three main issues which arise from neglecting all higher eigenvalues.

The first problem is the errors in the coefficients, $C(v,\tilde{v})$, in (5.3.35). This issue was considered in detail in Section 5.3.1 for the two bin problem (see the discussion around (5.3.13)–(5.3.14)). The $C(v,\tilde{v})$ are determined by (5.3.39) and (5.3.44). In particular, (5.3.44) is obtained by matching the similarity solution to the non-self similar region at low z using the flux of oil droplets (see (5.3.40)–(5.3.44)). If we were to include all higher eigenvalues, instead of (5.3.35), ϕ would have the form

$$\phi(v,\xi,z) = \sum_{n=1}^{\infty} \int_v^1 \frac{C^n(v,\tilde{v})\; h^n(\tilde{v},\xi)}{\left(\delta(z)/\hat{\delta}\right)^{m^n(\tilde{v})}}\,\mathrm{d}\tilde{v}. \tag{5.4.1}$$

Then, matching the flux of oil drops, as in (5.3.40)–(5.3.44), would yield

$$\sum_{n=1}^{\infty} \int_v^1 C^n(v,\tilde{v})\,\mathrm{d}\tilde{v} = S(v), \tag{5.4.2}$$

instead of (5.3.44). Comparing (5.3.44) with the full eigenvalue expression, (5.4.2), it is evident that, to obtain (5.3.44), we have assumed that the coefficients corresponding to all higher eigenvalues ($C^n(v,\tilde{v})$ for $n > 1$) are zero. Whilst the higher eigenvalue terms decay more quickly at large z and thus are of less interest, this assumption (which was made for convenience rather than any physical reason) is not necessarily correct and may be leading to some inaccuracies in the evaluation of the smallest eigenvalue term, $C^1(v,\tilde{v})$ or $C(v,\tilde{v})$.

The second problem is that the way we have neglected powers of δ^{-1} may not be asymptotically consistent. The exponents $m(K)$ increase monotonically with K, tending to infinity as K does so. Recall the value of $m^n(K)$ as a function of K was shown in Figure 5.4 for $n = 1, 2, 3$. We have assumed that all higher eigenvalue terms, with eigenvalues $m^n(v)$ for $n > 1$, are of lower order and can be neglected. However, we could encounter the case where $K(v_a)$ is large and $K(v_b)$ is small so the smallest eigenvalue of $L[K(v_a)]$, $m^1(K(v_a))$, is larger than $m^2(K(v_b))$. Then we would be keeping the term $\delta^{-m^1(K(v_a))}$ which, at large δ, is smaller than the neglected term, $\delta^{-m^2(K(v_b))}$. In principle, it would be inconsistent to keep terms where $m^1(K(v)) > \min_{K(v),n>1} m^n(K(v)) = 3$. (Here the eigenvalue $m = 3$ is the second smallest eigenvalue when $K = 0$, as noted in Section 5.2.3.)

The third issue is that at smaller values of z the approximate similarity solution may be inaccurate. For small heights, higher order terms, which come from considering higher eigenvalues, become important. The inaccuracies in the approximate similarity solution at smaller heights and the need for higher eigenvalue terms are illustrated and discussed in Section 5.4.5 (see in particular Figure 5.17).

In addition to neglecting higher eigenvalue terms, in Section 5.3 we begin by assuming the form of the similarity solution for ϕ. This ansatz works for any monotonic breakup rate function but may not hold in other cases. It is more insightful here, whilst including all higher eigenvalues, to directly find a general solution for ϕ without making any assumptions of the form of the solution. This alternative approach enables us to understand where the similarity solution comes from, to understand more fully the loss of accuracy in disregarding higher eigenvalues and, looking forward, will help us understand what happens in the case when the breakup rate $K(v)$ is non-monotonic in Section 5.5.

5.4.2 General approach

We seek a general solution for ϕ for monotonic breakup rate functions $K(v)$. Note that, for simplicity, we will consistently approximate the similarity solution for the energy dissipation as in Section 5.1.3.1 so ϕ satisfies (5.1.11)–(5.1.12).

Boundary conditions are given by

$$\phi(v,\xi,\hat{z}) = F(v,\xi), \qquad \frac{\partial\phi}{\partial\xi}(v,0,z) = 0, \qquad \phi(v,\xi,z) \to 0, \text{ as } \xi \to \infty. \tag{5.4.3}$$

These are similar to the boundary conditions (4.2.9) for the full problem for ϕ from Chapter 4. However, since the similarity solutions for W, U and ϵ are not defined for small z, instead of a boundary condition at $z = 0$, in (5.4.3), it is more straightforward to set ϕ at $z = \hat{z}$ and solve for $z > \hat{z}$. Note that we used different boundary conditions to find the approximate similarity solutions in Section 5.3; there we, instead, match to the flux of oil drops in the non-self-similar region using (5.3.41). The flux of oil, $S(v)$, can be related to $F(v,\xi)$ by

$$S(v) = \int_0^\infty \frac{\xi F(v,\xi)}{(1+\xi^2)^2}\,\mathrm{d}\xi, \tag{5.4.4}$$

using (5.3.41).

As noted in Section 5.2, for each value of K, there is a countably infinite set of eigenvalues and eigenfunctions. The full solution to $\phi(v,\xi,z)$ will be a superposition of all of the eigenfunctions corresponding to all of the drop sizes greater than or

equal to v. Instead of having to deal with all of these sets of eigenfunctions, we find that the most straightforward approach is to write the solution in terms of only one set of eigenfunctions, namely the eigenfunctions for $L[0]$.[1] Let m^n be the nth smallest eigenvalue and $g^n(\xi)$ the corresponding eigenfunction to the eigenproblem (5.2.2)–(5.2.3) with $K = 0$. They satisfy

$$L[0]g^n = m^n \xi g^n \tag{5.4.5}$$

with boundary conditions (5.2.3) and are given by $m^n = n(n+1)/2$ and (5.2.24).

We let

$$t = \log(\delta/\hat{\delta}) \tag{5.4.6}$$

which means that $\delta = \hat{\delta}$ corresponds to $t = 0$. Then (5.1.11) reduces to

$$\xi \frac{\partial \phi}{\partial t} + L[K(v)]\phi = \frac{\xi^2}{1+\xi^2} \int_v^1 K(\tilde{v}) \chi(v, \tilde{v}) \phi(\tilde{v}, \xi, z) \, \mathrm{d}\tilde{v}. \tag{5.4.7}$$

As discussed in Section 5.2, since the $g^n(v, \xi)$ are eigenfunctions of a Sturm-Liouville problem, they form an orthogonal basis satisfying (5.2.4)–(5.2.6). Hence ϕ can be written as a linear combination of these basis functions, i.e.

$$\phi = \sum_{n=1}^{\infty} b^n(v, t) g^n(\xi). \tag{5.4.8}$$

We denote the vectors with components $b^n(v, t)$ and $g^n(\xi)$ as $\mathbf{b}(v, t)$ and $\mathbf{g}(\xi)$, respectively. The boundary condition at $z = \hat{z}$ from (5.4.3), then yields

$$F(v, \xi) = \sum_{n=1}^{\infty} b^n(v, 0) g^n(\xi) \tag{5.4.9}$$

and, taking the inner product with g^l and using the orthogonality of the eigenfunctions, we find

$$\mathbf{b}(v, 0) = \langle F(v, \xi), \mathbf{g}(\xi) \rangle \,, \tag{5.4.10}$$

where, recall, the functional inner product is defined as (5.2.5). The other boundary conditions in (5.4.3) are identical to those for $g^n(\xi)$ (see (5.2.3)) and so are automatically satisfied.

[1] We have explored other approaches to tackle this problem. One such approach is to move to the Laplace transform space, which enables us to convert (5.1.11)–(5.1.12) into an ODE. Its results are equivalent to those presented here.

The problem now is to determine $b^n(v,t)$. Inserting (5.4.8) into (5.4.7) and using (5.4.5) yields

$$\sum_{n=1}^{\infty} \frac{\partial b^n}{\partial t} g^n + b^n m^n g^n + b^n K \frac{\xi}{1+\xi^2} g^n = \frac{\xi}{1+\xi^2} \int_v^1 K(\tilde{v}) \chi(v,\tilde{v}) \sum_{n=1}^{\infty} b^n(\tilde{v},t) g^n(\xi)\, \mathrm{d}\tilde{v}. \tag{5.4.11}$$

Taking $\langle \cdot, g^l \rangle$, we find that

$$\frac{\partial b^l}{\partial t} + m^l b^l + K \sum_{n=1}^{\infty} A_{ln} b^n = \int_v^1 K(\tilde{v}) \chi(v,\tilde{v}) \sum_{n=1}^{\infty} A_{ln} b^n(\tilde{v},t)\, \mathrm{d}\tilde{v}, \tag{5.4.12}$$

where

$$A_{ln} = \left\langle \xi g^l/(1+\xi^2), g^n \right\rangle. \tag{5.4.13}$$

We can write (5.4.12) as the vector equation

$$\frac{\partial \mathbf{b}(v,t)}{\partial t} + (K(v)A + M)\mathbf{b}(v,t) = \int_v^1 K(\tilde{v}) \chi(v,\tilde{v}) A \mathbf{b}(\tilde{v},t)\, \mathrm{d}\tilde{v}, \tag{5.4.14}$$

where M is the diagonal matrix whose lth diagonal is the lth smallest eigenvalue m^l of (5.4.5), i.e. $M = \mathrm{diag}_{n=1}^{\infty}\big(n(n+1)/2\big)$, and A is the symmetric matrix with components A_{ln}. The entries of A can all be found analytically, using the analytical expression for the eigenfunctions, $g^n(\xi)$, in (5.2.24): for example $A_{11} = 15\pi/128$. For illustrative purposes, the first few numerical values of the upper triangular part of A are given by

$$A = \begin{pmatrix} 0.368 & -0.095 & -0.0703 & -0.016 & \dots \\ \cdot & 0.368 & -0.054 & -0.082 & \dots \\ \cdot & \cdot & 0.352 & -0.0356 & \dots \\ \cdot & \cdot & \cdot & 0.343 & \dots \\ \vdots & \vdots & \vdots & \vdots & \ddots \end{pmatrix}. \tag{5.4.15}$$

We see that A is diagonally dominant. Note that the discussion in this section makes no assumptions of the form of $K(v)$ and so (5.4.14) holds generally, whether or not $K(v)$ is monotonic.

The equation (5.4.14) is essentially a first order ODE and so it is fairly straightforward to solve numerically. The homogeneous version of (5.4.14) has solution

$$\mathbf{b}(v,t) = \sum_{n=1}^{\infty} C^n(v) \exp(-m^n(v)t) \mathbf{v}^n(v), \tag{5.4.16}$$

where $C^n(v)$ is a function of v to be determined, and $m^n(v)$ and $\mathbf{v}^n(v)$ are eigenvalues and unit eigenvectors of the matrix $K(v)A + M$. Note that, since $K(v)A + M$ is symmetric, the eigenvectors $\mathbf{v}^n(v)$ for $n = 1, 2, \cdots$, form an orthonormal basis.

At this point, it is interesting to compare (5.4.7) and (5.4.14) to see that $K(v)A + M$ is the matrix corresponding to the linear operator $L[K(v)]$. Thus, the eigenvalues of the matrix are the same as the eigenvalues, $m^n(K(v))$ of $L[K(v)]$, given by the solution to (5.2.2)–(5.2.3). In addition, the nth eigenvector, $\mathbf{v}^n(v)$, of $K(v)A + M$ is related to the eigenfunction $g^n(K(v), \xi)$ of $L[K(v)]$ through

$$g^n(K(v), \xi) = \mathbf{v}^n(v) \cdot \mathbf{g}(\xi). \tag{5.4.17}$$

Equation (5.4.17) is determined by using a similar argument to (5.4.8)–(5.4.14) to solve the eigenproblem for the linear operator $L[K(v)]$ given by

$$L[K(v)]g^n(K(v), \xi) = m^n(K(v))\xi g^n(K(v), \xi). \tag{5.4.18}$$

This yields $g^n(K(v), \xi) = \overline{\mathbf{b}} \cdot \mathbf{g}$ where the equation for $\overline{\mathbf{b}}$, corresponding to (5.4.14) is

$$(K(v)A + M)\overline{\mathbf{b}} = m^n\overline{\mathbf{b}}. \tag{5.4.19}$$

Then $\overline{\mathbf{b}} = \mathbf{v}^n(v)$, which yields (5.4.17).

We can find analytic solutions to (5.4.14) when K is monotonic and, to guide us through the general case, let us first consider some simpler cases, namely the total oil fraction and the three bin problem, analogous to that discussed in Section 5.3.2.

5.4.3 Total oil fraction Φ - 'zero bins'

The total oil fraction, Φ, corresponds to the case where $K = 0$. Hence,

$$\Phi(\xi, z) = \sum_{n=1}^{\infty} b^n(t)g^n(\xi), \tag{5.4.20}$$

with

$$\mathbf{b}(t) = \sum_{n=1}^{\infty} C^n \exp(-m^n t)\mathbf{v}^n, \tag{5.4.21}$$

where C^n is a constant and the m^n and $\mathbf{v}^n$ are the eigenvalues and eigenvectors of the matrix M. In fact, since M is a diagonal matrix, the eigenvectors are identically the standard unit vectors, namely $\mathbf{v}^n = \mathbf{e}_n$. Also, the eigenvalues of the matrix M are identical to the eigenvalues of the operator $L[0]$ and are given by $m^n = n(n + 1)/2$.

Analogously to the first boundary condition in (5.4.3), we set $\Phi(\xi, \hat{z}) = F_\Phi(\xi)$ and so, as in (5.4.10), $\mathbf{b}(0) = \langle F_\Phi, \mathbf{g} \rangle$. Using this in (5.4.21), we obtain

$$C^n = \langle F_\Phi(\xi), g^n(\xi) \rangle \,. \tag{5.4.22}$$

Hence

$$\Phi = \sum_{n=1}^{\infty} \left(\int_0^\infty s F_\Phi(s) g^n(s) \, \mathrm{d}s \right) g^n(\xi) \exp(-n(n+1)/2t), \tag{5.4.23}$$

and so, in terms of the height z,

$$\Phi(\xi, z) = \sum_{n=1}^{\infty} \left(\int_0^\infty s F_\Phi(s), g^n(s) \, \mathrm{d}s \right) \frac{g^n(\xi)}{(\delta(z)/\hat{\delta})^{n(n+1)/2}}. \tag{5.4.24}$$

With the velocity field given by the similarity solutions, this is an exact solution for the total oil fraction Φ.

In the limit of large z, using (5.2.24), (5.4.24) reduces to

$$\Phi \sim \int_0^\infty \frac{6s}{(1+s^2)^2} F_\Phi(s) \, \mathrm{d}s \; \frac{1}{(1+\xi^2)^2 \left(\delta/\hat{\delta}\right)}. \tag{5.4.25}$$

This is proportional to the similarity solution (5.1.4). However, the constants of proportionality are different here. The coefficient in (5.1.4) is obtained by prescribing the total flux of oil (see Section 4.3). However, in doing so, we assume that all of the oil is in the smallest eigenvalue term, namely that the coefficients of the higher eigenvalue terms are identically zero. Recall this assumption was discussed in Section 5.3.1 (see (5.3.13)–(5.3.14)) and Section 5.4.1. In this section, we set the coefficients using the actual value of Φ at $\delta = \hat{\delta}$. Here, as seen from (5.4.24), the coefficient for the smallest eigenvalue is independent of the values of the higher coefficients. Therefore, we can determine the value of the coefficient of the leading order term without needing to make any questionable assumptions about the coefficients of the higher eigenvalue terms. We, thus, expect that the approach used here to determine the constants of proportionality is more accurate.

5.4.4 Three bins

To understand the general solution of (5.4.14), let us now consider the three bin case, analogous to Section 5.3.2. For $i = 2, 3$, ϕ_i is given by the discrete equivalent to (5.4.7), i.e.

$$\xi \frac{\partial \phi_i}{\partial t} + L[K_i]\phi_i = \frac{\xi^2}{1+\xi^2} \sum_{j=i+1}^{3} K_j \chi_{ij} \phi_j (\triangle v). \tag{5.4.26}$$

We can write

$$\phi_i = \sum_{n=1}^{\infty} b_i^n(t) g^n(\xi). \tag{5.4.27}$$

Then, analogously to (5.4.14), the $\mathbf{b}_i^n$ are given by

$$\frac{d\mathbf{b}_i(t)}{dt} + (K_i A + M)\mathbf{b}_i(t) = \sum_{j=i+1}^{3} K_j \chi_{ij} A \mathbf{b}_j(t)(\triangle v) \tag{5.4.28}$$

subject to

$$\mathbf{b}_i(0) = \langle F_i, \mathbf{g} \rangle, \tag{5.4.29}$$

given $\phi_i(\xi, \hat{z}) = F_i(\xi)$.

Let us first consider ϕ_3. Here the right-hand side of (5.4.28) is zero so, as with (5.4.16), the solution is given by

$$\mathbf{b}_3 = \sum_{n=1}^{\infty} C_{33}^n \exp(-m_3^n t)\mathbf{v}_3^n(\triangle v), \tag{5.4.30}$$

where C_{33}^n is the constant given by

$$C_{33}^n(\triangle v) = \langle F_3, \mathbf{g} \rangle \cdot \mathbf{v}_3^n, \tag{5.4.31}$$

and m_3^n is the nth smallest eigenvalue of $K_3 A + M$ with corresponding eigenvector $\mathbf{v}_3^n$. Hence

$$\phi_3 = \sum_{n=1}^{\infty} C_{33}^n \mathbf{v}_3^n \cdot \mathbf{g} \frac{1}{(\delta/\hat{\delta})^{m_3^n}}(\triangle v). \tag{5.4.32}$$

For $\mathbf{b}_2$, (5.4.28) is inhomogeneous. Let us assume that $K_2 \neq K_3$ i.e. that the breakup rate is strictly monotonic. Then we look for a solution of the form

$$\mathbf{b}_2 = \sum_{n=1}^{\infty} \left[C_{22}^n \exp(-m_2^n t)\mathbf{v}_2^n + \mathbf{c}_2^n \exp(-m_3^n t) \right](\triangle v), \tag{5.4.33}$$

where the first term is the homogeneous solution, corresponding to (5.4.16), and the second is motivated by the presence of $\mathbf{b}_3$ on the right-hand side of (5.4.28) and the form of $\mathbf{b}_3$ in (5.4.30). Substituting (5.4.33) into (5.4.28) suggests

$$\mathbf{c}_2^n = C_{23}^n \mathbf{v}_3^n, \tag{5.4.34}$$

where

$$C_{23}^n = C_{33}^n \frac{K_3 \chi_{23} \triangle v}{K_2 - K_3} \tag{5.4.35}$$

and C_{33}^n is given by (5.4.31). Now, using the boundary condition (5.4.29), we obtain

$$C_{22}^n(\triangle v) = \langle F_2, \mathbf{g} \rangle \cdot \mathbf{v}_2^n - \sum_{l=1}^{\infty} C_{23}^l \mathbf{v}_3^l \cdot \mathbf{v}_2^n (\triangle v) \tag{5.4.36}$$

and hence

$$\phi_2 = \sum_{n=1}^{\infty} \left[C_{22}^n \mathbf{v}_2^n \cdot \mathbf{g} \frac{1}{(\delta/\hat{\delta})^{m_2^n}} + C_{23}^n \mathbf{v}_3^n \cdot \mathbf{g} \frac{1}{(\delta/\hat{\delta})^{m_3^n}} \right] (\triangle v). \tag{5.4.37}$$

We use conservation of mass to determine the drop size distribution for the smallest drops so

$$\phi_1 = \Phi/(\triangle v) - \phi_3 - \phi_2, \tag{5.4.38}$$

where Φ is given by (5.4.24), ϕ_3 by (5.4.32) and ϕ_2 by (5.4.37).

In practice, to calculate the ϕ_i, we must truncate the sums. The g^n and m^n can be determined analytically for all n from (5.2.24). For some large n_t, say $n_t = 25$, we truncate the matrices $K_i A + M$ and hence find the n_t first eigenvalues and eigenvectors. To determine $\mathbf{b}$, $\mathbf{b}_3$ and $\mathbf{b}_2$ (corresponding to the total oil, large bin and medium bin) we need to truncate the sums in (5.4.21), (5.4.30), and (5.4.33) and (5.4.36), respectively. We find that, as will be illustrated in Section 5.4.5, keeping the first term is generally sufficient and, except for small values of z, little is gained by taking more than the first five terms.

5.4.5 Comparison with approximate similarity solution

The full solutions for the three bin case, (5.4.32) and (5.4.37), have a very similar form to the approximate similarity solutions in Section 5.3.2. To leading order in z, (5.4.32) with (5.4.31) yields

$$\phi_3 \sim C_{33}^1 \mathbf{v}_3^1 \cdot \mathbf{g} \frac{1}{(\delta/\hat{\delta})^{m_3^1}} \triangle v, \tag{5.4.39}$$

where $C_{33}^1 \triangle v = \langle F_3, \mathbf{v}_3^1 \cdot \mathbf{g} \rangle$. Noting from (5.4.17), that $\mathbf{v}_3^1 \cdot \mathbf{g} = g_3^1$, (5.4.39) is proportional to the approximate similarity solution (5.3.17). The key difference here is the constant coefficient in front of the $\delta^{-m_3^1}$ term (as was the case with the total oil fraction in Section 5.4.3). This difference is to be expected because of the way the

problem for the similarity solution is posed. Here, in fully solving for ϕ_3, we set the drop size distribution itself at $\delta = \hat{\delta}$, whilst, in the approximate similarity solution, at $\delta = \hat{\delta}$ we use a matching condition, setting the flux of the drop size distribution. In matching the similarity solution using the flux of oil, we must make the assumption, outlined in Section 5.4.1, that $C_{33}^n = 0$ for $n > 1$. Using ϕ_3 at $\delta = \hat{\delta}$, as we have done to obtain (5.4.39), is more accurate because, in determining C_{33}^1, we do not have to make any such assumptions.

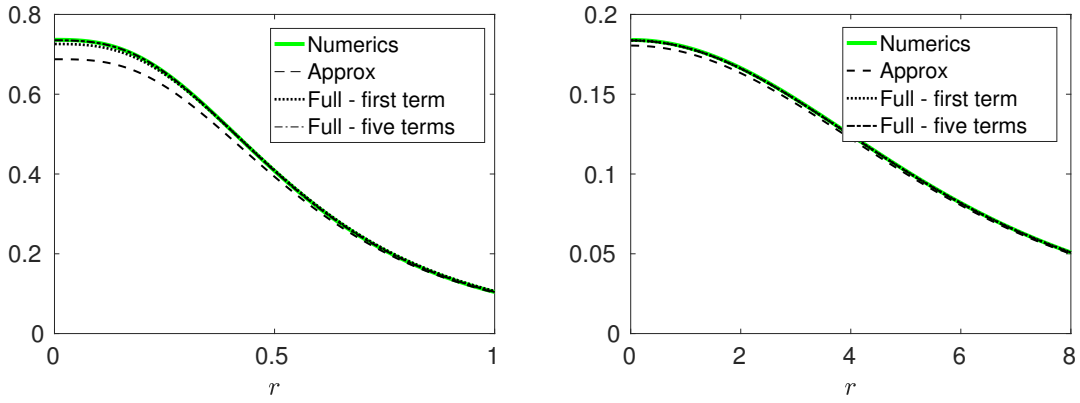
We can similarly compare the full solution for ϕ_2, (5.4.37), with the approximate similarity solution, (5.3.28). The first thing to note is that the method used to determine the coefficients in Section 5.4.4 is similar to that in Section 5.3.2 for the approximate similarity solution. In (5.4.37), the coefficients C_{23}^n are determined by the solvability condition (5.4.35), similar to (5.3.27). The other coefficients C_{22}^n are determined by the initial condition at $\delta = \hat{\delta}$ as are the coefficients in (5.3.29) although, as we have discussed, in the approximate and full similarity solutions the conditions used are different.

To directly compare ϕ_2 in (5.4.37) to the approximate similarity solution, we make certain assumptions. We suppose that $m_2^1 < m_3^i$ for all $i > 1$ and $m_3^1 < m_2^i$ for all $i > 1$ and so the two dominant terms of ϕ_2 for large z arise from the terms with exponent $\delta^{-m_2^1}$ and $\delta^{-m_3^1}$. Hence, to first order for large z, (5.4.37) yields

$$\phi_2 \sim \left[C_{22}^1 (\mathbf{v}_2^1 \cdot \mathbf{g}) \frac{1}{(\delta/\hat{\delta})^{m_2^1}} + C_{23}^1 (\mathbf{v}_3^1 \cdot \mathbf{g}) \frac{1}{(\delta/\hat{\delta})^{m_2^1}} \right] \triangle v, \tag{5.4.40}$$

where C_{23}^1 and C_{22}^1 are given by (5.4.35)–(5.4.36). Again noting from (5.4.17) that $\mathbf{v}_2^1 \cdot \mathbf{g} = g_2^1$ and $\mathbf{v}_3^1 \cdot \mathbf{g} = g_3^1$, we see (5.4.40) has the same form as the approximate similarity solution (5.3.28) except, as discussed previously, for the coefficients set by the different initial conditions. In addition, for the full solution, C_{22}^1 depends on the coefficients for higher eigenvalues.

We now illustrate the differences between the full solution in Section 5.4.4, the approximate similarity solution and the numerics. Recall, the approximate solution and numerics were compared in Section 5.3.2 (see Figure 5.10). We use the results from Section 5.3.2, and now additionally compute the corresponding full solution, given by (5.4.32), (5.4.37) and (5.4.38). We truncate the sums to include the first term and the first five terms. As in Section 5.3.2, we take $K_i = v_i^{-1/2}$, $\chi_{ij} = 1/v_{j-1}$ and $\hat{z} = 5$. We find that all three approaches give very similar results. The only discernible difference between the approximate and full similarity solutions is in ϕ_1 and thus this is illustrated in Figure 5.16.

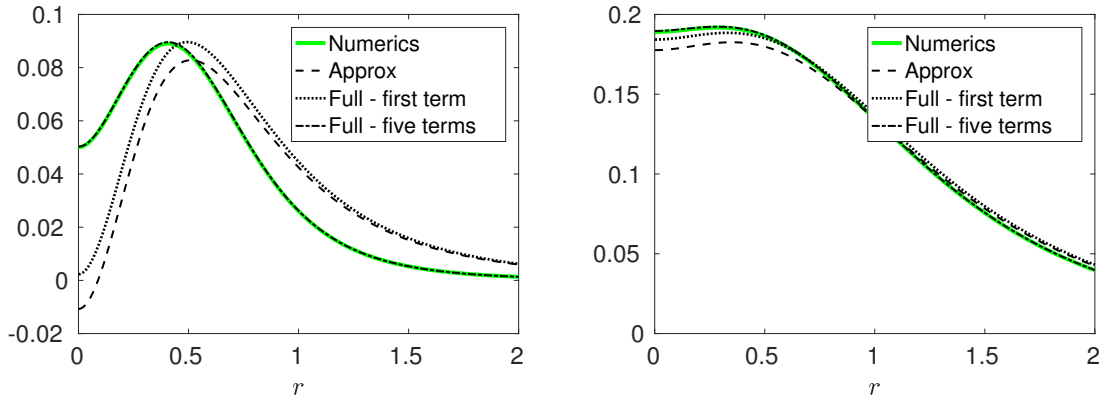


(a) $z = 5$ (b) $z = 50$

Figure 5.16: Drop size distribution for ϕ_1 in three bin case for the same problem as in Figure 5.10. We compare numerics (solid green), the approximate similarity solution (dashed black), the full solution with only the first eigenvalue term (dotted black), and the full solution with the first five eigenvalue terms (dash-dot black). (a) $z = 5$ (b) $z = 50$.

In Figure 5.16, we plot ϕ_1 for the numerics, the approximate similarity solution, the full similarity solution truncating so there is only one term in the sums, and the full similarity solution keeping the first five terms. There are some small inconsistencies between the numerical solution and the approximate similarity solution for ϕ_1. These are rectified by using only the first eigenvalue term in the full similarity solution. This suggests that it is the difference in the calculation of the coefficients C_{ij} which is causing the inaccuracies in the approximate similarity solution. Recall, as illustrated in Figure 5.1(b), that the eigenvalues monotonically increase with K, so are smallest when $K = 0$. This means that the first order term in Φ will always decay slower than the first order term in ϕ_2 or ϕ_3. Thus, any errors in determining the coefficients will be worse when considering the total oil fraction Φ and hence $\phi_1 = \Phi - \phi_3 - \phi_2$. This is why we only observe these errors in ϕ_1. Including more terms in the series only slightly improves the solution and this occurs only at small values of z in Figure 5.16(a).

Let us construct an example to better illustrate the effect of the higher eigenvalue terms. We consider the same problem, but instead we take $\hat{z}_n = 5$ and $\hat{z} = 5.1$. Here, since the point at which we match to the similarity solution, $\hat{z}$, is so close to $\hat{z}_n = 5$, there has not been enough time for the functions ϕ_i to become self-similar and so we expect the higher eigenvalue terms to play a bigger role. We see this is the case in Figure 5.17(a). At $z = 6$, the approximate similarity solution takes negative values. Using the full solution and truncating so only the first term is included causes only a



(a) $z = 6$ (b) $z = 10$

Figure 5.17: Drop size distribution for ϕ_1 in three bin case for a similar problem to that in Figure 5.10 but with $\hat{z}_n = 5$ and $\hat{z} = 5.1$. We compare numerics (solid green), the approximate similarity solution (dashed black), the full solution with only the first eigenvalue term (dotted black), and the full solution with the first five eigenvalue terms (dash-dot black). (a) $z = 6$ (b) $z = 10$.

slight improvement. We need the first five eigenvalue terms for accuracy. Nonetheless, by around $z = 10$, both the approximate similarity solution and the first term of the full solution show fairly good agreement with the numerics. Therefore, in general, we conclude that keeping the first eigenvalue term appears to be sufficient once initial transients close to $z = \hat{z}$ have decayed.

5.4.6 N bin and continuous volume model

We generalise (5.4.33)–(5.4.37) to the N bin case, finding that

$$\phi_i = \sum_{j=i}^{N} \sum_{n=1}^{\infty} C_{ij}^n \mathbf{v_j^n} \cdot \mathbf{g} \frac{1}{(\delta/\hat{\delta})^{m_j^n}} (\triangle v), \tag{5.4.41}$$

with the coefficients C_{ij}^n given by

$$C_{ij}^n = \frac{\sum_{k=i+1}^{j} C_{kj}^n K_k \chi_{ik} \triangle v}{K_i - K_j} \tag{5.4.42}$$

for $i < j$ and

$$C_{ii}^n(\triangle v) = \langle F_i, \mathbf{g} \rangle \cdot \mathbf{v}_i^n - \sum_{j=i+1}^{N} \sum_{l=1}^{\infty} C_{ij}^l \mathbf{v}_j^l \cdot \mathbf{v}_i^n (\triangle v). \tag{5.4.43}$$

This can easily be extended to continuous volume models by taking the limit $N \to \infty$ in (5.4.41)–(5.4.43), resulting in

$$\phi(v,\xi,z) = \int_v^1 \sum_{n=1}^{\infty} C^n(v,\tilde{v})\mathbf{v}^n(\tilde{v}) \cdot \mathbf{g} \frac{1}{(\delta/\hat{\delta})^{m^n(\tilde{v})}} \,\mathrm{d}\tilde{v}, \tag{5.4.44}$$

with the functions C^n given by solutions of the Volterra integral equation

$$C^n(v,\tilde{v}) = \frac{\displaystyle\int_v^{\tilde{v}} C^n(s,\tilde{v})K(s)\chi(v,s)\,\mathrm{d}s}{K(v) - K(\tilde{v})} \tag{5.4.45}$$

for $v < \tilde{v}$ and the initial condition

$$\langle F(v), \mathbf{g}\rangle \cdot \mathbf{v}^n(v) = \int_v^1 \sum_{l=1}^{\infty} C^l(v,\tilde{v})\mathbf{v}^l(\tilde{v}) \cdot \mathbf{v}^n(v)\,\mathrm{d}\tilde{v}. \tag{5.4.46}$$

5.4.7 Discussion

We have found a procedure to easily compute full similarity solutions for the drop size distribution when the breakup rate function $K(v)$ is monotonic. These do not have the inaccuracies, described in Section 5.4.1, of the approximate similarity solutions. Firstly, we set the coefficients differently, using the value of ϕ at $z = \hat{z}$ rather than its flux. In doing so, we no longer need to rely on the somewhat inconsistent assumption that the coefficients of all the rapidly decaying terms are zero at all z. The second problem in the approximate similarity solution is that we might not always consistently keep the correct terms at large z. The truncated full similarity solution has the same conceptual problem but by taking, say, the first five eigenvalue terms in each sum we ensure that any term we do not include is negligibly small. Finally, by including higher eigenvalue terms, we find we can accurately determine ϕ at small z which, in some cases, is not possible using the approximate similarity solutions. We note that, comparatively, the approximate similarity solutions are fairly accurate but only at large enough heights, when there is enough height for the self-similar behaviour to develop.

Now that we have a full analytic solution for ϕ, it is interesting to consider what determines the leading-order behaviour at large z. This will correspond to the smallest exponent of δ^{-1}, which will be the smallest eigenvalue $m^1(v)$ for some v. First let us suppose that $K(v)$, and so $m^1(v)$, is a monotonically increasing function. Since $\phi(v,\xi,z)$ depends on the $m^n(\tilde{v})$ for $\tilde{v} \geq v$, the term with the smallest exponent of δ^{-1} is that corresponding to the eigenvalue $m^1(v)$. Therefore, the leading order decay in

z of $\phi(v, \xi, z)$ is governed by the breakup of droplets of size v itself. The coefficients C depend on the breakup and behaviour of the drop size distribution for larger drops. If $K(v)$ is monotonically decreasing, the leading order term corresponds to that with eigenvalue $m^1(1)$, namely the largest drop. All smaller drops are breaking up quickly so the behaviour of the largest drop dominates at large z.

5.5 Non-monotonic breakup rates

5.5.1 What goes wrong?

We have thus far limited our discussion to monotonic breakup rate functions $K(v)$ as outlined in Section 5.1.3.3. In reality, the breakup rate is commonly assumed to increase with volume, reach some local maximum and then decrease. Let us assume that $K(v)$ is of this form so it has a single turning point at $v = v_t$. Then it is reasonable to say that there will exist some $v < v_t$ and some $\tilde{v} > v_t$ such that $K(v) = K(\tilde{v})$

However, this means that the approximate, (5.3.35), and full, (5.4.44), solutions we have found for ϕ no longer make sense. In both the approximate and full similarity solutions, the coefficients, given by (5.3.39) and (5.4.45), respectively, involve terms which are singular when $K(v) = K(\tilde{v})$. The reason behind the appearance of these singularities can be explained by returning to the problem for the full solution to ϕ_2 in the three bin case in Section 5.4.4. The vector $\mathbf{b}_2$ satisfies (5.4.28) with $i = 2$ and has solution (5.4.33). The solution is made up of the homogeneous solution to (5.4.28) and a particular integral which is a linear combination of $\exp(-m_3^n t)$ (for $n = 1, 2, \cdots$) since $\mathbf{b}_3$ is a linear combination of $\exp(-m_3^n t)$ in (5.4.30). If $K_2 = K_3$, then the exponents m_3^n and m_2^n would be the same and hence, instead of a particular integral which is a linear combination of $\exp(-m_3^n t)$, we would get secular terms like $t \exp(-m_3^n t)$. In terms of z, we expect to encounter log terms such as $\log(\delta/\hat{\delta})(\delta/\hat{\delta})^{-m_3^n}$. Therefore, the assumed form of the approximate similarity solution, (5.3.35), is no longer appropriate and the discussion in Sections 5.4.4–5.4.6, to determine the full similarity solution, (5.4.44), must be modified.

5.5.2 Approximate similarity solution

Let us first generalise the approximate similarity solution in Section 5.3 for the case when K is non-monotonic. We do so by discussing the discrete volume formulation from Section 5.3.3 and considering what happens in the limit $K_j \to K_i$.

For monotonic breakup rates, the drop size distribution, ϕ_i, for drops with volume v_i is given by (5.3.31)–(5.3.34). In particular, the coefficients C_{ij} are given by (5.3.33)–(5.3.34), namely

$$C_{ij} = \frac{\sum_{k=i+1}^{j} C_{kj} K_k \chi_{ik} \triangle v}{K_i - K_j}, \tag{5.5.1}$$

for $i < j$ and

$$S_i = \sum_{j=i}^{N} C_{ij} \triangle v. \tag{5.5.2}$$

Let us suppose K has a turning point at v_t. For ϕ_i, when $i < t$, there may be some $j > t$ such that $K_i = K_j$, and thus there appears to be a singularity in (5.5.1). This is not the case for ϕ_i with $i \geq t$ because ϕ_i depends only on K_j, where $j \geq i \geq t$ but these K_j will never repeat.

How can we make sense of the possible appearance of a singularity in (5.5.1)? The first step is to rewrite ϕ_i in a form more amenable to taking the limit $K_{\hat{i}} \to K_i$. Recall that, in the case where K is a monotonic function, ϕ_i is given by (5.3.31). We use (5.5.2) to rearrange (5.3.31) and yield

$$\phi_i = \frac{S_i h_i(\xi)}{\left(\delta(z)/\hat{\delta}\right)^{m_i}} + \sum_{j=i+1}^{N} C_{ij} \left(\frac{h_j(\xi)}{\left(\delta(z)/\hat{\delta}\right)^{m_j}} - \frac{h_i(\xi)}{\left(\delta(z)/\hat{\delta}\right)^{m_i}} \right) \triangle v, \tag{5.5.3}$$

where the sum consists of terms

$$C_{ij} \left(\frac{h_j(\xi)}{\left(\delta(z)/\hat{\delta}\right)^{m_j}} - \frac{h_i(\xi)}{\left(\delta(z)/\hat{\delta}\right)^{m_i}} \right) = \left(\sum_{k=i+1}^{j} C_{kj} K_k \chi_{ik} \triangle v \right) \frac{\frac{h_j(\xi)}{\left(\delta(z)/\hat{\delta}\right)^{m_j}} - \frac{h_i(\xi)}{\left(\delta(z)/\hat{\delta}\right)^{m_i}}}{K_i - K_j}, \tag{5.5.4}$$

for $j > i$. Note the equality in (5.5.4) comes from (5.5.1).

Let us consider (5.5.4) for some $i < t$ and $j = \hat{i} > t$, where i and $\hat{i}$ are such that $K_i = K_{\hat{i}}$. In this case, $C_{k\hat{i}}$ is finite for $i < k \leq \hat{i}$.[2] Thus, so is the term $\sum_{k=i+1}^{\hat{i}} C_{k\hat{i}} K_k \chi_{ik} \triangle v$, on the right-hand side of (5.5.4).

[2]When $k < \hat{i}$, from (5.5.1), the constant coefficients are given by

$$C_{k\hat{i}} = \frac{\sum_{l=k+1}^{\hat{i}} C_{l\hat{i}} K_l \chi_{kl} \triangle v}{K_k - K_{\hat{i}}}. \tag{5.5.5}$$

The other term on the right-hand side of (5.5.4) looks like 0/0. Using l'Hopital's rule, as $K_{\hat{i}} \to K_i$, the right-hand side of (5.5.4) can instead be written as

$$D_{ii}\left(M_i h_i \frac{\log\left(\delta/\hat{\delta}\right)}{\left(\delta/\hat{\delta}\right)^{m_i}} - H_i \frac{1}{\left(\delta/\hat{\delta}\right)^{m_i}}\right), \tag{5.5.6}$$

where

$$D_{ii} = \sum_{k=i+1}^{\hat{i}} C_{k\hat{i}} K_k \chi_{ik} \triangle v, \tag{5.5.7}$$

$$H_i = \left(\frac{\partial h}{\partial K}\right)_i \tag{5.5.8}$$

and

$$M_i = \left(\frac{dm}{dK}\right)_i. \tag{5.5.9}$$

We consider every such pair $(i, \hat{i})$ where $i < t$, $\hat{i} > t$ and $K_i = K_{\hat{i}}$. We remove the terms with singularities by setting

$$C_{ij} = 0, \text{ for } j > t \text{ such that } K_i = K_j \tag{5.5.10}$$

and restoring their contribution by adding in (5.5.6).

The $C_{i\hat{i}}$ terms also affect other constant terms through (5.5.1)–(5.5.2). This means that, for each ϕ_i, we do not merely have to add a term like (5.5.6) to ϕ_i but also must include other D_{ij} terms which, analagously to (5.5.1), are given by

$$D_{ij} = \sum_{k=i+1}^{j} \frac{D_{kj} K_k \chi_{ik} \triangle v}{K_i - K_j}. \tag{5.5.11}$$

In all, ϕ_i is given by

$$\begin{aligned}\phi_i = \frac{S_i h_i(\xi)}{\left(\delta/\hat{\delta}\right)^{m_i}} + \sum_{j=i+1}^{N} C_{ij}\left(\frac{h_j(\xi)}{\left(\delta/\hat{\delta}\right)^{m_j}} - \frac{h_i(\xi)}{\left(\delta/\hat{\delta}\right)^{m_i}}\right)\triangle v \\ + \sum_{j=i}^{t-1} D_{ij}\left(M_j h_j \frac{\log\left(\delta/\hat{\delta}\right)}{\left(\delta/\hat{\delta}\right)^{m_j}} - H_j \frac{1}{\left(\delta/\hat{\delta}\right)^{m_j}}\right)\triangle v,\end{aligned} \tag{5.5.12}$$

Now, $i < k < \hat{i}$ so, since there is only one turning point in K, $K_k \neq K_{\hat{i}}$. In addition, the sum depends on $C_{l\hat{i}}$ where $k < l \leq \hat{i}$; again $i < l < \hat{i}$ so, since there is only one turning point in K, $K_l \neq K_{\hat{i}}$. This argument can be recursively applied and we conclusde that $C_{k\hat{i}}$ is finite when $i < k < \hat{i}$. When $k = \hat{i}$, we consider $C_{\hat{i}\hat{i}}$, which is given by (5.5.2). This depends on $C_{\hat{i}q}$ where $q > \hat{i}$, which are coefficients in $\phi_{\hat{i}}$. We have noted before that no singularities arise in $\phi_{\hat{i}}$ where $\hat{i} > t$ so there can be none in $C_{\hat{i}\hat{i}}$.

where $C_{ij} = 0$ for $j > t$ such that $K_i = K_j$,

$$D_{ii} = \begin{cases} \displaystyle\sum_{k=i+1}^{\hat{i}} C_{k\hat{i}} K_k \chi_{ik} \triangle v, & \text{if } \exists \hat{i} > t \text{ such that } K_i = K_{\hat{i}}, \\ 0, & \text{otherwise} \end{cases} \tag{5.5.13}$$

and, for $i < j$, D_{ij} is given by (5.5.11). Note that this is merely a more generalised version of (5.3.31)–(5.3.34), and if K is monotonic reduces to it.

Here we have assumed that there is only one turning point in K and so a value of K is repeated, at most, twice. If there were more turning points in K, the multiple repetitions of a certain value of K would yield higher powers of $\log(\delta)$.

It remains to determine M_i and H_i. These are the volume discretised equivalents of the functions dm/dK and $\partial h/\partial K$. These can be calculated numerically by finding $m(K)$ and $h(K, \xi)$ from solving (5.3.37) and then taking the derivative with respect to K. Alternatively, by differentiating the equation $L[K]h = m\xi h$, for h, with respect to K, we find that $H = \partial h/\partial K$ satisfies

$$L[K]H - m(K)\xi H = \xi h \left(M(K) - \frac{\xi}{1+\xi^2} \right). \tag{5.5.14}$$

From the Fredholm Alternative, the solvability condition for (5.5.14) sets

$$M = \frac{\displaystyle\int \frac{\xi^2 h(\xi)^2}{1+\xi^2} \, \mathrm{d}\xi}{\displaystyle\int \xi h(\xi)^2 \, \mathrm{d}\xi}. \tag{5.5.15}$$

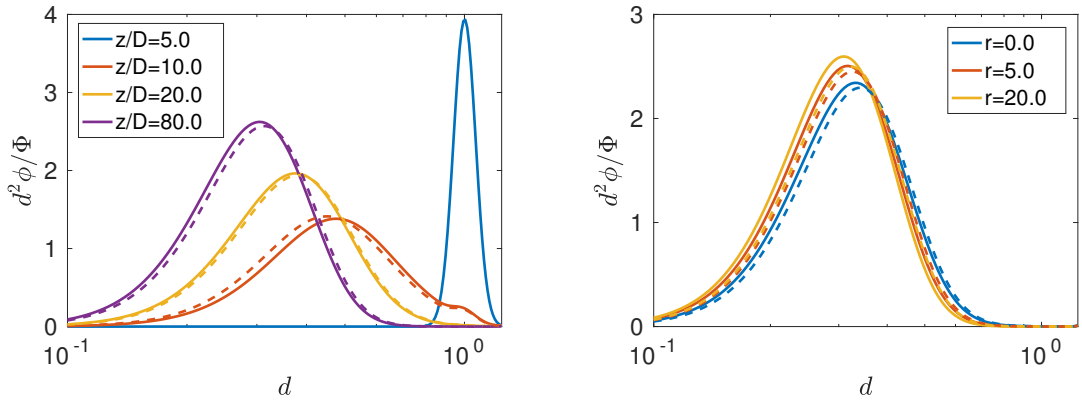
We can then solve (5.5.14) and the boundary conditions of $L[K]$ (given in (5.1.12)) are satisfied by setting

$$H \sim a_0 - 2\left(h(0)M + a_0 m\right)\xi^2 + \cdots \text{ as } \xi \to 0 \tag{5.5.16}$$

and shooting with the parameter a_0 so the far field boundary condition is satisfied.

We compare the similarity solution here to the numerics in an identical manner to the comparison in Section 5.3.4.2 except here we use a non-monotonic breakup rate, $K_i = 50 v_i (1 - v_i)$. As seen in Figure 5.18, there is good agreement between the similarity solution and the numerics, indicating its validity.

Unlike with monotonic breakup rate functions $K(v)$ in Section 5.3.4, it is not straightforward to extend the discrete to the continuous volume case. Therefore, we now investigate if we can make any further progress by considering the full similarity solution.



(a) Fixed $r = 0.1$ (b) Fixed $z = 40$

Figure 5.18: Comparison of similarity solution for ϕ_i (dotted line) with full numerical results (full line). We consider different heights at fixed $r = 0.1$ in (a) and different widths at fixed $z = 40$ in (b). We set $K_i = 50v_i(1 - v_i)$ and the daughter size distribution as the discrete equivalent of (3.2.32). The initial condition for ϕ at $z = \hat{z}_n = 5$, for the numerics, is given by (4.4.5), and the similarity solution is used from $\hat{z} = 10$.

5.5.3 Full similarity solution

The general approach to finding the full solution for ϕ in Section 5.4.2 is independent of the form of $K(v)$. Therefore, when $K(v)$ is non-monotonic, ϕ is still given by (5.4.8) and the solution to (5.4.14) subject to (5.4.10). As previously mentioned, it is fairly straightforward to numerically solve (5.4.14) since it is essentially a first order ODE.

However, it is difficult to find a simple formula for ϕ as in the monotonic case. Nonetheless, using the discrete volume formulation, we can recursively find analytic solutions for ϕ_i. We present the methodology for the simplest case, the three bin case from (5.4.4).

Let us consider the three bin problem in Section 5.4.4. We first assume that one of the eigenvalues of $K_2A + M$ is equal to some eigenvalue of $K_3A + M$ since, as mentioned at the beginning of this section, problems arise if there are repeated eigenvalues. We set $m_2^p = m_3^q$ for some p and q. To more easily examine the difference from the solution, (5.4.37), for ϕ_2 when no eigenvalues are repeated, here we assume that K_2 is not necessarily equal K_3 so $\mathbf{v}_2^p$ and $\mathbf{v}_3^q$ are not necessarily equal and no other eigenvalues are repeated.

The drop size distribution for the large bins is given by $\phi_3 = \mathbf{b}_3 \cdot \mathbf{g}$, where $\mathbf{b}_3$ is given by (5.4.30). We solve for $\phi_2 = \mathbf{b}_2 \cdot \mathbf{g}$, where $\mathbf{b}_2$ satisfies (5.4.28) subject to

(5.4.29) with $i = 2$, that is

$$\frac{d\mathbf{b}_2}{dt} + (K_2A + M)\mathbf{b}_2 = K_3\chi_{23}(\triangle v)^2 \sum_{\substack{n=1 \\ n\neq q}}^{\infty} C_{33}^n \exp(-m_3^n t)\mathbf{v}_3^n + K_3\chi_{23}(\triangle v)^2 C_{33}^q \exp(-m_3^q t)\mathbf{v}_3^q. \tag{5.5.17}$$

Then, similarly to (5.4.33), we seek solutions of the form

$$\mathbf{b}_2 = \sum_{n=1}^{\infty} [C_{22}^n \exp(-m_2^n t)\mathbf{v}_2^n + \mathbf{c}_2^n \exp(-m_3^n t)] \triangle v + \hat{\mathbf{c}}_2^q t \exp(-m_3^q t)\triangle v, \tag{5.5.18}$$

where the first term is the homogeneous solution and the second and third terms are motivated by the right-hand side of (5.5.17). Note the third term in (5.5.18) is the secular term which comes from the fact that the term $\exp(-m_3^q t) = \exp(-m_2^p t)$ occurs in the homogeneous solution of (5.5.17). Subsituting (5.5.18) into (5.5.17), we find that, as with (5.4.34)–(5.4.35), for $n \neq q$

$$\mathbf{c}_2^n = C_{23}^n \mathbf{v}_3^n, \tag{5.5.19}$$

where

$$C_{23}^n = C_{33}^n \frac{K_3\chi_{23}\triangle v}{K_2 - K_3}. \tag{5.5.20}$$

Furthermore, the terms involving the repeated eigenvalues yield

$$\hat{\mathbf{c}}_2^q = \hat{C}_{23}^q \mathbf{v}_2^p, \tag{5.5.21}$$

where $\hat{C}_{23}^q$ is a constant to be determined and

$$[(K_2A + M) - m_2^p]\mathbf{c}_2^q = K_3\chi_{23}(\triangle v)C_{33}^q A\mathbf{v}_3^q - \hat{C}_{23}^q \mathbf{v}_2^p. \tag{5.5.22}$$

Using the Fredholm alternative, for (5.5.22) to have a non-trivial solution for $\mathbf{c}_2^q$, we must have

$$\hat{C}_{23}^q = C_{33}^q K_3\chi_{23}\triangle v A\mathbf{v}_3^q \cdot \mathbf{v}_2^p. \tag{5.5.23}$$

Now it remains to solve (5.5.22) for $\mathbf{c}_2^q$. Since the set of eigenvectors $\mathbf{v}_2^n$ for $n = 1, 2, \cdots$ forms a basis, we write

$$\mathbf{c}_2^q = \sum_{n=1}^{\infty} d^n \mathbf{v}_2^n, \tag{5.5.24}$$

where we can without loss of generality absorb the $\mathbf{v}_2^p$ term into the first term in (5.5.18) so $d^p = 0$. Inserting (5.5.24) into (5.5.22) yields, for $n \neq p$,

$$d^n = \frac{C_{33}^q K_3 \chi_{23} \triangle v \, (A\mathbf{v}_3^q \cdot \mathbf{v}_2^n)}{m_2^n - m_2^p}. \tag{5.5.25}$$

Hence, we can write (5.5.18) as

$$\begin{aligned} \mathbf{b}_2 = &\sum_{n=1}^{\infty} C_{22}^n \exp(-m_2^n t)\mathbf{v}_2^n \triangle v + \sum_{\substack{n=1 \\ n\neq q}}^{\infty} C_{23}^n \exp(-m_3^n t)\mathbf{v}_3^n \triangle v \\ &+ \sum_{\substack{n=1 \\ n\neq p}}^{\infty} d^n \exp(-m_3^q t)\mathbf{v}_2^n \triangle v + \hat{C}_{23}^q t \exp(-m_3^q t)\mathbf{v}_2^p \triangle v, \end{aligned} \tag{5.5.26}$$

with (5.5.20), (5.5.23) and (5.5.25).

The constants C_{22}^n in (5.5.26) are determined by the condition (5.4.29) at $t = 0$, which yields

$$\langle F_2, \mathbf{g} \rangle = \sum_{n=1}^{\infty} C_{22}^n \mathbf{v}_2^n \triangle v + \sum_{\substack{n=1 \\ n\neq q}}^{\infty} C_{23}^n \mathbf{v}_3^n \triangle v + \sum_{\substack{n=1 \\ n\neq p}}^{\infty} d^n \mathbf{v}_2^n \triangle v, \tag{5.5.27}$$

so

$$C_{22}^n \triangle v = \langle F_2, \mathbf{g} \rangle \cdot \mathbf{v}_2^n - \sum_{\substack{n=1 \\ n\neq q}}^{\infty} C_{23}^n \mathbf{v}_3^n \cdot \mathbf{v}_2^n \triangle v - d^n \triangle v. \tag{5.5.28}$$

Here we have assumed only one of the eigenvalues is repeated. If $K_2 = K_3$ then all eigenvalues are repeated, namely $m_2^p = m_3^p$ for all p. Hence $\phi_2 = \mathbf{b}_2 \cdot \mathbf{g}$ with

$$\mathbf{b}_2 = \sum_{n=1}^{\infty} \left[C_{22}^n \exp(-m_2^n t)\mathbf{v}_2^n + \sum_{p=1}^{\infty} d^{np} \exp(-m_2^n t)\mathbf{v}_2^p + \hat{C}_{23}^n t \exp(-m_2^n t)\mathbf{v}_2^n \right] \triangle v, \tag{5.5.29}$$

where, for simplicity, we express the eigenvalues and eigenfunctions as those of the second bin (so with subscript 2). Here $\hat{C}_{23}^n$ is given by (5.5.23) and the d^{np} are given, similarly to (5.5.25), by

$$d^{np} = \frac{C_{33}^n K_3 \chi_{23} \triangle v \, (A\mathbf{v}_2^n \cdot \mathbf{v}_2^p)}{m_2^p - m_2^n}, \tag{5.5.30}$$

for $p \neq n$ and $d^{nn} = 0$. The initial condition sets C_{22}^n as

$$C_{22}^n \triangle v = \langle F_2, \mathbf{g} \rangle \cdot \mathbf{v}_2^n - \sum_{l=1}^{\infty} d^{ln}. \tag{5.5.31}$$

Hence

$$\phi_2 = \sum_{n=1}^{\infty} \left[C_{22}^n (\mathbf{v_2^n} \cdot \mathbf{g}) + \sum_{p=1}^{\infty} d^{np} (\mathbf{v}_2^p \cdot \mathbf{g}) \right] \triangle v \frac{1}{\left(\delta/\hat{\delta}\right)^{m_2^n}} + \sum_{n=1}^{\infty} \hat{C}_{23}^n (\mathbf{v}_2^n \cdot \mathbf{g}) \triangle v \frac{\log(\delta/\hat{\delta})}{\left(\delta/\hat{\delta}\right)^{m_2^n}}. \tag{5.5.32}$$

Note, to compute ϕ_2 in practice, one would need to truncate the sum in (5.5.31) and the two sums over n in (5.5.32).

A careful comparison between the largest two terms in (5.5.32) and the three bin expression for ϕ_2 from the approximate similarity solution, (5.5.12) of Section 5.5.2, shows they are almost identical. The only difference is that in (5.5.32), the constant C_{22}^n is set by the initial condition at $z = \hat{z}$ rather than by the flux of oil as in Section 5.5.2.

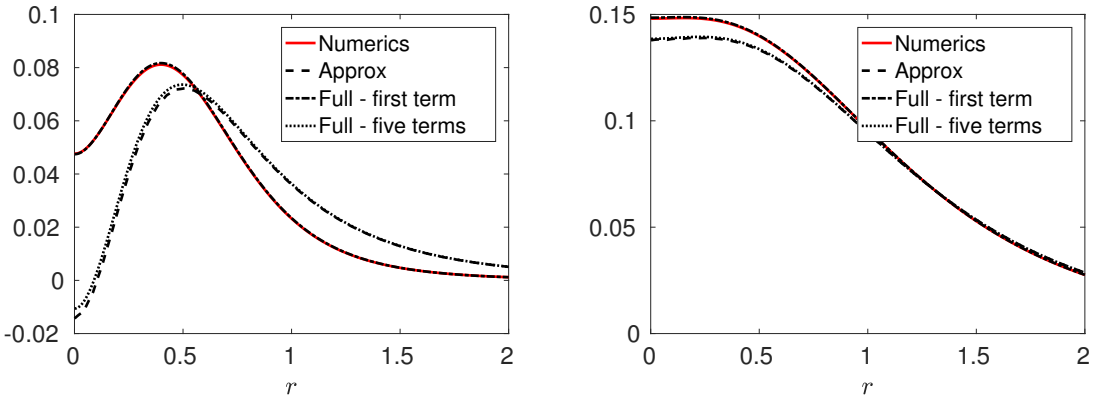
We now illustrate the differences between the full solution, the approximate similarity solution from Section 5.5.2, and the numerics. We formulate a very similar problem to that in Section 5.3.2 (see Figure 5.10), where we compared the numerics and the approximate similarity solution for a monotonic breakup rate. Here we take a constant breakup rate so $K_2 = K_3 = 1$ and we take $\hat{z}_n = 5$ and $\hat{z} = 5.1$. Our results for ϕ_2 are shown in Figure 5.19. We note that at smaller heights, we need the higher eigenvalue terms for accuracy. At larger heights, keeping only the first term in the sums in (5.5.31)–(5.5.32) is sufficient to give good agreement with the numerics. It must be noted that, at large enough heights, the approximate similarity solution agrees well with the numerics and so the full solution is not so necessary here.

For the N volume bin model, where N is larger than 3, solutions when the values of K_i are repeated can be found similarly.

5.5.4 Discussion

When the breakup rate function K is non-monotonic, the form of the solution becomes more complicated. We have made some progress in finding a formula, (5.5.12), for the discrete volume ϕ_i using the approximate similarity solutions. In addition, the full similarity solution can be found by numerically solving the simple first order ODE given by (5.4.14) subject to (5.4.10), and using (5.4.8). However, finding a formula for the full solution for ϕ in cases beyond the three bin discrete model is fairly complicated.

We have been able to make more progress when using the simpler approximate similarity solutions since we only keep terms which decay the most slowly with height z. However, as we have discussed, neglecting higher eigenvalue terms is not the most



(a) $z = 6$ (b) $z = 10$

Figure 5.19: Drop size distribution for ϕ_2 in three bin case for constant breakup rate K. We consider a similar problem to that discussed in Figure 5.10 except we take $K_3 = K_3 = 1$. We solve numerically for $z > \hat{z}_n = 5$ and start the similarity solutions at $\hat{z} = 5.1$. We compare numerics (solid red), the approximate similarity solution (dashed black), the full solution with only the first eigenvalue term (dotted black), and the full solution with the first five eigenvalue terms (dash-dot black). (a) $z = 6$ (b) $z = 10$.

consistent approach. One possible alternative way forward would be to take the full similarity solution (with all the higher eigenvalue terms) and instead truncate terms with large breakup rates K. For these terms the exponent $m^n(K)$ of $1/\delta(z)$ is small and they will decay quickly at large z.

Let us consider the case where the breakup rate $K(v)$ increases from 0 at $v = 0$ to some maximum and then decreases. Then, since $m(K)$ is monotonically increasing, $m(v)$ will be given as illustrated in the schematic in Figure 5.20. Let v_B be the drop size at which $m(v_B) = m(1)$ and the region B be the region in which $v \in (v_B, 1]$, as shown in Figure 5.20. For $v \in B$, the leading order term in $\phi(v, \xi, z)$ will correspond to that with eigenvalue $m^1(1)$. For $v \approx v_B$ the leading order terms will be correspond to both the eigenvalue $m^1(1)$ and $m^1(v_B)$. For drop sizes smaller than v_B (namely region A depicted in Figure 5.20), the leading order term in $\phi(v, \xi, z)$ comes from its smallest eigenvalue $m^1(v)$. It will still depend on the behaviour of the larger drops but these will come into the coefficients C.

If the non-monotonic breakup rate behaves like $K(v) = v(1 - v)$ in that it is zero at $v = 0$ and $v = 1$, the situation becomes even simpler. The leading order terms in ϕ will always correspond to the behaviour near $v = 0$ and $v = 1$, namely the eigenvalues $m^1(0)$ and $m^1(1)$ respectively. In this case, instead of truncating higher eigenvalue terms in a somewhat *ad-hoc* way as in Section 5.5.2, we could more systematically

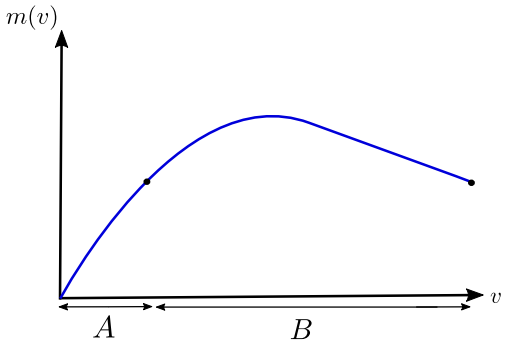


Figure 5.20: Schematic of $m(v)$ for an example when the breakup rate is non-monotonic.

truncate terms involving drop sizes where the breakup rate is large. We would only need to consider three drops sizes: $v \approx 0, v \approx 1$ and the intermediate sized drops between them. For large δ, ϕ would be asymptotically small everywhere except at boundary layers near $v = 0$ and $v = 1$, where its behaviour could be determined using boundary layer theory.

5.6 Conclusions

In this chapter, we find approximate analytical solutions for the drop size distribution ϕ. In Chapter 2, we used the self-similarity of a turbulent jet to obtain similarity solutions for the jet velocity and energy, and here we also do so for ϕ. We find that ϕ can be expressed in an unusual form, as the integral of a continuous family of second kind similarity solutions.

There is a cascade in information since, for each v, $\phi(v, \xi, z)$ depends on the drop size distribution of all of the drops larger than v. The basis of the solution for ϕ is the eigenvalues and eigenvectors of the linear operator, $L[K]$, where K is the droplet breakup rate. This linear operator is an ordinary differential operator in ξ, in which K acts as a parameter. For fixed K, $L[K]$ has an infinite set of eigenvalues m and eigenfunctions $g(\xi)$. The drop size distribution, $\phi(v, \xi, z)$, is made up of terms corresponding to all of the eigenvalues of all of the drop sizes greater than or equal to v. The eigenvalues m determine the exponents of z^{-1} in ϕ whilst the eigenfunctions encode the variation of ϕ with width variable ξ. Coefficients C depend on the breakup rate K, the daughter drop distribution χ, and the behaviour of ϕ at small z which is used to match to the non-self-similar flow.

We initially consider the case where the breakup rate is monotonic because, given this assumption, we can find analytic formulae for both approximate and full sim-

ilarity solutions for ϕ. The approximate solutions assume that at all heights, the higher eigenvalue terms in ϕ (which decay quicker at large z) are negligible. There are some inconsistencies in doing so, in particular in setting the coefficients C. So, for completeness, these are addressed by looking for a full solution including all higher eigenvalues. We do so by writing ϕ as a linear combination of the complete set of eigenfunctions for the operator $L[0]$ (which corresponds to the total oil fraction or the problem when there is no breakup). The formula for ϕ is slightly more complicated here in that the coefficients C are interdependent on higher eigenvalue terms.

Both the approximate and full similarity solutions agree well with numerics. In fact, despite the slightly *ad hoc* assumptions made by the approximate solution, it fits the numerics almost as well as the full similarity solution at larger heights, where the self-similar behaviour has had time to develop. In either case, these formulae for ϕ are far easier and quicker to compute than using the full numerical method described in Section 4.4.1.

After understanding the case where $K(v)$ is monotonic, we consider what happens when the breakup rate is non-monotonic. The form of this solution is more complicated as an additional series of logarithmic terms arises. To find the full solution, with all higher eigenvalues, we must solve the first order integro-differential equation, (5.4.14) subject to (5.4.10), for $\mathbf{b}$ and then $\phi = \mathbf{b} \cdot \mathbf{g}$, where the components of $\mathbf{g}$ are the eigenfunctions of $L[0]$. This can only be solved numerically in general. An approximate formula for ϕ can be found by truncating higher eigenvalue terms. Another possible way forward could be, instead, to truncate terms involving drop sizes where the breakup rate is large, as discussed in Section 5.5.4. At large z these drops would have already broken up and thus have little effect on the distributions of other drop sizes.

Throughout this chapter, in the breakup rate, we predominantly use the outer solution to the energy dissipation (2.4.35) as it makes the problem a little more tractable. However, we later find that using the full similarity solution (2.4.31)–(2.4.32) for the energy dissipation does not make the problem significantly harder and also agrees well with the numerics.

In all of the approaches in this chapter, we encounter some limitations in describing the true physical situation. We can never completely capture the behaviour at smaller z as we are using the similarity solution to the jet's velocities and energy dissipation, which is not valid for small z. Nevertheless, we find not only the leading order solution to ϕ but also higher order terms, which go some way in describing the behaviour at smaller heights. In addition, to make progress in this chapter we must impose certain

constraints on the breakup rate which may not best describe the physical situation. These constraints also mean that it is difficult as it stands to include models for the effect of surfactant addition.

Chapter 6

Surfactants

We have successfully modelled the distribution of droplet size in a turbulent jet. Interventions in oil spills usually involve spraying dispersants i.e. surfactants, so we now consider the effect of adding surfactants to the jet. Currently, models do not exist for the evolution of drop size distribution with varying surface tension. We determine the variation in the oil-water surface tension by modelling the concentration of surfactant adsorbed at the surface of the oil drops, following well established models for the behaviour of surfactant monomers and micelles and their effect on surface tension (Chang and Franses, 1995; Breward and Howell, 2004; Breward et al., 2015).

To better understand the effect of the surfactants on droplet breakup, we begin by modelling their effect without the complications of the jet's behaviour. We use an approach similar to that in Chapter 3: we model the evolution of the droplet size distribution with time, in a region of fixed energy dissipation. Jet effects, including advection, turbulent diffusion, and spatially varying energy dissipation, are then combined with the surfactant and droplet models to model surfactant addition in a turbulent jet.

The addition of surfactants makes the model more difficult to solve numerically. Therefore, for simplicity, we explore not only width-averaged models, but also those averaged over drop volume. This captures much of the basic physics of the system. We then extend these models to consider the full variation with droplet volume. As with the drop size distributions in Chapter 4, we evaluate the accuracy of our width-averaged models by comparing with experimental results (Brandvik et al., 2014, 2013; Johansen et al., 2013), which enables us to also fit any free parameters in the model.

6.1 Assumptions

We assume that, whilst the surfactant is advected and diffused by the turbulent jet, the presence of surfactant does not affect the jet's behaviour. (This is similar to our approach in Chapter 4, where we assume the presence of the oil droplets does not affect the evolution of the jet.) In reality, the addition of surfactants reduces the size of the oil droplets, thus affecting their buoyancy, and this has been experimentally observed to affect the plume structure over larger scales than those considered here (Murphy et al., 2016).

In oil spills, BP use the dispersant Corexit, which contains the surfactant Aerosol OT (AOT), and thus we predominantly set the parameters of our models to be consistent with using this surfactant. In the literature, AOT has many equivalent names, including di(2-ethylhexyl)sulfosuccinate sodium salt (DESS) and dioctyl sodium sulfosuccinate. The precise make-up of the Corexit dispersant is proprietary but the surfactant probably forms around 10-15 percent of the volume (personal communication, BP).

6.2 Surfactant models

6.2.1 Introduction to surfactants

Surfactants are organic compounds, made up of a hydrophilic (water-attracting) head and hydrophobic (water-repelling) tail. Rather than remain dissolved in a bulk water phase, it is more energetically favourable for a surfactant monomer to adsorb to an oil-water interface, with the hydrophobic tail expelled from the water. This reduces the oil-water surface tension. If the bulk surfactant concentration is large, as well as the hydrophobic tails adsorbing to the interface, they form aggregates in the bulk called micelles. A micelle consists of anywhere between 15 to 100 surfactant monomers (Moulik and Mukherjee, 1996; Alargova et al., 1998) grouped together so the hydrophilic heads of the surfactant monomers are in contact with the surrounding water whilst the hydrophobic tails are in the interior.[1] The bulk surfactant concentration above which these micelles form is called the CMC (critical micelle concentration).

[1] AOT is unusual in that the monomers and micelles are soluble in the oil, as well as the water. AOT is known to form reverse micelles in a bulk oil phase, where the hydrophilic heads are grouped together around a water drop and the hydrophobic tails are in the oil. For simplicity, we have neglected this effect so far in our models.

6.2.2 Relating surface tension to surfactant concentration

We measure the concentration of surfactant monomers, c, and micelles, c_m, in the bulk in units of moles per unit volume, while the surface concentration, Γ, is measured in moles of adsorbed surfactant per unit area. The addition of surfactant into a system increases Γ, which serves to reduce the surface tension σ.

We model the dependence of σ on Γ using the Frumkin equation (Chang and Franses, 1995),

$$\sigma = \sigma_0 + RT\Gamma_m \log\left(1 - \frac{\Gamma}{\Gamma_m}\right), \tag{6.2.1}$$

where σ_0 is the undisturbed surface tension (when there are no surfactants in the system), R is the gas constant, T is the (assumed constant) temperature, and Γ_m is the theoretical maximum surface concentration. We see that, as the surface concentration increases, the surface tension decreases from its undisturbed value σ_0. For the surface tension from (6.2.1) to be non-negative, the surface concentration must be lower than the critical value

$$\Gamma_c = \Gamma_m\left(1 - \exp\left(-\frac{\sigma_0}{RT\Gamma_m}\right)\right). \tag{6.2.2}$$

We present here a derivation of the Frumkin equation (6.2.1) under equilibrium conditions. The Gibbs adsorption equation states that, at a constant temperature T, the variation in surface tension σ due to a small change in the local bulk concentration c is given by

$$\delta\sigma = -RT\Gamma\frac{\delta c}{c}. \tag{6.2.3}$$

The Gibbs adsorption equation, (6.2.3), assumes that the surfactant concentration is below the CMC and the solution is dilute (Chang and Franses, 1995).

Let us assume that the adsorbed phase is in thermodynamic equilibrium with the surfactant monomers close to the interface. Then we can find a constitutive relation for $\Gamma(c)$ and so, by integrating (6.2.3), we can express surface tension as a function of surface concentration Γ. The most commonly used relation between the bulk and surface concentration is the Langmuir isotherm

$$\Gamma = \Gamma_m\frac{K_L c}{1 + K_L c}, \tag{6.2.4}$$

where K_L ($\mathrm{m^3\,mol^{-1}}$) is the Langmuir equilibrium adsorption constant. The Langmuir isotherm imposes that, with increasing $K_L c$, Γ increases and saturates to its maximum value, Γ_m. Combining (6.2.3) and (6.2.4), yields (6.2.1).

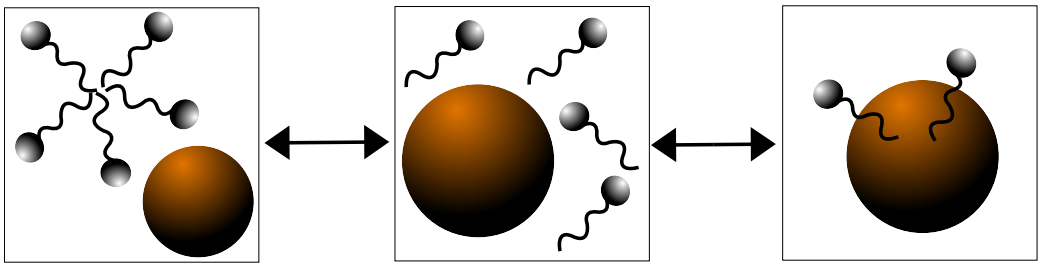


Figure 6.1: Schematic of interactions between surfactant micelles and monomers (grey), and oil drops (orange). Surfactant can exist as either aggregates of monomers called micelles (first panel) or free monomers (second panel). The micelles can disassociate into monomers and the monomers can aggregate into micelles. Only free monomers can adsorb onto the surface of an oil droplet (third panel). These adsorbed monomers can also disassociate from the droplet surface into the bulk, becoming free monomers.

The variation of surface tension with surface concentration is less well understood when the system is not in thermodynamic equilibrium or when the surfactant concentration is above the CMC. It is common in the literature to assume that (6.2.1) holds regardless (Chang and Franses, 1995), and, for simplicity, we will do likewise.

6.2.3 Surfactant interactions

Given (6.2.1), it remains to determine the surface concentration Γ. We do so by considering interactions between micelles, surfactant monomers and adsorbed surfactant, which are illustrated in Figure 6.1.

6.2.3.1 Formation of micelles

Surfactant in the bulk occurs as either monomers or micelles. Monomers can aggregate to form micelles or the micelles can break up into monomers (as illustrated in the first and second panels in Figure 6.1). The rate, j_m, at which surfactant monomers aggregate into micelles, is modelled, as in (Breward et al., 2015), using the law of mass action:

$$j_m = k_0^+ c^{N_m} - k_0^- c_m, \tag{6.2.5}$$

where k_0^+ and $k_0^-(\mathrm{s}^{-1})$ are the rates at which micelles are formed and break up, respectively. We suppose that all micelles consist of the same number N_m of monomers, which is typically large and so consider $N_m \gg 1$.

6.2.3.2 Adsorption of surface monomers onto droplets

Let us consider some small control volume V, made up of approximately spherical oil droplets in water with locally constant surface concentration Γ of surfactant. The total number, T_v, of moles of surfactant adsorbed on the surface of the drops of volume v in this control volume V is given by

$$T_v = 4\pi r_v^2 n_v \Gamma. \tag{6.2.6}$$

Here r_v is the radius of a drop of volume v, and n_v is the number of drops of volume v. Recall that the number of drops per unit volume is given by $\phi/v\,\mathrm{d}v$ so $n_v = (\phi/v\,\mathrm{d}v)\,V$, and hence

$$T_v = (6\sqrt{\pi})^{2/3}\frac{\phi}{v^{1/3}}\,\mathrm{d}v\Gamma V. \tag{6.2.7}$$

The total number of moles, per unit volume, on the surface of all drops is then

$$\frac{\int_0^{v_\infty} T_v\,\mathrm{d}v}{V} = (6\sqrt{\pi})^{2/3}\int_0^{v_\infty}\frac{\phi}{v^{1/3}}\,\mathrm{d}v\;\Gamma, \tag{6.2.8}$$

where we make the assumption that the surface concentration is independent of drop size. We set

$$S = (6\sqrt{\pi})^{2/3}\int_0^{v_\infty}\frac{\phi}{v^{1/3}}\,\mathrm{d}v \tag{6.2.9}$$

and so S is the droplet surface area per unit volume, and ΓS is the number of moles of adsorbed surfactant per unit volume.

The exchange flux, j_{sd} between adsorbed and dissolved surfactant monomer is modelled by the Langmuir-Hinshelwood equation (Chang and Franses, 1995) as

$$j_{sd} = -k_d\Gamma S + \frac{k_a}{\Gamma_m}c(\Gamma_m - \Gamma)S. \tag{6.2.10}$$

Here c is the surfactant concentration adjacent to the interface, and k_a ($\mathrm{m\,s^{-1}}$) and k_d ($\mathrm{s^{-1}}$) are parameters relating to the rates of adsorption and desorption, respectively. From the first term in (6.2.10), the rate of desorption is proportional to the concentration of monomers on the surface of the drops. The second term on the right hand side of (6.2.10) is non-linear: the rate at which monomers are adsorbed onto the surface is proportional to not only on the concentration of surfactant monomers in the bulk c, but also to the amount of uncovered surface available $(\Gamma_m - \Gamma)S$. In thermodynamic equilibrium, when the rates of adsorption and desorption are large, we recover the Langmuir isotherm (6.2.4), with $K_L = k_a/(k_d\Gamma_m)$.

6.2.3.3 Production of free monomers

Free monomers in the bulk are produced both when surfactant desorbs from the surface and when micelles break up, as seen in Figure 6.1. Hence the rate, j_c, at which monomers are produced is

$$j_c = -N_m j_m - j_{sd}. \tag{6.2.11}$$

Here the extra factor of N_m in the first term on the right hand side occurs because, when a micelle breaks, it produces N_m monomers.

Let us introduce $\mathcal{C}$, the total number of moles of surfactant per unit volume, given by

$$\mathcal{C} = c + \Gamma S + N_m c_m, \tag{6.2.12}$$

where a factor of N_m arises because a micelle is made up of N_m monomers. The rate of change of $\mathcal{C}$ is then

$$j_{\mathcal{C}} = j_c + j_{sd} + N_m j_m = 0, \tag{6.2.13}$$

so the total concentration of surfactant is conserved.

In summary, using the evolution equations for c, ΓS, c_m and $\mathcal{C}$ are given by

$$\frac{dc}{dt} = -N_m \left[k_0^+ c^{N_m} - k_0^- c_m\right] - \frac{k_a}{\Gamma_m} c(\Gamma_m - \Gamma)S + k_d \Gamma S, \tag{6.2.14}$$

$$\frac{d\left(\Gamma S\right)}{dt} = \frac{k_a}{\Gamma_m} c(\Gamma_m - \Gamma)S - k_d \Gamma S, \tag{6.2.15}$$

$$\frac{dc_m}{dt} = k_0^+ c^{N_m} - k_0^- c_m, \tag{6.2.16}$$

$$\frac{d\mathcal{C}}{dt} = 0, \tag{6.2.17}$$

where S is defined by (6.2.9) and $\mathcal{C}$ is given by (6.2.12).

6.2.4 Non-dimensionalisation

The effect of surfactants is modelled by (6.2.1), (6.2.9), (6.2.12) and (6.2.14)–(6.2.17). We non-dimensionalise with (3.1.15)–(3.1.16), $t = \tau t^*$, where the time-scale τ will be chosen later, and

$$c = c_{cmc} c^*, \quad \Gamma = \Gamma_m \Gamma^*, \quad S = \left(6\sqrt{\pi}\right)^{2/3} \psi v_\infty^{-1/3} S^*, \quad c_m = \frac{c_{cmc}}{N_m} c_m^*, \quad \mathcal{C} = c_{cmc} \mathcal{C}^*. \tag{6.2.18}$$

Here, as in Breward and Howell (2004), we define the CMC for the surfactant as

$$c_{cmc} = \left(\frac{k_0^-}{N_m k_0^+} \right)^{1/(N_m-1)}. \tag{6.2.19}$$

Then the dimensionless equations, with asterisks dropped, are

$$\sigma = 1 + \theta \log(1-\Gamma), \tag{6.2.20}$$

$$S = \int_0^1 \frac{\phi}{v^{1/3}} dv, \tag{6.2.21}$$

$$\frac{dc}{dt} = -\mathcal{K}_0 \left[c^{N_m} - c_m \right] - \mathcal{K}_a \mathcal{R}_0 \left[(1-\Gamma) c S - \eta \Gamma S \right], \tag{6.2.22}$$

$$\frac{d(\Gamma S)}{dt} = \mathcal{K}_a \left[(1-\Gamma) c S - \eta \Gamma S \right], \tag{6.2.23}$$

$$\frac{dc_m}{dt} = \mathcal{K}_0 \left[c^{N_m} - c_m \right], \tag{6.2.24}$$

$$\mathcal{C} = c + \mathcal{R}_0 \Gamma S + c_m, \tag{6.2.25}$$

where the dimensionless parameters are

$$\theta = \frac{RT\Gamma_m}{\sigma_0}, \quad \eta = \frac{k_d \Gamma_m}{k_a c_{cmc}}, \quad \mathcal{K}_0 = k_0^- \tau, \quad \mathcal{K}_a = \frac{\tau k_a c_{cmc}}{\Gamma_m}, \quad \mathcal{R}_0 = \frac{(6\sqrt{\pi})^{2/3} \psi \Gamma_m}{c_{cmc} v_\infty^{1/3}}. \tag{6.2.26}$$

Here, θ could be referred to as a Frumkin number (since it appears in the Frumkin equation). It measures the potential change in surface tension due to the variation in the adsorbed surfactant concentration. The parameter η is a Langmuir equilibrium constant, which corresponds to the ratio of the rate of surfactant desorption to the rate of adsorbtion. If η is small, surfactant monomers rapidly adsorb onto the droplet surface. The ratio between the rate at which micelles disassociate into monomers to the jet shear rate is given by $\mathcal{K}_0$. Similarly, $\mathcal{K}_a$ is the ratio at which monomers adsorb onto the surface of droplets to the shear rate. Finally, Γ_m / c_{cmc} is often associated with the length-scale of the layer of surfactant monomers on the surface of the drops whilst $v_\infty^{1/3}$ represents a typical droplet diameter. Thus, $\mathcal{R}_0$ corresponds to how much surfactant can typically be on the surface of the droplets compared to how much is in the bulk. If $\mathcal{R}_0$ is small much of the surfactant remains in the bulk.

Below, in Section 6.3, we will show how to close the system with an evolution equation for ϕ, thereby coupling (6.2.20)–(6.2.25) to a model of droplet breakup.

6.2.5 Equilibrium

In equilibrium, the association and disassociation between micelles, monomers and adsorbed surfactant occurs rapidly. Hence $\mathcal{K}_0$ and $\mathcal{K}_a$ are large, so the terms in square brackets in (6.2.22)–(6.2.24) are approximately zero. Then

$$c = \frac{\eta\Gamma}{1-\Gamma}, \quad \text{or equivalently} \quad \Gamma = \frac{c}{\eta + c} \tag{6.2.27}$$

and

$$c_m = c^{N_m}. \tag{6.2.28}$$

We can combine (6.2.27)–(6.2.28) with (6.2.25) to write (6.2.22)–(6.2.25) as

$$\mathcal{C} = c + \frac{\mathcal{R}_0 c S}{\eta + c} + c^{N_m}. \tag{6.2.29}$$

Given the total surfactant concentration $\mathcal{C}$ and surface area S, this yields c. Then c_m and Γ follow from (6.2.27)–(6.2.28).

Note, from (6.2.28) with $N_m \gg 1$, that if the free monomer concentration is less than the CMC, so $c < 1$, then $c_m \sim 0$; there are no micelles. If the free monomer concentration is slightly greater than the CMC i.e. $c \gtrsim 1$, then from (6.2.28) $c_m > 1$; micelles are being formed. For an $\mathcal{O}(1)$ value of $\mathcal{C}$, c cannot exceed 1 by more than $\mathcal{O}(1/N_m)$ so, once the bulk concentration reaches the CMC, it approximately stays there.

6.2.6 Parameter values from literature

The parameters N_m, Γ_m, k_0^-, k_a, c_{cmc} and $K_L = k_a/(k_d\Gamma_m)$ are properties of the surfactant. For the surfactant AOT, $\Gamma_m = 1.3 \times 10^{-6}\,\mathrm{mol\,m^{-3}}$, $c_{cmc} = 2.43\,\mathrm{mol\,m^{-3}}$ and $K_L = k_a/(k_d\Gamma_m) = 200\,\mathrm{m^3\,mol^{-1}}$ (Chang and Franses, 1992; Fan et al., 2005). A monomer of AOT contains a hydrophilic head and two hydrophobic tails so the minimum number of monomers in a micelle, 15, is smaller than that of many other surfactants. It is observed that N_m increases linearly with the square root of concentration of AOT (Moulik and Mukherjee, 1996) so it seems reasonable to take $N_m = 20$.

There is less certainty in the literature about the approximate sizes of both k_0^- and k_a. According to Chang and Franses (1995), micelles aggregate and disassociate very quickly, on a time-scale of one millisecond to seconds so $k_0^- = 1$–$1000\,\mathrm{s^{-1}}$. For convenience, we often set the rate of micellar disassociation as $k_0^- = 1000\,\mathrm{s^{-1}}$ as

this yields large values of $\mathcal{K}_0$ and so corresponds to the regime where micelles and monomers are in equilibrium. In the case where the surfactant is below the CMC, and thus where there is not a significant concentration of micelles, we have found that the value of the non-dimensional parameter, $\mathcal{K}_0$, (which is where k_0^- appears in the model) does not greatly affect the dynamics.

The parameter k_a describes the rate of adsorption of free monomers onto the interface. Chang and Franses (1992) fit this to experiments from Hua and Rosen (1988) and find that the value of k_a varies slightly with the initial surfactant concentration, c_0. When $c_0 = 0.584\,\mathrm{mol\,m^{-3}}$, they find $k_a = 9.3 \times 10^{-5}\,\mathrm{m\,s^{-1}}$ and when $c_0 = 0.884\,\mathrm{mol\,m^{-3}}$, $k_a = 5.6 \times 10^{-4}\,\mathrm{m\,s^{-1}}$. One option is to take some averaged value of these, say, $k_a = 2 \times 10^{-4}\mathrm{m\,s^{-1}}$. However, the dispersants used by oil producers contain not only the surfactants themselves but also a co-surfactant and additional salts which serve to increase k_a. These make up 85–90 percent of the volume of the dispersant so will have a significant effect. Therefore, we are not completely confident of the order of magnitude of k_a in the dispersant used in a real oil spill. We, instead, treat this as a fitting parameter. Later in this chapter, by fitting to experiments, we will find that $k_a = \mathcal{O}(10^{-2})$–$\mathcal{O}(10^{-1})\,\mathrm{m\,s^{-1}}$.

We note the gas constant is $R = 8.314\,\mathrm{J\,K^{-1}\,mol^{-1}}$ and assume the system is at room temperature so $T = 300\,\mathrm{K}$.

Other parameters are dependent on the droplets. The total oil fraction injected into the jet, ψ, is assumed to be small; we take it to be $\psi = 0.2$ here. We take the largest drop size, v_∞, to correspond to the jet nozzle width. In a realistic ocean setting the nozzle diameter is $D = 0.5\,\mathrm{m}$ so $v_\infty = 0.130\,\mathrm{m}^3$. The time-scale here, τ, is the shear time-scale, in the jet, defined as D/W_0. If, say $W_0 = 10\,\mathrm{m\,s^{-1}}$, then $\tau = 0.05\,\mathrm{s}$.

All of the above means that the sizes of the dimensionless parameters are approximately $\theta = \mathcal{O}(10^{-1})$, $\mathcal{K}_a\mathcal{R}_0 = \mathcal{O}(10^{-2})$, $\eta = \mathcal{O}(10^{-3})$, $\mathcal{R}_0 = \mathcal{O}(10^{-6})$, $\mathcal{K}_a = \mathcal{O}(10^4)$ and $\mathcal{K}_0 = \mathcal{O}(10^{-1})$–$\mathcal{O}(10^2)$.

The relative sizes of these parameters yield some useful initial insights. From (6.2.23), since $\mathcal{K}_a$ is large, the surfactant very quickly adsorbs onto the surface of the droplets. Similarly if we assume that k_0^- is large enough that $\mathcal{K}_0$ is large, then the micelles and free monomers are in equilibrium and the micelles in the surfactant very quickly disassociate. In addition, since $\mathcal{R}_0$ is small, by (6.2.25), it seems that most of the total surfactant remains in the bulk and only a small fraction adsorbs onto the drops.

In the small-scale experiments by SINTEF (Brandvik et al., 2014, 2013; Johansen et al., 2013), three of the non-dimensional parameters have different sizes: $\mathcal{K}_0$, $\mathcal{R}_0$ and $\mathcal{K}_a$. The nozzle diameter, D, is approximately $D = \mathcal{O}(10^{-3})\,\mathrm{m}$ and the outlet velocity, W_0, is approximately $W_0 = \mathcal{O}(10)\,\mathrm{m\,s^{-1}}$ so the shear time-scale is $\tau = \mathcal{O}(10^{-4})\,\mathrm{s^{-1}}$. This is significantly smaller than in a real-life scenario. Hence, $\mathcal{K}_0 = \mathcal{O}(10^{-4})$–$\mathcal{O}(10^{-1})$, so the disassociation of micelles into monomers is slow. Secondly, if we suppose the largest drop size corresponds to the nozzle diameter, then $v_\infty = \mathcal{O}(10^{-9})\,\mathrm{m^3}$ which means that $\mathcal{R}_0 = \mathcal{O}(10^{-4})$. This is two orders of magnitude larger than the real scenario but is still small and so has a similar effect in (6.2.25). Thirdly, the parameter $\mathcal{K}_a$ has size $\mathcal{O}(10)$ rather than around $\mathcal{O}(10^4)$. Although this is still large, it does have some effect on the surfactant behaviour. Since the rate at which the surfactant adsorbs onto the drops is not that much larger than the shear rate, the surface surfactant and surfactant monomers do not go into equilibrium as rapidly as they do in a more realistic scenario. Therefore, the scalability of the experimental results is somewhat questionable.

6.3 Zero-dimensional model

We now examine how the addition of surfactants interacts with droplet breakup. In this section we consider a simple 'box model', similar to that presented in Chapter 3, which is zero-dimensional in that it only varies with time. We imagine the fluid is subject to some constant energy dissipation which causes the droplets to break up. Surfactant is injected into the box at time $t = 0$ and we track how this brings about droplet breakup. By first using this simple box model, we can more fully understand the interaction between the surfactant and the drops without the additional complications which arise from the jet dynamics.

6.3.1 Model

Using the model for $\phi(v,t)$ from (3.1.17) and the surfactant model (6.2.20)–(6.2.25), the drop size distribution is modelled by

$$\frac{\partial \phi}{\partial t} = -\gamma(v,\epsilon,\sigma)\phi(v,t) + \int_v^1 \gamma(\tilde{v},\epsilon,\sigma)\chi(v,\tilde{v})\phi(\tilde{v},t)\,\mathrm{d}\tilde{v}, \tag{6.3.1}$$

$$S = \int_0^1 \frac{\phi}{v^{1/3}}\,\mathrm{d}v, \tag{6.3.2}$$

$$\sigma = 1 + \theta\log(1-\Gamma), \tag{6.3.3}$$

$$\frac{dc}{dt} = -\mathcal{K}_0\left[c^{N_m} - c_m\right] - \mathcal{K}_a\mathcal{R}_0\left[(1-\Gamma)cS - \eta\Gamma S\right], \tag{6.3.4}$$

$$\frac{d(\Gamma S)}{dt} = \mathcal{K}_a\left[(1-\Gamma)cS - \eta\Gamma S\right], \tag{6.3.5}$$

$$\frac{dc_m}{dt} = \mathcal{K}_0\left[c^{N_m} - c_m\right], \tag{6.3.6}$$

$$\mathcal{C} = c + \mathcal{R}_0\Gamma S + c_m. \tag{6.3.7}$$

Adding (6.3.4)–(6.3.6), we see that $d\mathcal{C}/dt = 0$, which reflects the fact that no additional surfactant is added at later times and $\mathcal{C}$ remains fixed at its initial value, $\mathcal{C}_0$, for all $t > 0$. Hence $\mathcal{C} \equiv \mathcal{C}_0$. This means that instead of having to solve the three differential equations, (6.3.4)–(6.3.6), for $c, \Gamma S$ and c_m, we only need to solve two of these, say (6.3.5)–(6.3.6), and the third quantity, c, is determined using (6.3.7), namely using

$$\mathcal{C}_0 = c + \mathcal{R}_0\Gamma S + c_m. \tag{6.3.8}$$

At $t = 0$, surfactant is added to the system. There is initially no surfactant on the oil drops and we assume that the micelles and monomers in the injected surfactant are already in equilibrium with each other. Hence, the initial conditions are given by

$$c = c_0, \quad c_m = c_0^{N_m}, \quad \Gamma = 0, \tag{6.3.9}$$

where, from (6.3.7), c_0 and the total surfactant concentration, $\mathcal{C}_0$, are related using $\mathcal{C}_0 = c_0 + c_0^{N_m}$. The drop size distribution ϕ is also specified at $t = 0$.

6.3.2 Moments

To simplify the model (6.3.1)–(6.3.7), instead of considering the full-volume range, we take moments of the equation for the drop size distribution, (6.3.1), and then impose a simplified form for ϕ, which can be more easily solved.

Let us multiply (6.3.1) by v^n and then integrate from $v = 0$ to $v = 1$ to yield

$$\frac{d}{dt}\int_0^1 v^n\phi\,\mathrm{d}v = -\int_0^1 v^n\gamma(v,\epsilon,\sigma)\phi(v,t)\,\mathrm{d}v + \int_0^1\int_v^1 v^n\gamma(\tilde{v},\epsilon,\sigma)\chi(v,\tilde{v})\phi(\tilde{v},t)\,\mathrm{d}\tilde{v}\,\mathrm{d}v. \tag{6.3.10}$$

We approximate the drop size distribution with a delta-function of the form

$$\phi = \Phi_0\delta_v(v - \overline{v}(t)), \tag{6.3.11}$$

so at time t the distribution is localised around the average volume $\overline{v}(t)$. (Note that here δ_v is the Dirac delta function.) Then from the first moment, taking $n = 0$ in (6.3.10), we recover the equation, (3.1.13), for the conservation of total oil fraction, namely $d\Phi/dt = 0$. Taking $n = 1$ yields

$$\frac{d\overline{v}}{dt} = \gamma(\overline{v},\epsilon,\sigma)\left[-\overline{v} + \int_0^{\overline{v}}\chi(v,\overline{v})v\,\mathrm{d}v\right]. \tag{6.3.12}$$

We take the simplest possible form for χ, setting it to be uniform so $\chi(v,\overline{v}) = 1/\overline{v}$ so that (6.3.12) reduces to

$$\frac{d\overline{v}}{dt} = -\frac{\gamma(\overline{v},\epsilon,\sigma)\overline{v}}{2}. \tag{6.3.13}$$

Initially, the drops are all assumed to be the largest possible size so

$$\overline{v}(0) = 1. \tag{6.3.14}$$

It remains to set the breakup rate, γ. We use the simplest possible form which encapsulates the dependence of droplet breakup on surface tension. The scaling law

$$\gamma = K_0\frac{\epsilon^{3/5}}{\sigma^{2/5}}, \tag{6.3.15}$$

from (3.2.10) is, therefore, used here. Note that (6.3.15) depends only on energy dissipation and surface tension, and not droplet size. A more complex breakup rate will be considered in Section 6.3.5.

The assumed form of ϕ in (6.3.11) immediately sets S as

$$S = \frac{\Phi_0}{\overline{v}^{1/3}} \tag{6.3.16}$$

so, as the drop size decreases with time, the droplet surface area increases.

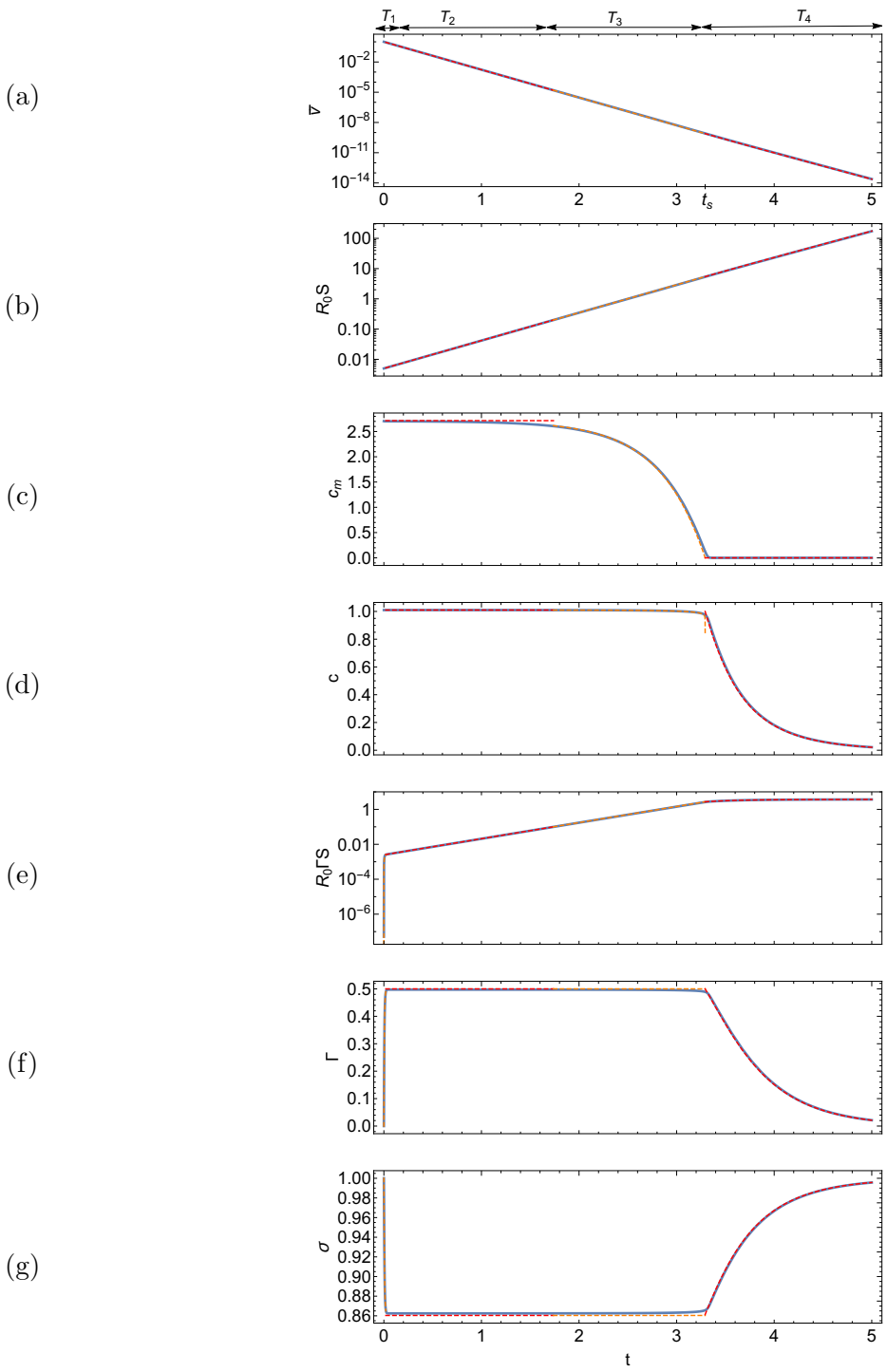


Figure 6.2: Solution to (6.3.3)–(6.3.7), (6.3.13) and (6.3.16), with breakup rate (6.3.15) and initial conditions (6.3.14) and (6.3.9) with $c_0 = 1 + 1/N_m$. We set $\mathcal{R}_0 = 1/\mathcal{K}_0 = 1/\mathcal{K}_a = 1/N_m = 10^{-2}$ and $\eta = 1$, $\Phi_0 = 0.5$, $\gamma_0 = 6$ and $\theta = 0.2$. Numerical solution is shown in blue. Asymptotics are shown in dashed lines (orange for T_1 and T_3, red for T_2 and T_4). (a) Average drop volume $\bar{v}$; (b) drop surface area $\mathcal{R}_0 S$; (c) micelle concentration c_m; (d) free monomer concentration c; (e) adsorbed surfactant concentration per unit volume, $\mathcal{R}_0 \Gamma S$; (f) adsorbed surfactant concentration per unit area, Γ; (g) surface tension σ.

6.3.3 $\mathcal{R}_0$, $1/\mathcal{K}_0$, $1/\mathcal{K}_a$, $1/N_m$ small

We first consider the simplest situation, which captures most of the important features of the problem. We take parameter values consistent with the real-life scenario discussed in Section 6.2.6. The surfactant monomers are assumed to rapidly disassociate from micelles and rapidly adsorb onto the droplet surfaces. This corresponds to considering large values of $\mathcal{K}_0$ and $\mathcal{K}_a$, respectively. We also take N_m, the number of monomers in a micelle, to be large, and $\mathcal{R}_0$ to be small. Let us set ε to be a small parameter and suppose

$$\mathcal{K}_0 = \varepsilon^{-1}\hat{\mathcal{K}}_0, \quad \mathcal{K}_a = \varepsilon^{-1}\hat{\mathcal{K}}_a, \quad N_m = \varepsilon^{-1}\hat{N}_m, \quad \mathcal{R}_0 = \varepsilon\hat{\mathcal{R}}_0, \tag{6.3.17}$$

where the hatted quantities are $\mathcal{O}(1)$. From Section 6.2.6, we know that η should be small but, for simplicity, we take $\eta = \mathcal{O}(1)$ here. We will discuss the behaviour for small η in Section 6.3.4. The parameter θ in the equation, (6.3.3), for surface tension is also taken to be order one.

Then, the equations (6.3.3)–(6.3.8) and (6.3.13)–(6.3.16) with breakup rate (6.3.15) can be written as

$$\frac{d\overline{v}}{dt} = -\gamma_0 \left[1 + \theta \log(1-\Gamma)\right]^{-2/5} \overline{v}, \tag{6.3.18}$$

$$S = \frac{\Phi_0}{\overline{v}^{1/3}}, \tag{6.3.19}$$

$$\varepsilon\frac{d(\Gamma S)}{dt} = \hat{\mathcal{K}}_a \left[(1-\Gamma)c - \eta\Gamma\right] S, \tag{6.3.20}$$

$$\varepsilon\frac{dc_m}{dt} = \hat{\mathcal{K}}_0 \left[c^{\hat{N}_m/\varepsilon} - c_m\right], \tag{6.3.21}$$

$$\mathcal{C}_0 = c + \varepsilon\hat{\mathcal{R}}_0\Gamma S + c_m. \tag{6.3.22}$$

Here (6.3.18) is (6.3.13), with breakup rate (6.3.3) and surface tension given by (6.3.15), and $\gamma_0 = K_0\epsilon^{3/5}/2$ is a constant. Let us suppose at $t = 0$, the initial conditions are given by (6.3.14) and (6.3.9) with $c_0 = 1 + 1/N_m = 1 + \varepsilon/\hat{N}_m$ so the surfactants are injected into the system above the CMC.

We find that there are four time periods, T_1 to T_4, where different behaviour can be observed. These are illustrated in Figure 6.2 for parameter values $\eta = 1$, $\Phi_0 = 0.5$, $\gamma_0 = 6$ and $\theta = 0.2$. We also take $\mathcal{R}_0 = 1/\mathcal{K}_0 = 1/\mathcal{K}_a = 1/N_m = 10^{-2}$.

T_1 In T_1, for $t \lesssim \mathcal{O}(\varepsilon)$, all the terms in (6.3.20) balance. Other than Γ, all other quantities are constant and set by their initial values. Solving (6.3.20) yields

$$\Gamma \sim \frac{c_0}{c_0+\eta}\left[1 - \exp\left(-\varepsilon^{-1}\hat{\mathcal{K}}_a(c_0+\eta)t\right)\right]. \tag{6.3.23}$$

We see that the system very quickly moves into equilibrium as the rate at which the surfactant adsorbs onto droplet surfaces is large. From (6.3.3), we see that the surface tension, in turn, rapidly decreases.

Once, $t \gg \mathcal{O}(\varepsilon)$, the two terms on the right hand side of (6.3.20) balance and the left hand side is asymptotically smaller; so the equation for Γ asymptotes to (6.2.27). Similarly, the equation, (6.3.21), for c_m asymptotes to (6.2.28), and the system is therefore in equilibrium. In the time periods T_2 and T_3, $c > 1$ so the system is above the CMC, whilst in T_4, $c < 1$.

T_2 The time period T_2 is that where $t \gg \varepsilon$. Here micelles are present and c is close to one so we let

$$c \sim 1 + \varepsilon \frac{c_1}{\hat{N}_m}. \tag{6.3.24}$$

Substituting this into (6.3.22), we find that

$$c_m \sim \mathcal{C}_0 - 1. \tag{6.3.25}$$

From (6.2.28), $c_m \sim \exp(c_1)$ so

$$c_1 \sim \log(\mathcal{C}_0 - 1). \tag{6.3.26}$$

In addition, since $c \sim 1$, from (6.2.27), we obtain

$$\Gamma \sim \frac{1}{\eta + 1}, \tag{6.3.27}$$

which we note matches with (6.3.23). The constant surfactant surface concentration gives rise to a constant surface tension

$$\sigma \sim 1 + \theta \log\left(\frac{\eta}{\eta + 1}\right). \tag{6.3.28}$$

This result is of particular interest since, as illustrated in Figure 6.2(g), it represents the maximum reduction in surface tension due to surfactants. Using (6.3.28) in (6.3.18) yields

$$\overline{v} \sim \exp\left(-\gamma_c t\right), \tag{6.3.29}$$

where

$$\gamma_c = \gamma_0 \left[1 + \theta \log\left(\frac{\eta}{\eta + 1}\right)\right]^{-2/5}. \tag{6.3.30}$$

Hence, from (6.3.19),

$$S = \Phi_0 \exp\left(\frac{\gamma_c}{3} t\right). \tag{6.3.31}$$

We observe that, whilst drops are breaking up and increasing the droplet surface area, the surfactant concentrations do not depend on droplet breakup and are approximately constant. Even though the surfactant must be shared with an exponentially increasing droplet surface area, there is enough surfactant that only a negligibly small decrease in c and c_m is needed to maintain the same surface concentration per unit area, Γ.

T_3 By some time $t = \mathcal{O}(1/\gamma_c \log(1/\varepsilon))$, the droplet surface area S will have increased such that $\varepsilon S = \mathcal{O}(1)$. Then the increase in surface surfactant, $\varepsilon\hat{\mathcal{R}}_0\Gamma S$, in (6.3.22), will cause an appreciable decrease in c and c_m. We scale,

$$S = \varepsilon^{-1}\hat{S}, \tag{6.3.32}$$

where $\hat{S} = \mathcal{O}(1)$, and

$$\overline{v} = \varepsilon^3 \hat{v}, \tag{6.3.33}$$

where $\hat{v} = \mathcal{O}(1)$. (Note that with these scalings, (6.3.19) still holds for $\hat{S}$ and $\hat{v}$.) In this region c is still close to one so we again obtain (6.3.27)–(6.3.31). However, if we use (6.3.24) in (6.3.22), we find

$$c_m \sim \mathcal{C}_0 - 1 - \frac{\hat{\mathcal{R}}_0\hat{S}}{1+\eta} \sim \mathcal{C}_0 - 1 - \frac{\varepsilon\hat{\mathcal{R}}_0\Phi_0}{1+\eta}\exp\left(\frac{\gamma_c}{3}t\right), \tag{6.3.34}$$

where the second equality comes from (6.3.31). Then, using $c_m \sim \exp(c_1)$,

$$c_1 \sim \log\left(\mathcal{C}_0 - 1 - \frac{\varepsilon\hat{\mathcal{R}}_0\Phi_0}{1+\eta}\exp\left(\frac{\gamma_c}{3}t\right)\right). \tag{6.3.35}$$

Here, monomers are still constantly adsorbing onto the surface of the drops and the surface concentration per unit area, Γ, is still maintained as the same constant value as in T_2. However, the surfactant has started to run out. In disassociating into free monomers and adsorbing onto the surface of droplets, the micelle concentration starts to rapidly decrease. In turn, the concentration of free monomers decreases as their main source (the micelles) is being depleted.

Eventually, from (6.3.34), all the micelles have disassociated and $c_m = 0$ at

$$t = t_s = \frac{3}{\gamma_c}\log\left(\frac{(\eta+1)(\mathcal{C}_0-1)}{\varepsilon\hat{\mathcal{R}}_0\Phi_0}\right). \tag{6.3.36}$$

At this time, $\hat{v} = v_s = \varepsilon^{-3}\exp(-\gamma_c t_s)$. Note that the assumed form of the free monomer concentration, given by (6.3.24) and (6.3.35), ceases to make sense once the argument of the log in (6.3.35) reaches zero. This occurs when $t = t_s$.

$\boldsymbol{T_4}$ In T_4, the free monomer concentration c is now less than one and so, from (6.2.28), $c_m \sim 0$. Using (6.3.22) and (6.2.27), we find that the free monomer concentration is given by

$$\mathcal{C}_0 \sim c + \frac{\hat{\mathcal{R}}_0 \hat{S} c}{\eta + c}. \tag{6.3.37}$$

Using (6.3.3) and (6.2.27) to express the breakup rate (6.3.15) in terms of only c and $\hat{S}$, and using (6.3.37) to express c in terms of only S, we find that (6.3.18) yields

$$\frac{d\hat{v}}{dt} = -\gamma_0 \hat{v}\left[1 + \theta \log\left(\frac{2\eta}{\eta - \hat{\mathcal{R}}_0\hat{S} + \mathcal{C}_0 + \sqrt{(\eta + \hat{\mathcal{R}}_0\hat{S} - \mathcal{C}_0)^2 + 4\eta\mathcal{C}_0}}\right)\right]^{-2/5}, \tag{6.3.38}$$

with $\hat{S} = \Phi_0 \hat{v}^{-1/3}$. This is a separable autonomous first-order ODE for $\hat{v}$ with matching condition $\hat{v}(t_s) = v_s$. Note that (6.3.38) implies that $\hat{v}$ decreases exponentially and so $\hat{S}$ increases exponentially. The solution to (6.3.38) is plotted in Figure 6.2(a) and we note in Figure 6.2(d) that there is a corresponding rapid decrease in the free monomer concentration c. In this regime, the drop surface area is still increasing but there are no micelles to supply surfactant monomers to the increased droplet surface area and so both c and consequently Γ decrease. The surface tension, in turn, begins to increase.

At longer times, the free monomer concentration c has decreased such that $c \sim 0$ and so there is now no supply for the droplet adsorbed surfactant. From (6.3.22), we see that $\hat{\mathcal{R}}_0 \Gamma \hat{S} \sim \mathcal{C}_0$: all the surfactant monomers have now adsorbed to the droplets and the surface surfactant concentration per unit volume is constant. New droplet area is still being created so Γ decreases like $\hat{S}^{-1}$. Therefore, the surface tension increases to its undisturbed value, $\sigma = 1$.

In Figure 6.2 we compare the results of our asymptotics to the numerical solution of (6.3.18)–(6.3.22), subject to (6.3.9) and (6.3.14). We see good agreement over all four time regimes.

The discussion here highlights that $\mathcal{K}_a$ is an important parameter because it determines how quickly the system reaches equilibrium in (6.3.23). We also note that the smallness of $\mathcal{R}_0$ is significant; it enables σ to remain at its minimum constant value

without the increase in droplet area reducing the efficacy of the surfactant. Only once the droplet surface area has increased so much that $\mathcal{R}_0 S = \mathcal{O}(1)$ does c_m start to decrease, which eventually causes c to decrease, Γ to decrease and thus σ to increase. Since the breakup rate, (6.3.15), allows all sizes of drops to break up, S can increase without bound and so this increase in σ will always ultimately occur. Finally, it is important to mention that η is an important parameter as it controls the minimum surface tension in (6.3.28); smaller values of η will result in lower values of the surface tension.

6.3.4 Small η

We have thus far assumed that η is an order one parameter when it is, in fact, small. We now verify that the conclusions we have made are still applicable. In Figure 6.3 we illustrate the numerical results for the same problem as Figure 6.2 but with $\eta = 10^{-2}$. We find that the behaviour is very similar to the behaviour when η is order one, and the key features can be explained by the η order one asymptotics. The asymptotics for small η are similar. One important difference is the behaviour in the region T_2. Here the evolution of c and c_m is again given by (6.3.24)–(6.3.26). However, assuming $\mathcal{K}_a \eta = \mathcal{O}(1)$, Γ now depends on the evolution of the droplet surface area, through $(-1/S)dS/dt$. We set $\eta = \varepsilon\hat{\eta}$. From (6.3.20), the adsorbed surfactant concentration is given by

$$\Gamma \sim 1 - \varepsilon\Gamma_1, \tag{6.3.39}$$

with

$$\frac{1}{S}\frac{dS}{dt} = \hat{\mathcal{K}}_a \left[\Gamma_1 - \hat{\eta}\right]. \tag{6.3.40}$$

In this case, since we use moments to average over volume, we can use (6.3.18)–(6.3.19) to write

$$\frac{1}{S}\frac{dS}{dt} = \frac{\gamma_0}{3}\left[1 + \theta \log\left(\varepsilon\Gamma_1\right)\right]^{-2/5}. \tag{6.3.41}$$

Then equating (6.3.40)–(6.3.41), Γ_1 is a constant, given implicitly by

$$\Gamma_1 = \hat{\eta} + \frac{\gamma_0}{3\hat{\mathcal{K}}_a}\left[1 + \theta \log\left(\varepsilon\Gamma_1\right)\right]^{-2/5}. \tag{6.3.42}$$

Hence, in T_2, the evolution of c and c_m is decoupled from that of Γ, S and $\overline{v}$, and Γ and S are now interdependent. Further details are given in Appendix B.1.

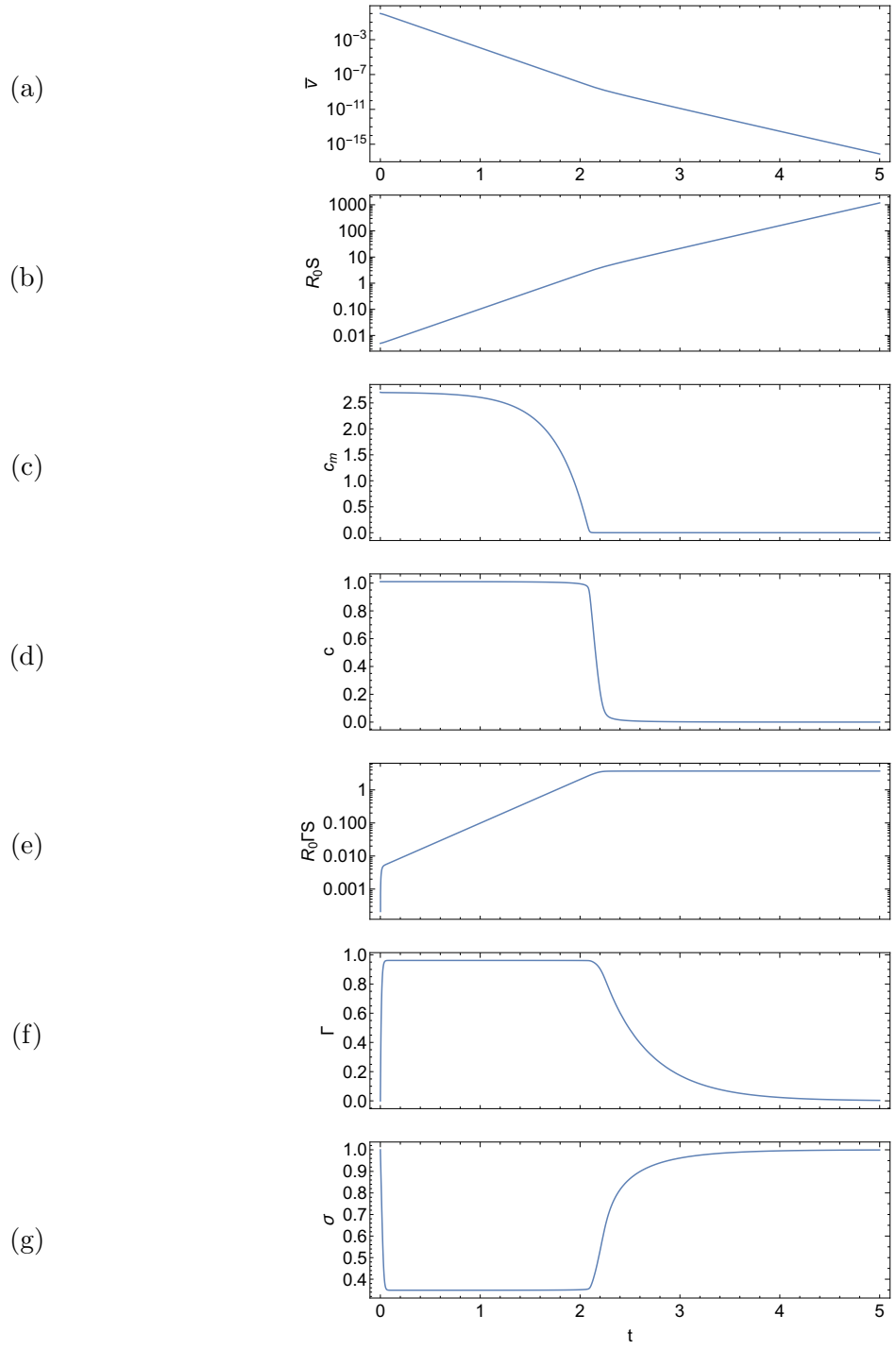


Figure 6.3: Numerical solution to (6.3.3)–(6.3.7), (6.3.13) and (6.3.16), with breakup rate (6.3.15) and initial conditions (6.3.14) and (6.3.9) with $c_0 = 1 + 1/N_m$. We set $\eta = \mathcal{R}_0 = 1/\mathcal{K}_0 = 1/\mathcal{K}_a = 1/N_m = 10^{-2}$ and $\Phi_0 = 0.5$, $\gamma_0 = 6$ and $\theta = 0.2$. (a) Average drop volume $\bar{v}$; (b) drop surface area $\mathcal{R}_0 S$; (c) micelle concentration c_m; (d) free monomer concentration c; (e) adsorbed surfactant concentration per unit volume, $\mathcal{R}_0 \Gamma S$; (f) adsorbed surfactant concentration per unit area, Γ; (g) surface tension σ.

6.3.5 Full distribution model

We now relax the constraint, (6.3.11), which imposes that the distribution ϕ is concentrated about a particular drop size. In addition, we use a more complex breakup rate, which has some volume dependence, given by

$$\gamma = K_0 v^{-2/9}\epsilon^{1/3}\left(1 - C_1\sigma v^{-5/9}\epsilon^{-2/3}\right)^{1/2}\mathcal{H}\left(1 - C_1\sigma v^{-5/9}\epsilon^{-2/3}\right), \tag{6.3.43}$$

with non-dimensional parameters

$$K_0 = K_{00}D^{2/3}v_\infty^{-2/9} \tag{6.3.44}$$

and

$$C_1 = \frac{C^{5/3}(\pi/6)^{5/9}\sigma_0 D^{2/3}}{\rho W_0^2 v_\infty^{5/9}} \tag{6.3.45}$$

as in (3.2.20). The model (6.3.43) was used extensively in Chapter 4. Recall it includes a Heaviside term which imposes that small droplets, subject to high surface stresses, cannot break up. We take the values of the non-dimensional parameters as $K_0 = 42.72$ and $C_1 = 1.76 \times 10^{-6}$.

The full-volume model (6.3.1)–(6.3.7) is solved numerically, using the method of lines. We discretise drop size uniformly in $\log d$, using 500 bins. We suppose that the daughter drop distribution is given by (3.2.32). Non-dimensional parameters are taken to be $\theta = 0.11$, $\mathcal{K}_0 = 10$, $\mathcal{K}_a = 186.93$, $\mathcal{R}_0 = 3.21 \times 10^{-5}$, $\eta = 2.06 \times 10^{-3}$ and $N_m = 20$. We also take $\epsilon = 0.2$. At $t = 0$, we take the initial drop size distribution to be proportional to $F(v)$ in (4.4.6) and normalise so the total oil fraction $\int_0^1 \phi \, \mathrm{d}v = 1$ initially.

Our results are shown in Figure 6.4. The drop size distribution evolves similarly to the no surfactant case in Section 3.3. But, as seen in Figure 6.4(a)–(c), adding surfactant increases droplet breakup and so more small droplets and a greater droplet surface area is produced.

As in Sections 6.3.3–6.3.4, we observe a decrease in the mean drop size, $\int_0^1 v\phi \, \mathrm{d}v$, in Figure 6.4(b). The Heaviside term in the breakup rate imposes that smaller drops cannot break up. This means that once all the droplets have become smaller than some critical volume, droplet breakup ceases and a steady state is reached. Thus, for around $t > 1.2$, the mean drop size is constant in Figure 6.4(b). We gain further insights by examining the full distribution in Figure 6.4(a). As in Section 3.3, there is a spike in the distribution at smaller volumes. This occurs at the critical drop size, d_{max}; the surface stresses on droplets smaller than d_{max} are too large for these drops

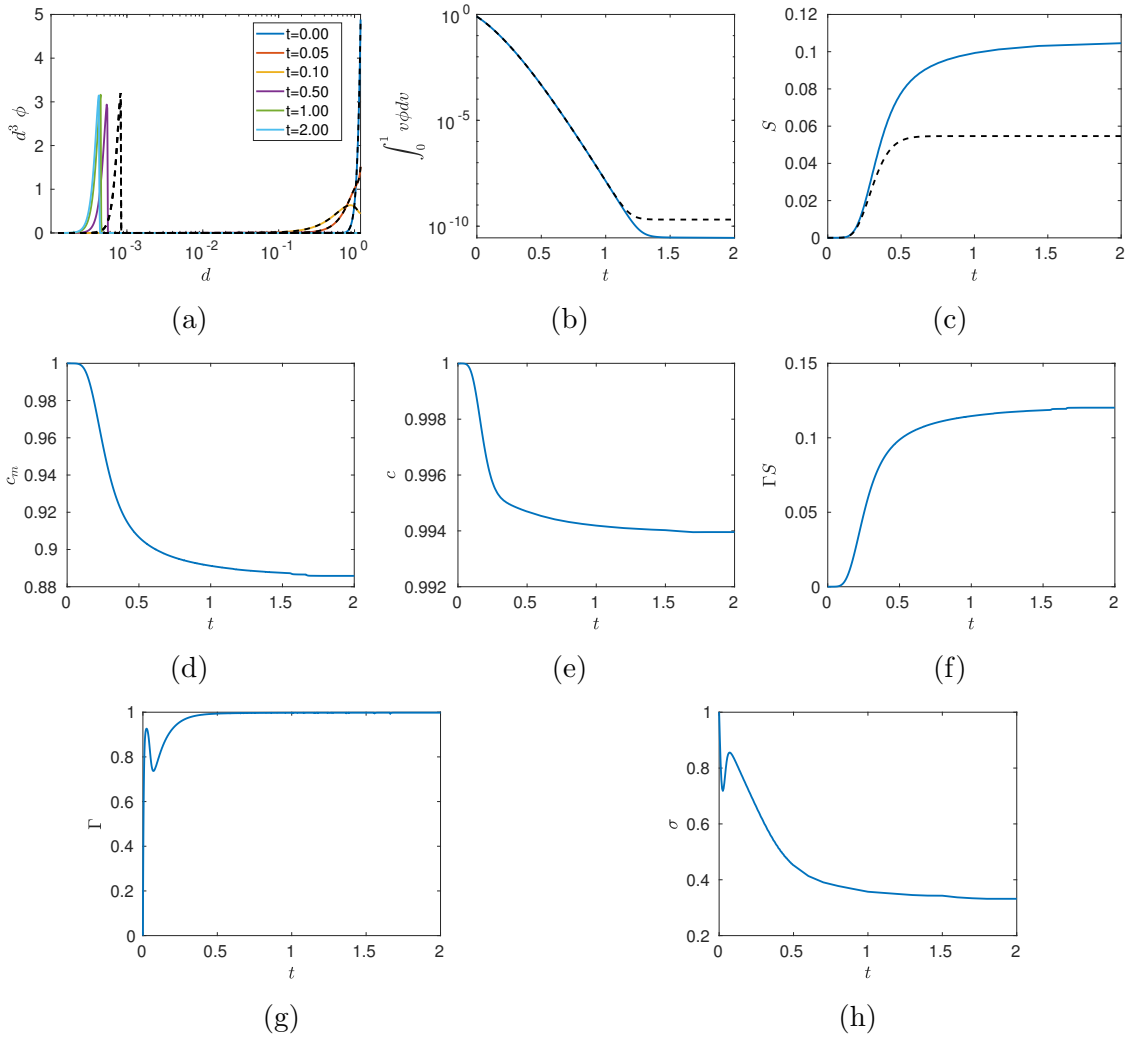


Figure 6.4: Full numerical solution for droplet and surfactant behaviour with time, using more realistic breakup rate (6.3.43) and full-volume range. We suppose that the daughter drop distribution is given by (3.2.32). Non-dimensional parameter values are given by $\theta = 0.11$, $\mathcal{K}_0 = 10$, $\mathcal{K}_a = 186.93$, $\mathcal{R}_0 = 3.21 \times 10^{-5}$, $\eta = 2.06 \times 10^{-3}$ and $N_m = 20$. In the breakup rate (6.3.43), we take $K_0 = 42.72$ and $C_1 = 1.76 \times 10^{-6}$, and set $\epsilon = 0.2$. At $t = 0$, the drop size distribution is set to be proportional to $F(v)$ in (4.4.6). (a) Drop size distribution $d^3\phi$ at different fixed times; (b) mean drop size $\int_0^1 v\phi\,\mathrm{d}v$ (equivalent to $\bar{v}$ in Sections 6.3.3–6.3.4); (c) droplet surface area S; (d) micelle concentration c_m; (e) free monomer concentration c; (f) concentration of adsorbed surfactant per unit volume, ΓS; (g) concentration of adsorbed surfactant per unit area, Γ; (h) surface tension σ. In (a)–(c) we also illustrate the corresponding quantities when there is no surfactant (see dotted black line).

to break up. The spike is caused by all larger drops breaking into this and smaller drop sizes.

The qualitative behaviour here is similar to the smaller time behaviour in the averaged volume approach, illustrated in Figure 6.3. The main difference is that the magnitude of S is much smaller here than when using the averaged volume approach. This is due to both the Heaviside term in (6.3.43) and the fact that we have now included the full-volume range. The surface area per unit volume, $\mathcal{R}_0 S$, never reaches order one. This means that, unlike in Section 6.3.3, the droplet surface area does not increase enough that the surfactant runs out. In fact, the majority remains in the bulk, and c and c_m are not significantly lower than their initial values. Since its source does not run out, the surface surfactant Γ does not decrease at larger times and so the surface tension does not increase.

The behaviour of the surface surfactant, shown in Figure 6.4(g), is interesting as there is a local minimum in Γ. This can be explained by referring to the asymptotic analysis in Sections 6.3.3–6.3.4. Initially, Γ rapidly increases from zero, corresponding to the region T_1. For the remainder of the time, some of the surfactant monomers are still in micelles and the droplet surface area has not increased enough that $\mathcal{R}_0 S$ is order one. This corresponds to the region T_2 in the case where η is small. Here, because the droplet surface area is so small, the bulk surfactant concentrations, c and c_m, are decoupled from the evolution of Γ, S and ϕ. As discussed in Section 6.3.4, the behaviour of Γ is instead highly dependent on that of $(-1/S)\, dS/dt$, through (6.3.39)–(6.3.40). Between approximately $t \in [0.02, 0.1]$, as the droplets begin to break up, S is small but rapidly increases. Hence Γ decreases. After some time, the drops have become smaller so, from the breakup rate (6.3.43), they are more difficult to break up or cannot break up at all. This means that droplet surface area is being produced much more slowly whilst the free monomers are continuing to adsorb onto the droplets. Hence, for $t > 0.1$, Γ increases.

6.4 Combining jet, droplet and surfactant models

We have gained some insights into how the addition of surfactants interacts with the droplet breakup process. We now combine the droplet and surfactant models with those for a turbulent jet, from Chapter 2.

In this section, we present the full model, which combines the interactions between the jet, droplets and surfactants. This incorporates ideas and results from earlier chapters and previous sections in this chapter. Jet models for the velocity

components, U and W, energy dissipation ϵ, and turbulent diffusion ν_T are given as in Chapter 2. The drop size distribution ϕ is given by the solution to (4.2.6), with breakup rate $\gamma(v, \epsilon, \sigma)$ and daughter drop distribution $\chi(v, \tilde{v})$ to be later specified. The droplet surface area per unit volume, $S(r, z)$, is defined as (6.2.9) and the surface tension, σ, is set by (6.2.1). The equations for the flux of free surfactant concentration, c, micelle concentration, c_m, and surface concentration, Γ, now also include the effects of advection and turbulent diffusion and so, using the argument in Section 4.2.1, we impose

$$U\frac{\partial c}{\partial r} + W\frac{\partial c}{\partial z} - \frac{1}{r}\frac{\partial}{\partial r}\left(r\nu_T\frac{\partial c}{\partial r}\right) = j_c, \tag{6.4.1}$$

$$U\frac{\partial (\Gamma S)}{\partial r} + W\frac{\partial (\Gamma S)}{\partial z} - \frac{1}{r}\frac{\partial}{\partial r}\left(r\nu_T\frac{\partial (\Gamma S)}{\partial r}\right) = j_{sd}, \tag{6.4.2}$$

$$U\frac{\partial c_m}{\partial r} + W\frac{\partial c_m}{\partial z} - \frac{1}{r}\frac{\partial}{\partial r}\left(r\nu_T\frac{\partial c_m}{\partial r}\right) = j_m, \tag{6.4.3}$$

where j_c, j_{sd} and j_m are given by (6.2.11), (6.2.10) and (6.2.5) respectively.

The total surfactant concentration $\mathcal{C}$, is defined as (6.2.12), and, adding (6.4.1)–(6.4.3), we find that it satisfies

$$U\frac{\partial \mathcal{C}}{\partial r} + W\frac{\partial \mathcal{C}}{\partial z} - \frac{1}{r}\frac{\partial}{\partial r}\left(r\nu_T\frac{\partial \mathcal{C}}{\partial r}\right) = 0. \tag{6.4.4}$$

Note that this is the same as Equation (4.2.11) for Φ and can be solved similarly. If the surfactant is released with the oil jet, then $\mathcal{C}$ is proportional to Φ. Therefore, for simplicity, we can generally solve (6.4.2)–(6.4.4) and then use the definition of the total surfactant concentration, (6.2.12), to find c.

We non-dimensionalise as in Section 6.2.4 with the time-scale τ again set as $\tau = D/W_0$, corresponding to the shear rate. Hence, ϕ is given by (4.2.6), and σ and S are given by (6.2.20) and (6.2.21), respectively. Equations (6.4.2)–(6.4.3) become

$$U\frac{\partial (\Gamma S)}{\partial r} + W\frac{\partial (\Gamma S)}{\partial z} - \frac{1}{r}\frac{\partial}{\partial r}\left(r\nu_T\frac{\partial (\Gamma S)}{\partial r}\right) = \mathcal{K}_a\left[(1-\Gamma)cS - \eta\Gamma S\right], \tag{6.4.5}$$

$$U\frac{\partial c_m}{\partial r} + W\frac{\partial c_m}{\partial z} - \frac{1}{r}\frac{\partial}{\partial r}\left(r\nu_T\frac{\partial c_m}{\partial r}\right) = \mathcal{K}_0\left[c^{N_m} - c_m\right]. \tag{6.4.6}$$

Equation (6.4.4) for $\mathcal{C}$ is unchanged, and c is determined from the total surfactant concentration $\mathcal{C}$, using (6.2.25).

6.5 One-dimensional jet models

Chapter 4 demonstrated that much of the behaviour of the drop size distribution can be captured using width-averaged models. Because of this and for simplicity, we solely consider width-averaged models for the remainder of this chapter. Equations (6.4.4)–(6.4.6) are width-averaged as in Section 2.5 for the jets model and Section 4.5 for the drop size distribution.

Recall the jet width, $\delta(z)$, average velocity, $\overline{W}$, and average dissipation, $\bar{\epsilon}$, are given by (2.5.12), namely

$$\delta = \delta_0 + \alpha z, \quad \overline{W}(z) = 0.46\frac{\delta_0\omega_0}{\delta(z)}, \quad \bar{\epsilon}(z) = \frac{\epsilon_0}{\delta(z)^4}, \tag{6.5.1}$$

where $\epsilon_0 = 0.0316\ \omega_0^3\delta_0^3$. The width-averaged drop size distribution $\overline{\phi}$ is given by (4.5.4), namely

$$Q_0\frac{\partial}{\partial z}\left(\delta\overline{\phi}(v,z)\right) = -\overline{\gamma}(v,\epsilon)\overline{\phi}(v,z)\delta^2 + \int_v^1 \overline{\gamma}(\tilde{v},\epsilon)\overline{\chi}(v,\tilde{v})\overline{\phi}(\tilde{v},z)\delta^2\,\mathrm{d}\tilde{v}, \tag{6.5.2}$$

where the constant $Q_0 = \delta\overline{W}$ is the square root of the momentum flux given by (4.5.5). We suppose that the quantities of the surfactant, c, Γ and c_m, have top hat profiles so they are given by $\overline{c}(z)$, $\overline{\Gamma}(z)$ and $\overline{c_m}(z)$ for $r < \delta(z)/2$, and are zero in the exterior. Then (6.4.4)–(6.4.6) reduce to

$$Q_0\frac{d}{dz}\left(\delta\Gamma S\right) = \mathcal{K}_a\left[(1-\Gamma)cS - \eta\Gamma S\right]\delta^2, \tag{6.5.3}$$

$$Q_0\frac{d}{dz}\left(\delta c_m\right) = \mathcal{K}_0\left[c^{N_m} - c_m\right]\delta^2, \tag{6.5.4}$$

$$\frac{d}{dz}\left(\delta\mathcal{C}\right) = 0, \tag{6.5.5}$$

where

$$\mathcal{C} = c + \mathcal{R}_0 S\Gamma + c_m \tag{6.5.6}$$

and

$$S = \int_0^1 \frac{\phi}{v^{1/3}}\,\mathrm{d}v \tag{6.5.7}$$

Here and henceforth we drop all bars relating to width-averaging since, from this point, we will only consider the width-averaged jet model.

Solving (6.5.5), we find that the total surfactant concentration is given by

$$\mathcal{C} = \frac{\mathcal{C}_0}{\delta(z)} \tag{6.5.8}$$

so (6.5.6) becomes

$$\frac{\mathcal{C}_0}{\delta(z)} = c + \mathcal{R}_0 S\Gamma + c_m. \tag{6.5.9}$$

The total surfactant concentration, $\mathcal{C}$ in (6.5.8) is proportional to the width-averaged velocity W in (6.5.1), and the total oil fraction Φ in (4.5.11). Similarly, $\mathcal{C}$ decreases with height due to dilution.

This one-dimensional jet model is very similar to the one dimensional models in time which are examined in Section 6.3. Here the height z is a time-like variable. The main difference is the addition of the $\delta(z)$ terms, which relate to advection and dilution effects.

6.5.1 Boundary conditions

In practice, the surfactant is either premixed with the oil before it is released or injected into the jet at some fixed height. Let us first consider the latter case. Suppose the (conserved) flux of total surfactant, $Q_s = \int_0^\infty rW\mathcal{C}\,\mathrm{d}r$, is given. Then, using the width-averaged vertical velocity in (6.5.1) and total surfactant concentration, (6.5.8), the constant in (6.5.8) is given by $\mathcal{C}_0 = 2\beta Q_s/(\delta_0\omega_0)$. We assume that at $z = z_a$, say, the micelles and monomers are in equilibrium whilst the surface surfactant concentration is zero so

$$c = c_0, \quad c_m = c_0^{N_m}, \quad \Gamma = 0, \tag{6.5.10}$$

where c_0 is the solution to $c_0 + c_0^{N_m} = \mathcal{C}_0/\delta_a = 2\beta Q_s/(\delta_0\omega_0\delta_a)$, with δ_a the value of δ at $z = z_a$. The boundary conditions (6.5.10) assume that at $z = z_a$ the surfactant instantaneously becomes well mixed in the oil jet.

However, we cannot impose the boundary condition (6.5.10) at $z = 0$ because the width-averaged jet models are based on the similarity solution for the jet, which does not hold for small z. We must instead start the model at some height $\hat{z} > 0$. How do we determine the values of ϕ, c, c_m, Γ and $\mathcal{C}$ here?

One option would be to solve the full axisymmetric model, with the CFD numerics for the velocity field and energy dissipation, at smaller heights and use the results to set boundary conditions at $z = \hat{z}$. However, this full model is complex to solve and we leave the solving of the full 2D problem to future work.

Instead, as in Sections 4.5.4–4.5.6 for ϕ, we make a reasonable choice of the values of c, c_m, Γ and $\mathcal{C}$ at $z = \hat{z}$. The flux of $\mathcal{C}$ is conserved so given the total rate at which

surfactant is injected into the jet, it is straightforward to determine $\mathcal{C}$ at $\hat{z}$. In a real-life scenario (if we suppose $k_0^- = 100$–$1000\,\mathrm{s}^{-1}$), $\mathcal{K}_0$, the rate at which the micelles disassociate into monomers, is generally large so for the majority of the jet flow, c and c_m are in equilibrium. In addition, the rate at which monomers adsorb to the oil droplets, $\mathcal{K}_a$, is large. As we will discuss in Section 6.5.4, this doesn't necessarily mean that Γ and c are in equilibrium but it does mean that Γ will rapidly rise from zero, as seen in the box models in Section 6.3. Therefore, at $z = \hat{z}$ we set $\Gamma = 0$, and take c and c_m to be in equilibrium, i.e. we take (6.5.10) as boundary conditions at $z = \hat{z}$. In a small region near $z = \hat{z}$, the model will be inaccurate as Γ increases but, after this point, the model will give a reasonable approximation. This choice of boundary condition is further discussed in Section 6.5.5.

In the opposite regime where $\mathcal{K}_a$ and $\mathcal{K}_0$ are small, the shear rate is much more rapid than the rate of surfactant adsorption and micellar breakup. The rapid shear slows down the action of the surfactant and so very little surfactant evolution occurs between $z = 0$ and $z = \hat{z}$. Hence, it would also be reasonable to take (6.5.10) as boundary conditions at $z = \hat{z}$.

In small-scale experiments, $\mathcal{K}_0 = \mathcal{O}(10^{-4})$–$\mathcal{O}(10^{-1})$ and $\mathcal{K}_a = \mathcal{O}(10)$. Since $\mathcal{K}_0$ is small, the micelles only break up at large heights; elsewhere, their effect is weak. In addition, the fact that $\mathcal{K}_a$ is close to one may mean that the behaviour at small z could be significantly different from that at equilibrium, Thus, the initial behaviour may be more difficult to predict. For simplicity, we choose to again take (6.5.10) as boundary conditions at $z = \hat{z}$. We further discuss this choice in Section 6.6.

6.5.2 Moments

We have reduced the model by width-averaging, so it only depends on one spatial variable. To further simplify, as in Section 6.3.2, we reduce the volume variation, at each height, to one parameter by taking moments and assuming the form of ϕ. We multiply (6.5.2) by v^n and then integrate across the entire volume range, from $v = 0$ to $v = 1$, to yield

$$\begin{aligned} Q_0 \frac{d}{dz}\left(\delta \int_0^1 v^n \phi(v,z)\,\mathrm{d}v\right) = &- \int_0^1 v^n \gamma(v,\epsilon,\sigma)\phi(v,z)\,\mathrm{d}v\delta^2 \\ &+ \int_0^1 \int_v^1 v^n \gamma(\tilde{v},\epsilon,\sigma)\chi(v,\tilde{v})\phi(v,z)\,\mathrm{d}\tilde{v}\,\mathrm{d}v\delta^2. \end{aligned} \tag{6.5.11}$$

We suppose the drop size distribution, at each height, is concentrated at a particular drop size $\overline{v}(z)$ so

$$\phi = \Phi\delta_v(v - \overline{v}(z)) = \frac{T_\Phi \delta_v(v - \overline{v}(z))}{\delta(z)}, \tag{6.5.12}$$

where the second equality comes from the width-averaged total oil fraction in (4.5.11), where recall $T_\Phi = 4\Phi_0\delta_0/\beta$. As in Section 6.3.2, we again take the simplest possible form for χ, setting it to be uniform so $\chi(v, \overline{v}) = 1/\overline{v}$. Then taking the first moment ($n = 1$) in (6.5.11) yields

$$Q_0 \frac{d\overline{v}}{dz} = -\frac{\gamma(\overline{v}, \epsilon, \sigma)\delta(z)\overline{v}}{2}, \tag{6.5.13}$$

which we solve subject to

$$\overline{v}(\hat{z}) = 1. \tag{6.5.14}$$

The droplet surface area per unit volume, S is then

$$S(z) = \frac{T_\Phi}{\delta(z)\overline{v}^{1/3}}. \tag{6.5.15}$$

The breakup rate is taken, as in Section 6.3.2, to be (6.3.15). Hence we write (6.5.13) as

$$Q_0 \frac{d\overline{v}}{dz} = -\gamma_0 \overline{v}\delta^{-7/5} \left[1 + \theta \log(1 - \Gamma)\right]^{-2/5}, \tag{6.5.16}$$

with

$$\gamma_0 = \frac{K_0 \epsilon_0^{3/5}}{2}, \tag{6.5.17}$$

where recall, from (6.5.1), that $\epsilon = \epsilon_0\delta^{-4}$.

We solve (6.5.3)–(6.5.4) and (6.5.9) for the surfactant concentrations, coupled with the droplet equations (6.5.15)–(6.5.16). At $z = \hat{z}$ we suppose boundary conditions are given by (6.5.10), with $c_0 = 1 + 1/N_m$, and (6.5.14).

6.5.3 $\mathcal{R}_0$, $1/\mathcal{K}_0$, $1/\mathcal{K}_a$, $1/N_m$ small

Let us first consider the simplest parameter regime, analogous to the box model in Section 6.3.3, where $\mathcal{R}_0$, $1/\mathcal{K}_0$, $1/\mathcal{K}_a$ and $1/N_m$ are small and η is order one. As in (6.3.17), we let ε be small and suppose

$$\mathcal{K}_0 = \varepsilon^{-1}\hat{\mathcal{K}}_0, \quad \mathcal{K}_a = \varepsilon^{-1}\hat{\mathcal{K}}_a, \quad N_m = \varepsilon^{-1}\hat{N}_m, \quad \mathcal{R}_0 = \varepsilon\hat{\mathcal{R}}_0, \tag{6.5.18}$$

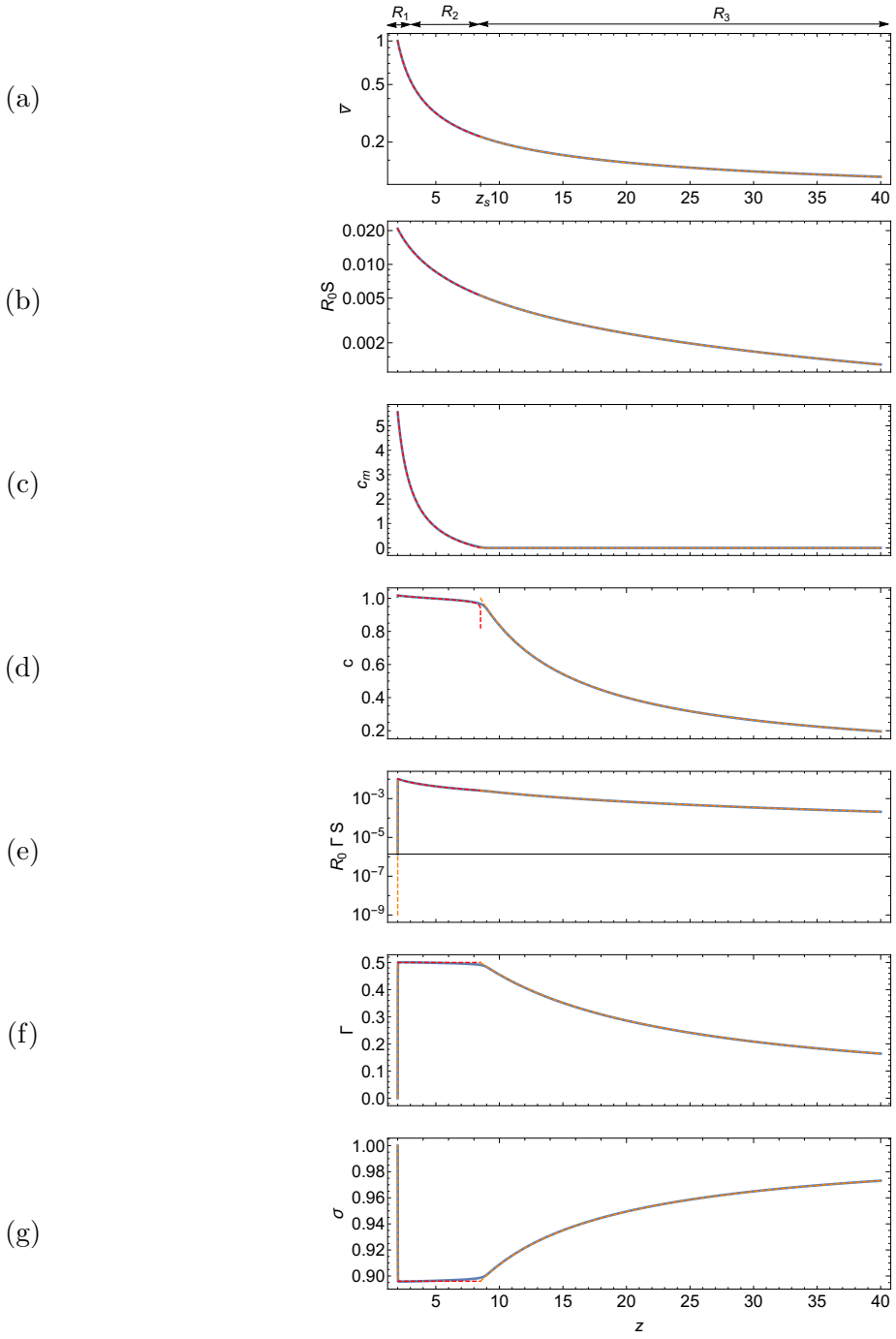


Figure 6.5: Solution to (6.5.3)–(6.5.4), (6.5.9) and (6.5.15)–(6.5.16). At $z = \hat{z}$ we use boundary conditions (6.5.10), with $c_0 = 1 + 1/N_m$, and (6.5.14). We take $\theta = 0.15$, $\gamma_0 = 1$, $\eta = 1$ and $\mathcal{R}_0 = 1/\mathcal{K}_0 = 1/\mathcal{K}_a = 1/N_m = 10^{-2}$. Numerical solution is shown in blue. Asymptotics are shown in dashed lines (orange for R_1 and R_3, red for R_2). (a) Average drop volume $\bar{v}$; (b) drop surface area $\mathcal{R}_0 S$; (c) micelle concentration c_m; (d) free monomer concentration c; (e) adsorbed surfactant concentration per unit volume, $\mathcal{R}_0 \Gamma S$; (f) adsorbed surfactant concentration per unit area, Γ; (g) surface tension σ.

with $\eta = \mathcal{O}(1)$ and $\theta = \mathcal{O}(1)$. The equations (6.5.3)–(6.5.4), (6.5.9), and (6.5.15)–(6.5.16) then give

$$Q_0 \frac{d\overline{v}}{dz} = -\gamma_0 \overline{v} \delta^{-7/5} \left[1 + \theta \log(1-\Gamma)\right]^{-2/5} \tag{6.5.19}$$

$$S = \frac{T_\Phi}{\delta \overline{v}^{1/3}} \tag{6.5.20}$$

$$\varepsilon Q_0 \frac{d}{dz}(\delta \Gamma S) = \hat{\mathcal{K}}_a \left[(1-\Gamma) c S - \eta \Gamma S\right] \delta^2 \tag{6.5.21}$$

$$\varepsilon Q_0 \frac{d}{dz}(\delta c_m) = \hat{\mathcal{K}}_0 \left[c^{\hat{N}_m/\varepsilon} - c_m\right] \delta^2 \tag{6.5.22}$$

$$\frac{\mathcal{C}_0}{\delta} = c + \varepsilon \hat{\mathcal{R}}_0 \Gamma S + c_m. \tag{6.5.23}$$

As in Section 6.3.3, we find there are various regions with different behaviour, which are illustrated in Figure 6.5. We use the parameter values $\eta = 1$, $\theta = 0.15$, $\gamma_0 = 1/2$ and $\mathcal{R}_0 = 1/\mathcal{K}_0 = 1/\mathcal{K}_a = 1/N_m = 10^{-2}$.

$\boldsymbol{R_1}$ We first consider the region close to $z = \hat{z}$. We scale

$$z = \hat{z} + \varepsilon \tilde{z}. \tag{6.5.24}$$

Then there is a dominant balance between all the terms in (6.5.21) and all other quantities are constant. So (6.5.21) reduces to

$$Q_0 \frac{d\Gamma}{d\tilde{z}} = \hat{\mathcal{K}}_a \hat{\delta} \left(c_0 - \Gamma(c_0 + \eta)\right), \tag{6.5.25}$$

which has solution

$$\Gamma = \frac{c_0}{c_0 + \eta} \left[1 - \exp\left(-\frac{\varepsilon^{-1} \hat{\mathcal{K}}_a (c_0 + \eta) \hat{\delta}}{Q_0} (z - \hat{z})\right)\right]. \tag{6.5.26}$$

The surface concentration exponentially increases from zero, reaching equilibrium in a very small height. After this region, from (6.5.21)–(6.5.22), the micelles, monomers and surface surfactant are in equilibrium and so (6.5.21)–(6.5.22) asymptote to (6.2.27)–(6.2.28), respectively.

$\boldsymbol{R_2}$ The free monomer concentration c is above the CMC at $z = \hat{z}$ and so we can expand

$$c \sim 1 + \varepsilon \frac{c_1}{\hat{N}_m}, \tag{6.5.27}$$

where $c_1(\hat{z}) = 1$. Then

$$\Gamma \sim \frac{1}{1+\eta} \tag{6.5.28}$$

from (6.2.27) so

$$Q_0 \frac{d\overline{v}}{dz} = -\gamma_c \delta^{-7/5} \overline{v}, \tag{6.5.29}$$

where

$$\gamma_c = \gamma_0 \left[1 + \theta \log \left(\frac{\eta}{\eta + 1} \right) \right]^{-2/5} \tag{6.5.30}$$

is the constant breakup rate. Hence

$$\overline{v} = \exp \left[\frac{5\gamma_c}{2\alpha Q_0} \left(\delta^{-2/5} - \hat{\delta}^{2/5} \right) \right] \tag{6.5.31}$$

and so

$$S = \frac{T_\Phi}{\delta} \exp \left[-\frac{5\gamma_c}{6\alpha Q_0} \left(\delta^{-2/5} - \hat{\delta}^{-2/5} \right) \right]. \tag{6.5.32}$$

To determine c_1 and c_m we use (6.5.23), which, to leading order, gives

$$c_m = \frac{\mathcal{C}_0}{\delta} - 1 \tag{6.5.33}$$

and

$$c_1 = \log \left(\frac{\mathcal{C}_0}{\delta} - 1 \right). \tag{6.5.34}$$

Here the micelle concentration is decreasing solely due to the effects of dilution. From (6.5.33), it eventually reaches zero at $z = z_s = (\mathcal{C}_0 - \delta_0)/\alpha$.

***R*$_3$** For $z > z_s$, $c_m = 0$ and so (6.5.23) yields

$$c \sim \frac{\mathcal{C}_0}{\delta}. \tag{6.5.35}$$

From (6.5.21),

$$\Gamma \sim \frac{\mathcal{C}_0}{\eta\delta + \mathcal{C}_0}. \tag{6.5.36}$$

The average volume then satisfies

$$Q_0 \frac{d\overline{v}}{dz} = -\gamma_0 \overline{v} \delta^{-7/5} \left[1 + \theta \log \left(\frac{\eta\delta}{\eta\delta + \mathcal{C}_0} \right) \right]^{2/5} \tag{6.5.37}$$

so $\overline{v}$ decreases exponentially due to breakup and dilution.

The results of our asymptotics and the numerics are compared in Figure 6.5 and agree well over all three regimes identified. The behaviour here has some similarities with that of the zero-dimensional models in Section 6.3. In both we observe the same rapid rise to equilibrium, a quasi-steady region when micelles are present, and finally a region where the surfactant's efficacy has waned and surface tension increases.

The main difference is the effect of dilution. This causes a more rapid decrease in surfactant concentration and so limits its efficacy in breaking up the oil droplets. In our fixed box models in Section 6.3.3, we use the same breakup rate, (6.3.15), so even the very smallest drops are allowed to break up. The only way in which the effect of surfactants decreases is if the droplet surface area increases to such an extent that there is too much surface area for the monomers to cover. However, in the analogous jet models, this does not occur. Dilution spreads out the droplets and surfactant monomers and makes it more difficult for the surfactant to adsorb onto the drops, and for the droplets to break up. Unless the breakup rate is very large, the drops will not break up enough that $\mathcal{R}_0 S = \mathcal{O}(1)$.

The weakness of droplet breakup compared to dilution is illustrated in Figure 6.5(b). Although droplets are breaking up, the droplet surface area, $\mathcal{R}_0 S$, decreases with height as droplet breakup is dominated by dilution. A mathematically interesting and useful consequence of this is that, in this parameter regime, the surfactant behaviour is independent of that of the droplets.

6.5.4 η small

Thus far, in this section, we have taken η to be order one but, as noted in the box models, η is, in fact, small. Much of the asymptotics can be explained by taking the limit of small η in the asymptotics in Section 6.5.3. However, there are some exceptions. Therefore, here we explore the behaviour and corresponding asmpytotics for small η. We scale all parameters as in (6.5.18), where $\varepsilon \ll 1$, and also set

$$\eta = \nu\hat{\eta}, \tag{6.5.38}$$

where $\nu \ll 1$. Different behaviours are observed depending on the relative sizes of $1/\mathcal{K}_a$ and η, or equivalently the relative sizes of ε and ν. In the following asymptotics, as in Section 6.5.3, we take θ to be order one. However, in this section, we will find that in certain regions, $1-\Gamma = \mathcal{O}(\eta)$ or $1-\Gamma = \mathcal{O}(1/\mathcal{K}_a)$ and this could yield negative values of σ in (6.2.20); θ must therefore satisfy the constraints that $\theta < 1/\log(\mathcal{K}_a)$ and $\theta < -1/\log(\eta)$. Therefore, we treat $\log(\eta)$ and $\log(1/\mathcal{K}_a)$ as order one.

The behaviour in the case where $\varepsilon/\nu = \mathcal{O}(1)$ is shown in Figure 6.6. We use the parameter values $\theta = 0.15$, $\gamma_0 = 1/2$ and $\eta = \mathcal{R}_0 = 1/\mathcal{K}_0 = 1/\mathcal{K}_a = 1/N_m = 10^{-2}$.

$\boldsymbol{R_1}$ In the region where $z - \hat{z} = \mathcal{O}(\varepsilon)$, there is a dominant balance between the first two terms in (6.5.21) and all other quantities are constant. Hence

$$\Gamma = 1 - \exp\left(-\frac{\varepsilon^{-1}\hat{\mathcal{K}}_a c_0 \hat{\delta}(z - \hat{z})}{Q_0}\right), \tag{6.5.39}$$

which is equivalent to taking the limit of small η in (6.5.24)–(6.5.26). In this small region, the surface concentration exponentially increases from zero. Note that as $\varepsilon^{-1}\hat{\mathcal{K}}_a(z - \hat{z}) \to \infty$, then $\Gamma \to 1$. This is problematic because, for values of Γ close to one, the surface tension in (6.2.20) becomes negative. The regime must stop before this occurs. After R_1, the micelles and free monomers are in equilibrium and so (6.5.22) asymptotes to (6.2.28).

$\boldsymbol{R_2}$ The free monomer concentration is above the CMC, and c and c_m are given by (6.5.27) and (6.5.33)–(6.5.34). Thus, the behaviour of c and c_m is decoupled from the rest of the problem. The behaviour of Γ and $\overline{v}$ varies depending on the relative sizes of η and $1/\mathcal{K}_a$. If $\mathcal{K}_a\eta \gg 1$ i.e. $\nu/\varepsilon \gg 1$, then Γ and c are in equilibrium and the behaviour is the same as in Section 6.5.3. For $\mathcal{K}_a\eta \sim 1$ (or $\nu/\varepsilon \sim 1$), the free and surface monomers are not in equilibrium and there is actually a dominant balance between all three terms in (6.5.21). Hence

$$\Gamma \sim 1 - \varepsilon\Gamma_1 \tag{6.5.40}$$

and (6.5.21) yields

$$\frac{Q_0}{S\delta^2}\frac{d(S\delta)}{dz} = \hat{\mathcal{K}}_a\left[\Gamma_1 - \frac{\nu}{\varepsilon}\hat{\eta}\right]. \tag{6.5.41}$$

Using (6.5.19)–(6.5.20) we obtain

$$\frac{Q_0}{S\delta^2}\frac{d(S\delta)}{dz} = \frac{\gamma_0}{3\delta^{12/5}}\left[1 + \theta\log(\varepsilon\Gamma_1)\right]^{-2/5} \tag{6.5.42}$$

and equating (6.5.41) with (6.5.42) we find $\Gamma_1(z)$ is determined by the solution to

$$\Gamma_1 = \frac{\nu}{\varepsilon}\hat{\eta} + \frac{\gamma_0}{3\hat{\mathcal{K}}_a\delta^{12/5}}\left[1 + \theta\log\left(\varepsilon\Gamma_1\right)\right]^{-2/5}. \tag{6.5.43}$$

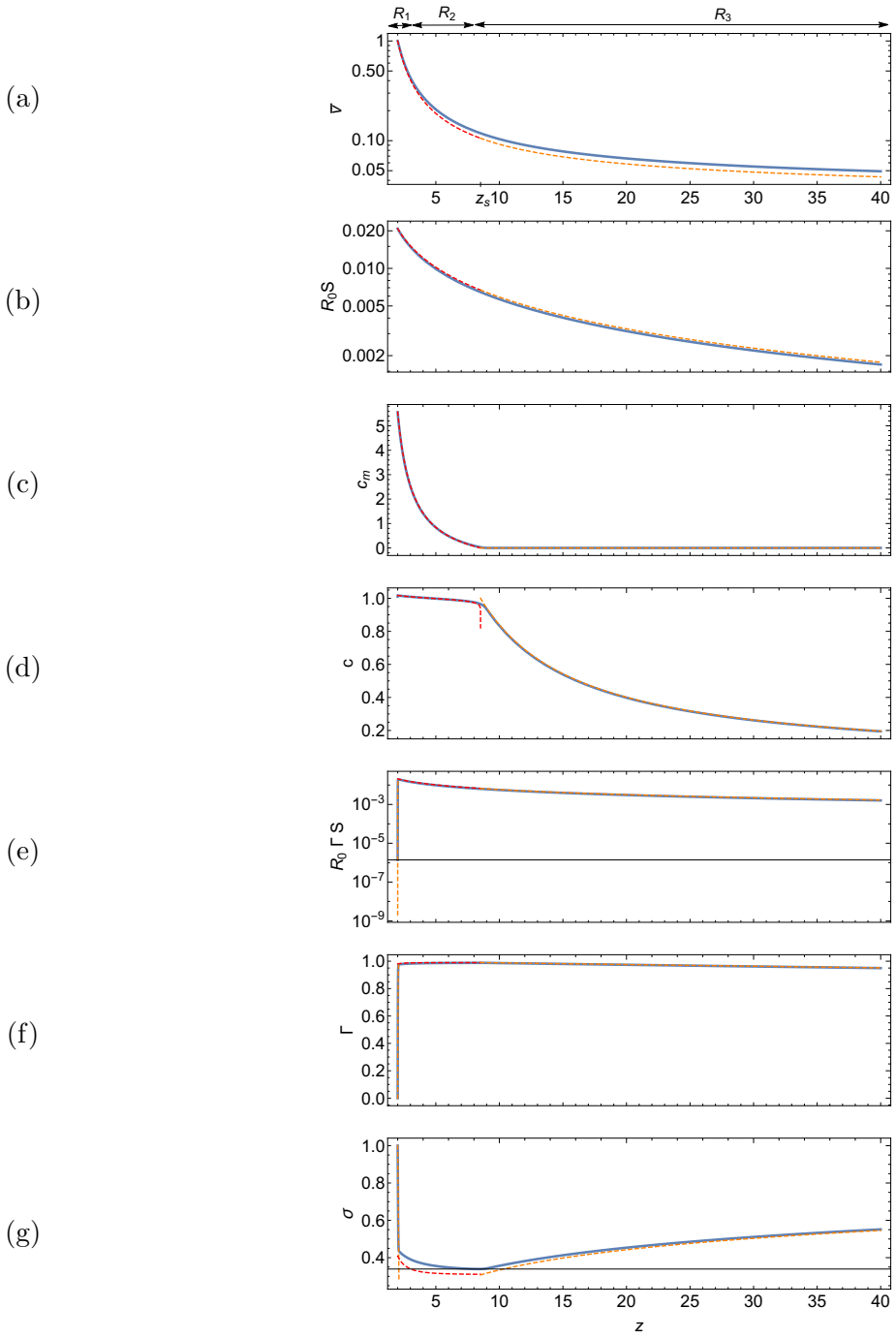


Figure 6.6: Solution to (6.5.3)–(6.5.4), (6.5.9) and (6.5.15)–(6.5.16). At $z = \hat{z}$ we use boundary conditions (6.5.10), with $c_0 = 1 + 1/N_m$, and (6.5.14). We take $\theta = 0.15$, $\gamma_0 = 1$ and $\eta = \mathcal{R}_0 = 1/\mathcal{K}_0 = 1/\mathcal{K}_a = 1/N_m = 10^{-2}$. Numerical solution is shown in blue. Asymptotics are shown in dashed lines (orange for R_1 and R_3, red for R_2). (a) Average drop volume $\bar{v}$; (b) drop surface area $\mathcal{R}_0 S$; (c) micelle concentration c_m; (d) free monomer concentration c; (e) adsorbed surfactant concentration per unit volume, $\mathcal{R}_0 \Gamma S$; (f) adsorbed surfactant concentration per unit area, Γ; (g) surface tension σ.

We note that $\Gamma_1(z)$ is a decreasing function of z so Γ increases with height as seen in Figure 6.6. The average drop size $\overline{v}$ then satisfies

$$Q_0 \frac{d\overline{v}}{dz} = -3\hat{\mathcal{K}}_a \overline{v}\delta(z)\left(\Gamma_1(z) - \frac{\nu}{\varepsilon}\hat{\eta}\right). \tag{6.5.44}$$

So $\overline{v}$ decreases due to breakup and the rate at which this occurs decreases with height. Here drops are breaking up but, due to dilution and the decrease in ϵ with height, the rate at which droplets break up and increase the droplet surface area is lower than that at which the surfactant adsorbs to the droplets. Hence Γ increases.

In the case where $\mathcal{K}_a\eta \ll 1$ (or $\nu/\varepsilon \ll 1$) the behaviour is similar but we take the limit of small ν so the first two terms in (6.5.21) balance and, instead of (6.5.43), Γ_1 satisfies

$$\Gamma_1 = \frac{\gamma_0}{3\hat{\mathcal{K}}_a\delta^{12/5}}\left[1 + \theta\log\left(\varepsilon\Gamma_1\right)\right]^{-2/5}. \tag{6.5.45}$$

In region R_2, the dominant balance therefore occurs when $\nu/\epsilon = \mathcal{O}(1)$.

By $z = z_s = (\mathcal{C}_0 - \delta_0)/\alpha$, the micelle concentration c_m in (6.5.33) has decreased to zero due to dilution alone.

R_3 For $z > z_s$, since $c_m \sim 0$, c is given by (6.5.35). When $\mathcal{K}_a\eta \gg 1$ or $\mathcal{K}_a\eta \sim 1$ ($\nu/\varepsilon \gg 1$ or $\nu/\varepsilon \sim 1$), the free monomers and surface surfactants are now in equilibrium and the behaviour is as in Section 6.5.3. When $\mathcal{K}_a\eta \ll 1$ i.e. $\nu/\varepsilon \ll 1$, the terms in (6.5.21) balance so

$$\Gamma = 1 - \varepsilon\Gamma_1, \tag{6.5.46}$$

Using a similar argument to (6.5.41)–(6.5.43) we find that Γ_1 is determined by

$$\Gamma_1\left(\frac{\mathcal{C}_0}{\delta}\right) = \frac{\gamma_0}{3\hat{\mathcal{K}}_a\delta^{12/5}}\left[1 + \theta\log\left(\varepsilon\Gamma_1\right)\right]^{-2/5}, \tag{6.5.47}$$

which is solved along with

$$Q_0 \frac{d\overline{v}}{dz} = -3\hat{\mathcal{K}}_a \overline{v}\delta(z)\Gamma_1(z) \tag{6.5.48}$$

to determine $\Gamma_1(z)$ and $\hat{v}$ (and so $\hat{S}$).

The asmpytotics derived in this section are shown in Figure 6.6 and agree well with the corresponding numerical solutions.

We observe that the small η behaviour is qualitatively similar to the order one η behaviour. The main quantitative difference with small η is that it gives greater values of Γ and slows down the decrease in Γ. This means that the surface tension is lower and the average drop size, $\overline{v}$, is smaller. This can be seen by comparing Figure 6.5(g) and Figure 6.6(g).

6.5.5 Full distribution models

A great deal of insight is gained from the volume averaged models considered above. However, we now examine the effects of using the full-volume range as well as more complex breakup rates. We model ϕ using (6.5.2), and the surfactant concentrations by (6.5.3)–(6.5.4) and (6.5.9). We take the breakup rate as (6.3.43)–(6.3.45), with parameters $K_{00} = 0.7$ and $C = 11$. (These are determined from experimental comparisons in Section 6.6). We suppose that the daughter drop distribution is given by (3.2.32).

At $z = \hat{z} = 2$, we suppose boundary conditions are given by (6.5.10), and the initial distribution, ϕ, is weighted towards the largest drops and given by (4.4.6). We take the parameters $\mathcal{C}_0 = 2$, $k_a = 1.1 \times 10^{-1}\,\mathrm{m\,s^{-1}}$, $k_0^- = 1000\,\mathrm{s^{-1}}$. All other parameters are taken as those corresponding to a real oil spill in Table 1.1 and Section 6.2.6.

We solve numerically using the method of lines and discretise drop size according to $\log d$ with 200 size bins. Our results are shown in Figure 6.7. Low down the jet, the micelles start to disassociate into free monomers and these then adsorb onto the drops, quickly decreasing the surface tension. By around $z = 7$, the micelles have all been broken down. Since there is now no store of surfactant to continue adsorbing onto the diluting system, the surface surfactant concentration decreases and the surface tension starts to increase. The droplet surface area per unit volume, S, demonstrates some interesting behaviour, particularly in the interplay of dilution and breakup. For the majority of heights below around $z = 15$, S increases as the large energy dissipation precipitates rapid droplet breakup. For larger heights the breakup wanes and dilution becomes more dominant, causing S to decrease. There is some unusual behaviour at small z in that, although this is the region with most rapid breakup, S decreases here. One possible reason for this may be that, as seen in Figure 6.7(a), the largest drops are only present at smaller heights. Large drops breaking into medium drops produces less surface area than medium drops breaking into many small drops. Note that throughout the height of the jet, $\mathcal{R}_0 S$ is small and so the droplet surface area does not increase to such an extent as to diminish the efficiency of the surfactant. Higher up the jet, by $z = 50$, the droplets stop breaking up due to a combination of the rising surface tension and, more importantly, the decrease in dissipation.

Further insights into the surfactant concentrations can be gained by considering the asymptotic limits when $\mathcal{K}_a, \mathcal{K}_0$ and N_m are large, and $\mathcal{R}_0$ and η are small. The details are very similar to those in Sections 6.5.3–6.5.4.

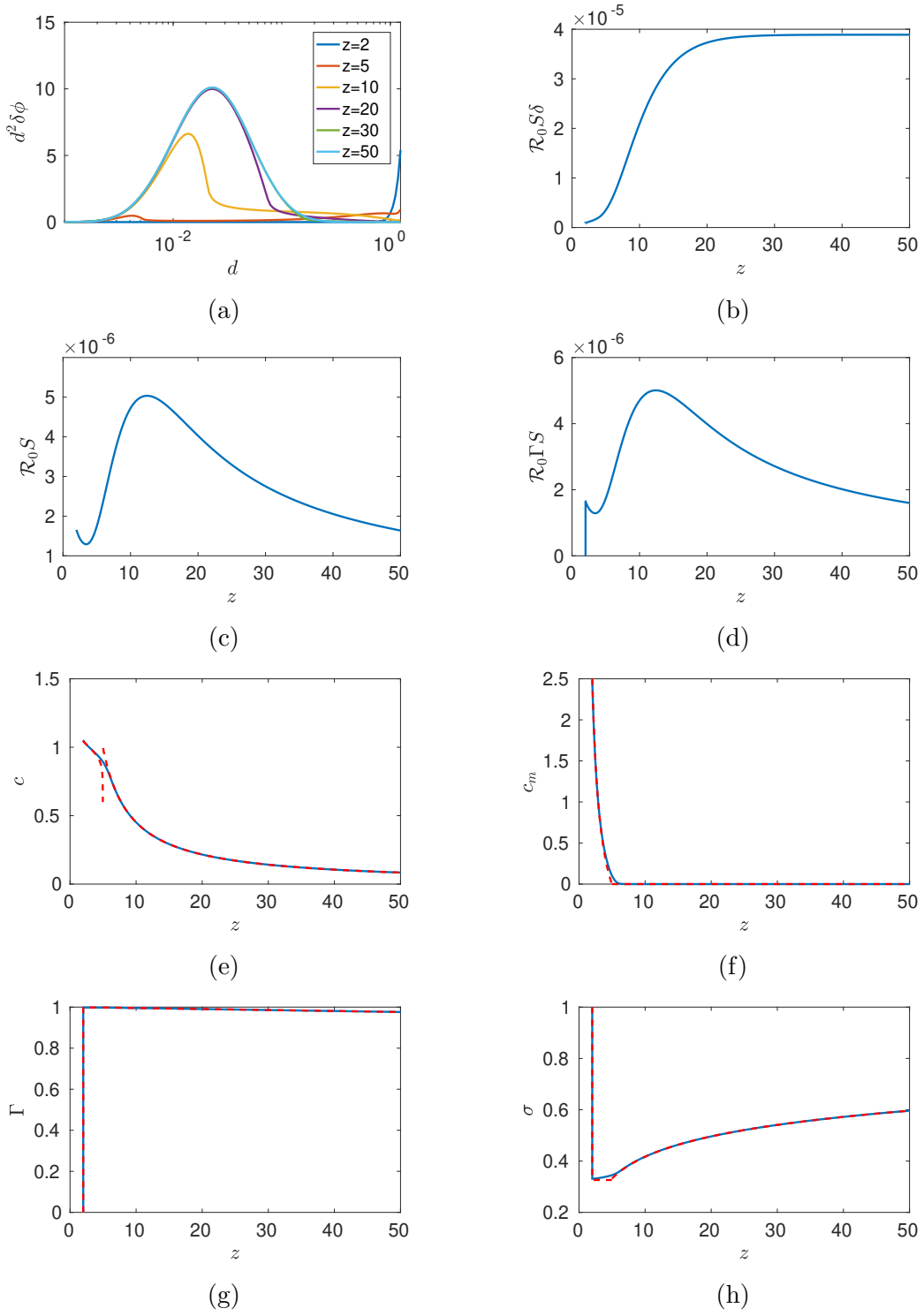


Figure 6.7: Variation of drop and surfactant behaviour with height, using width-averaged, full-volume models. (a) Drop size distribution normalised to eliminate dilution, $d^2\delta\phi$; (b) drop surface area per unit volume, normalised to eliminate dilution, $\mathcal{R}_0 S\delta$; (c) drop surface area per unit volume, $\mathcal{R}_0 S$; (d) adsorbed surfactant concentration per unit volume, $\mathcal{R}_0\Gamma S$; (e) free monomer concentration, c; (f) micelle concentration, c_m; (g) adsorbed surfactant concentration per unit area, Γ; (h) surface tension, σ.

In the first region, R_1, Γ rapidly increases from zero, as given by (6.5.26). We note that the surface tension rapidly decreases and tends to $1 + \theta \log(\eta/(c_0 + \eta))$, which is approximately equal to 0.33 for the parameters used here. As can be seen in Figure 6.7, this provides a good estimate of the minimum value of σ, the value at which the surfactant is most effective.

In the second region, R_2, the micelles and monomers are in equilibrium, but the free and adsorbed monomers are not. The free monomer concentration is above the CMC, and c and c_m are given by (6.5.27) and (6.5.33)–(6.5.34). In a realistic scenario, $\mathcal{K}_a\eta \sim 1$ and hence Γ and ϕ are determined by solving (6.5.40)–(6.5.41) in conjunction with (6.5.2). Here the evolution of Γ is dependent on a combination of dilution, and the droplets breaking up and increasing the surface area onto which the surfactant can adsorb.

Eventually in the final region, higher up the jet, the micelles have all disassociated; $c_m = 0$ for $z > z_s = (\mathcal{C}_0 - \delta_0)/\alpha$. This region corresponds to R_3 in Section 6.5.4. Here the surfactant concentrations decrease solely due to dilution, according to (6.5.35)–(6.5.36). This causes the surface tension to increase.

These asymptotic results and their prediction of σ are illustrated in Figures 6.7(e)–(h). We do not solve (6.5.40)–(6.5.41) with (6.5.2) for Γ and ϕ in R_2. Instead we take Γ as (6.5.26) for $z < z_s$, i.e. in both R_1 and R_2. This is primarily because the approximation in R_2 does not greatly simplify the system. In any case, we find that this region — where the drop and surfactant behaviour are highly coupled — actually only occupies a small region in the jet. We observe good agreement with the numerics. A useful insight here is that, after a small height, by around $z = 7$, all the micelles have broken down and we reach the third region, where dilution controls Γ. This means that we only need to solve the full problem for smaller z. For the majority of the jet, Γ is decoupled from the jet behaviour and can be found using (6.5.36) before solving for ϕ. A similar principle could be used to solve the full axisymmetric problem. From a more physical viewpoint, we find that once all the micelles have disassociated, the surface tension must increase due to dilution. This suggests that, unsurprisingly, it is best to apply the surfactant with the free monomer concentration well above the CMC.

The results of this model and the associated asymptotics provide some assurance and insight into our choice of boundary condition. Recall that, in the case where the surfactant is released with the oil at $z = 0$, we set $\Gamma = 0$ and c and c_m in equilibrium at $z = \hat{z}$ (see (6.5.10)). The asymptotics shows that, indeed, c and c_m are generally in equilibrium. In addition, as mentioned in Section 6.5.1, Γ rapidly

increases near $z = \hat{z}$ so taking Γ to be zero here does not cause any significant inaccuracy. In fact, numerical experiments show that the global behaviour of $\Gamma(z)$ is essentially independent of the choice of $\hat{z}$ and the initial value of Γ (as long as it does not exceed $c_0/(c_0 + \eta)$, the value to which Γ asymptotes in the region R_1, from (6.5.26)). Nonetheless, it is important to note that the regions where the surfactant is most effective occur at smaller z. This is where the larger values of Γ and so the smallest values of σ occur. If we take too large values of $\hat{z}$, the model will begin at a height where much of the interesting droplet breakup and surfactant interaction has occurred. Therefore, we choose $\hat{z} = 2$ here and for the remainder of this chapter.

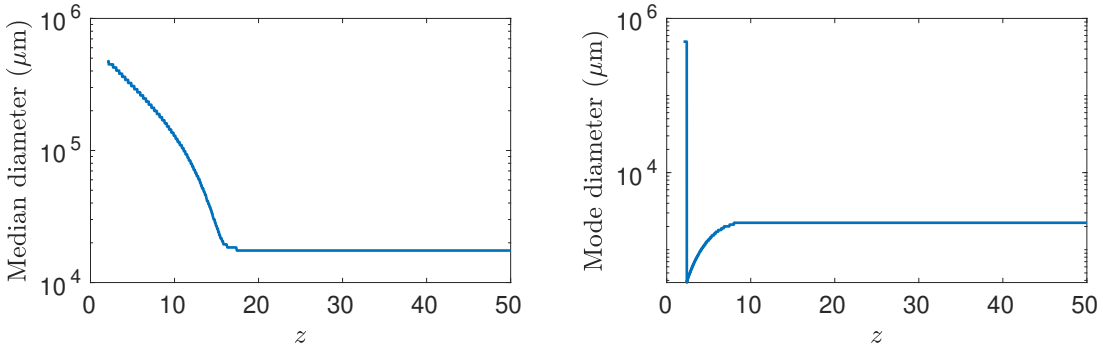
6.5.6 Evaluating the efficiency of dispersants

We want to use our models to evaluate the efficiency of dispersants. Some useful measures of this are the median and the mode of the droplet size distribution, and the fraction of smaller drops produced. The median drop diameter d_m (with corresponding volume v_m) is defined such that $\int_0^{v_m} \phi \, \mathrm{d}v = 1/2$. These quantities are plotted in Figure 6.8. Note that the staircase behaviour in the median and mode drop sizes is an artefact of our discretisation of drop size: each 'stair' corresponds to a drop size bin.

The median drop size in Figure 6.8(a) decreases with height. By around $z = 20$, the median reaches a constant value, though the largest drops are still breaking up here (see Figure 6.7(a)). This is because the median drop size is an indicator of the medium and larger drops. After around $z = 20$, since only the very large drops are breaking up, medium and large drops are mostly produced and the median is constant.

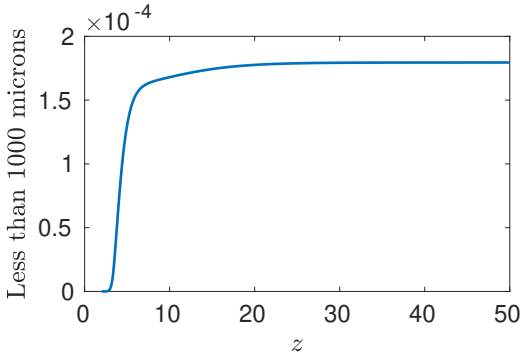
From Figure 6.8(b), we observe that the drop size distribution is bimodal for small heights and the mode very quickly reduces by around four orders of magnitude. As more larger drops break up, producing more of the medium-sized drops, the mode drop diameter increases. It is roughly constant after around $z = 10$. This is because, at larger heights only the larger drops break up.

Similar behaviour is seen by considering the total volume fraction of oil which consists of drops smaller than some critical diameter. In this case, we take this to be 1000 microns, in Figure 6.7(c). We see that most of the breakup occurs at small heights, with small drops being rapidly produced here. At larger heights droplet breakup still occurs but only the largest drops can break up, so the fraction of drops below this critical size remains largely the same.



(a) Median

(b) Mode



(c) Less than 1000 microns

Figure 6.8: Effectiveness of droplet breakup in the presence of surfactant using width-averaged, full-volume models. We plot the variation with height of the (a) median drop diameter; (b) mode drop diameter; and (c) volume fraction less than 1000 microns.

The volume fraction of 1000 micron drops is very small given that we expect to be producing droplets with diameter below 50 microns. One reason for this might be the choice of $\chi(v, \tilde{v})$ in (3.2.32). We assume that droplet breakup is unlikely to produce a large volume of smaller droplets. Instead, we could use the daughter distribution (3.2.24), which sets χ to be uniform and so a greater volume of small droplets are produced. This increases the volume fraction of small droplets (as was observed in Figure 3.5(a)) but the model still does not predict that there is a significant volume fraction of droplets with diameter below 50 microns. This issue is, thus, more likely due to the fact that, at the starting height $\hat{z}$, we have assumed that most of the drops have the same diameter as the jet nozzle. This simplification could be relaxed in future work.

DOR	1:1000	1:500	1:250	1:100	1:50	1:25
$\mathcal{C}_0$	0.0550	0.1098	0.2192	0.5447	1.0785	2.1158

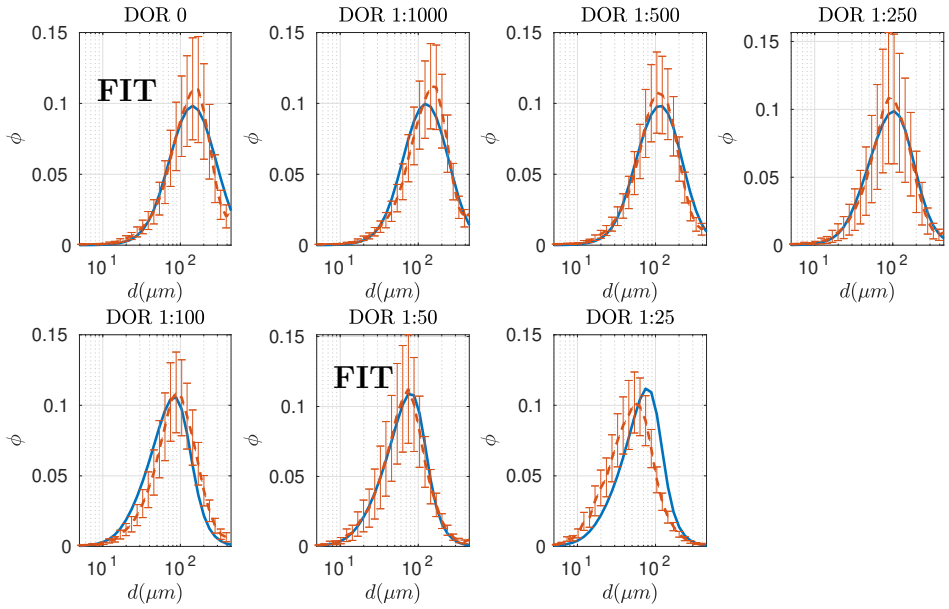
Table 6.1: The value of $\mathcal{C}_0$ in the total surfactant concentration $\mathcal{C} = \mathcal{C}_0/\delta$ for each experimental DOR (dispersant to oil ratio).

6.6 Comparison to experiments

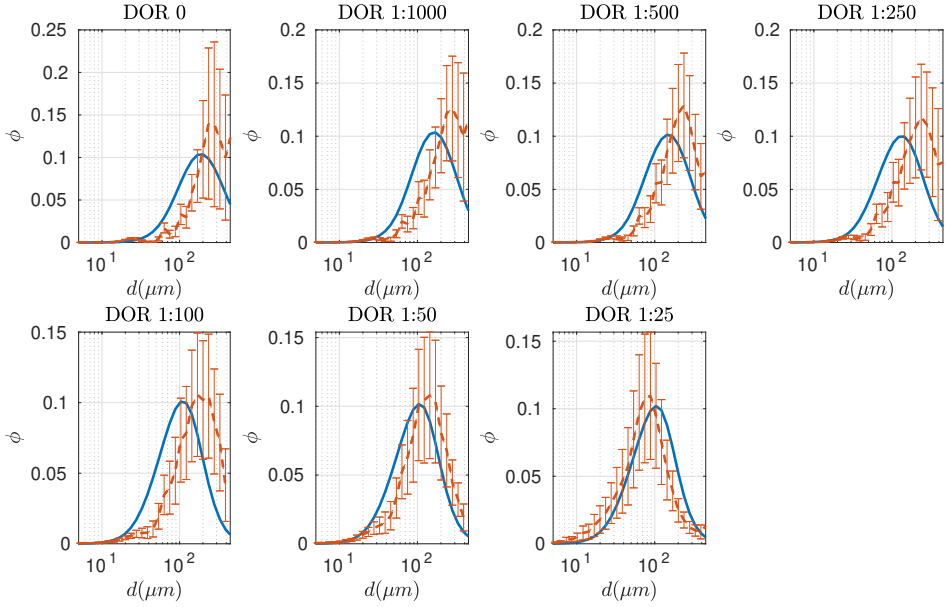
We now fit our width-averaged models to the small scale SINTEF experiments (Brandvik et al., 2014, 2013; Johansen et al., 2013). We consider experiments where the surfactant has been premixed with the oil and then is released with it. This correlates with the implicit assumption of these width-averaged models that the surfactant instantaneously becomes well mixed in the oil once added to the jet. However, there are a number of caveats to this experimental comparison. In particular, as was discussed in Section 6.2.6, the fact that the shear rate is much greater in the experiments means that $\mathcal{K}_a$ (the ratio of the shear rate to the adsorption rate) and $\mathcal{K}_0$ (the ratio of the shear rate to the rate of micellar disassociation) are not as large as they are in a more realistic scenario. This means that the behaviour we are fitting to is somewhat different from the full scale situation.

We solve the full model as in Section 6.5.5, taking the breakup rate as (6.3.43) and the daughter drop distribution as (3.2.32). At $z = \hat{z}$, we set ϕ as (4.4.6) and use the initial conditions (6.5.10), where the free monomer concentration, c_0, at $z = \hat{z}$ is given by $c_0 + c_0^{N_m} = \mathcal{C}_0/\hat{\delta} = 2\beta Q_s/(\delta_0\omega_0\hat{\delta})$. Recall Q_s is the surfactant flux. We now determine how to set the value of Q_s from the experimental dispersant to oil ratio. The molecular mass of AOT is $444.56\,\mathrm{g\,mol^{-1}}$ (Moulik and Mukherjee, 1996). Its density at 25^oC is around $700\,\mathrm{kg\,m^{-3}}$ (D'Aprano et al., 1992), and it is thought that the surfactant makes up around a tenth of the volume (personal communication, BP). Therefore, if the dispersant to oil ratio (DOR) is $1:R$, the dimensionless total concentration of surfactant is $C_R = 157.46/(c_{cmc}(1+R))\,\mathrm{mol/m^3}$.[2] In this section, we consider experiments where the surfactant is premixed with the oil so this is the total concentration $\mathcal{C}$ at $z = 0$. We determine the value of $\mathcal{C}$ at $z = \hat{z}$ using conservation of the flux of $\mathcal{C}$ i.e. the fact that $\int_0^\infty rW\mathcal{C}\,\mathrm{d}r$ is constant. At $z = 0$, since we assume the surfactant is premixed with the oil, $\mathcal{C} = C_R$ for $r < 1/2$ and zero otherwise. Therefore, the dimensionless flux, Q_s, of $\mathcal{C}$ is $Q_s = C_R/8$. Hence, $\mathcal{C}_0 = \beta C_R/(4\delta_0\omega_0)$. The values of $\mathcal{C}_0$ corresponding to the experimental dispersant to oil ratios are shown in Table 6.1.

[2] $C_R = \frac{1}{c_{cmc}} 700 \times 10^3 \times \frac{1}{444.559} \times \frac{1}{10} \times \frac{1}{1+R}$.



(a) $W_0 = 14.1\,\mathrm{m\,s^{-1}}, \sigma_0 = 0.0132$



(b) $W_0 = 11.3\,\mathrm{m\,s^{-1}}, \sigma_0 = 0.0151$

Figure 6.9: Comparison between model and small-scale experiments for different surfactant concentrations from no surfactant up to a dispersant to oil ratio of 1:25. We use data and parameters for (a) Experiment 1 and (b) experiment 4 in Table 4.1. We take $k_0^- = 1\,\mathrm{s^{-1}}$ so $\mathcal{K}_0 = 10^{-4}$. We set $\hat{z} = 2$. The parameters $K_{00} = 0.7, C = 11$ and $k_a = 0.11\,\mathrm{m\,s^{-1}}$ have been fitted with the case with no dispersant and that with 1:50 dispersant to oil ratio, corresponding to experiment 1. The fully developed drop size distribution from the model, at $z = 400$, is shown in blue. The experiments are in dashed red and the associated error bars are in red.

As in Section 4.5.6, following Brandvik et al. (2013), we take the experimental results for the volume fraction of oil drops in each of the measured bin sizes and normalise by the sum of the observed volume fractions. To compare with the model, we take our computed value of ϕ, truncate it so it only varies over the experimental drop sizes, and then for each bin i calculate $\int_{v_i}^{v_{i+1}} \phi \, \mathrm{d}v$, namely the volume fraction of oil between v_i and v_{i+1}. We normalise the resulting distribution by its sum. We fit the model to two experiments, one with no dispersant and the other with a dispersant to oil ratio of 1:50. Both correspond to experiment 1 from Table 4.1. We fit the parameters K_{00} and C in the breakup rate (6.3.43)-(6.3.45), as well as k_a, the adsorption parameter, to minimise L_2 norm between the model and experiments in these two cases.

Recall that in Section 4.5.6, to fit to the experiment with no dispersant, we only fit K_{00}. The natural extension here would then be to fit K_{00} and k_a. However, we find if we do so, the model does not predict any great variation in ϕ with increasing surfactant concentrations. The reason for this is that the surface tension, σ, only appears multiplied by C in the breakup rate (6.3.43) and the value of C is too small. Therefore, here we fit K_{00}, C and k_a. We find that this also addresses the issue in Section 4.5.6 where the model consistently underestimates the amplitude of the distribution. Increasing C increases the critical drop size below which no drops can break up. This means that fewer medium drops break into small drops and so proportionately more large drops break into medium drops, thus increasing the amplitude of the distribution.

We set $K_{00} = 0.7$, $C = 11$, $k_a = 0.11\,\mathrm{m\,s^{-1}}$. Our results compared to experiment 1 from Table 4.1 for a range of surfactant concentrations are shown in Figure 6.9(a) and show good agreement. To better evaluate this fit, we also compare our model to experiment 4 from Table 4.1, as shown in Figure 6.9(b). Here, for small surfactant concentrations, much of the distribution lies outside the experimentally measurable drop size range. This may account for the disparity between the model and experiments. For larger dispersant to oil ratios, this is no longer the case and the agreement is fairly good.

Figure 6.9 illustrates the effect of adding different concentrations of surfactant. We see in Figure 6.9(a) that adding more surfactant decreases the volume fraction of the large droplets. In the experiment with no dispersant, there is a significant volume fraction of the largest drops but, when taking DOR 1:100, all the largest drops have broken up.

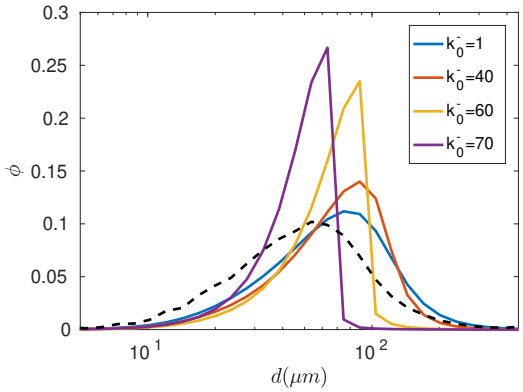


Figure 6.10: Variation of drop size distribution with varying k_0^-. We keep $K_{00} = 0.7, C = 11$ and $k_a = 0.11\,\mathrm{m\,s^{-1}}$ and vary k_0^- in the case in Figure 6.9(a) with dispersant to oil ratio (DOR) 1:25. Experimental data is shown by dotted black line.

It must be noted that, in the experiment that we fit to in Figure 6.9(a), there is not very good agreement between the model and experiment when the DOR is 1:25. The model predicts that the drop size distribution is almost the same for dispersant to oil ratios of 1:50 and 1:25. This is because, for a DOR of 1:25, the initial free monomer concentration is above the CMC. Therefore, any extra surfactant goes into producing more micelles, which cannot be adsorbed onto the droplet surface. This phenomenon is discussed further in Section 6.7. However, we do not see this effect in the experiments.

One possible reason for this is the value of k_0^- (the rate at which the micelles disassociate). We take $k_0^- = 1\,\mathrm{s^{-1}}$ here. Varying k_0^- only affects the case with DOR 1:25 because it is only here where c is significantly greater than one and so where there are sufficient micelles for the rate at which they disassociate to be important. We investigate the effect of changing k_0^- in the experiment in Figure 6.9(a) where the dispersant to oil ratio is 1:25. Our results are shown in Figure 6.10. Note that the results of the model appear jagged here because we are replicating the relatively few bins in the experimental data. We see that the mode can be captured by taking $k_0^- \approx 70\,\mathrm{s^{-1}}$. However, there is a significant discrepancy in the amplitude of the distribution.

Another more likely reason for the discrepancy is the choice of initial conditions for c and c_m. In (6.5.10), we assume that, at $z = \hat{z}$, c and c_m are in equilibrium (so $c = c_{eq}$, where $c_{eq} + c_{eq}^{N_m} = \mathcal{C}_0/\hat{\delta}$). However, as discussed in Sections 6.2.6 and 6.5.1, for the parameter values relevant to the experiments, $\mathcal{K}_0$ is small. This means that micellar breakup is slow so the association and disassociation of micelles between $z = 0$ and

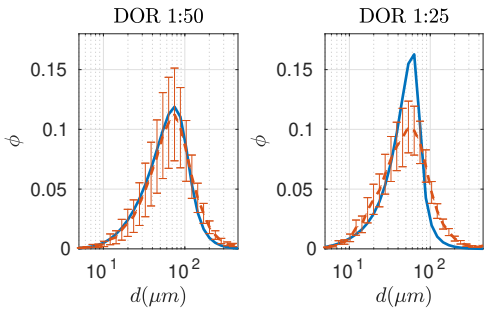


Figure 6.11: Considering a different value of the free monomer concentration at $\hat{z}$ for the same experiments in Figure 6.9(a) with DOR 1:50 and 1:25. In Figure 6.9, we assume c and c_m are in equilibrium at $\hat{z}$ and so take $c = c_{eq}$ where $c_{eq} + c_{eq}^{N_m} = \mathcal{C}_0/\hat{\delta}$. Here we take a larger initial value of c given by $c = c_{eq} + 1/5\left(\mathcal{C}_0/\hat{\delta} - c_{eq}\right)$. The fully developed distribution from the model is shown in blue, and the experiments and associated error bars are in red.

$z = \hat{z}$, which we are ignoring, may be important. Note that, except for the cases with DOR 1:50 and 1:25, there is a negligible concentration of micelles and so $c_{eq} \sim \mathcal{C}_0/\hat{\delta}$. We find that if we take some intermediate value, $c = c_{eq} + 1/5\left(\mathcal{C}_0/\hat{\delta} - c_{eq}\right)$, then the model and data show better agreement for higher dispersant to oil ratios. This is seen in Figure 6.11. Additionally, the reduction in breakup due to micelle formation only occurs at greater surfactant concentrations. The explanation of the experiments not being in equilibrium is possibly more plausible but, in any case, it may not be an issue in real situations where $\mathcal{K}_0$ is larger and c and c_m go to equilibrium more rapidly.

6.7 Adding different surfactant concentration

We have established that our models fit fairly well with experiments and have gained some initial insights into the effect of adding different amounts of surfactant to the jet. We now look to explore this further. In this section, we do so using real parameters rather than the experimental ones.

We use the fitted parameter values from Section 6.6, set $k_0^- = 1\,\mathrm{s}^{-1}$, and take realistic parameters for the jet and surfactant. We vary the value of $\mathcal{C}_0$ in the total surfactant concentration, given by $\mathcal{C} = \mathcal{C}_0/\delta$. Our results are shown in Figure 6.12. Note that the median and mode drops sizes in Figure 6.12(e)–(f) appear jagged here and, as in Figure 6.8, this staircase behaviour is due to the discretisation of droplet diameter; each 'stair' corresponds to one of the discrete drop diameters.

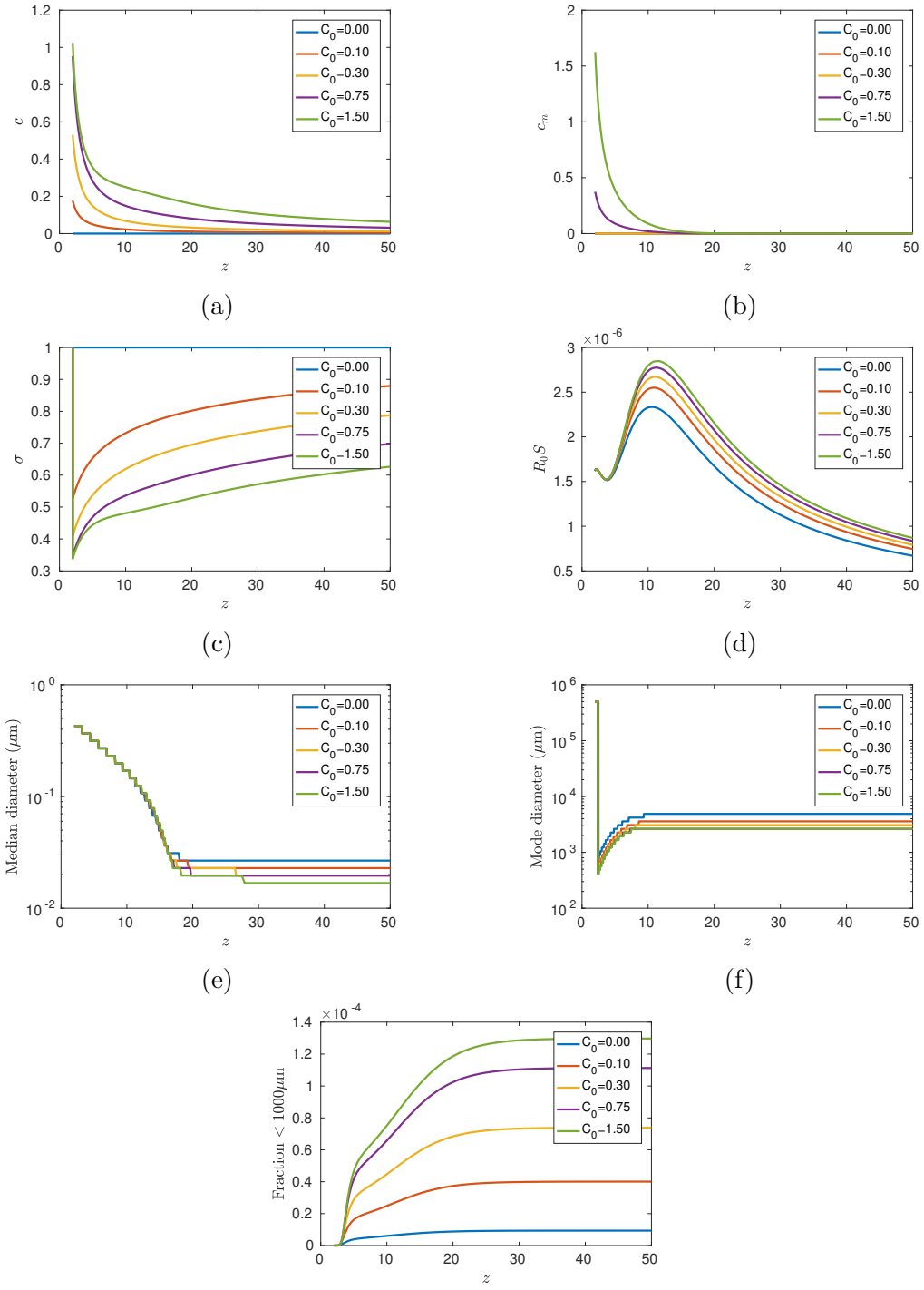


Figure 6.12: The effect of the addition of different concentrations of surfactant on drop and surfactant properties. We set $K_{00} = 0.7, C = 11$ and $k_a = 0.11\,\mathrm{m\,s^{-1}}$, and use realistic parameters for the jet and surfactant, with $k_0^- = 1\,\mathrm{s^{-1}}$. (a) Free monomer concentration, c; (b) micelle concentration, c_m; (c) surface tension, σ; (d) droplet surface area per unit volume, $\mathcal{R}_0 S$; (e) median dimensional drop diameter; (f) mode dimensional drop diameter; (g) fraction of drop with diameter below 1000 microns.

We observe that increasing the surfactant concentration amplifies its effect. It decreases the surface tension, increases the produced droplet surface area and increases the fraction of small droplets which are produced.

However, after a certain point, adding more surfactant has diminishing returns. This can be seen from the case where $\mathcal{C}_0 = 1.5$. Doubling the value of $\mathcal{C}_0$ from $\mathcal{C}_0 = 0.75$ to $\mathcal{C}_0 = 1.5$ only very slightly decreases the minimum surface tension in Figure 6.12(c). This is because, adding large concentrations of surfactant, with c greater than the CMC, means that, the extra surfactant monomers go into creating micelles rather than adsorbing onto droplet surfaces at small heights. At later heights, the additional micelles have broken up into free monomers which can adsorb to the droplet surface and so a greater difference in the surface tension is observed. Nevertheless, it is at smaller heights, where the energy dissipation is greatest, that droplet breakup is most effective. Therefore, this is where a decrease in surface tension has the greatest effect. This means that, as can be seen in Figure 6.12(g), doubling the value of $\mathcal{C}_0$ from $\mathcal{C}_0 = 0.75$ to $\mathcal{C}_0 = 1.5$, causes a relatively small increase in the fraction of droplets produced which are smaller than 1000 microns in diameter.

Adding surfactant increases the volume of small droplets produced by around one order of magnitude in Figure 6.12(g). However, we must note that even adding very large concentrations of surfactant does not dramatically reduce the median drop size distribution. This is because the median drop size is an indicator of the proportion of larger drops compared to small and medium drops. Adding surfactant allows medium drops to break into smaller drops but does not seem to greatly affect the volume of larger drops.

6.8 Addition of surfactant at different heights

Another question of interest is the optimum height of surfactant addition and the decrease in droplet breakup when surfactant is injected at other heights.

Let us first consider the effect of adding surfactant at different heights, $z = z_a$, in the jet. We compare the cases where $z_a = 5$, $z_a = 10$ and $z_a = 15$ with that where no surfactant is added. We take $K_{00} = 0.7$ and $C = 11$ in the breakup rate, and $k_a = 0.11\,\mathrm{m\,s^{-1}}$. We use realistic parameters for the jet and surfactant properties, with $k_0^- = 1000\,\mathrm{s^{-1}}$. The flux of surfactant, $Q_s = \int_0^\infty rW\mathcal{C}\,\mathrm{d}r$, is equal to $\mathcal{C}_0\delta_0\omega_0/(2\beta)$ so taking the same value of $\mathcal{C}_0$ in all three cases ensures that this quantity is kept fixed; we set $\mathcal{C}_0 = 2.722$ here. Droplet and surfactant properties are shown in Figure 6.13, and the drop size distribution at various heights is shown in Figure 6.14.

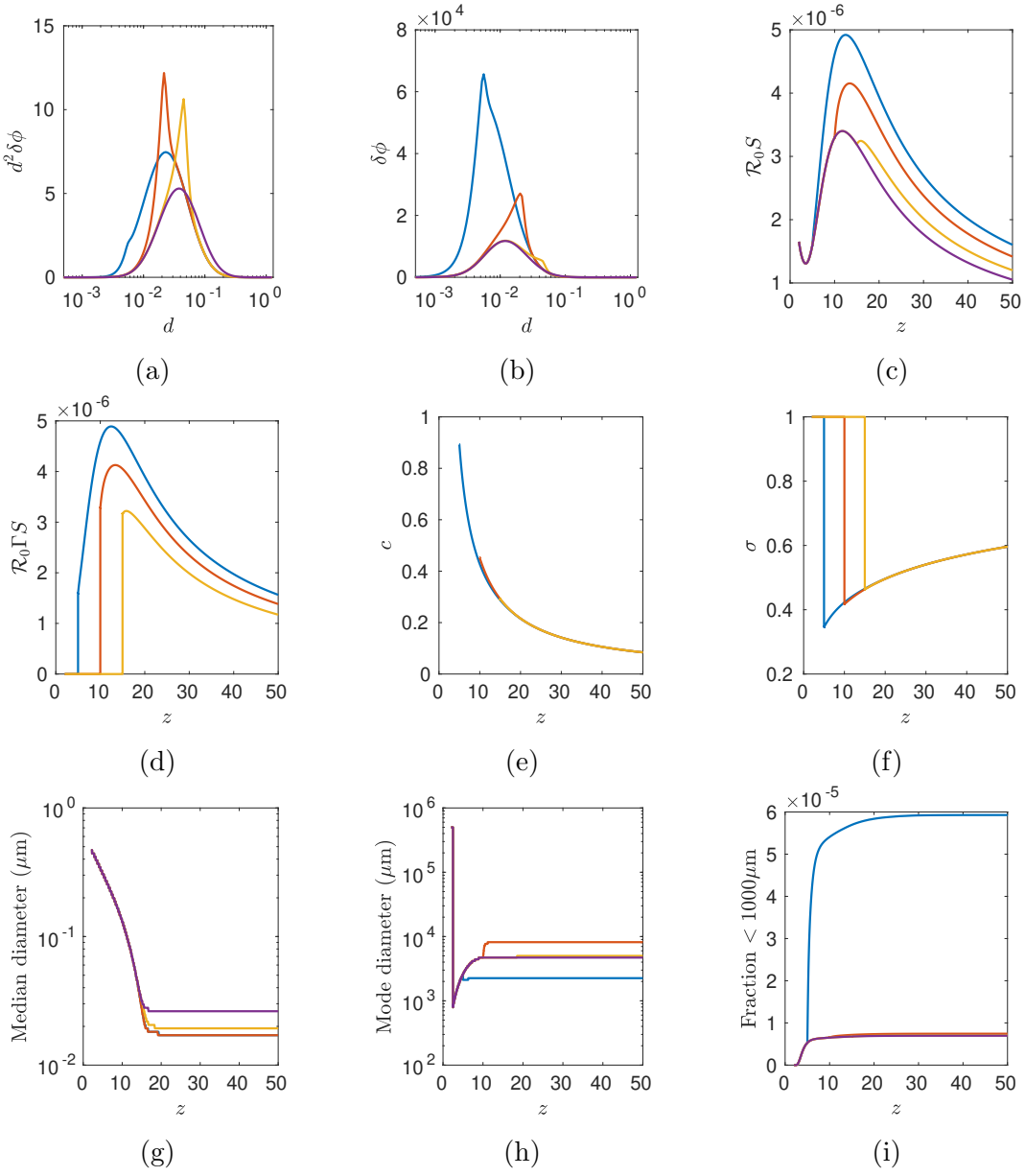
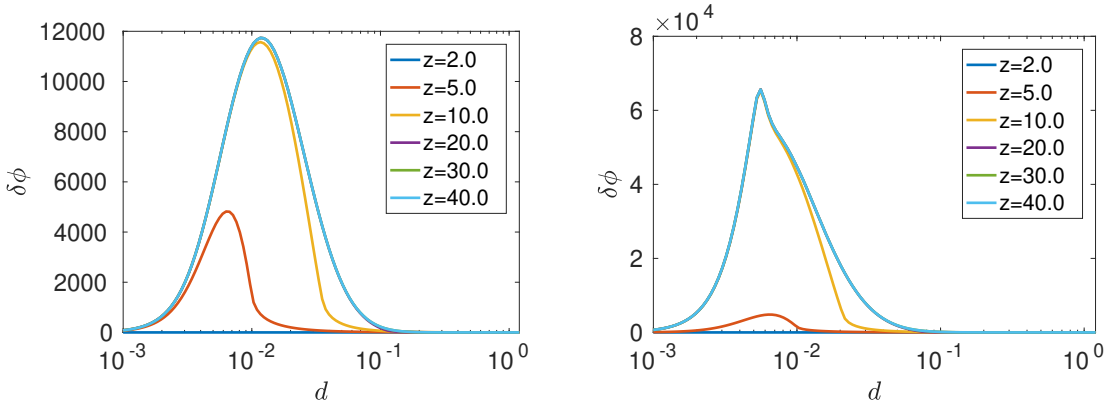
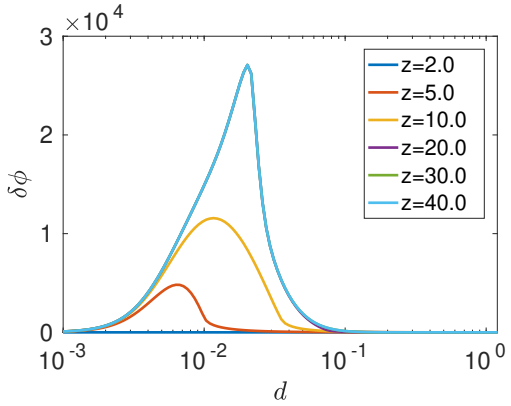


Figure 6.13: Evolution of droplet and surfactant properties with height, for different values of z_a. We take $z_a = 5$ (blue), $z_a = 10$ (red), and $z_a = 15$ (yellow). In certain cases we also compare with the case where no surfactant is injected (purple). (a) Fully developed drop size distribution (at $z = 55$) normalised to eliminate dilution and to better illustrate volume fraction of different sized drops, $d^2\delta\phi$; (b) fully developed distribution (at $z = 55$) normalised to eliminate dilution, $\delta\phi$; (c) droplet surface area, $\mathcal{R}_0 S$; (d) surface monomer concentration per unit volume, $\mathcal{R}_0\Gamma S$; (e) free monomer concentration, c; (f) surface tension, σ; (g) median drop size (microns); (h) mode drop size (microns); (g) fraction of droplets which have diameter below 1000 microns.

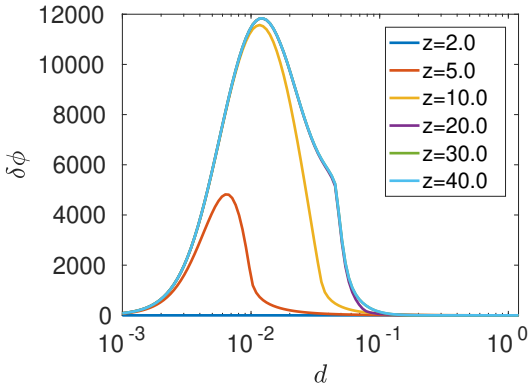


(a) No surfactant

(b) $z_a = 5$



(c) $z_a = 10$



(d) $z_a = 15$

Figure 6.14: Drop size distribution when injecting surfactant in the jet at different heights $z = z_a$. We normalise to eliminate dilution, plotting $\delta\phi$. We consider the realistic parameters from Section 6.2.6, set the fitting parameters as $K_{00} = 0.7$, $C = 11$ and $k_a = 0.11\,\mathrm{m\,s^{-1}}$, and take the total surfactant concentration such that $\mathcal{C}_0 = 2$. We compare the case where (a) no surfactant is injected with that where surfactant is injected at (b) $z_a = 5$; (c) $z_a = 10$; (d) $z_a = 15$.

We see that at the point of surfactant injection, droplet breakup immediately increases. The resulting drop size distributions have fewer large drops (see Figure 6.13(a)) and produce more droplet surface area (see Figure 6.13(c)) than in the case where no surfactant is added. Comparing the case where no surfactant is added and $z_a = 15$, we see, from Figure 6.13(a), that large drops break into medium drops. When the injection is at lower heights, say where $z_a = 5$, more large and medium drops break up and produce smaller drops.

We note that the median drop diameter in Figure 6.13(g) does not vary significantly with z_a. This is because, in Figure 6.13(a), the volume fraction of the larger drops is approximately the same in these cases and, as discussed previously, the median is an indicator of the largest drops. At large heights, there is only enough energy dissipation for very large drops to break up because of the Heaviside function in the breakup rate. What's more, a significant volume of large drops are produced in this process because we assume that when a drop breaks up, a significant volume fraction of droplets produced are around half the size of their parent drop. In all three cases, this process occurs and so the volume of large drops is relatively similar.

Apart from a small region near z_a, the surface tension is independent of the value of z_a, as seen in Figure 6.13(f). This can be explained by the asymptotics in Section 6.5.5, which shows that apart from at small heights in the jet where the breakup rate is larger, dilution is a dominant factor in the evolution of Γ and so σ. Therefore, it appears that it is best to inject the surfactant at as low a height as possible in the jet. This can also be demonstrated by examining the droplet surface area in Figure 6.13(c) and the volume fraction of droplets below a critical drop size (in this case 1000 microns) in Figure 6.13(i). Both are measures of the fraction of smaller droplets produced. To produce as great a volume fraction of small droplets as possible, injecting at smaller heights in the jet is most effective. Although the droplet surface area increases fairly linearly with z_a, we note that for $z_a \geq 10$ the volume fraction of 'small' drops is effectively that when no surfactant is added. This again comes down to the fact that the energy dissipation rapidly decreases with height and so only at smaller heights, even with the addition of surfactant, is there any possibility of the smaller drops breaking up and producing very small droplets.

The shapes of the distributions in Figure 6.13(b) are somewhat unusual and thus we now explore and discuss these in more detail. In Figure 6.14 we illustrate the evolution of drop size distribution with height for the different values of z_a. For $z < z_a$, the drop size distribution behaves as in Chapter 4. With increasing height, the critical size, $d_{\max}$, below which drops cannot break up, increases, and so only

larger drops break up, producing medium-sized drops; the mode drop size increases. For $z > z_a$, once the surfactant is injected, the distributions appear almost bimodal; there is a shift in the mode drop size distribution due to the decrease in surface tension encouraging further droplet breakup. In Figure 6.14(a), for $z_a = 5$, there is a suggestion of where the mode of the distribution would have been with no surfactant addition at $d \approx 0.01$ and we see the mode distribution with surfactant is at a lower drop size, at $d \approx 0.005$. For $z_a = 10$, the mode distribution is actually larger than that without surfactant (which can be also seen in Figure 6.13(h)). This is because, at $z = 10$, the energy dissipation has decreased to such an extent that, even with the addition of surfactants, only the medium and larger drops can break up. Through our choice of χ, we have imposed that when drops break up they produce a large volume of droplets around half the size of the parent drop, so this additional breakup produces droplets which are larger than the mode drop size without surfactant. Injecting surfactant higher up, at $z_a = 15$, causes some of the largest drops to break up and produce more medium drops at around $d \approx 0.04$. However, because the energy dissipation is fairly low by $z = 15$, except at large drop sizes, there is not a significant difference between the distribution in Figure 6.14(d) and that without the addition of surfactants in Figure 6.14(a).

To corroborate our results, we compare the model with small-scale experiments, where the surfactant is injected at the centre-line of the jet. The behaviour, seen in Figure 6.15, is generally similar. However, there are some disparities between the model and experiments. We notice that the model consistently under-predicts the volume fraction of small drops. This may be due to our choice of χ, the daughter drop distribution, or the fact that we have taken the largest drop size at the starting height to be the nozzle diameter i.e. $d_\infty = D$. Another possible limitation of our models is that they are width-averaged and assume that the surfactant becomes well-mixed in the jet as soon as it is added. This may be a particular issue in this section because, in reality, the surfactant can only be injected in a small region.

6.9 Conclusions

In this chapter we investigate the effect of surfactant on the breakup of droplets. We first consider simple 'box' models, where the droplets are subjected to a constant energy dissipation, and track the behaviour with time. We find there are various different time periods where the surface tension varies due to the interaction of surfactant and droplet breakup. Micelles disassociate into monomers, which can adsorb

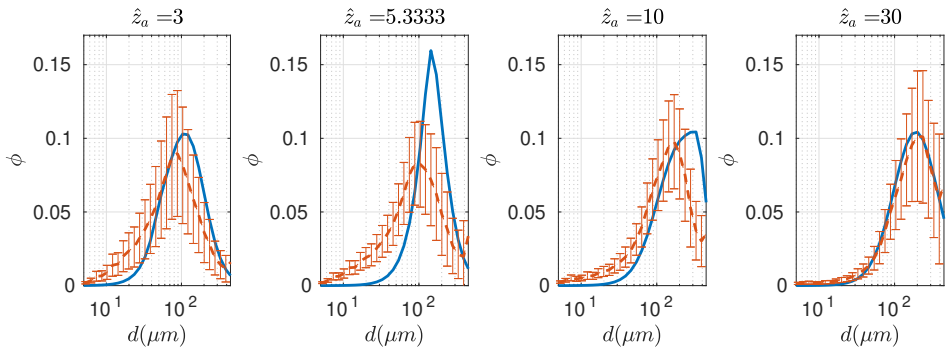


Figure 6.15: Comparison between model and small-scale experiments for different heights of surfactant injection. In this set of experiments, $D = 1.5 \times 10^{-3}\,\mathrm{m}$, $W_0 = 11.3\,\mathrm{m\,s^{-1}}$, $\sigma_0 = 0.0155\mathrm{kg\,s^{-2}}$ and the dispersant to oil ratio is 1:100. The parameters $K_{00} = 0.7, C = 11$ and $k_a = 0.11\,\mathrm{m\,s^{-1}}$ are chosen as in Section 6.6. The fully developed drop size distribution from the model, at $z = 400$, is shown in blue. The experiments are in dashed red and the associated error bars are in red.

onto droplet surfaces. The adsorption of surfactant makes it easier for droplets to break up and thus the droplet surface area increases. The interaction between the adsorbed surfactant concentration and droplet surface area has a significant effect. In these volume-averaged models, the breakup rate allows drops of any size to break up. This means that the droplet surface area will eventually increase to such an extent that there is too much area for the surfactant to be spread over. Then, for monomers to continue to adsorb onto drops, the micelle concentration rapidly decreases. This leads the monomer concentration to decrease and eventually the surface tension increases back to its undisturbed value.

We extend these volume-averaged models to consider the full volume range. Here, we additionally impose that small droplets cannot break up and thus do not allow the droplet surface area, S, to grow so significantly. Because of this, the surfactant concentration is so great that the majority remains in the bulk. This means that we can decouple the behaviour of c and c_m from that of Γ, S and ϕ.

Having understood the effect of surfactant addition on droplet breakup, we combine the surfactant and drop models with width-averaged models of a turbulent jet. We find that the behaviour has many similarities with that in the box models and various similar regions are observed. The main difference is the effect of dilution. It makes it more difficult for the surfactant to adsorb onto the droplets and causes a more rapid increase in the surface tension.

We examine both volume-averaged and full-volume models. Three regions can be identified. In the first, the surfactant rapidly adsorbs onto the surface of the

droplets; Γ rapidly increases and all other quantities remain the same. In the second region, when micelles are present, the surface concentration of surfactant, Γ, and drop size distribution, ϕ, are highly coupled with each other but independent of the bulk surfactant concentration. The micelle and bulk surfactant concentrations decrease due to dilution alone. The surface tension is at or close to its minimum value here. In the third region, which corresponds to the majority of the height of the jet, the only change in the surfactant concentrations is due to dilution, and the surface tension increases. This analysis is useful since we find that, throughout the jet, Γ can be determined independently of the evolution of both c and c_m.

We examine the effect of adding different concentrations of surfactant to the jet. We find that increasing the surfactant concentration allows greater droplet breakup. However, increasing the surfactant monomer concentration beyond the CMC has diminishing returns. This is because the additional surfactant forms micelles. These eventually disassociate into monomers which can adsorb onto the droplet surface and reduce the surface tension. However, by the height this has occurred, the energy dissipation is much smaller and the system is in the third region mentioned above, where the surface tension is increasing; the opportunity for significant droplet breakup has been missed. The important rate limiting parameter here is $\mathcal{K}_0$, which corresponds to the ratio of the rate at which the micelles disassociate to the jet's shear rate. An optimum surfactant would have a very large value of $\mathcal{K}_0$ so that the micelles would rapidly disassociate into monomers low down in the jet. This would cause a greater decrease in the surface tension at lower heights, where the energy dissipation is larger, and so would incite further droplet breakup.

We also investigate the effect of injecting the surfactant at different heights. We find that the global behaviour of the surface tension is essentially independent of the injection height. Therefore, it is best to inject the surfactant as close to the nozzle as possible. This would allow us to take advantage of the regions at low heights where the surface tension is lowest and the energy dissipation is greatest. Higher up the jet, even if surfactant has been injected here, the energy dissipation is too low for considerable droplet breakup to occur and only the largest drops break up.

Our models generally agree well with small-scale experimental results. There are three parameters which are fitted to the experiments; two relate to the breakup rate and the third, k_a, controls the rate at which surfactant adsorbs onto the droplet surface. However, the magnitude of some of the dimensionless parameters is different in the small-scale experiments and a realistic scenario. The models we have presented

give a useful indication of the implication of the differences between the behaviour in the lab and in an ocean setting.

In a deep-sea oil spill, a fixed quantity of dispersant is transported to the site of the oil spill and is injected over the course of a number of days. An interesting problem arises of how to best prescribe the flux of injected surfactant. An extension of the work here would be to pose and solve this optimisation problem, using the models in this chapter.

Chapter 7

Conclusions

7.1 Summary of Results

In this thesis we have combined models for a turbulent jet, the breakup of droplets and droplet-surfactant interactions to generate the drop size distribution at various locations in the jet. These models describe the breakup of droplets in a deep-sea oil spill.

We begin by considering the macroscale turbulent jet in Chapter 2. We use the inherent self-similarity of a turbulent jet to show that the velocity components and turbulent energy can be described using similarity solutions. We do not consider the similarity solution to the full $k-\epsilon$ model but assume that the eddy viscosity, ν_T, is constant; this means that the properties of the jet can either be described analytically or are simple to compute. Nonetheless, the model gives a very good representation of the solution compared to the numerical CFD results. Given that they are similarity solutions, they are not very accurate in describing the jet behaviour at small heights; the similarity solutions for velocity apply after a couple of jet diameters whilst that for the energy dissipation take around 15 jet diameters to hold. We can width-average these similarity solutions to produce one-dimensional jet models, which vary only with height. These are used extensively in this thesis as they are easier to understand and effectively replicate the jet's behaviour. An important variable introduced in this chapter is the energy dissipation, ϵ, which determines the energy available for droplet breakup. It decreases rapidly with height, decaying like z^{-4}.

We next turn to the microscopic droplet scale in Chapter 3. We introduce droplet population models which describe the breakup of drops and production of smaller droplets. The results of these models are strongly dependent on (i) the rate at which droplets break up and (ii) the range of droplet sizes produced when a drop breaks up (the daughter drop distribution); these are functions of, not only drop size, but also

jet behaviour (through the energy dissipation) and surfactant concentration. The remainder of this chapter outlines the different breakup rates and daughter drop distributions used and some motivation behind our choices. For much of the subsequent Chapters, 4 and 6, we choose a breakup rate which increases with drop size, reaches a maximum and then decreases. This captures the ideas that small drops have large surface stresses and are difficult to break up, and very large drops are also difficult to break. This breakup rate also includes a Heaviside function which prevents droplets smaller than a critical drop size from breaking up; for these droplets surface stresses are greater than the deformation from the energy in the turbulent jet.

In Chapter 4, we combine the large-scale jet and small-scale droplet models to produce drop size distributions at various locations in the jet. We do so here without the effect of surfactants.

The model shows that, with increasing height and with increasing width from the jet outlet, the droplets break up, decreasing in size. At intermediate heights, the distribution is bimodal as small droplets have been produced but some of the largest drops still remain. Once the largest drops have broken up, we find that the mode drop size increases slightly with height. This is because, due to the Heaviside function in the breakup rate, at greater heights only the larger drops can break up and these produce more medium-sized drops. Eventually, far from the nozzle, the turbulent energy decreases and droplet breakup slows; the distribution reaches a fully developed state.

There are three general approaches in this chapter. We first use the CFD numerics for the jet behaviour and solve numerically for ϕ. We can also numerically determine ϕ using the similarity solutions for the jet and, apart from at small heights, the results agree well with the full numerics. Finally, we width-average to obtain one-dimensional models in space. These simplified one-dimensional models capture the general behaviour reasonably well. The one-dimensional models are fitted with small-scale experiments to determine the parameter, K_{00}, which is a constant of proportionality in the breakup rate. We find the fully developed distribution predicted by model agrees fairly well with experimental results.

Whilst in Chapter 4 we calculate the drop size distribution, ϕ, solely numerically, in Chapter 5 we attempt to find similarity solutions to ϕ, using the jet similarity variable, ξ. We find that ϕ can be expressed an the integral of a continuous family of second kind similarity solutions.

An important parameter here is the volume dependent term in the breakup rate, denoted $K(v)$. In the case where K is monotonic, we can find a full formula for

ϕ. However, when K is non-monotonic (as is more physically realistic) this is more difficult. We instead find an approximate solution which neglects some of the terms which are small at large heights. This agrees fairly well with the numerics, except at small heights. However, it relies on various slightly *ad hoc* assumptions.

The similarity solutions for ϕ are mathematically interesting but practically are possibly not so useful. For similarity solutions to exist, we impose tight constraints on the form of the breakup rate, namely that the volume dependent term, $K(v)$, is separable from the energy dissipation. This means that we cannot include a Heaviside term in the breakup rate to impose that, after a certain height, smaller drops cannot break up, as is done in Chapters 4 and 6. Thus the results produced may not be completely physically realistic.

Finally, in Chapter 6, we introduce the effect of surfactants. We first consider a simple 'box' model, where the surfactant and droplets interact without the complications of the jet behaviour. The oil-water surface tension is controlled by the concentration, Γ, of surfactant monomers per unit area, which have adsorbed onto the surface of the oil droplets. We see that the surfactant monomers very quickly adsorb onto the drop surface and aid droplet breakup. With increasing time, micelles disassociate into monomers; this increases the reserve of monomers which can be adsorbed onto the droplet surface. If droplet breakup is large enough, the droplet surface area will increase to such an extent that there is not enough surfactant to fully cover the drops, and the surface tension starts to increase.

We extend these models to consider the effect of surfactant in a turbulent jet. The main difference with the 'box' models is that, here, dilution is a strong effect. It spreads out the surfactant monomers and oil droplets and so, at larger heights, Γ decreases more significantly. Useful insights are obtained by exploring the asymptotics of the model. We find that Γ does not depend on the evolution of the free monomer concentration, c, but merely on its initial value. Much of the free surfactant monomers remain in the bulk. At low heights, for say the first 10 nozzle diameters, Γ is instead highly dependent on the variation of droplet surface area. For the majority of the height of the jet, however, dilution is the main driver for Γ.

The width-averaged models are fitted to small-scale experiments. This process is used to determine the constant of proportionality in the breakup rate, K_{00}, the parameter C in the breakup rate which controls the critical drop size below which no drops can break up, and the rate of surfactant adsorption onto the droplets, k_a. There is good agreement between the model and experiments.

We examine the question of how much surfactant should be added to the system. As expected, increasing the surfactant concentration improves the breakup process. However, adding surfactant where the free monomer concentration, c, is above the CMC has diminishing returns. This is because the additional monomers form micelles which only break up and become available to adsorb onto the oil droplets after some height in the jet. By this height the regions with the greatest energy dissipation have been passed and the additional decrease in surface tension has less of an effect on droplet breakup. We also investigate where in the jet the surfactant should be injected. We find that the most important regions for droplet breakup are at small heights where the surface tension is at its minimum and energy dissipation is largest. So it seems best to inject the surfactant as close to the nozzle as possible.

7.2 Future Work

We have made progress in modelling the droplet breakup in a turbulent jet, and the effect of surfactant injection into the system. However, in order to be able to make said progress, there are a number of simplifying assumptions we have made. We highlight these assumptions, their appropriateness, and the limitations they place on the applicability of our models, and discuss possible changes and improvements. We also highlight certain areas where further investigations could be useful.

- One of the major simplifications we make is to consider a water jet with a small volume fraction of oil. Whilst we believe this is a reasonable assumption at larger heights where dilution has spread out the oil droplets, it may not be so appropriate at smaller heights. Therefore, it would be interesting to explore a multiphase approach. Here we could no longer separate the macroscopic and microscopic scales since the oil could no longer be treated as droplets. A multiphase approach would allow us to consider a higher oil volume fraction or perhaps an oil spill which releases a mixture of oil and gas. In addition, in Chapter 6 we briefly mentioned that the surfactant AOT also forms reverse micelles in a bulk oil phase - this would be an interesting effect to explore and we would be able to do so using a multiphase approach. However, it must be noted this approach would be far more computationally complex.

- In Chapter 2, we model a purely momentum driven jet, neglecting the subsequent buoyancy driven plume. This is a fairly good assumption as the majority

of the droplet breakup will occur in the momentum-driven region. Nevertheless, it may be interesting to include the effects of buoyancy and ocean currents which occur at much greater heights. This could be coupled with models for the proliferation of microbes to provide a more comprehensive picture of the effect of the oil spill and the injection of dispersants.

- In determining the breakup rates in Chapter 3, we have relied on empirical scaling laws. These are difficult to test against experiments and thus there is still some uncertainty as to whether the breakup rate we have chosen is appropriate. It would be interesting to more fully investigate the effect of different breakup rates on the drop size distribution. In particular, we assume throughout this thesis that the daughter drop distribution, χ, only depends on drop size and it may be interesting to relax this simplification. The drop size distributions produced by various different choices of γ and χ could be fitted with and compared to experimental data from Brandvik et al. (2014), Brandvik et al. (2013), and Johansen et al. (2013). In this thesis we have used only a selection of these experimental results and so there is data available to do additional comparisons. However, these experiments only measure the fully developed drop size distribution. To more accurately and reliably predict the correct forms for the breakup rate functions, it would be useful to have empirical data on the evolution of ϕ with height in the jet. The only attempt to record this has been in large-scale experiments by (Johansen et al., 2001) but the authors warn that their measured drop size distributions may be inaccurate and thus their results have not been used in this thesis.

- There is some uncertainty in the value of some of the parameters we used in the surfactant models of Chapter 6, in particular the rate at which surfactant monomers adsorb onto droplets and the total concentration of surfactant given the volume of dispersant injected. It would be useful to have access to experiments where these could be determined more accurately.

- The surfactant behaviour in the jet is explored using width-averaged models in Chapter 6. There are two main limitations in using the width-averaged models. Firstly, they implicitly assume that the surfactant becomes well mixed across the jet as soon as it is injected. In addition, they are based on the jet similarity solutions from Chapter 2 and so do not hold for small z. This means that we must make a reasonable guess of the surfactant concentrations at some height

$\hat{z} > 0$ where we start the model. These issues could be resolved by numerically solving the full axisymmetric problem, which was set up in Section 6.4. This may have the most significant effect on the results of Section 6.8, where we consider the difference in injecting surfactant at different heights in the jet. The surfactant is typically injected, using a fine nozzle, in a small region of the jet. It must then be mixed by the jet to reach the oil droplets and this would be difficult higher up the jet, where there is a much greater width for the surfactant to spread over. An axisymmetric model may be able to better capture this physical phenomenon. In general, the surfactant may not be injected at the jet's centre line and we would then need to consider a non-axisymmetric model.

Appendix A

Boundary conditions for $k-\epsilon$ numerical implementation

A.1 Wall functions

This section is predominantly based on the discussions of wall functions in Versteeg and Malalasekera (2007), Kuzmin et al. (2007), Kuzmin and Hamalainen (2014), and Pope (2000).

Consider the region close to a wall in a turbulent flow, governed by the $k-\epsilon$ model given by (2.2.4), (2.2.9), (2.2.11) and (2.3.1). Whilst the outer flow is high Reynolds number and viscosity is negligible, in the inner region near the wall we need to account for viscous effects. It is computationally expensive to do so. Instead, wall functions are used which approximate the flow at some distance from the wall.

As in the literature we present these wall functions in a two-dimensional setting. The wall lies along the x-axis (at $y=0$) and y is the perpendicular distance from the wall. The mean velocity is $\mathbf{U}=(U,V)$, where U is the velocity parallel to the wall. Near the wall, U and V are independent of x. By mass conservation and assuming no flux at the wall, V is identically zero and so we only need to determine $U(y)$.

In the inner region, we rescale

$$U = u_\tau U^+, \tag{A.1.1}$$

and

$$y = \frac{\nu}{u_\tau} y^+. \tag{A.1.2}$$

Here u_τ is the so-called wall friction velocity, the characteristic velocity due to the wall. Matching yields the famous log law of the wall

$$U^+ = \frac{1}{\kappa} \log E y^+, \tag{A.1.3}$$

where the von Karmen constant is determined experimentally to be universally $\kappa = 0.41$ and, for a smooth wall, $E = 9.793$ (Versteeg and Malalasekera, 2007). Closer to the wall, between the wall and the so-called log-law region where (A.1.3) holds, there is an inner viscous sublayer. Here, the velocity satisfies

$$U^+ = y^+. \tag{A.1.4}$$

(For a good explanation of this see Schlichting and Gersten (2003)).

At the point, y_c^+, where the viscous sublayer and the log law region meet, for (A.1.3) and (A.1.4) to both hold, we must have

$$y_c^+ = \frac{1}{\kappa} \log E y_c^+, \tag{A.1.5}$$

yielding

$$y_c^+ = 11.53. \tag{A.1.6}$$

The near wall behaviour is generally set at some point, y_P, in the log-law region, so for $y_P^+ > 11.53$. Here the velocity, U_P, is given by (A.1.1) and (A.1.3), and the turbulent kinetic energy and energy dissipation are given by

$$k_P = \frac{u_\tau^2}{\sqrt{C_\mu}} \tag{A.1.7}$$

and

$$\epsilon_P = \frac{u_\tau}{\kappa y}. \tag{A.1.8}$$

as in (Pope, 2000).

However, for numerical robustness, these conditions are not used directly. Instead we introduce the nominal friction velocity as

$$u_\tau^* = C_\mu^{1/4} k_p^{1/2} \tag{A.1.9}$$

and the nominal distance from the wall

$$y_P^{+,*} = \frac{y_P u_\tau^*}{\nu}, \tag{A.1.10}$$

which follows from (A.1.2). From (A.1.8), the boundary condition for ϵ is then

$$\epsilon_P = \frac{u_\tau^*}{\kappa y_P}. \tag{A.1.11}$$

We also impose that there is no flux of the gradient of the turbulent energy through the wall so

$$\nabla k \cdot \mathbf{n} = 0 \text{ at } y = y_P. \tag{A.1.12}$$

The nominal mean velocity, using (A.1.3), is given by

$$U_P^* = \frac{u_\tau^*}{\kappa} \log\left(E y_P^{+,*}\right). \tag{A.1.13}$$

However, for numerical robustness, we do not set this but instead set the nominal eddy viscosity

$$\nu_{T,P}^* = \nu \left(\frac{\kappa y_P^{+,*}}{\log(E y_P^{+,*})} - 1 \right). \tag{A.1.14}$$

We present a heuristic argument for the choice (A.1.14). The shear stress is specified as

$$(\nu + \nu_T) \frac{\partial U}{\partial y} = (u_\tau^*)^2 \frac{U_P}{U_P^*}. \tag{A.1.15}$$

Then since $\partial U / \partial y \sim U_P / y$, we set

$$(\nu + \nu_T) = \frac{u_\tau^* y_P}{U_P^*}. \tag{A.1.16}$$

Rearranging and using (A.1.10) and (A.1.13) yields (A.1.14).

Appendix B

Extra surfactant asymptotics

B.1 Box - η, $\mathcal{R}_0$, $1/\mathcal{K}_0$, $1/\mathcal{K}_a$, $1/N_m$ small

We now consider the case where, as in Section 6.3.3, $\mathcal{R}_0$, $1/\mathcal{K}_0$, $1/\mathcal{K}_a$, $1/N_m$, and θ are small, but we also take η to be small. As in (6.5.18), we set

$$\mathcal{K}_0 = \varepsilon^{-1}\hat{\mathcal{K}}_0, \quad \mathcal{K}_a = \varepsilon^{-1}\hat{\mathcal{K}}_a, \quad N_m = \varepsilon^{-1}\hat{N}_m, \quad \mathcal{R}_0 = \varepsilon\hat{\mathcal{R}}_0, \quad \eta = \nu\hat{\eta}, \tag{B.1.1}$$

where $\varepsilon, \nu \ll 1$. For small η there are various distinguished limits depending on the relative sizes of η and $\mathcal{K}_a$, and these will be explored. For all intents and purposes, we take θ to be order one. However, in this section, we will find that in certain regions, $1-\Gamma = \mathcal{O}(\eta)$ or $1-\Gamma = \mathcal{O}(1/\mathcal{K}_a)$ and this could yield negative values of σ in (6.3.3); θ must therefore satisfy the constraints that $\theta < 1/\log(\mathcal{K}_a)$ and $\theta < -1/\log(\eta)$. Therefore, we treat $\log(\eta)$ and $\log(1/\mathcal{K}_a)$ as order one.

We again solve (6.3.18)–(6.3.22) subject to initial conditions (6.3.14) and (6.3.9) with $c_0 = 1 + 1/N_m$ so the surfactants are injected into the system above the CMC. We find five distinct time regions. These are illustrated in Figure B.1 for parameter values $\eta = \mathcal{R}_0 = 1/\mathcal{K}_0 = 1/\mathcal{K}_a = 1/N_m = 10^{-2}$. We also take $\Phi_0 = 0.5$, $\gamma_0 = 6$ and $\theta = 0.2$.

$\boldsymbol{T_1}$ In T_1, for $t \lesssim \mathcal{O}(\varepsilon)$, the behaviour is given by taking the results in Section 6.3.3 in the limit of small η. Hence, all quantities are constant except Γ which is given, from (6.3.23), by

$$\Gamma \sim 1 - \exp\left(-\varepsilon^{-1}\hat{\mathcal{K}}_a c_0 t\right). \tag{B.1.2}$$

The surface surfactant concentration rapidly increases to close to its maximum value. Correspondingly the surface tension decreases linearly, namely

$$\sigma \sim 1 - \varepsilon^{-1}\hat{\mathcal{K}}_a c_0 \theta t. \tag{B.1.3}$$

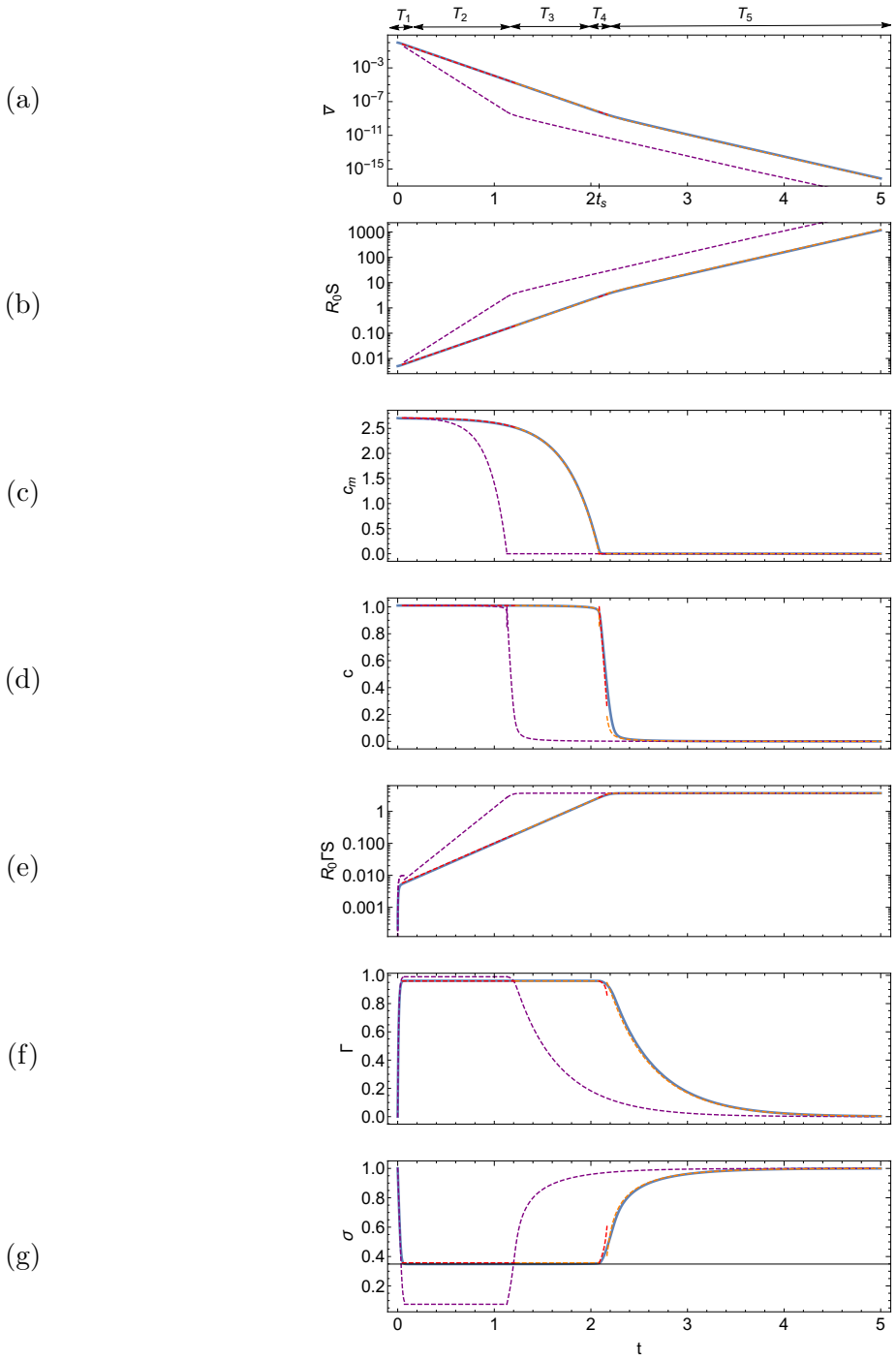


Figure B.1: Variation of droplet and surfactant behaviour with time, when setting $\eta = \mathcal{R}_0 = 1/\mathcal{K}_0 = 1/\mathcal{K}_a = 1/N_m = 10^{-2}$. Other parameter values are given by $\Phi_0 = 0.5$, $\gamma_0 = 6$ and $\theta = 0.2$. The numerical solution is shown in blue, and the asymptotics are shown in alternative dashed lines (orange for T_1, T_3 and T_5, red for T_2 and T_4). The asymptotics for η order one from Section 6.3.3 are in purple. (a) Average drop volume $\bar{v}$; (b) drop surface area $\mathcal{R}_0 S$; (c) micelle concentration c_m; (d) free monomer concentration c; (e) adsorbed surfactant concentration per unit volume, $\mathcal{R}_0 \Gamma S$; (f) adsorbed surfactant concentration per unit area, Γ; (g) surface tension σ.

This seems like the model allows the surface tension to take negative values at finite time but, as t increases the assumption that the other quantities are constant becomes less appropriate and this regime ends.

T_2 Again, T_2 represents the initial region where $c > 1$. Here, as in Section 6.3.3, c and c_m are given by (6.3.24)–(6.3.25). However, different behavior occurs depending on the relative sizes of η and $\mathcal{K}_a$.

If $\mathcal{K}_a\eta \gg 1$ (so $\nu/\varepsilon \gg 1$) then, as in Section 6.3.3, Γ and $\overline{v}$ are given by (6.3.27)–(6.3.31).

For $\mathcal{K}_a\eta \sim 1$ (i.e. $\nu/\varepsilon \sim 1$), all terms in (6.3.20) balance. This means that

$$\Gamma \sim 1 - \varepsilon\Gamma_1. \tag{B.1.4}$$

Here the order ε term is important as Γ appears as $\log(1-\Gamma)$ in the surface tension σ in (6.3.3). To leading order, (6.3.20) yields

$$\frac{1}{S}\frac{dS}{dt} = \hat{\mathcal{K}}_a\left[\Gamma_1 - \frac{\nu}{\varepsilon}\hat{\eta}\right]. \tag{B.1.5}$$

Using (6.3.18)–(6.3.19) we find that

$$\frac{1}{S}\frac{dS}{dt} = \frac{\gamma_0}{3}\left[1 + \theta\log\left(\varepsilon\Gamma_1\right)\right]^{-2/5}, \tag{B.1.6}$$

so equating these expressions gives an implicit formula for Γ_1, namely

$$\Gamma_1 = \frac{\nu}{\varepsilon}\hat{\eta} + \frac{\gamma_0}{3\hat{\mathcal{K}}_a}\left[1 + \theta\log\left(\varepsilon\Gamma_1\right)\right]^{-2/5}. \tag{B.1.7}$$

From (B.1.7), Γ_1 is constant and hence the surface tension is constant, given by

$$\sigma \sim 1 + \theta\log\left(\varepsilon\Gamma_1\right). \tag{B.1.8}$$

Surface tension depends on properties of the surfactant, through $\mathcal{K}_a$ and η, and the breakup rate, through Γ_1. Equation (B.1.8) yields

$$\overline{v} \sim \exp\left(-\gamma_c t\right), \tag{B.1.9}$$

where γ_c is a different constant to that in Section 6.3.3, given by

$$\gamma_c = \gamma_0\left[1 + \theta\log\left(\varepsilon\Gamma_1\right)\right]^{-2/5} \tag{B.1.10}$$

and so, from (6.3.19),

$$S = \Phi_0\exp\left(\frac{\gamma_c}{3}t\right). \tag{B.1.11}$$

Here, as in Section 6.3.3, there is enough surfactant that, even though the drops are rapidly breaking and the droplet surface area is rapidly increasing, the surfactant concentrations remain approximately constant.

In the case where $\mathcal{K}_a\eta \ll 1$ and $\nu/\varepsilon \ll 1$, the left hand side and the first term on the right hand side of (6.3.20) balance. Hence, as above,

$$\Gamma \sim 1 - \varepsilon\Gamma_1, \tag{B.1.12}$$

where, analogous to (B.1.7), Γ_1 is a constant given by

$$\Gamma_1 = \frac{\gamma_0}{3\hat{\mathcal{K}}_a}\left[1 + \theta\log\left(\varepsilon\Gamma_1\right)\right]^{-2/5}. \tag{B.1.13}$$

$\boldsymbol{T_3}$ By some time $t \sim \mathcal{O}(1/\gamma_c\log(\varepsilon))$, the droplet surface area per unit volume, S, will increase such that $\varepsilon S \sim \mathcal{O}(1)$. In this region, we rescale S and $\overline{v}$ as in (6.3.32)–(6.3.32), c and c_m are then given by (6.3.35)–(6.3.34), and the remaining variables are as in T2. The micelle concentration is starting to decrease, which in turn decreases the concentration of free monomers, which go to maintaining the surface concentration per unit area Γ.

$\boldsymbol{T_4}$ At $t = t_s$, the micelle concentration has decreased such that $c_m = 0$ and this sets t_s corresponding to (6.3.36). For T_4, $c < 1$ and from (6.3.22),

$$c \sim \mathcal{C}_0 - \hat{\mathcal{R}}_0\Gamma\hat{S}. \tag{B.1.14}$$

For $\mathcal{K}_a\eta \gg 1$, we proceed as in Section 6.3.3. However, otherwise, unlike (6.3.37), we cannot necessarily assume the free and surface surfactant concentrations are in equilibrium. For $\mathcal{K}_a\eta \sim 1$, all three terms in (6.3.20) balance and so the problem becomes numerically solving (6.3.18) and (6.3.20) for $\overline{v}$ and Γ, given (B.1.14). If $\mathcal{K}_a\eta \ll 1$, the behaviour is similar - we just take the limit $\eta \to 0$.

$\boldsymbol{T_5}$ After some time, $c \sim 0$ and so all the surfactant has adsorbed to the oil droplets. By (6.3.22),

$$\hat{\mathcal{R}}_0\Gamma\hat{S} \sim \mathcal{C}_0. \tag{B.1.15}$$

Then the right hand side of (6.3.20) is approximately zero so the free and surface monomers are in equilibrium and $\hat{v}$ satisfies (6.3.38).

The results of our asymptotics and the numerical solution of (6.3.18)–(6.3.22) with initial conditions (6.3.9), are shown in orange in Figure B.1. We see that the asymptotics and numerics agree well.

Although η is small, rather than order one as in Section 6.3.3, the behaviour is qualitatively fairly similar. In Figure B.1, we also plot the simpler asymptotics from Section 6.3.3 which do not take into account the smallness of η and see that these do capture the qualitative behaviour. The main difference is they predict the droplets break up more rapidly and so the surfactant concentrations start decreasing much earlier.

Bibliography

R. G. Alargova, I. I. Kochijashky, M. L. Sierra, and R. Zana. Micelle aggregation numbers of surfactants in aqueous solutions: a comparison between the results from steady-state and time-resolved fluorescence quenching. *Langmuir*, 14(19): 5412–5418, 1998.

B. P. BP Brent Crude assay, 2014. `http://www.bp.com/en/global/bp-crudes/assays/europe/brent.html` [Accessed: 2015-06-26].

U. C. Bandara and P. D. Yapa. Bubble sizes, breakup, and coalescence in deepwater gas/oil plumes. *Journal of Hydraulic Engineering*, 137(7):729–738, 2011.

G. I. Barenblatt. *Scaling, Self-Similarity, and Intermediate Asymptotics: Dimensional Analysis and Intermediate Asymptotics*, volume 14. Cambridge University Press, 1996.

P. J. Brandvik, Ø. Johansen, F. Leirvik, U. Farooq, and P. S. Daling. Droplet breakup in subsurface oil releases–Part 1: Experimental study of droplet breakup and effectiveness of dispersant injection. *Marine Pollution Bulletin*, 73(1):319–326, 2013.

P. J. Brandvik, Ø. Johansen, U. Farooq, G. Angell, and F. Leirvik. *Sub-Surface Oil Releases - Experimental Study of Droplet Distributions and Different Dispersant Injection Techniques - Version 2. A Scaled Experimental Approach Using the SINTEF Tower Basin.* SINTEF report no: A26122. Trondheim Norway, 2014.

P. J. Brandvik, E. Davies, D. F. Krause, P. A. Beynet, M. Agrawal, P. Evans, et al. Subsea mechanical dispersion, adding to the toolkit of oil spill response technology. In *SPE International Conference and Exhibition on Health, Safety, Security, Environment, and Social Responsibility*. Society of Petroleum Engineers, 2016.

C. J. W. Breward and P. D. Howell. Straining flow of a micellar surfactant solution. *European Journal of Applied Mathematics*, 15(5):511–531, 2004.

C. J. W. Breward, I. M. Griffiths, P. D. Howell, and C. E. Morgan. Straining flow of a weakly interacting polymer–surfactant solution. *European Journal of Applied Mathematics*, 26(05):743–772, 2015.

R. V. Calabrese, T. P. K. Chang, and P. T. Dang. Drop breakup in turbulent stirred-tank contactors. Part I: Effect of dispersed-phase viscosity. *American Institute of Chemical Engineers Journal*, 32(4):657–666, 1986.

C.-H. Chang and E. I. Franses. Modified Langmuir Hinselwood kinetics for dynamic adsorption of surfactants at the air/water interface. *Colloids and Surfaces*, 69(2-3): 189–201, 1992.

C.-H. Chang and E. I. Franses. Adsorption dynamics of surfactants at the air/water interface: a critical review of mathematical models, data, and mechanisms. *Colloids and Surfaces A: Physicochemical and Engineering Aspects*, 100:1–45, 1995.

J. Clark, G. M. Coelho, C. Huber, and A. Lewis. *BP Oil Spill Dispersant Use Manual*. BP, 2014.

P. H. Clay. The mechanism of emulsion formation in turbulent flow. *Proceedings of the Section of Sciences*, 43:852–965, 1940.

S. B. Collins and J. G. Knudsen. Drop-size distributions produced by turbulen pipe flow of immiscible liquids. *American Institute of Chemical Engineers Journal*, 16 (6):1072–1080, 1970.

C. A. Coulaloglou and L. L. Tavlarides. Description of interaction processes in agitated liquid-liquid dispersions. *Chemical Engineering Science*, 32(11):1289–1297, 1977.

A. D'Aprano, I. D. Donato, M. Goffredi, and V. T. Liveri. Volumetric and transport properties of Aerosol-OT reversed micelles containing light and heavy water. *Journal of Solution Chemistry*, 21(4):323–332, 1992.

P. Davidson. *Turbulence: An Introduction for Scientists and Engineers*. Oxford University Press, USA, 2015.

T. A. Driscoll, N. Hale, and L. N. Trefethen. *Chebfun Guide*. Pafnuty Publications, Oxford, 2014.

Y. Fan, Y. Li, G. Yuan, Y. Wang, J. Wang, C. C. Han, H. Yan, Z. Li, and R. K. Thomas. Comparative studies on the micellization of sodium bis (4-phenylbutyl) sulfosuccinate and sodium bis (2-ethylhexyl) sulfosuccinate and their interaction with hydrophobically modified poly (acrylamide). *Langmuir*, 21(9):3814–3820, 2005.

A. Ganesan. *I. A Modified $k - \epsilon$ Turbulence Model for High Speed Jets at Elevated Temperatures. II. Modeling and a Computational Study of Spliced Acoustic Liners.* PhD thesis, Florida State University, 2005.

N. A. Ghazzawi and N. J. Rabadi. Self-similar solutions for axisymmetric jets using two turbulence models. *International Journal for Numerical Methods in Engineering*, 37(11):1915–1930, 1994.

R. P. Hesketh, A. W. Etchells, and T. W. F. Russell. Experimental observations of bubble breakage in turbulent flow. *Industrial & Engineering Chemistry Research*, 30(5):835–841, 1991.

J. O. Hinze. Fundamentals of the hydrodynamic mechanism of splitting in dispersion processes. *American Institute of Chemical Engineers Journal*, 1(3):289–295, 1955.

J. O. Hinze. *Turbulence*. McGraw-Hill, New York, 1975.

X. Y. Hua and M. J. Rosen. Dynamic surface tension of aqueous surfactant solutions: I. Basic paremeters. *Journal of Colloid and Interface Science*, 124(2):652–659, 1988.

Ø. Johansen. DeepBlow–a Lagrangian plume model for deep water blowouts. *Spill Science & Technology Bulletin*, 6(2):103–111, 2000.

Ø. Johansen, H. Rye, A. G. Melbye, H. V. Jensen, B. Serigstad, and T. Knutsen. Deep Spill JIP experimental discharges of gas and oil at Helland Hansen-June 2000. *SINTEF Rep. 5TF66 F01082*, pages 1–159, 2001.

Ø. Johansen, P. J. Brandvik, and U. Farooq. Droplet breakup in subsea oil releases–Part 2: Predictions of droplet size distributions with and without injection of chemical dispersants. *Marine Pollution Bulletin*, 73(1):327–335, 2013.

D. Kuzmin and J. Hamalainen. *Finite Element Methods for Computational Fluid Dynamics: A Practical Guide*. Computational Science and Engineering. Society for Industrial and Applied Mathematics, 2014.

D. Kuzmin, O. Mierka, and S. Turek. On the implementation of the $k-\epsilon$ turbulence model in incompressible flow solvers based on a finite element discretisation. *International Journal of Computing Science and Mathematics*, 1(2-4):193–206, 2007.

C. H. Lee, L. E. Erickson, and L. A. Glasgow. Dynamics of bubble size distribution in turbulent gas-liquid dispersions. *Chemical Engineering Communications*, 61(1-6): 181–195, 1987.

W. J. Lehr. Review of modeling procedures for oil spill weathering behaviour. *Advances in Ecological Sciences*, 9:51–90, 2001.

Y. Liao and D. Lucas. A literature review of theoretical models for drop and bubble breakup in turbulent dispersions. *Chemical Engineering Science*, 64(15):3389–3406, 2009.

J. Lyklema. *Fundamentals of Interface and Colloid Science: Soft Colloids*, volume 5. Elsevier, 2005.

C. Martínez-Bazán, J. L. Montanes, and J. C. Lasheras. On the breakup of an air bubble injected into a fully developed turbulent flow. Part 1. Breakup frequency. *Journal of Fluid Mechanics*, 401:157–182, 1999a.

C. Martínez-Bazán, J. L. Montanes, and J. C. Lasheras. On the breakup of an air bubble injected into a fully developed turbulent flow. Part 2. Size PDF of the resulting daughter bubbles. *Journal of Fluid Mechanics*, 401:183–207, 1999b.

J. Michel, E. H. Owens, S. Zengel, A. Graham, Z. Nixon, T. Allard, W. Holton, P. D. Reimer, A. Lamarche, M. White, et al. Extent and degree of shoreline oiling: Deepwater Horizon oil spill, Gulf of Mexico, USA. *PLOS ONE*, 8(6):e65087, 2013.

B. R. Morton, G. Taylor, and J. S. Turner. Turbulent gravitational convection from maintained and instantaneous sources. In *Proceedings of the Royal Society of London A: Mathematical, Physical and Engineering Sciences*, volume 234, pages 1–23. The Royal Society, 1956.

S. P. Moulik and K. Mukherjee. On the versatile surfactant Aerosol-OT (AOT): its physicochemical and surface chemical behaviours and uses. *Proceedings – Indian National Science Academy Part A*, 62:215–236, 1996.

D. W. Murphy, X. Xue, K. Sampath, and J. Katz. Crude oil jets in crossflow: Effects of dispersant concentration on plume behavior. *Journal of Geophysical Research: Oceans*, 121(6):4264–4281, 2016.

I. D. Nissanka and P. D. Yapa. Calculation of oil droplet size distribution in an underwater oil well blowout. *Journal of Hydraulic Research*, 54(3):307–320, 2016.

E. A. Norse and J. Amos. Impacts, perception, and policy implications of the deep-water horizon oil and gas disaster. *Environmental Law Institute, Washington, DC*, 40:11058, 2010.

P. N. Papanicolaou and E. J. List. Investigations of round vertical turbulent buoyant jets. *Journal of Fluid Mechanics*, 195:341–391, 1988.

E. L. Paul, V. A. Atiemo-Obeng, and S. M. Kresta. *Handbook of Industrial Mixing: Science and Practice*. John Wiley & Sons, 2004.

A. J. Paullay, R. E. Melnik, A. Rubel, S. Rudman, and M. J. Siclari. Similarity solutions for plane and radial jets using a $k-\epsilon$ turbulence model. *Journal of Fluids Engineering*, 107(1):79–85, 1985.

S. B. Pope. *Turbulent Flows*. Cambridge University Press, 2000.

M. J. Prince and H. W. Blanch. Bubble coalescence and break-up in air-sparged bubble columns. *American Institute of Chemical Engineers Journal*, 36(10):1485–1499, 1990.

H. Schlichting and K. Gersten. *Boundary-Layer Theory*. Springer Science & Business Media, 2003.

T.-H. Shih, W. W. Liou, A. Shabbir, Z. Yang, and J. Zhu. A new $k-\epsilon$ eddy viscosity model for high Reynolds number turbulent flows. *Computers & Fluids*, 24(3):227–238, 1995.

S. A. Socolofsky, E. E. Adams, M. C. Boufadel, Z. M. Aman, Ø. Johansen, W. J. Konkel, D. Lindo, M. N. Madsen, E. W. North, C. B. Paris, et al. Intercomparison of oil spill prediction models for accidental blowout scenarios with and without subsea chemical dispersant injection. *Marine Pollution Bulletin*, 2015.

H. Tennekes and J. L. Lumley. *A First Course in Turbulence*. MIT Press, 1972.

Y. Tominaga and T. Stathopoulos. Turbulent schmidt numbers for CFD analysis with various types of flowfield. *Atmospheric Environment*, 41(37):8091–8099, 2007.

C. Tsouris and L. L. Tavlarides. Breakage and coalescence models for drops in turbulent dispersions. *American Institute of Chemical Engineers Journal*, 40(3):395–406, 1994.

N. Vankova, S. Tcholakova, N. D. Denkov, I. B. Ivanov, V. D. Vulchev, and T. Danner. Emulsification in turbulent flow: 1. Mean and maximum drop diameters in inertial and viscous regimes. *Journal of Colloid and Interface Science*, 312(2):363–380, 2007.

H. K. Versteeg and W. Malalasekera. *An Introduction to Computational Fluid Dynamics: The Finite Volume Method*. Pearson Education, 2007.

H. G. Weller, G. Tabor, H. Jasak, and C. Fureby. A tensorial approach to computational continuum mechanics using object-oriented techniques. *Computers in Physics*, 12(6):620–631, 1998.

D. C. Wilcox. *Turbulence Modeling for CFD*, volume 2. DCW Industries, La Cañada, CA, 1993.

Poojitha D Yapa and Zheng Li. Simulation of oil spills from underwater accidents I: Model development. *Journal of Hydraulic Research*, 35(5):673–688, 1997.

L. Zhao, M. C. Boufadel, S. A. Socolofsky, E. Adams, T. King, and K. Lee. Evolution of droplets in subsea oil and gas blowouts: Development and validation of the numerical model VDROP-J. *Marine Pollution Bulletin*, 83(1):58–69, 2014a.

L. Zhao, J. Torlapati, M. C. Boufadel, T. King, B. Robinson, and K. Lee. VDROP: A comprehensive model for droplet formation of oils and gases in liquids-incorporation of the interfacial tension and droplet viscosity. *Chemical Engineering Journal*, 253: 93–106, 2014b.

L. Zheng, P. D. Yapa, and F. Chen. A model for simulating deepwater oil and gas blowouts-Part I: Theory and model formulation. *Journal of Hydraulic Research*, 41 (4):339–351, 2003.